THE UNIVERSITY *of* EDINBURGH

Crustal properties and heat flow in Victoria Land and Wilkes Subglacial Basin, Antarctica - forward and inverse modelling of gravity and magnetic data coupled with petrological measurements

Maximilian Lowe

Doctor of Philosophy

THE UNIVERSITY OF EDINBURGH

2024

For Lara, Tom, and Emil

Abstract

This thesis utilises inverse and forward modelling of geophysical data to investigate the subglacial geology and influences on geothermal heat flow in northern Victoria Land and in Wilkes Subglacial Basin, a region of East Antarctica adjacent to the Transantarctic Mountains (TAM) that is comprehensively covered by ice. The TAM separate the warmer lithosphere of the Cretaceous-Tertiary West Antarctic Rift System and the colder and older provinces of East Antarctica. Low velocity zones beneath the TAM imaged in recent seismological studies have been interpreted as warm low-density mantle material, suggesting a strong contribution of thermal support to the uplift of the TAM.

For the first of the three main studies that comprise this thesis (Chapter 2), I present new Curie Point Depth (CPD) and geothermal heat flow (GHF) maps of the northern TAM and adjacent Wilkes Subglacial Basin (WSB) based exclusively on high resolution magnetic airborne measurements. I find shallow CPD and high GHF beneath the northern TAM, reinforcing the hypothesis of thermal support of the topography of the mountain range. Additionally, the study demonstrates that limiting spectral analysis to areas with a high density of aeromagnetic measurements increases the resolution of CPD estimates, revealing localised shallow CPD and associated high heat flow. The recovered CPD and GHF estimates show a good agreement to sparse in situ GHF measurements and the location of active volcanoes.

Subglacial geology influences geothermal heat flow. However, due to the lack of geological information most GHF models do not account for a heterogeneous crust since direct geological information in Antarctica is limited to ice-free regions along the coast, high mountain ranges or isolated nunataks. Therefore, indirect methods are required to interpret subglacial geology and heterogeneities in crustal properties. In Chapter 3 I present a 3D crustal model of density and susceptibility distribution in WSB and TAM region based on joint inversion of airborne gravity and magnetic data. This model reveals a large body located in the interior of WSB interpreted as a batholithic structure, as well as a linear dense body at the margin of the adjacent Terre Adélie Craton. Density and susceptibility relationships are used to interpret petrophysical properties and permit the reconstruction of those crustal bodies. The petrophysical relationships indicate that the postulated batholith is granitic in composition. Emplacement of a large volume of granite batholiths can potentially elevate local geothermal heat flow significantly. Finally, I present a new conceptual tectonic model for this region based on the inversion results.

Chapter 4 addresses the validation of geophysical modelling to constrain hidden subglacial geology. I present a new rock property catalogue containing density and susceptibility measurements on 320 rock samples from northern Victoria Land. This catalogue is used to assess the reliability of local and regional scale inverse results. I compare those measurements to the

inverted values. The close correspondence between inverted and measured rock properties allows us to predict locations of rock types where currently such information is missing.

The presented studies in this thesis demonstrate that subglacial geology matter for geothermal heat flow. Future heat flow models need to account for heterogeneities in subglacial geology and crustal properties in terms of radiogenic heat production and thermal conductivity. To obtain such information the broader geophysical community needs to increase their efforts of imaging geology hidden beneath the ice in Antarctica. This thesis provides evidence that joint inversion of gravity and magnetic airborne data is a powerful tool to infer subglacial geology and crustal properties. Furthermore, this thesis provides a workflow that can be followed for joint inversion studies in other areas of Antarctica where sufficient airborne data exists.

Lay Summary

Antarctic is, for the western world, the most remote continent on planet Earth. Furthermore, the harsh environmental conditions in Antarctica provide an additional obstacle for studying this content. As a result, the geoscientific understanding of Antarctica is lagging behind most other continents especially Europe, north America, or Australia. However, there is no reason to believe that Antarctica is less complex from a geoscientific viewpoint than any other continent. Moreover, Antarctica is covered by ice up to 4.5 km thick. This makes studying the geology of the continent even more difficult because most of the geology (more than 99%) is hidden beneath the ice. To overcome the obstacle of a thick ice sheet geophysical experiments and measurements can be used to infer the sub ice geology and properties of the crust (Earths thin outermost layer). To do so, physical quantities are measured and based on the measured behaviour it is possible, indirectly, to draw conclusions on certain crustal properties. Typical geophysical applications include measuring the gravitational field (measuring the acceleration due to gravity [g]) to infer density distribution in the subsurface or measuring the magnetic field to inferred susceptibility distributions. Other methods include measuring the delay travel time between sending out electromagnetic waves and receiving backscatter energy of those waves to infer the depth of the interface between ice and hard rock or measuring acoustic (pressure) waves originating from earthquakes or from synthetic sources to infer, for example, regions within the Earth where waves travel faster or slower depending on density and temperature or to illuminate the interface between Earth's crust and mantle (called the Mohorovičić discontinuity, or Moho) by measuring the offset in arrival times between pressure and shear waves. Geophysical gravity and magnetic measurements can be carried out using a variety of platforms from ground-based measurements through airborne based platforms such as airplanes, helicopters, and UAVs to satellite mission. The rule of thumb for both gravity and magnetic measurements is that the resolution decreases with increasing height above Earth surface. Therefore, the best data is recovered by ground measurement. However, due to the harsh environmental condition alluded to earlier, covering large areas with ground-based surveys is extremely challenging. Satellite and airborne measurements provide a good spatial coverage with the disadvantage of lower data resolution. We have established so far, that subglacial and crustal properties can be revealed by geophysical methods. We therefore turn our attention now to the justification why it is time critical to understand the subsurface (solid Earth) in Antarctica. The solid Earth can influence the overlying ice sheet through the thermal properties of the crust. Geothermal heat flow is a process in the solid Earth that describes the heat transport from the interior of the Earth to the surface. However, radiogenic decay of elements commonly concentrated in crustal rocks can elevate local heat flow and therefore contribute to the melting at the base of the ice sheet and facilitate ice flow. Those processes

can contribute to the instability of the thick ice sheets and in last consequence contribute to future sea level rise. To identify regions of potentially high geothermal heat flow as well as predict heat flow values we first need to understand geology and crustal properties and crustal heterogeneities in those regions. Additionally, understanding the solid Earth in Antarctica is also crucial to understand the subglacial geology and its evolution through geological times scales.

This thesis sets out to reveal properties of the solid Earth in part of Antarctica, to identify crustal thermal structures, illuminate potential rock provinces and their potential emplacement and evolution, as well as validate geophysical models with petrophysical measurements on rock samples from Antarctica, thereby bridging geophysical modelling and geological observables in the subsequently presented chapters (chapter 2-4).

Chapter 2 uses airborne magnetic data to estimate the depth to the bottom of magnetised material. Rocks lose their magnetic properties at the so-called Curie Temperature at 580°C. By finding the bottom of the magnetic source body you can assume you found the 580°C isotherm, which can be used to infer knowledge about the thermal structure of the crust. However, this approach usally assumes that the crust is a homogeneous body. In chapter 3 the magnetic as well as gravity field, measured from airplanes, is used to reveal heterogeneities in the crustal domain by inferring susceptibility and density distributions. Those distributions are used to infer a tectonic sketch of the crustal evolution. Chapter 4 uses the previously established density and susceptibility distribution together with a new rock catalogue containing density and susceptibility measurements on Antarctic rock samples to validate a geophysical model, thereby relating the geophysical model to geological observables.

Acknowledgements

Science is a team sport, and I am grateful for so many amazing and inspiring people I had the pleasure of meeting and working with during my PhD, who all contributed to the success of the thesis in front of you.

First at all, I want to thank the SENSE CDT for providing the funding for the project through a NERC studentship as well as the University of Edinburgh and the British Antarctic Survey (BAS) for providing the infrastructure to succeed in a PhD. In this regard I also want to thank Fausto Ferraccioli for proposing this PhD project to the SENSE CDT. Furthermore, I want to thank all occupants of the student office room 39, present and past, as well as all the members of the Palaeo Environments, Ice Sheets and Climate Change team (PICC) at BAS, especially the regular attendees of PICC coffee, for a lovely and caring work environment.

I want to thank Graeme Eagles and Robert Bingham, who examined this thesis, for an enjoyable viva and their thorough reports, suggestions, and their time spend on this thesis.

During my PhD I had the pleasure of working with the most amazing co-authors possible including Ben Mather, Max Moorkamp, Antonia Ruppel, Nikola Koglin, Andreas Läufer, Mareen Lösing, Teal Riley, Jonas Liebsch, and Mikhail Ginga. I sincerely hope that we can materialise further collaborations and projects in the future.

During my PhD I have experienced the highs and lows of academia and I am grateful to a number of people who not only provide valuable scientific guidance, scientific feedback, and supervision, but also helped me navigate academia in periods of hardship, effectively steering the PhD project back into calm waters. I want to dedicate the next paragraphs to those heroes.

I want to begin by thanking Robert Larter and Daniel Goldberg for taking on the role of a supervisor without being deeply involved the research discipline. Both have demonstrated sharp analyses of my research environment at a moment when my view was heavily blurred, and I thank both for being a voice of reason during this critical time and for facilitate the restructuring of the supervisory team. Next, I want to express my full-hearted gratitude to Chris Green for being an exceptional supervisor and taking the time to have a weekly science chat during the time of restructuring the PhD project and supervisory team, providing ideas to test and being interested in my scientific advancement. Those regular meetings played an enormous part in realising my first PhD paper before being phased down once I had grown into a more independent working PhD student, while Chris always made time in his diary for me when needed.

Subsequently, I want to thank the two persons, who have contributed the most to the success of my PhD thesis and are the reason for staying on the PhD program. First up Tom Jordan, who volunteered a considerable amount of his time by accepting me as a refugee student. I have learned a lot from Tom regarding airborne surveying, potential field modelling, controlling

Geosoft and in particular Antarctic geology. Tom restored my faith in academia on a weekly basis by an extraordinary positive outlook on science, especially questionable reviews, and life in general. This leads us to Jörg Ebbing who is not only a great scientist, mentor but the kindest soul I know in academia. He holds the most responsibility of where I am today. He appeared at every importing career junction over the last 8 years. From the decision to switch from geosciences in my bachelor studies to geophysics for my master studies; providing the opportunity of being a research assistant (HiWi) during my master studies while slowly infesting me with the love for potential field data; providing the opportunity of getting a foot into the academic door by providing multiple short term contracts after the birth of my twin boys, which kept us off the street; encouraging me to leave my comfort zone by making the move over into Brexit Britan during a global pandemic; helping to restructure my PhD project. Both Tom and Jörg are academic role models and if I can become a fraction of the scientists they are I will be pleased with myself.

Most importantly, perhaps, I want to thank the love of my life Lara and our equally loved twin boys Tom and Emil. Only their tireless and unconditionally support has enabled me to write this thesis. I have not done a PhD; we have completed a PhD! I love you to the moon and back and thank you for being the positive force in my life.

Lastly, I would like to thank my mother, Helen Lowe and my grandmother Christa Lowe for believing in us and the continuous financial support, which allowed us, as a family of four, a somewhat financially trouble-free life in England. It is a chicken and egg question if NERC PhD stipends are too low for families or rents and childcare are too high in England. Regardless, dear United Kingdom please get a grip.

Declaration

I declare that the thesis has been composed by myself and that the work has not be submitted for any other degree or professional qualification.
I confirm that the work submitted is my own, except where work which has formed part of jointly-authored publications has been included. My contribution and those of the other authors are described in the opening sections of Chapters 2, 3 and 4. I confirm that appropriate credit has been given within this thesis where reference has been made to the work of others.

Maximilian Lowe

Date: 02/09/2024

Contents

Figures and Tables

Figures

Tables

Chapter 1

Introduction

Antarctica is covered by up to 4.5 km thick ice sheets (Fretwell et al., 2013; Morlighem et al., 2020). Therefore, more than 99% of Antarctic geology is hidden (Burton-Johnson et al., 2020). Direct geological information from rock outcrops is limited to ice free regions along the coast, high mountain ranges or isolated nunataks (Cox et al., 2023; Thomson and Cooper, 1993), while the origin of geological material transported by glaciers themselves is often ambiguous (Figure 1.1).

1.1 Motivation

Understanding subglacial geology and crustal properties is not only crucial for better understanding of the geological evolution of Antarctica but also very important for modelling the interaction between the solid Earth and the cryosphere, particularly through geothermal heat flow (GHF), which links both domains (Burton-Johnson et al., 2020; Reading et al., 2022). Petrophysical rock properties such as radiogenic heat production and thermal conductivity, which are tightly linked to Antarctica's geology, can influence local heat flow (Artemieva and Mooney, 2001; Burton-Johnson et al., 2020; Hasterok and Chapman, 2011; Reading et al., 2022). For instance GHF can influence the rheology of the ice as well as cause basal melting, and both processes have the potential to facilitate enhanced ice flow, contributing to instability of the ice sheet and global sea level rise (Larour et al., 2012; Llubes et al., 2006; Pittard et al., 2016; Winsborrow et al., 2010). It has been demonstrated that a difference of 20 $\mathrm{mW\ m^{-2}}$ in Antarctica can lead to an increase in basal melt rate from 6.7 to 18 $\mathrm{km^3\ yr^{-1}}$ (Llubes et al., 2006). Furthermore, GHF remains poorly constrained in Antarctica and therefore it is common practice in ice-sheet modelling to use a constant average or a long wavelength GHF field (low spatial resolution) (McCormack et al., 2022). A sensitivity study in Aurora Subglacial Basin in East Antarctica showed that meltwater estimates increase significantly in ice sheet models with increased GHF resolution, concluding that ice sheet models with a mean or spatial low resolution GHF model systematically underpredict melt water rates (McCormack et al., 2022). Furthermore, the same study showed that GHF is potentially the dominating heat

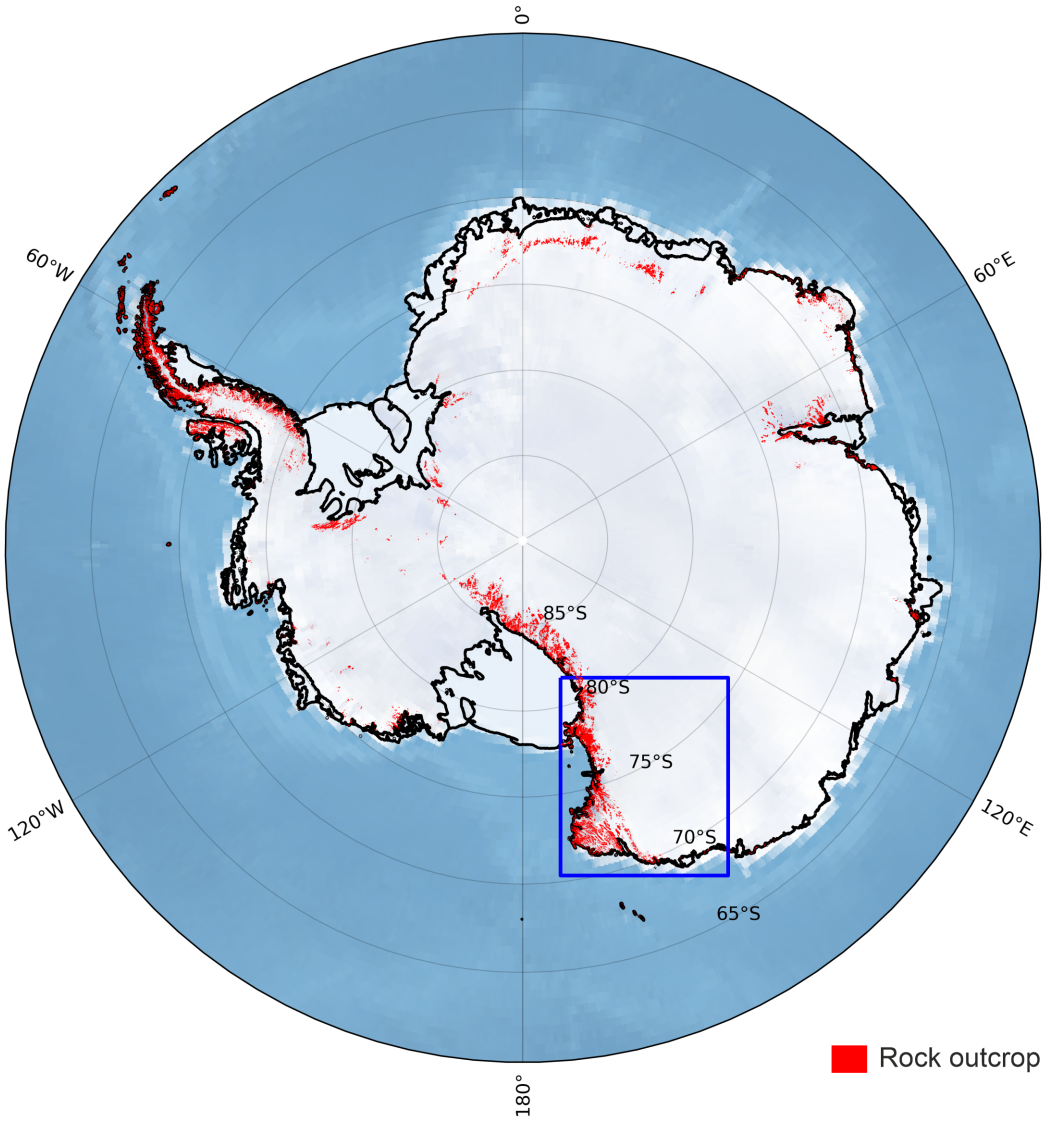

Figure 1.1: Rock outcrop and coastline data taken from GeoMap (Cox et al., 2023). Blue square marks the regional focus of this thesis, which includes northern Victoria land, the Transantarctic mountains, and Wilkes Subglacial Basin.

source where the ice sheet is flowing by sliding (defined where the surface speed is <300 $\mathrm{m\ yr^{-1}}$) (McCormack et al., 2022). To improve GHF predictions a better understanding of the subglacial geology and lithospheric properties are required beforehand.

1.1.1 Solid Earth

A wide range of geophysical methods is used to image subglacial geology and lithospheric properties including active seismic experiments (Eisen et al., 2015), passive seismological experiments (An et al., 2015; Hansen et al., 2016; Lloyd et al., 2020; Shen et al., 2018), magnetotelluric (Wannamaker et al., 2017), radar (Fretwell et al., 2013; Morlighem et al., 2020), gravity (Scheinert et al., 2016), magnetics (Golynsky et al., 2018), and GNSS (Global navigation satellite system) data (Whitehouse et al., 2019). Ground based geophysical observations are challenging due to the remote location of Antarctica and the harsh environmental conditions and therefore often require combined international logistical efforts for their realisation. Therefore, survey coverage of ground based geophysical campaigns is limited (Lloyd et al., 2020; Whitehouse et al., 2019). Gravity and magnetic data products from satellite missions such as the GOCE (Gravity field and steady-state ocean circulation explorer) mission from the European Space Agency (ESA) (Bouman et al., 2016), or the satellite magnetic model LCS-1 based on the SWARM Satellite mission (Olsen et al., 2017), provide a full data coverage of Antarctica except close to the South Pole due to the inclination of the satellite orbit (Jordan et al., 2018). However, the resolution of the potential field signal decreases with increasing distance between the source and sensor ($1/\mathrm{r}^2$ for gravity and $1/\mathrm{r}^3$ for magnetics respectively, where r is the distance) (Blakely, 1996). Therefore, satellite data contain only long wavelength information resulting in the lowest resolution for local crustal modelling, whereas ground survey data contain the short wavelength content and therefore, provide the best suitable data resolution for crustal model results. Airborne platforms such as airplanes, helicopters and UAVs provide the possibility to mount gravity, magnetic, and radar systems simultaneously for geophysical surveys. Airborne surveys are settled in between the two end members (ground surveys and satellites), providing increased coverage while capturing shorter wavelength content through the lower altitude compared to satellites (Ferraccioli et al., 2009a; Golynsky et al., 2018; Jordan et al., 2013; Mieth et al., 2014; Mieth and Jokat, 2014; Ruppel et al., 2018; Scheinert et al., 2016).

Gravity and magnetic maps provide a powerful tool to trace geological units and tectonic processes such as suture zones, cratonic blocks, and rift margins, even correlating with features on other continents that used to be contiguous within the Gondwana supercontinent (Aitken et al., 2014; Ebbing et al., 2021; Finn et al., 2006; Goodge and Finn, 2010; Jordan et al., 2022). However, it is when applying forward or inverse modelling techniques, where density and susceptibility source bodies are placed with depths in the model domain to explain the observed gravity and magnetic field, that we can draw quantitative conclusions about the lithosphere and its properties, such as crustal thinning and rifting, sediment location and thickness, crustal intrusion emplacement, and crustal architecture overall (Aitken et al. 2014; Ferraccioli et al. 2011, 2009a; Frederick et al. 2016; Goodge and Finn 2010; Jordan et al. 2013, 2023; Lösing et al. 2022; Bingham et al. 2012; Morales-Ocaña et al. 2023).

Additional crustal characteristics, which can be derived from potential field data include depth

to the magnetic sources, for instance the bottom of the magnetised layer. This is linked to the 580 ℃ Curie temperature (temperature at which crustal materials typically lose their magnetic properties) (Telford et al., 1990) and therefore is a proxy for thermal boundaries in the mid to lower crust, commonly referred to the Curie Point Depth (CPD), which can be used as a proxy for GHF (Dziadek et al., 2021; Martos et al., 2017). CPD can also be used in magnetic modelling to constrain the maximum depth of the modelled magnetic body. Furthermore, the top of the magnetic layer can be inferred by magnetic data using, for example, Werner deconvolution, Euler deconvolution, or Tilt Derivative applications. These methods can be applied to identify, for example, the depth to basement of nonmagnetic sedimentary basins (Aitken et al., 2014; Bingham et al., 2012; Ferraccioli et al., 2009a; Frederick et al., 2016; Jordan et al., 2023). Moreover, the transition zone between crust and mantle, the so-called Moho interface, can be estimated with a high accuracy by a single seismometer method called receiver function analysis (Chaput et al. 2014; Finotello et al. 2011; Hansen et al. 2009, 2016). Receiver functions provide a point measurement of the Moho discontinuity but due to the lack of station coverage the Moho interface is spatially not well constrained by receiver functions. Gravity inversion based on gravity data measured by satellites provides large spatial coverage of Moho depth variation with the caveat of having higher uncertainties associated with them compared to receiver functions (Pappa et al., 2019a). Since the Moho interface is a deep lithospheric feature, which usually shows smooth variation, long wavelength satellite data are sufficient to capture long wavelength variation in the Moho interface, while modelling shallower and more rapid changing crustal structure require higher resolution data (short wavelength) provided by ground or airplane-based measurements.
Recent internationally coordinated efforts to close gravity and magnetic airborne data gaps in Antarctica combined with open access / data sharing agreements provide the possibility of localised crustal and lithospheric studies with the best possible data coverage. Prominent geophysical data compilations are the magnetic data compilation ADMAP-2 (Golynsky et al., 2018) and the gravity data compilation AntGG (Scheinert et al., 2016), which build the foundation of the presented PhD thesis.

1.1.2 Heat flow

An important conceptual interface between the solid Earth and the cryosphere in Polar regions is GHF (Burton-Johnson et al., 2020; Davies, 2013; Fahnestock et al., 2001; Reading et al., 2022). Heat flow describes the transport of heat energy from the interior of the Earth to the surface (Pollack et al., 1993; Turcotte and Schubert, 2014). Primordial heat remaining from the formation of the Earth is not the only heat source contributing to GHF. A second relevant heat source is radioactive decay of isotopes of heat producing elements such as potassium, thorium, and uranium, which are concentrated in crustal rocks (Beardsmore and Cull, 2001; Burton-Johnson et al., 2020; Lowrie, 2007; McDonough and s. Sun, 1995). Heat

can be transported by either conduction or convection (Beardsmore and Cull, 2001; Turcotte and Schubert, 2014). Conduction describes the heat transport from a warmer to a colder region and therefore a spatial temperature variation is required, while convection describes the motion of material (Turcotte and Schubert, 2014). For the continental crust and lithosphere the dominating heat transport is conductive while convection is the dominant mechanism in the deeper mantle (Turcotte and Schubert, 2014)

Heat transport can be described by Fourier's law (Equation 1.1), which states that the heat flux (q) at a point is proportional to the temperature gradient at the given point (Turcotte and Schubert, 2014).

$$q = -\kappa \frac{\delta T}{\delta y} \tag{1.1}$$

where κ is thermal conductivity, y is coordinate of the direction of the temperature variation and T temperature. The minus sign indicates that the heat flow is in the direction of decreasing y (normally up for Earth) (Turcotte and Schubert, 2014). However, heat production is neglected here. Incorporating a crustal radiogenic heat production which exponentially decreases with depth yields equation (1.2) which provides the heat flux at any depth (Turcotte and Schubert, 2014).

$$q = -q_m - \rho H_0 h_r e^{-\frac{y}{h_r}} \tag{1.2}$$

Where H_0 is the surface radiogenic heat production rate per unit mass, h_r is a length scale for the decrease in H with depth, q_m boundary condition on the heat flux at depth, here mantle heat flux at the base of the lithosphere, ρ is the density of the material / slab (Turcotte and Schubert, 2014). For in depth heat transfer discussion and full derivation of heat transfer equations the reader to Turcotte and Schubert (2014, section 4.8, Continental Geotherms).

Rocks with a high concentration of heat producing elements such as potassium (K), thorium (Th), and uranium (U) can significantly increase local GHF. Granites are rocks that can have a high concentration of heat producing elements. Examples of granites with a high concentration of heat producing elements, which elevate local GHF in Antarctica, include granites in the Weddell Sea region (Leat et al., 2018) and southern Prydz Bay (Carson et al., 2014). An additional example is the granitic batholith in south west England (Cornwall) where a GHF anomaly of up to 138 $\mathrm{mW\,m^{-2}}$ is reported (Beamish and Busby, 2016). Therefore, understanding subglacial geology and crustal properties in terms of petrophysical parameters (density, thermal conductivity, and radioactive heat production) is crucial for heat flow estimation. However, direct geological information is largely missing in Antarctica as discussed above (Figure 1.1). Potential field modelling can provide estimates of density and susceptibility distribution in the subsurface and help identify geological provinces. The density and susceptibility relationship allows linking such provinces to rock types using measured dens-

ity and susceptibility values on rock samples. Moreover, petrophysical datasets containing density and susceptibility measurements, ideally on Antarctic rocks, are important to validate geophysical models. Rock catalogues containing either density (Sanchez et al., 2021) or susceptibility (Bozzo et al., 1992; Lanza and Tonarini, 1998; Ohneiser et al., 2015) values exist for Antarctic rocks. However, density and susceptibility measurements on the same rock sample are lacking in the literature. Such a rock catalogue would enable geophysical models to be validated with greater confidence. Therefore, some authors (e.g. Lösing et al. 2022) use a global rock catalogue or catalogues containing petrological properties on Australian rocks (Barlow, 2004) or from the Indian Shield (Subrahmanyam et al., 1981).

1.1.3 Geological overview of nothern Victoria Land

Northern Victoria Land (NVL) is located at the Pacific end of the Transantarctic Mountains (TAM) (Figure 1.2). The basement of the TAM consists of the western and inboard polymetamorphic and magmatic Wilson Terrane, the central volcanic and clastic Bowers Terrane, and the eastern turbiditic Robertson Bay Terrane, which formed by accretionary processes at the East Gondwana active continental margin during the late Ediacaran-early Palaeozoic Ross Orogeny (e.g. Goodge 2020). The metamorphic basement of the Wilson Terrane comprises low- to high-grade up to granulite-facies metamorphic rocks, involving, e.g., the Wilson metamorphic and polymetamorphic complexes, the Berg Group or the Wilson Schists. The metamorphic country rocks are intruded by the voluminous Granite Harbour Intrusive (GHI) Complex, including the Antarctic Oates Coast granitoids. The majority of the plutonic rocks consist of granitoids with subordinate intermediate to mafic varieties as well as some ultramafics. The Bowers Terrane comprises very low- to low-grade metavolcanics and associated metavolcaniclastics, which formed in an island arc or fore-/back-arc tectonic setting and grade into molasse-type clastic metasedimentary rocks (Bowers Supergroup, Figure 1.2). The outboard Robertson Bay Terrane consists of mostly distal turbidites of the Robertson Bay Group (Figure 1.2). The Wilson-Bowers terrane boundary is defined by the strongly deformed Lanterman-Mariner Fault Zone in the Lanterman Range and along the western margin of Mariner Glacier, whereas the Millen Schist Belt represents the boundary between the Bowers and Robertson Bay terranes. Post-Ross geology is characterised by the mid-Palaeozoic felsic Admiralty Igneous Complex comprising the Admiralty granitoids and the Gallipoli volcanics. They are unconformably overlain by late Palaeozoic to early Jurassic clastic Beacon Supergroup and sills and lavas of the Jurassic Ferrar Supergroup, i.e. Ferrar Dolerite and Kirkpatrick Basalt including the volcaniclastic Exposure Hill-type deposits (e.g. Ganovex Team and others 1987, Elliot et al. 2021. Youngest rocks in the region involve Cenozoic alkaline to peralkaline magmatic rocks of the McMurdo Igneous Complex, related to West Antarctic rifting, and glacial sediments.

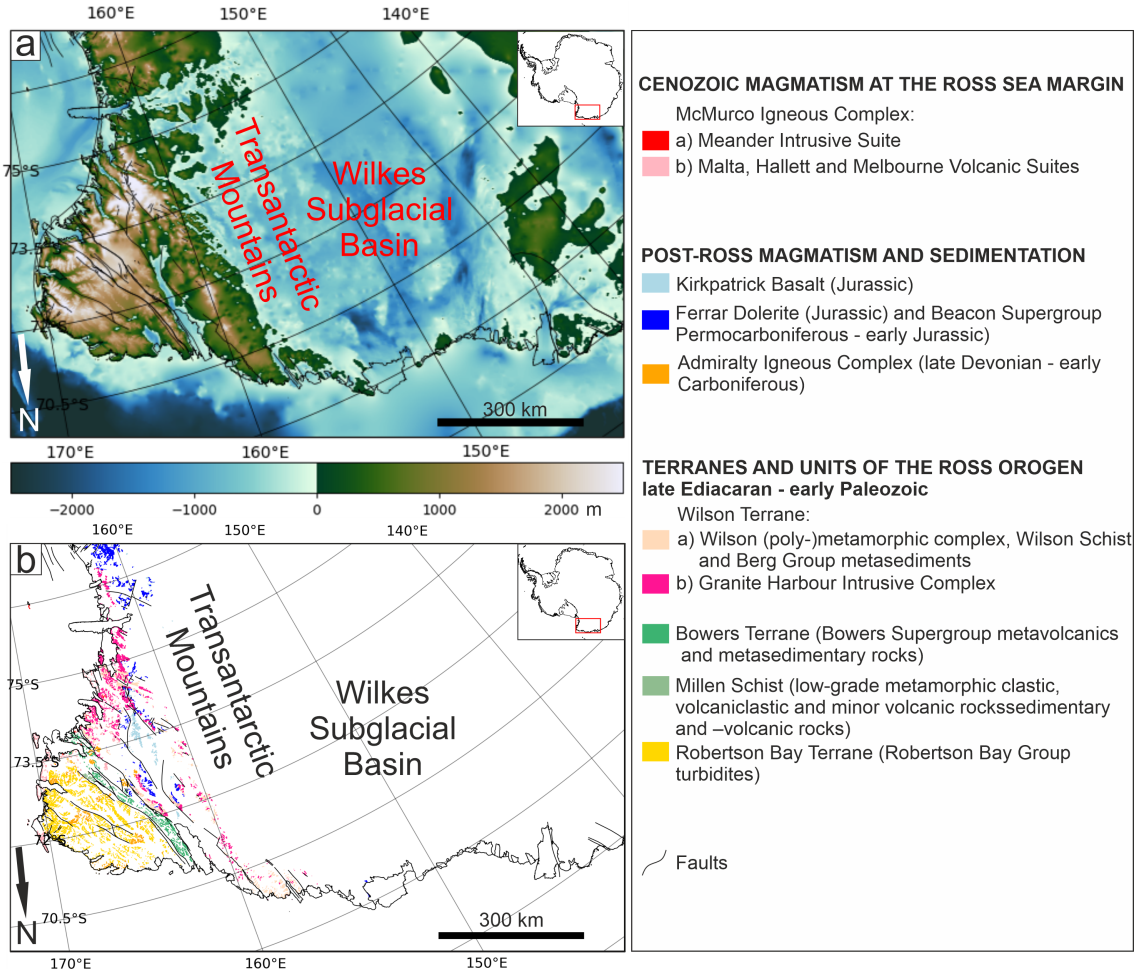

Figure 1.2: a) Bedrock topography of the Transantarctic Mountains and Wilkes Subglacial Basin (WSB) from the Bedmachine model version 3 (Morlighem et al., 2020). Black lines indicate faults based on (Cox et al., 2023). b) Geological map of northern Victoria Land and Oates Land. Geological data taken from (Cox et al., 2023). Based on (Läufer et al., 2011; Pertusati et al., 2016; Roland et al., 2002)

Most of Wilkes Subglacial Basin is below sea level (Figure 1.2a), making it one of the largest regions grounded below sea level in East Antarctica (Morlighem et al., 2020). Due to this geometry WSB is at potentially high risk of ice sheet retreat under a concept known as Marine Ice Sheet Instability (MISI), which states that a groundling line is unstable when the ice-sheet bed slopes downwards from the coast towards the interior. Under MISI, warm seawater causing basal melting at the grounding line can induce ice-shelf thinning and a consequent acceleration of the glacier, ultimately resulting in an inland retreat of the groundling line until a stable bedrock configuration is reached (Mercer, 1978; Schoof, 2007)

1.1.4 Research aim and objectives

We have established so far that subglacial geology and crustal properties are of interest in Antarctica not only for the thermal regime but also to better understand the tectonic evolution of the most remote continent on planet Earth. We have also seen that geophysical imaging, in particular gravity and magnetic applications, are suitable for unravelling lithospheric structures and properties on different scales, including rock provinces, boundaries such as the Moho interface or thermal limits such as CPD to draw conclusions on the internal structure of the Antarctic crust underlying the ice sheets. Open questions in Antarctic research are quantifying heterogeneity in the lithosphere of Antarctica, understanding how thermal variations are influenced by geological evolution and their contribution to the development of the modern topography, how well inverted petrophysical parameters correspond to their measured counterparts in the laboratory and how to link petrological information to geophysical models on different scales. An omnipresent challenge in Antarctic research is data coverage and how to deal with data gaps as well as varying data resolution, for example from flight line spacing of airborne measurements, and choosing an adequate model resolution for the data resolution of a given dataset in terms of wavelength content, and spatial coverage. This thesis tries to take on those open questions in the following three research chapters (chapter 2 - 4) in the region of northern Victoria Land (nVL) including the TAM as well as WSB in East Antarctica (Figure 1.1). The study area for all three research chapters was chosen, because I) the region is, for Antarctica, exceptionally well surveyed with airborne geophysical measurements. The main survey of this area is the WISE-ISODYN survey flown in 2005 and 2006 by the British Antarctic Survey with a line spacing of 10km and tighter (Jordan et al., 2013). II) Direct geological information and rock samples exist in the TAM region. III) Seismological studies indicate that the TAM are not in isostatic equilibrium but rather are potentially thermally supported (Hansen et al., 2016), a hypothesis that can be evaluated using potential field data, and IV) WSB host one of the largest marine-based sectors in East Antarctica reaching bedrock topography depth of over 2 km below the sea level (Ferraccioli et al., 2009a; Jordan et al., 2013; Morlighem et al., 2020). Sub sea level basins like WSB pose a potentially high, but poorly constrained risk for future sea level rise, as they are more vulnerable to melting by warming of the surrounding ocean. Such melting could potentially trigger mechanisms of unstable retreat (Pollard et al., 2015; Schoof, 2007). Significant long-term contribution from the WSB region to future sea-level rise is predicted (DeConto and Pollard, 2016; Stokes et al., 2022). Understanding WSB is time critical in context of future sea level rise and the potential role East Antarctica will play in the long term. For these reasons, nVL and WSB serves as an ideal study area to address those open questions articulated above.

1.2 Thesis structure

Chapter 2 addresses the thermal state of the TAM and WSB region by assessing CPD estimation from magnetic spectra analysis of magnetic airborne measurements. Forward calculation from CPD to subglacial heat flow shows an elevated thermal regime beneath the TAM indicating that the TAM are thermally supported, a hypotheses which was previously formulated by seismological experiments (e.g. Hansen et al. 2016). Additionally, the chapter investigates different aspects of CPD uncertainty, which are routinely overlooked in the literature, such as the influence of window size and the chosen wavelength range im the magnetic spectrum to estimate the CPD. Furthermore, suitable wavelengths of airborne and satellite measurements and data coverage for robust CPD estimation are assessed and recommendations are provided for not using satellite magnetic data, or at least only with extreme caution.

Chapter 3 is concerned with imaging crustal heterogeneities by using joint inversion of airborne gravity and magnetic data. The inversion model is constrained at the top by radar estimation of the bedrock and at depth by the CPD from the previous chapter for the susceptibility inversion, and by Moho depth estimation derived from gravity satellite data for the density inversion. Inverted density and susceptibility distributions indicate a large-scale batholith intrusion in WSB. Based on the density–susceptibility relationship the batholith is speculated to be of granitic composition. Moreover, the craton margin to the west of WSB is imaged and petrophysically characterised. Based on the geophysical joint inversion model a tectonic evolution sketch for WSB is developed. Furthermore, the implication for the cryosphere is discussed in regions where a granitic batholith is present, which has typically a higher concentration of heat producing elements, by linking the interpreted location of the batholith to subglacial lakes. Lastly, advantages of jointly inverting both the gravity and magnetic field compared to separately inverting both fields are emphasised.

Chapter 4 links geophysical inversion models on different scales with petrophysical measurements and therefore, bridges geophysics and geology. To do so, 320 density and susceptibility measurements, on the same Antarctic rock samples, are presented. The new petrophysical rock catalogue is used to validate the inversion model from the previous chapter. Additionally, a high-resolution magnetic only inversion based on a helicopter survey with a line spacing of 500 m in the Mesa Range carried out by the German “Federal Institute for Geosciences and Natural Resources” (BGR) is presented and also validated with the petrophysical rock catalogue. Advantages and disadvantages of regional and local scale inversion resolution are discussed as well as flight line spacing of airborne geophysical surveys. Incentive to fly gravity surveys on comparable tight flight line spacing as high-resolution magnetic surveys is provided by the density susceptibility relationship of the measured rock samples, which shows that rock types can be discriminated with a higher confidence when also considering their density.

Finally, the thesis ends with a synthesis and conclusion chapter which also provides an outlook of potential future work.

Chapter 2

Anomalously high heat flow regions beneath the Transantarctic Mountains and Wilkes Subglacial Basin in East Antarctica inferred from Curie depth

2.1 Context

The following chapter uses spectral analysis after Tanaka et al. (1999) of airborne magnetic data from the ADMAP-2 data compilation (Golynsky et al., 2018) to estimate the bottom of the magnetic layer, the so-called Curie Point Depth (CPD). As rocks lose their magnetic properties at the Curie temperature associated with the 580 ℃ isotherm, CPD can be used as a proxy for the thermal structure in crust. However, CPD can also be used as a boundary condition for magnetic / susceptibility modelling as we will see later (Chapter 3 and 4) and therefore it is crucial for this thesis to establish first the CPD and its associated uncertainties for the region. Here, often overlooked sources of uncertainties are discussed, such as window size or the potential biases introduced by picking the appropriate wavenumber range.
CPD can be used to forward calculate geothermal heat flow (Dziadek et al., 2021; Martos et al., 2017) by assuming a simplified and homogeneous crust. Such a forward calculation is performed in the following chapter as well. Validating heat flow maps is challenging due to the lack of direct heat flow measurements. This chapter attempts to validate the heat flow map against the sparse direct heat flow measurements and to thermal proxies in form of active volcanoes as well as comparing the resulting heat flow map to other heat flow predictions obtained through different methods and geophysical datasets.

2.2 Author contribution

The work presented in this chapter has been published as: M. Lowe, B. Mather, C. Green, T. A. Jordan, J. Ebbing and R. Larter (2023) Anomalously high heat flow regions beneath the Transantarctic Mountains and Wilkes Subglacial Basin in East Antarctica inferred from Curie depth. *Journal of Geophysical Research: Solid Earth*, 128(1), e2022JB025423.

conceptualised: M. Lowe; Data curation: M. Lowe; Formal analysis: M. Lowe, C. Green, T. A. Jordan; Funding acquisition: R. Larter; Investigation: M. Lowe, R. Larter; Methodology: M. Lowe, B. Mather, C. Green, T. A. Jordan, J. Ebbing; Project Administration: R. Larter; Software: M. Lowe, B. Mather; Supervision: C. Green, T. A. Jordan, J. Ebbing, R. Larter; Validation: M. Lowe, C. Green, T. A. Jordan, J. Ebbing, R. Larter; visualisation: M. Lowe; Writing – original draft: M. Lowe; Writing – review & editing: M. Lowe, Ben Mather, C. Green, T. A. Jordan, R. Larter.

2.3 Introduction

The evolution of both the Transantarctic Mountains (TAM) and Wilkes Subglacial Basin (Figure 2.1) as well as their coupling are not fully resolved, despite their crucial role in potential future sea level rise (DeConto and Pollard, 2016; Ferraccioli et al., 2009a; Hansen et al., 2016; Jordan et al., 2013; Paxman et al., 2019). TAM are the largest non-contractional mountain range on Earth (Figure 2.1) and divide East Antarctica from the West Antarctic Rift System (Morelli and Danesi, 2004; Robinson and Splettstoesser, 1986; Ten Brink and Stern, 1992). The approximately 4000 km long and up to 400 km wide mountain range, with a peak elevation of 4000 m (Morlighem et al., 2020), has a complex tectonic history with numerous proposed uplift mechanisms. Uplift models include flexural uplift (Paxman et al., 2019; Ten Brink et al., 1997; Wannamaker et al., 2017; Yamasaki et al., 2008), thermal mantle support (Brenn et al., 2017; Lawrence et al., 2006; Smith and Drewry, 1984) as well as density variation and crustal thickening (Bialas et al., 2007; Huerta, 2007). A local study investigating crustal structures beneath the northern TAM based on receiver function data concluded that the crust beneath the TAM is up to 46 km thick, which is significantly less than the 57 km required to support the mountains isostatically (Hansen et al., 2016). They instead suggest broad flexure of the East Antarctic lithosphere and uplift along the western edge as a result of lateral heat conduction from the hotter West Antarctic mantle in line with the uplift model proposed by Stern and ten Brink (1989), Ten Brink and Stern (1992), Ten Brink et al. (1997). Recent studies based on new seismic tomography models (Brenn et al., 2017; Graw et al., 2016; Lloyd et al., 2020; Shen et al., 2018; Wiens et al., 2023) show large low velocity zones beneath the northern TAM, which are interpreted as warm and less dense mantle material. This observation suggests that the warmer mantle beneath the highest topographic features in Northern Victoria Land provides a strong contribution of thermal support to the uplift of this region (Wiens et al.,

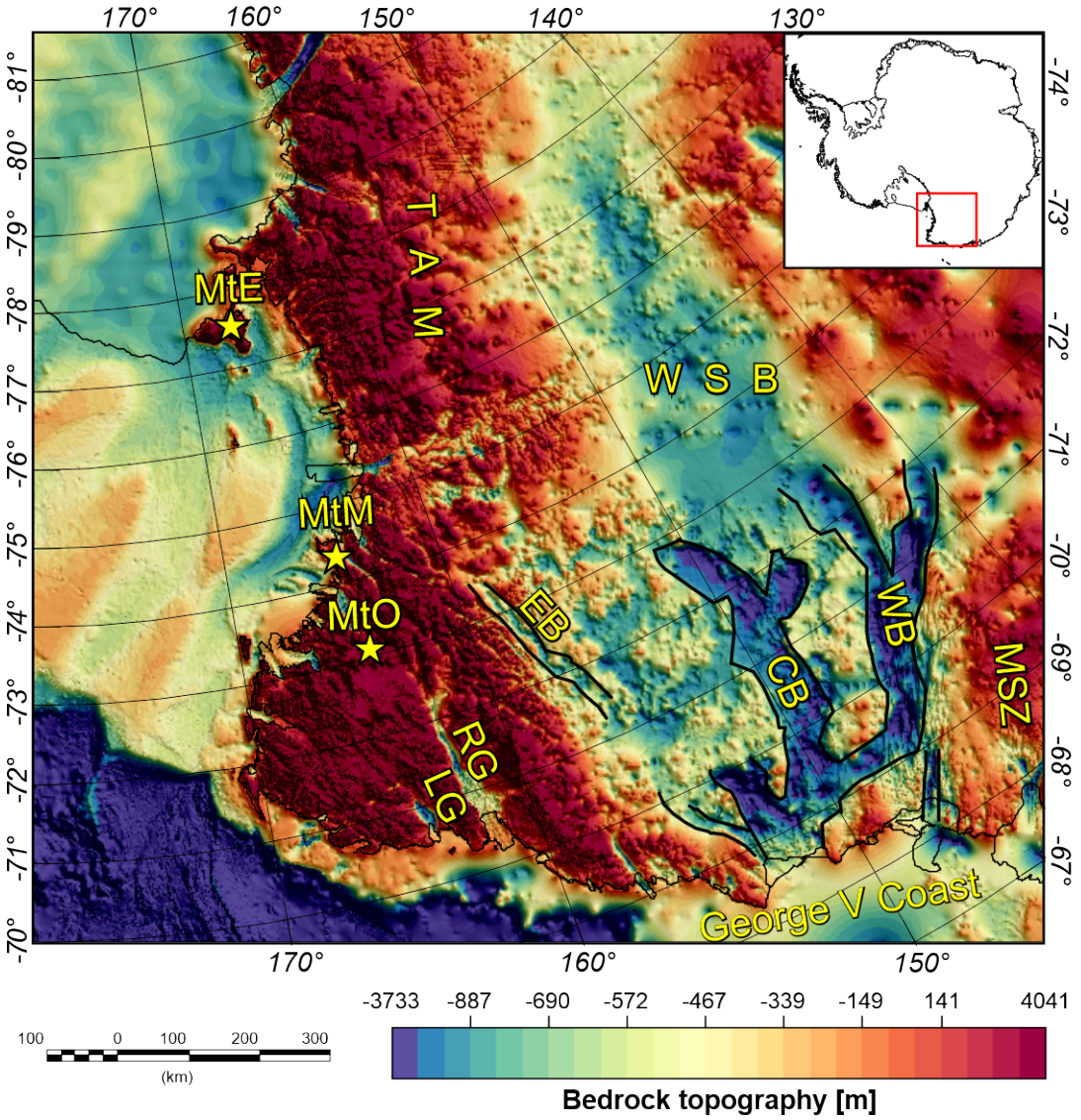

Figure 2.1: Bedrock topography of the Transantarctic Mountains and Wilkes Subglacial Basin from BedMachine Antarctica version 2 (Morlighem et al., 2020). Black lines delimit more deeply incised sub-basins within the wider Wilkes Subglacial Basin region. Yellow stars indicate the location of recently active volcanoes. LG: Lillie Graben; RG: Rennick Graben; EB: Eastern Basin; CB: Central Basin; WB: Western Basin; MSZ: Mertz Shear Zone; WSB: Wilkes Subglacial Basin; TAM: Transantarctic Mountains; MtE: Mount Erebus; MtM: Mount Melbourne; MtO: Mount Overlord.

2023).

Wilkes Subglacial Basin (WSB) located in the hinterland of the TAM, is a major below-sea-level topographic feature, lying 2-3 km beneath the surface of the East Antarctic Ice Sheet (EAIS) (Figure 2.1). WSB was first described from radar data in the 1970s (Drewry, 1976), stretches approximately 1600 km from the George V Coast towards the South Pole, and comprises one of the largest marine-based sectors of the EAIS (Ferraccioli et al. 2009a, 2009b). The

bedrock elevation reaches depths of more than 2000 m below sea level within the locally more deeply incised sub-basins (Ferraccioli et al., 2009a; Morlighem et al., 2020). WSB is about 600 km wide close to the George V Coast (Ferraccioli et al., 2009b), decreasing to <100 km wide towards the South Pole (Studinger et al., 2004). The modern landscape formation of WSB is interpreted as being associated with flexural process of the TAM uplift and glacial erosion (Ferraccioli et al. 2009a; Jordan et al. 2013; Paxman et al. 2019, 2018). WSB is bounded by the Terre Adélie Craton, west of the Mertz Shear Zone (Finn et al., 2006) and by the TAM to the east. Direct information about the subglacial geology is limited to rock exposure close to the coast. West of the Mertz Shear Zone $\geq$ 2440 Ma paragneiss and granitoids have been reported, while to the east ca. 500 Ma granites have been mapped (Goodge and Fanning, 2010). Evidence exists for $\sim$680 Ma rifted margin in the central TAM (Goodge, 2020), and extensive Ross age (550-500 Ma) magmatism in the TAM (Lamarque et al., 2018). The presence of Beacon Supergroup sedimentary strata intruded by rocks of the Ferrar Large Igneous Province within WSB is interpreted from aeromagnetic measurements (Ferraccioli et al., 2009a). Provenance studies also indicate the bedrock of WSB includes Beacon Supergroup terrestrial sediments, rocks of the Ferrar Large Igneous Province, and Early Palaeozoic terranes (Cook et al., 2017).

Basins below sea level like WSB pose a potentially high but poorly constrained risk for future sea level rise, as they are more vulnerable to melting by warming of the surrounding ocean. Such melting could potentially trigger mechanisms of unstable retreat (Pollard et al., 2015; Schoof, 2007). A significant long-term contribution to future sea level rise has been predicted from the WSB region over the next two centuries, associated with eventual retreat of the ice sheet into northern WSB by the year 2500 (DeConto and Pollard, 2016; Stokes et al., 2022). Geothermal heat flow (GHF) is identified as a crucial contribution from the solid Earth which interacts with the cryosphere (Davies, 2013; Fahnestock et al., 2001). GHF influences the rheology of the ice and can lead to basal melting, factors which can both facilitate enhanced ice flow and consequently influence ice sheet stability (Larour et al., 2012; Llubes et al., 2006; Pittard et al., 2016; Winsborrow et al., 2010). GHF is therefore a crucial parameter for modelling ice sheets and future sea-level rise (Matsuoka et al., 2012; Pattyn, 2010; Pattyn et al., 2016; Pittard et al., 2016; Van Liefferinge et al., 2018; Whitehouse et al., 2019; Winkelmann et al., 2011). GHF also has the potential to shed light on the region's long-term tectonic evolution. Areas of elevated heat flow are often associated with regions of shallow warm mantle, and provide a test for the hypothesis that incursion of warmer West Antarctic mantle beneath the TAM provides thermal support to the mountain range, as suggested by Smith and Drewry (1984) and Hansen et al. (2016)

Although in-situ GHF measurements would be very significant, they are almost non-existent in WSB (Burton-Johnson et al., 2020). Consequently, GHF models are inferred from different geophysical techniques. Those techniques can be subdivided into two broad categories: modelling of geophysical data and machine learning or statistical correlation. Modelling

approaches include determining the depth of the 580℃ isotherm from magnetic data and subsequently calculating GHF from this isotherm (Martos et al., 2017) as well as calculating GHF based on seismologically derived upper mantle temperature (An et al., 2015). Statistical models include correlating seismic velocity structures in Antarctica to those in areas with good constraints on GHF (Shen et al., 2020), machine learning techniques where the model is trained in areas where the GHF is well understood (in-situ heat flow measurements exists) (Lösing and Ebbing, 2021; Lösing et al., 2020) and statistical similarity of multiple datasets which are compared to global GHF catalogues (Stål et al., 2021). The large-scale distinction between East and West Antarctica is recognised in most GHF models (An et al., 2015; Lösing and Ebbing, 2021; Martos et al., 2017; Shen et al., 2020; Stål et al., 2021). However, existing continental scale GHF models for Antarctica show remarkable inconsistency on a more local scale (Figure 2.2).

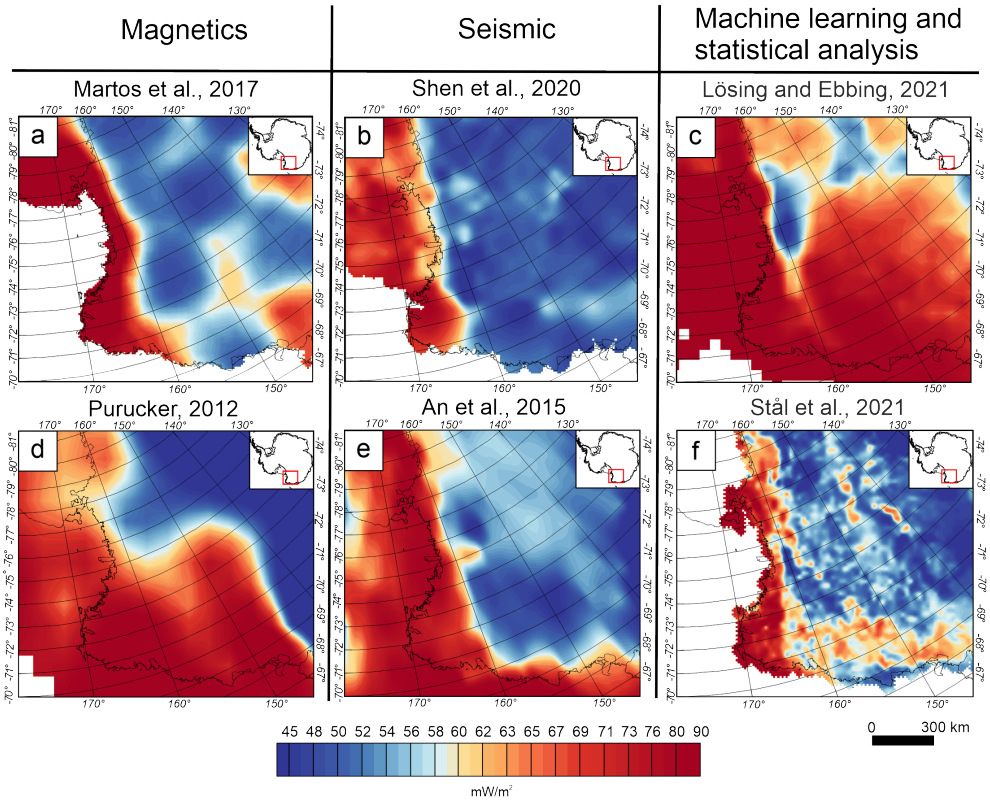

Figure 2.2: Continent-wide GHF models derived from various geophysical approaches. a) Magnetic derived GHF model (Martos et al., 2017). b) Seismological derived GHF model (Shen et al., 2020). c) GHF model derived from multiple data sets via machine learning (Lösing and Ebbing, 2021). d) GHF map derived from satellite magnetic data (Purucker, 2013) an update of Fox Maule et al. (2005). e) Seismologically inferred GHF model (An et al., 2015). f) GHF estimates derived by statistical analyses of multiple data sets (Stål et al., 2021). Identical colourmap used for Figure 2.2 (a-f).

In this study, in contrast to previous attempts to estimate CPD and GHF in Antarctica from spectral analysis of magnetic data, we use exclusively high resolution airborne magnetic data. We show that this exclusive use of airborne data improves existing GHF models based on CPD significantly in the TAM and WSB. We imaged elevated GHF beneath the northernmost part of the TAM, which verifies independent seismological findings of proposed thermal support for uplift in northern Victoria Land (Hansen et al., 2016; Lloyd et al., 2020; Wiens et al., 2023). Furthermore, our study reveals elevated GHF in WSB Central Basin and Rennick Graben which previous models were not able to image, which is consistent with an erosional or rifted origin.

2.4 Data

The ADMAP-2 compilation includes 3.5 million line-km of aeromagnetic and marine magnetic data in Antarctica and the Southern Ocean south of 60 °S (Golynsky et al., 2018). The gridded ADMAP-2 product (Figure 2.3a) has a grid spacing of 1.5 km and its production included correction for the International Geomagnetic Reference Field, diurnal effects, high-frequency error correction, levelling, regional gridding, and merging of regional grids into a continent-wide compilation (Golynsky et al., 2018).

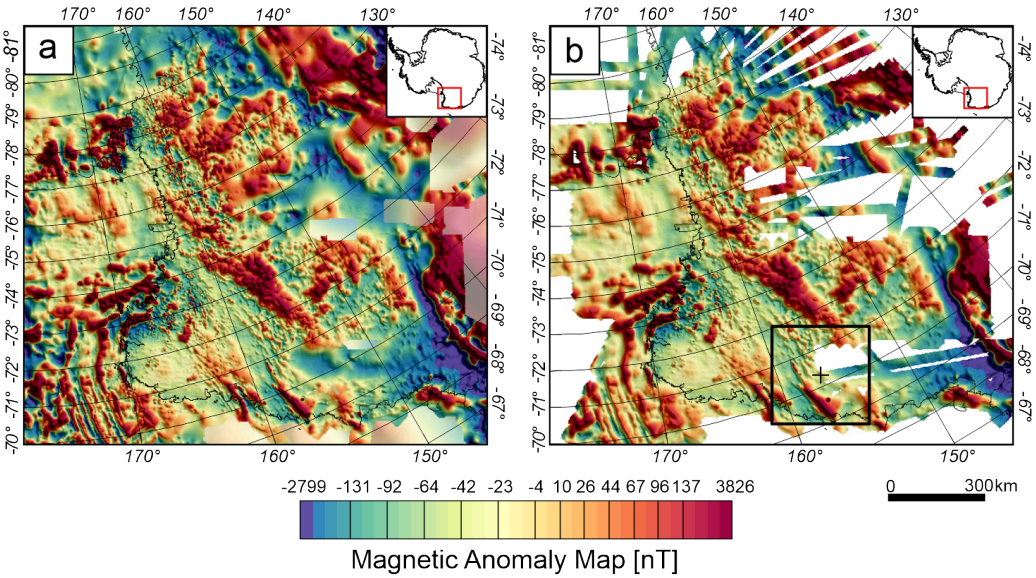

Figure 2.3: Airborne magnetic measurments. a) ADMAP-2 with a grid spacing of 1.5 km (Golynsky et al., 2018) superimposed on Satellite Magnetic Anomaly Map from the LCS 1 model (Olsen et al., 2017). b) Selected recent ADMAP-2 magnetic data, re-gridded and upward-continued to a constant height of 4 km. Black cross and black rectangle indicate the centroid and extension of window 645 with a window size of 300 km. Identical colourmap used for both panels.

For this study only recent (∼2000 - present) aeromagnetic data were selected from ADMAP-2 and a blanking distance of 15 km from flight lines was applied (Figure 2.3b). This was done for two reasons: a) To ensure that only flight lines with high precision positioning tracing (GPS) are used and b) interpolation between widely spaced flight line spacing is removed. Data were re-interpolated onto a 1.5 by 1.5 km mesh using a minimum curvature technique. The resulting magnetic grid was then upward continued to a constant height of 4 km above the ellipsoid (Figure 2.3b), based on the flight elevation data available in the ADMAP-2 compilation (see Appendix A.1).

2.5 Method

Magnetic materials typically lose their magnetisation (ability to induce a strong magnetic field) with increasing temperature (Blakely, 1996; Langel and Hinze, 1998). For magnetite, thought to be the most significant magnetic mineral in the crust, this so-called Curie temperature is ∼580 ℃ (Telford et al., 1990). The depth at which the crust reaches this temperature, and most rocks lose their magnetic properties, is the Curie Point Depth (CPD) and defines the Curie isotherm within the crust (Haggerty, 1978; Núñez Demarco et al., 2020). Estimating the depth of magnetic sources using the power spectrum of magnetic data was first established as a method in 1970 (Spector and Grant, 1970). Since then, numerous methods have been developed to estimate the bottom of all magnetic sources in an area, and hence the CPD. Established methods to estimate the CPD include the centroid method (Treitel et al. 1971, Bhattacharyya and Leu 1975a, Bhattacharyya and Leu 1975b, Blakely 1996, Okubo et al. 1985, Tanaka et al. 1999, Blakely 1996) spectral peak method (Blakely, 1996; Connard et al., 1983) and fractal methods (Bansal and Dimri, 2005; Bansal et al., 2011; Bouligand et al., 2009; Kumar et al., 2021; Li et al., 2019; Mather and Fullea, 2019; Maus and Dimri, 1995; Maus et al., 1997; Salem et al., 2014; Todoeschuck et al., 1992); for a more detailed discussion of these methods the reader is referred to Ravat et al. (2007) and Núñez Demarco et al. (2020).

In our study the centroid method after Tanaka et al. (1999) is used to calculate the CPD. This approach assumes a random distribution of magnetic sources in the crust. The radially averaged power spectrum was calculated using the python library Pycurious (Mather and Delhaye, 2019).

The radially averaged power spectrum $\Phi\Delta(|\kappa|)$ is defined as:

$$\Phi_{\Delta T}(|\kappa|) = Ae^{-2|\kappa|Z_t}(1 - e^{-|\kappa|(Z_b - Z_t)})^2 \tag{2.1}$$

where A is a constant, κ is the spatial wavenumber defined as $\kappa = \frac{2\pi}{\lambda}$, where λ is the wavelength, Z_t is the top of the assumed magnetic source and Z_b is the bottom of the assumed magnetic source and therefore $Z_b - Z_t$ describes the thickness of the magnetic source (Mather and Delhaye, 2019; Tanaka et al., 1999).

For shorter wavelengths (generally less than twice the source thickness), this approximates to:

$$\ln[\Phi_{\Delta T}(|\kappa|)^{\frac{1}{2}}] = \ln B - |\kappa| Z_t \tag{2.2}$$

where *B* is constant (Mather and Delhaye, 2019; Tanaka et al., 1999).

Equation 2.1 can be rewritten, with *Z0* as the centroid depth of the magnetic source (Mather and Delhaye, 2019; Tanaka et al., 1999):

$$\Phi_{\Delta T}(|\kappa|)^{\frac{1}{2}} = Ce^{-|\kappa|Z_0}(e^{-|\kappa|(Z_t - Z_0)} - e^{-|\kappa|(Z_b - Z_0)}) \tag{2.3}$$

where *C* is a constant.

For long wavelengths, where $2d$ is the magnetic source thickness we obtain equations 2.4 and 2.5 (Mather and Delhaye, 2019; Tanaka et al., 1999).

$$\Phi_{\Delta T}(|\kappa|)^{\frac{1}{2}} = Ce^{-|\kappa|Z_0}(e^{-|\kappa|(-d)} - e^{-|k|(d)}) \approx Ce^{-|\kappa|Z_0} 2|\kappa| d \tag{2.4}$$

$$\ln \frac{\Phi_{\Delta T}(|\kappa|^{\frac{1}{2}})}{|\kappa|} = \ln D - |\kappa| Z_0 \tag{2.5}$$

The depth to the top (Z_t) and centroid (Z_0) of the magnetic source are recovered by fitting a linear regression through the high-wavenumber and low-wavenumber part of the radially averaged spectrum of $\ln \Phi_{\Delta T}(|\kappa|)^{\frac{1}{2}}$ and $\ln \frac{\Phi_{\Delta T}(|\kappa|)^{\frac{1}{2}}}{|\kappa|}$ in equation 2.2 and 2.5 respectively (Tanaka et al., 1999). With Z_t and Z_0 the base of the magnetic source Z_b can be estimated applying equation 2.6 (Mather and Delhaye, 2019; Tanaka et al., 1999)

$$Z_b = Z_0 - (Z_t - Z_0) = 2Z_0 - Z_t \tag{2.6}$$

A random magnetisation model was chosen over a fractal model firstly because recent CPD studies in Antarctica and Greenland (Dziadek et al. 2021; Martos et al. 2017, 2018) have used a random magnetisation model and we want to obtain results that can be compared directly to previous studies. Secondly the subglacial geology in the area of the TAN and WSB is largely unknown. A fractal magnetisation model introduces a fractal exponent parameter β, which is related to geology (Bouligand et al., 2009). However, random magnetisation is an endmember of the fractal magnetisation model with fractal parameter β = 1 (Bouligand et al., 2009). For meaningful β values above 1 geological terrains need to be identified and constrained. Adding an unconstrained fractal parameter adds complexity which is difficult to tie

down since different geological terrains would require different β values. Fixing β to a constant value as previous studies have done (e.g. Sobh et al. 2021) will not provide an advantage over a random magnetisation model. A recent study illustrated the difficulty in estimating reliable β values and highlights the possibility that β is only valid in a limited bandwidth (Szwillus et al., 2022). To limit the complexity and ambiguity a fractal model would introduce, combined with ensuring comparability to previous Antarctic studies, we have chosen the standard approach of assuming random magnetisation over a fractal model.

2.5.1 Data preparation and window size

The window size is an influential parameter in spectral methods because it ultimately determines the maximum wavelength which will be captured in the subgrid and therefore controls the maximum depth that can be recovered (Núñez Demarco et al., 2020).
Various authors make conflicting suggestions regarding appropriate window sizes (Núñez Demarco et al., 2020) ranging from 3 times the depth of the magnetic layer (Hussein et al., 2013) to 10 times the recovered depth of the magnetic layer (Ravat et al., 2007). In contrast, Li et al. (2017) use several window sizes, where the recovered depths are averaged into the final CPD grid. Bouligand et al. (2009) use an iterative approach, where they expand the window around a given grid point until a depth of the bottom of the magnetic layer Z_b smaller than a tenth of the window size is recovered. In this study, we test recovery of the CPD beneath the TAM and WSB using analysis window sizes of 200 km by 200 km, 300 km by 300 km and 400 km by 400 km following the recommendation for a window size of 5 to 10 times the recovered CPD (Ravat et al., 2007). We discuss the differences in absolute value, resolution and accuracy of recovered CPD, and justify our choice of a 300 km preferred window size later (Section 2.7).
The Fourier transformation requires the windowed data to have no data gaps. However, Antarctica is not fully covered by magnetic airborne surveys. Previous studies in Antarctica have bypassed this problem by merging the airborne data with satellite magnetic data (Dziadek et al., 2021; Martos et al., 2017). Satellite magnetic data for estimating CPD should be used with caution because the analytical window functions as a high pass filter removing all wavelengths longer than the window size. However, satellite derived magnetic models only contain longer wavelengths, similar in length to the typical analysis window; for example the satellite derived magnetic model MF7 (Maus et al., 2007) only contains wavelengths larger than 300 km. It is therefore questionable whether merged satellite and airborne magnetic data can provide a representative CPD estimation due to the limited wavelengths in the power spectrum. This issue was recently discussed by Pappa and Ebbing (2023). In our study the problem regarding data gaps within the airborne data is overcome by interpolation of the airborne data to ensure only direct observations contribute to the spectral content in the window. Subsequently, we estimate the data coverage of every window and discard windows with less than 80% data coverage to ensure that the recovered CPD estimates are not dominated by interpolation effects.

It is common for spectral methods that the study area is subdivided into windows which have a large overlap between them (Audet and Gosselin, 2019; Blakely, 1988; Bouligand et al., 2009; Idárraga-García and Vargas, 2018; Leseane et al., 2015; Okubo et al., 1985). The overlap increases the number of depth estimates and is expected to increase resolution up to a point, which allows the investigation of lateral variations in CPD through the study area. The overlapping windows also allow smoothing of the more closely spaced CPD estimates (see Appendix A.2). In this study we use a step size of 20 km between the analytic windows, which results in a large overlap between the windows. A Hanning taper is applied to the windowed subgrid in the space domain to remove edge discrepancies. No further modification, corrections or filters have been applied to the magnetic grid and power spectrum in line with recommendations from previous authors (Audet and Gosselin, 2019; Núñez Demarco et al., 2020; Ravat et al., 2007).

Applying this approach, with a threshold of 80% data coverage, we obtain 2161 valid windows for a window size of 200 km, 1933 windows for a window size of 300 km and 1685 windows for the window size of 400 km. Our approach is limited to regions with relatively good airborne data coverage and therefore cannot be applied to the entire Antarctic continent. A fixed wavenumber range is used to estimate the CPD in each window. Z_0 is calculated in the wavenumber range 0.006 - 0.033 $|\kappa|/(2\pi)$ (167-30 km wavelength) and Z_t is calculated in range 0.04 - 0.2 $|\kappa|/(2\pi)$ (25-5 km wavelength) respectively. The ideal wavenumber range for Z_0 is defined as the first linear segment after the spectral peak in the low wavenumber part of the power spectrum, while the ideal range for Z_t is defined as the second linear segment in the power spectrum. The linear regression (Figure 2.4) to estimate Z_t and Z_0 is carried out using the function *curve fit* from the python library SciPy learn (Virtanen et al., 2020). The uncertainty of the fitted slope is calculated by estimating the standard deviations from the covariance matrix by taking the square root of the diagonals (Equation 2.7) and propagating the uncertainty (Equation. 2.8).

$$\sigma_{slope} = \sqrt{Cov_{diag}} \tag{2.7}$$

$$\sigma_{CPD} = \sqrt{\sigma^2_{slope[Z_t]}} \tag{2.8}$$

We note that the estimated uncertainty is a formal error, which describes how well the linear regression fits the radially averaged power for the predefined wavenumber range. The absolute uncertainty of the CPD estimation may surpass this formal error (see Section 2.7.1).

CPD estimations, which are an approximation for the 580°C Curie isotherm, can be used as a proxy for GHF. Where CPDs are shallow a higher GHF is expected and vice versa. A first order approximation of GHF from CPD estimates can be inferred from Fourier's Law (Equation 2.9) (Núñez Demarco et al., 2020; Turcotte and Schubert, 2014):

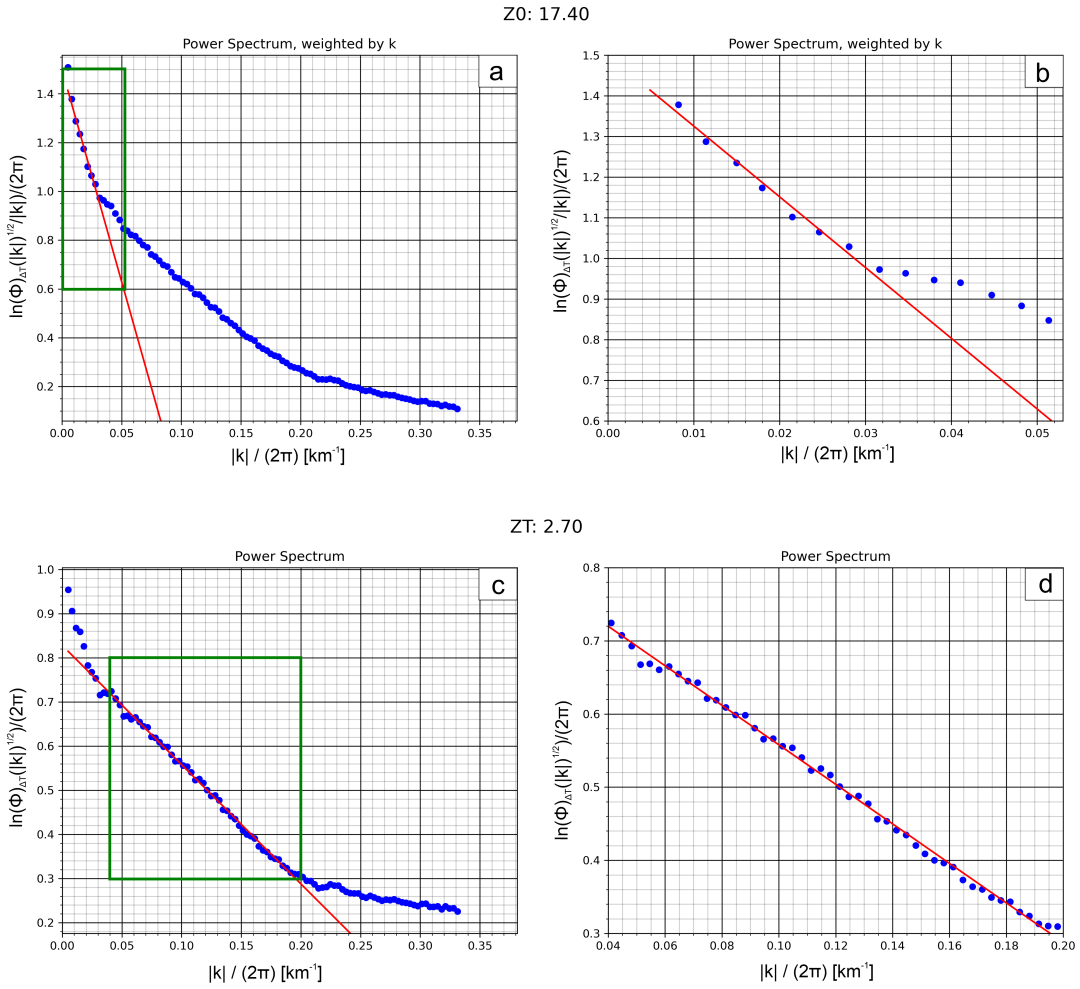

Figure 2.4: Power spectrum from window 645; centroid location and extension of the window are marked in Figure 2.3b. a) Power spectrum weighted by κ to estimate Z_t. Red line represents the fitted line through the low wavenumber part of the power spectrum. Green rectangle illustrates zoom in range for b). b) Zoomed in power spectrum weighted by κ. c) Power spectrum to estimate Z_t. Red line represents the fitted line through the high wavenumber part of the power spectrum. Green rectangle illustrates zoom in range for d). d) Zoomed in power spectrum.

$$Q = -\kappa \frac{\delta T}{\delta z} = -\kappa \frac{T_c - T_{surface}}{Z_b} \tag{2.9}$$

where Q is the heat flux at the bedrock interface, T_c is the Curie temperature (580 ℃), $T_{Surface}$ is the surface temperature, Z_b is the CPD and κ is the thermal conductivity. Here, a thermal conductivity of 2.5 $\mathrm{W\,mK^{-1}}$ is used, which is the average thermal conductivity of igneous rocks (Clauser and Huenges, 1995; Goes et al., 2020; Hasterok et al., 2018; Jennings et al., 2019). Temperature at the bedrock surface ($T_{surface}$) is set to 0 ℃ in line with previous spectral analysis studies in Antarctica (Dziadek et al., 2021; Martos et al., 2017). Assuming 0 ℃

at the bedrock interface is sufficient since most of the bottom of the ice sheet has been calculated to be at the pressure melting point around -2℃ with a variation of a few ℃, which results in a “wet base” of the ice sheet (Pattyn, 2010). This assumption breaks for areas with a cold (dry) ice-sheet base and areas with no ice cover. Over most of this region annual mean surface temperatures are -20 to -50℃ (Wang and Hou, 2009). We performed a sensitivity test for the cold-based ice sheet and ice-free scenario assuming an annual surface temperature of -30℃ (Figure A.3). This effect would bias averaged heat flow by 4 $\mathrm{mW\ m^{-2}}$, which is considerably less than the overall uncertainty estimated for the GHF (Figure 2.6 d-f). Therefore, this effect is considered negligible. Using an ice surface temperature is also problematic due to the potential for melting/freezing in the ice as well as fluid flow. Equation 2.9 is a strong simplification of the real world since it neglects spatial variation of thermal conductivity caused by e.g., geology as well as any heat production in the area due to e.g., radiogenic heat production in crustal rocks. Those parameters are strongly influenced by the composition of the present crustal rocks, which are poorly constrained in Antarctica due to the thick overlying ice sheet (Burton-Johnson et al., 2020). Martos et al. (2017) accounted for crustal heat production by using a constant value for the entire Antarctic continent, which does not help the conversation on spatial GHF variation caused by heterogeneity within the crust.

2.6 Results

The CPD estimates range between 15 and 35 km (Figure 2.5 a, c, e). As a reminder, from equation 2.9 a low CPD value indicates a shallow Curie isotherm of 580℃ and therefore implies a higher heat flow and vice versa. A prominent shallow CPD province is present beneath the TAM between -78° and -72° latitude for all three window size configurations. In the area of Rennick Graben a linear shallow feature is visible in the 200 and 300 km windows (Figure 2.5 a, c) but is much subdued in the 400 km window (Figure 2.5 e). Another linear feature is observed in the Central Basin (Figure 2.5 a-c). Again, this feature is subdued in the 400 km window (Figure 2.5). West of the Central Basin, deeper CPD values are observed, indicating an overall colder thermal structure. CPD estimates from the 200 km window have a higher frequency in their spatial pattern compared to window size configurations of 300 km and 400 km (Figure 2.5). With increasing window size, the range of recovered CPD decreases, while the mean depths become deeper (Figure 2.5, Figure 2.7 a-c). Moreover, the estimated uncertainties decrease with increasing window size (Figure 2.5 a,c,e). Linear transformation of CPD to GHF maps (see Equation. 2.9) yielded estimates ranging from 38 to 110 $\mathrm{mW\ m^{-2}}$. The spatial patterns in the GHF maps (Figure 2.6 a,c,e) are identical to those observed in the CPD map (Figure 2.5) due to the linear relationship between both maps. Again, the range of GHF values decreases with increasing window size while the error decreases also with increasing window size (Figure 2.6 a-f).

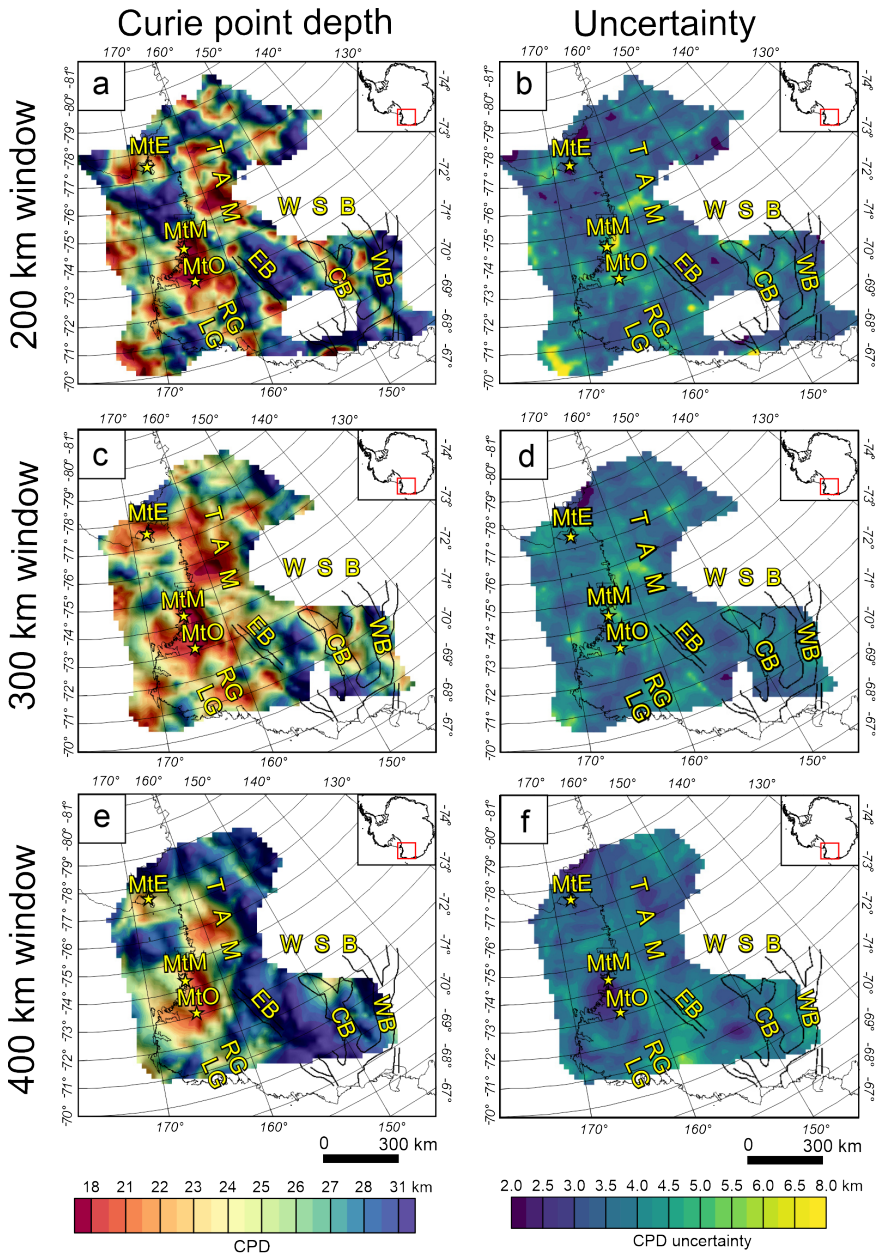

Figure 2.5: Estimated CPD for Victoria Land and Wilkes Subglacial Basin. Left column gives CPD estimates for different window sizes. Right column illustrates the corresponding uncertainty. a) CPD based on a 200 by 200 km window. b) uncertainty for CPD estimates based on a 200 by 200 km window. c) CPD estimates obtained with a 300 by 300 km window. d) uncertainty for CPD estimates obtained with a 300 by 300km window. e) Calculated CPD with a 400 by 400 km window. f) uncertainty for CPD estimates with a window size of 400 by 400km. LG: Lillie Graben; RG: Rennick Graben; EB: Eastern Basin; CB: Central Basin; WB: Western Basin; WSB: Wilkes Subglacial Basin; TAM: Transantarctic Mountains; MtE: Mount Erebus; MtM: Mount Melbourne; MtO: Mount Overlord. Identical colourmaps used for Figure 2.5 a, c, e and Figure 2.5 b, d, f.

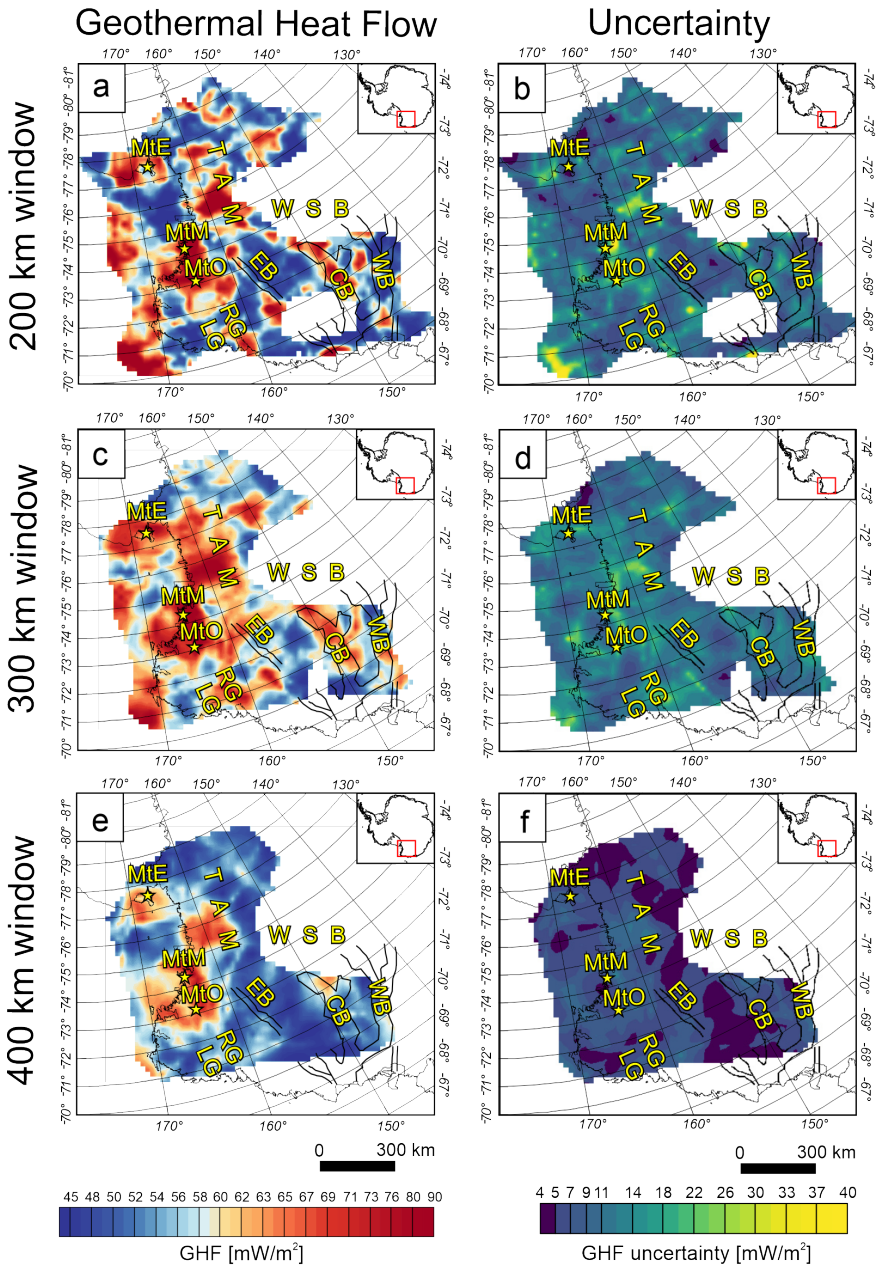

Figure 2.6: Estimated GHF for Victoria Land and Wilkes Subglacial Basin. Left column gives GHF estimates for different window sizes. Left column illustrates the corresponding uncertainty. a) GHF based on a 200 by 200 km window. b) Uncertainty for GHF estimates based on a 200 by 200 km window. c) GHF estimates obtained with a 300 by 300 km window. d) Uncertainty for GHF estimates obtained with a 300 by 300km window. e) Calculated GHF with a 400 by 400 km window. f) Uncertainty based on GHF estimates with a window size of 400 by 400km. LG: Lillie Graben; RG: Rennick Graben; EB: Eastern Basin, CB: Central Basin; WB: Western Basin; WSB: Wilkes Subglacial Basin; TAM: Transantarctic Mountains; MtE: Mount Erebus; MtM: Mount Melbourne; MtO: Mount Overlord. Identical colourmaps used for Figure 2.6 a, c, e and Figure 2.6 b, d, f.

2.7 Discussion

Results recovered from a window size of 300 km and 400 km are preferred for multiple reasons. First, the recommendation for an optimal window size is 5 – 10 times the recovered CPD (Ravat et al., 2007). (see section 2.5.1). The largest portion of recovered CPD across all window sizes is between 25 and 30 km (Figure 2.7). Aiming for a window size which is 10 times the recovered CPD the preferred windows size must be larger than 250 km and thus the 300 km window size in our study is best suited to satisfy this recommendation. In addition, a window size of 300 km recovers a larger number of valid CPD estimates for the study area in comparison to the 400 km window size (Figure 2.7 a, c, e).

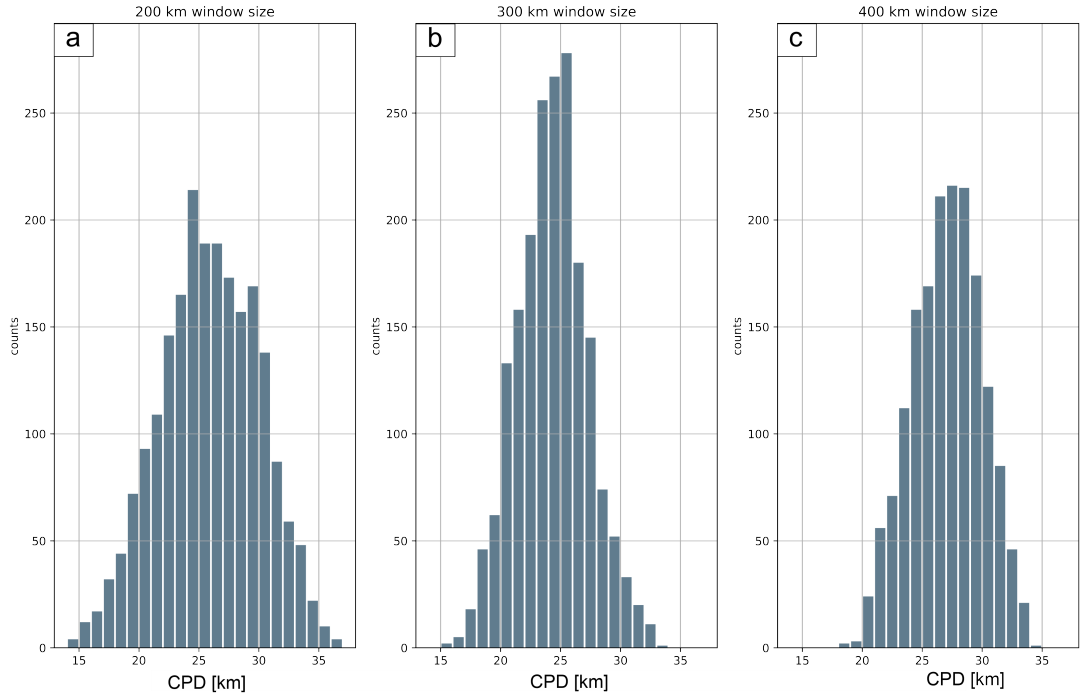

Figure 2.7: Histogram of recovered CPD depth for different window sizes with a bin size of 1 km. a) CPD estimates recovered from 200 by 200 km windows. b) CPD estimates obtained using 300 by 300 km windows. c) Recovered CPD based on 400 by 400 km windows.

The estimated error for the CPD estimates based on the fitting of the radially averaged power spectrum decreases with increasing window size (Figure 2.5 b, d, f), which points in the direction of missing low wavenumber content in the 200 km window, while larger window sizes are stabilised due to capturing a wider bandwidth. Moreover, high frequency of spatial variation in the CPD is observed in the 200 km window (Figure 2.5 a), while CPD from a larger window size (Figure 2.5 c, e) shows less spatial variation. A large change between the results obtained from a 200 to 300 km window is observed, although many key features persist. A much smaller change is observed between the result obtained from a 300 and 400 km window, suggesting the recovered CPD values stabilise for windows larger than 200 km.

Lastly, CPD resulting from a 300 km window displays spatial pattern, which are consistent with geological and topographic features such as Rennick Graben and the Central Basin. Based on the arguments above we prefer results obtained from a window size of 300 km.

CPD estimates are the result of the average Curie depth within the analysing window, although a strong depth variation within the window may bias the estimation to deeper or shallower values. Moho depth maps are a good control mechanism since Curie depths deeper than the Moho interface would imply that the upper mantle is magnetic, which is not typically assumed (e.g. Wasilewski et al. 1979), although this possibility has been suggested (Ferré et al., 2014). CPD estimations of this study are above the Moho interface onshore with a few exceptions near the edge of the magnetic data coverage (Figure 2.8). CPD estimates offshore in the Ross Sea show isolated areas with deeper CPD estimates compared to the Moho map from Pappa et al. (2019a).

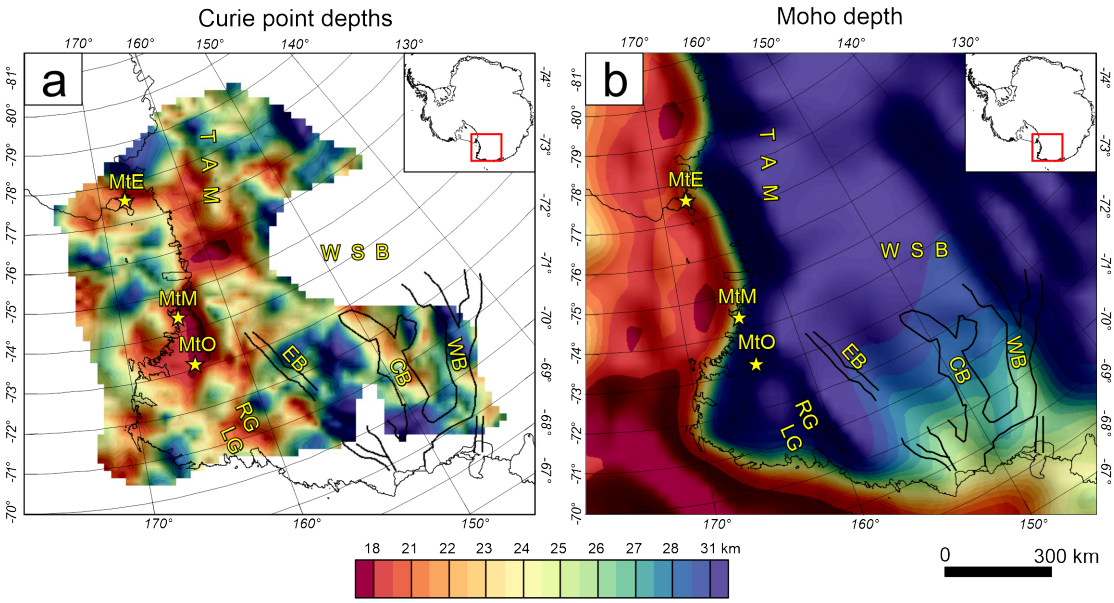

Figure 2.8: Comparison between CPD estimations and Moho depths. a) CPD estimates recovered with a 300 km window size. b) Moho depth map inferred from satellite gravity inversion (Pappa et al., 2019a). Yellow stars indicate the location of recent active volcanoes. LG: Lillie Graben; RG: Rennick Graben; EB: Eastern Basin; CB: Central Basin; WB: Western Basin; WSB: Wilkes Subglacial Basin; TAM: Transantarctic Mountains; MtE: Mount Erebus; MtM: Mount Melbourne; MtO: Mount Overlord. Identical colourmap used for Figure 2.8 a and b.

Recovered CPDs ranging from 15 to 35 km are not unusual compared to different regions elsewhere on the globe. CPDs for the mid-Norwegian margin in the area of the Trøndelag Platform and Vøring Basin are reported to range from 18 km to 20 km at the coast, around 12 km at the ocean continent transition zone and around 9 km beneath the oceanic plate (Ebbing et al., 2009). CPDs beneath the British Isles are reported to range from 15 km to 45 km (Mather and Fullea, 2019). CPDs in southern Africa are reported to range from 8 to 15 km

along the Okavango Rift Zone in Botswana and up to 50 km in the Kaapvaal Craton (Sobh et al., 2021). Curie depths substantially shallower are reported for the West Antarctic Rift System, reaching depths shallower than 10 km and up to extreme values of 4.8 km (Dziadek et al., 2021). Such extreme shallow CPD values are highly unlikely in the cratonic region of East Antarctica.

2.7.1 Uncertainty of CPD and GHF estimation

Uncertainty arising from fitting the slope of the predefined wavenumber range varies between 2 and 8 km throughout the study area (Figure 2.5 b, d, f), which translates to uncertainties of 2.9 $\mathrm{mW\,m^{-2}}$ to 48.8 $\mathrm{mW\,m^{-2}}$ for the GHF estimation (Figure 2.6 b, d, f). Uncertainty associated with choosing inappropriate size and range of the wavenumbers to calculate Z_0 and Z_t can lead to significantly different CPD results of the order of multiple km (See Appendix A.4). Uncertainty from the chosen window size is on the order of a few km (Figure 2.5). With increasing window size, the average recovered depth increases, while fewer extreme CPD values are recovered (Figure 2.5). Moreover, the composition of the magnetic material itself induces uncertainty since the Curie temperature is not a universal 580°C for all minerals (Blakely, 1988; Haggerty, 1978; Núñez Demarco et al., 2020). However, the effect of the mineral composition is almost impossible to quantify. Lastly, the linear transformation of CPD to GHF equation (2.9) does not consider heat production within the crust and assumes a constant thermal conductivity, which is a strong simplification of the crustal properties.
It is important to consider these effects when using absolute values of GHF estimates derived from bottom of the magnetic layer methods. However, many of the uncertainties discussed above relate to the absolute value of the CPD across the study. This method therefore provides a robust tool for imaging relative variation in CPD, but absolute values should be used with more caution.

2.7.2 Comparison to in-situ GHF measurements and previous GHF models

The global GHF catalogue (Lucazeau, 2019) reports a few in situ measurements for the study area (Figure 2.9). These measurements have been obtained using different techniques and equipment. Measurements in our study area have been conducted from boreholes, sediment and ice probes (Lucazeau, 2019). The measurements in the database are rated from A to C based on the variation of heat with depths, and labelled Z where heat flow with depth is not specified. A-rated GHF measurements (circles in Figure 2.9) are very sparse in the area. The three southernmost (longitude from 163° to 165°, latitude from -77° to -77.7°) A-rated measurements are conducted in boreholes and are consistent with our GHF estimates. A-rated measurements offshore are aligned at the edge of a high heat flow pattern. However, the negative heat flow pattern offshore arises from CPD estimates, which are below the Moho interface and therefore are less trustworthy as discussed in section 2.7. B- and Z-rated

GHF measurements are overall consistent with our GHF estimates. C-rated measurements onshore (triangles Figure 2.9) are in strong disagreement with our findings. Previous GHF models based on machine learning and multi statistical similarity analysis (Lösing and Ebbing, 2021; Stål et al., 2021) use in situ measurements in their approach. However, Stål et al. (2021) only used A-rated GHF measurements, while Lösing and Ebbing (2021) did not discriminate the measurements. We categorise the three borehole measurements taken beneath McMurdo Ice Shelf (longitude from 163° to 165°, latitude from -77° to -77.7°) to be the most trustworthy and are more cautious in regard to measurements obtained using sediment and ice probes.

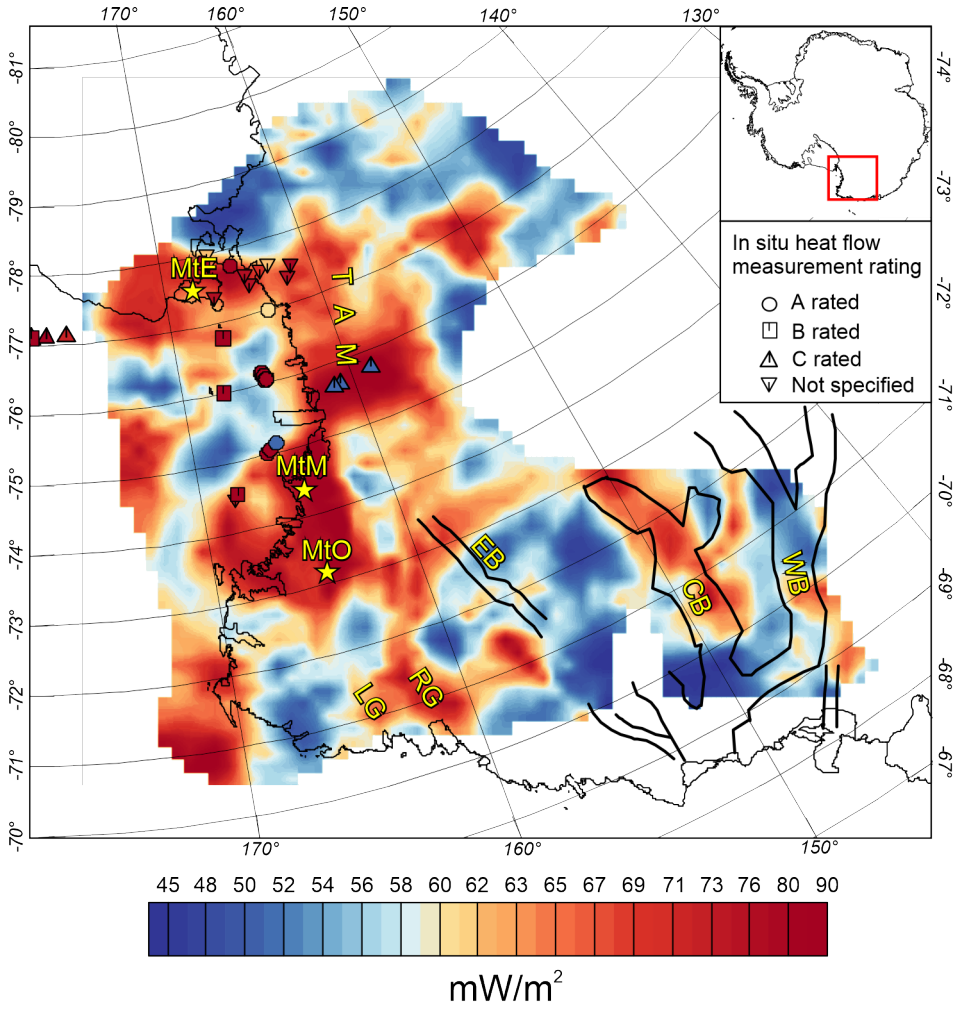

Figure 2.9: In situ GHF measurements (Lucazeau, 2019) superimposed on GHF estimates recovered based on an analytic window with a window size of 300 km. Circles represent A-rated GHF measurements, boxes represent B-rated GHF measurements, regular triangles represent C-rated GHF measurements and inverted triangles represent Z-rated (not specified) GHF measurements. Yellow stars indicate the location of recent active volcanoes. LG: Lillie Graben; RG: Rennick Graben; EB: Eastern Basin; CB: Central Basin; WB: Western Basin; WSB: Wilkes Subglacial Basin; TAM: Transantarctic Mountains; MtE: Mount Erebus; MtM: Mount Melbourne; MtO: Mount Overlord. Identical colourmap is applied to the GHF map and the measured heat flow values. Identical colourmap used for Figure 2.6 (a, c, f).

Difference-maps (Figure 2.10) between the GHF estimates based on a 300 by 300 km window to previous studies (Figure 2.2) show moderate differences in the order of ± 20 $\mathrm{mW\,m^{-2}}$ between most models with isolated areas with stronger disagreement ± 50 $\mathrm{mW\,m^{-2}}$ and more. All models predict a lower GHF beneath the southern TAM and a higher heat flow offshore. The seismic derived GHF estimates (An et al., 2015; Shen et al., 2020) show the least disagreement together with the statistically derived model from (Stål et al., 2021) to GHF estimates in this study.

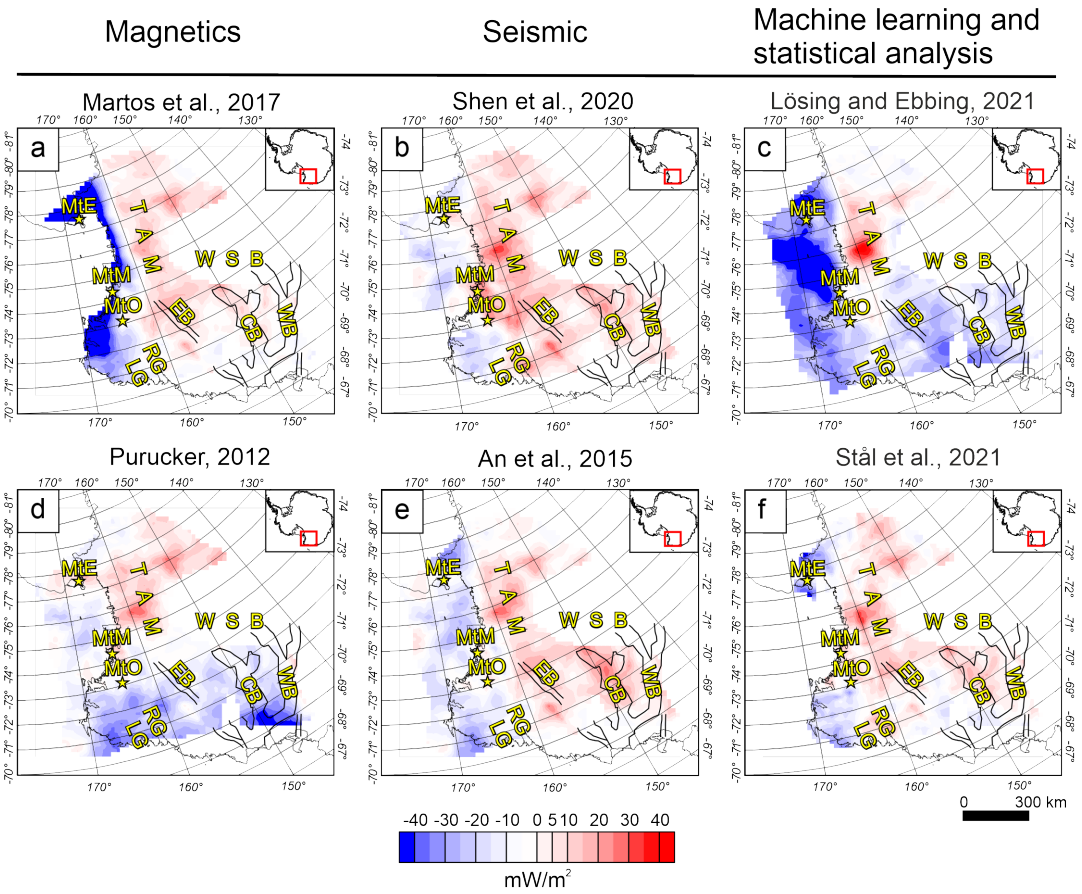

Figure 2.10: Difference-maps between GHF estimates of this study obtained with a window size of 300 by 300 km and existing continent wide GHF models shown in Figure 2.2. Blue colours show lower GHF values in GHF estimates in this study, while red colours indicate higher GHF estimates in this study. a) Difference in estimated GHF values compared to Martos et al. (2017). b) Difference in estimated GHF values compared to Shen et al. (2020). c) Difference in estimated GHF values compared to Lösing and Ebbing (2021). d) Difference in estimated GHF values compared to Purucker (2013) an update of Fox Maule et al. (2005). e) Difference in estimated GHF values compared to An et al. (2015). f) Difference in estimated GHF values compared to Stål et al. (2021). LG: Lillie Graben; RG: Rennick Graben; EB: Eastern Basin; CB: Central Basin; WB: Western Basin; WSB: Wilkes Subglacial Basin; TAM: Transantarctic Mountains; MtE: Mount Erebus; MtM: Mount Melbourne; MtO: Mount Overlord.

Those three models predict GHF values in the same order of magnitude with stronger disagreements in Rennick Graben, Central Basin and southern TAM. The GHF model derived from magnetically inferred CPD from Martos et al. (2017) shows a strong disagreement at the divide to West Antarctica and a moderate disagreement in East Antarctica. The strong disagreement might be due to the fact that Martos et al. (2017) applied different wavenumber ranges to the power spectrum to estimate the CPD for windows in West and East Antarctica, which systematically gives shallower CPD for West Antarctica and consequently results in higher heat flow. GHF prediction based on a machine learning approach by Lösing and Ebbing (2021) shows strong disagreement onshore beneath the southern TAM and offshore in the Ross Sea. The much lower GHF predictions in the Lösing and Ebbing (2021) model onshore beneath the TAM might be related to incorporating the three C-rated GHF in situ measurements from the global GHF catalogue (Lucazeau, 2019). The large difference in the Ross Sea to the Lösing and Ebbing (2021) model is located where our CPD estimates exceed the Moho depth and therefore are less trustworthy. Figure 2.10 illustrates that our results predict higher heat flow beneath the TAM extending westwards, while high heat flow values in previous models are limited to the region closer to the coastline.

2.7.3 Geological origins and implications of geothermal anomalies.

estimates and the GHF predictions derived from them reveal elevated heat flow beneath the northern TAM. Recently active volcanoes in the study area are: Mount Erebus, which is the southernmost active volcano on Earth (Sims et al., 2021), Mount Melbourne, a quiescent volcano, which is believed to have the potential to produce major explosive events (Gambino et al., 2021), and Mount Overlord, which was active during the Eocene (Perinelli et al., 2017). Those recently active volcanoes are consistent with the thermal anomaly pattern of this study since each volcano is centrally located in areas of elevated heat flow (Figure 2.9).

The high in heat flow in the TAM region is in line with the idea of warmer West Antarctic mantle beneath the TAM providing thermal support for the mountain range (as proposed by Hansen et al. 2016) and the low velocity mantle imaged by recent seismic tomography models (Lloyd et al., 2020; Wiens et al., 2023).

A linear high heat flow anomaly is observed in Rennick Graben. This high heat flow pattern leaks into nearby Lillie Graben. The opening of Rennick Graben was previously linked to mid Cretaceous (~ 100 Ma) rifting and interpreted as a failed rift arm (Fleming et al., 1993). This idea is challenged by fission track data (40–50 Ma), which indicate that Rennick Graben formed due to tectonic denudation (up to 5 km) combined with strike-slip deformation (Rossetti et al., 2003). A receiver function profile perpendicular to Rennick Graben (Station BI01 – BI03) indicates shallow crustal thickness of 24 km (Agostinetti et al., 2004). Both mechanisms combined, mid Cretaceous rifting *and* large amount of denudation, could explain elevated heat flow in Rennick Graben as seen in our results. Alternatively, small crustal thicknesses accompanied by a thin lithosphere can cause an elevation in heat flow. However, the thin

crust imaged by receiver functions is not limited to Rennick Graben and would cause broader high heat flow patterns in contrast to the narrow heat flow pattern imaged by our results.
Another linear geothermal feature is imaged in the Central Basin (Figure 2.6b). Competing models of WSB's origin have been proposed in the past, including continental rifting (Steed, 1983), which was partially supported by airborne geophysical data (Ferraccioli et al., 2001). However, interpretation of recent aerogeophysical data has suggested further that a rifting origin of the Central Basin is very unlikely (Ferraccioli et al., 2009a; Jordan et al., 2013). Alternative models include flexural down-warp of WSB in response to Cenozoic rift-flank uplift of the TAM caused by the neighbouring Ross Sea Rift (Stern and ten Brink, 1989; Ten Brink et al., 1997). Similarly, a recent model proposes that WSB developed as a result of flexural processes coupled with deep glacial erosion (Paxman et al., 2019). Both mechanisms, continental Cenozoic rifting, even though unlikely, and large-scale erosion, can cause elevated heat flow and might be connected to the high heat flow pattern observed in the Central Basin. The similarity in amplitude and linear pattern of heat flow in Rennick Graben and the Central Basin could be an indicator of a similar evolution mechanism. In the broader WSB area, except for Rennick Graben and the Central Basin, the CPD and GHF maps show overall deeper and lower values, respectively, and therefore indicate a much colder thermal structure.
The CPD and consequently GHF maps from this study have a higher spatial resolution than previous continental scale GHF estimates inferred from magnetic data (Figure 2.2a, d), due to a combination of smaller distance between evaluated windows (20 km) and using only high-resolution airborne data without substituting satellite measurements. Consequently, the spatial coverage of our approach is strongly limited to the region with a dense coverage of airborne measurements; however, where results are obtained, we believe them to be more robust.

2.8 Conclusion and future work

We have presented new CPD and GHF maps for the northern TAM and WSB area. Our spectral analysis of magnetic data provides a significant improvement over prior GHF maps of the region. We image elevated heat flow beneath the TAM, which extends further west than previously mapped. We also resolve elevated heat flow features in Rennick Graben and WSB's Central Basin that have not been imaged before. However, the overall spatial coverage of this analysis is limited by the extent of airborne surveys with close flight line spacing. Filling data gaps with satellite magnetic data, as previous studies in Antarctica have done (Dziadek et al., 2021; Martos et al., 2017) is not an effective solution due to the limited range of wavelengths it provides for the analytic window (Pappa and Ebbing, 2023). Previous Antarctic CPD studies have failed to report the centroid location of the analysed window, the power spectrum of the analysed window, or the intercept and slope values for the linear regression, which makes it impossible to directly reproduce them. We report for the first time all those parameters for

a CPD study in Antarctica, which makes this study fully reproducible. We encourage CPD studies in Antarctica to follow the guidance for reproducibility Núñez Demarco et al. (2020).

The shallow CPD values estimated beneath Northern Victoria Land and the TAM provide independent evidence favouring the hypothesis that warmer West Antarctic mantle provides thermal support for this part of the TAM, as imaged by seismological studies (Hansen et al., 2016; Lloyd et al., 2020; Wiens et al., 2023). High GHF values beneath the northern TAM and West Antarctica are also consistent with the presence of recently active volcanoes including Mount Erebus, Mount Melbourne and Mount Overlord.

Our GHF maps are a linear transformation from the CPD estimates and provide a good estimate of relative variations of the thermal structure. However, due to the high uncertainty of CPD estimates (section 2.7.1 and the simplified linear transformation to GHF (Equation 2.9)), absolute GHF values derived from spectral methods should be used with caution.

Despite the many assumptions and lack of onshore heat flow control data, the CPD and GHF results show convincing coherence and highlight interesting comparisons with known geological features. The approach of using exclusively high-resolution airborne data should be repeated in other areas of Antarctica with suitable magnetic data coverage to obtain relative variation in CPD. Future studies examining variation of β values could provide a meaningful tool for revealing subglacial geology in the area. Another, potentially more practical way could be to combine magnetic data with gravity data in a mutual information inversion framework to constrain subglacial geology and crustal boundaries like the depth to the bottom of magnetic sources (Lösing et al., 2022).

Chapter 3

The 3D crustal structure of Wilkes Subglacial Basin, East Antarctica, using Variation of Information joint inversion of gravity and magnetic data

3.1 Context

The previous chapter has illustrated how CPD can be used as a proxy for heat flow. However, this chapter also made it apparent that simplifying the crustal domain to a homogeneous slab effectively with constant physical properties is a source of potentially high error. This is especially the case because crustal heterogeneities in the form of crustal heat production caused by radiogenic decay can contribute up to 40% to the heat flow budget (Artemieva and Mooney, 2001; Haeger et al., 2019; Hasterok and Chapman, 2011). Therefore, the following chapter focuses on heterogeneities in crustal properties and subglacial geology and assesses their implications for the tectonic evolution of this region. To achieve this airborne gravity data are added to the modelling approach, which adds more complexity compared to the single data set approach pursued in chapter 2

3.2 Author contribution

The work presented in this chapter is under review for publication as: M. Lowe, T. A. Jordan, M. Moorkamp, J. Ebbing, C. Green, M. Lösing, T. Riley and R. Larter (in review) *Journal of Geophysical Research: Solid Earth*.

conceptualised: M. Lowe; Data curation: M. Lowe; Formal analysis: M. Lowe, T. A. Jordan; Funding acquisition: R. Larter; Investigation: M. Lowe; Methodology: M. Lowe, M. Moorkamp, T. A. Jordan, J. Ebbing, M. Lösing; Project Administration: R. Larter; Software: M. Lowe, M.

Moorkamp; Supervision: T. A. Jordan, J. Ebbing, C. Green, R. Larter; Validation: M. Lowe, T. A. Jordan, J. Ebbing, M. Moorkamp, C. Green, R. Larter; visualisation: M. Lowe; Writing – original draft: M. Lowe; Writing – review & editing: M. Lowe, T. A. Jordan, J. Ebbing, M. Moorkamp, T. Riley, C. Green, M. Lösing, R. Larter.

3.3 Introduction

Wilkes Subglacial Basin (WSB) lies between the Transantarctic Mountains (TAM) and Terre Adélie Craton (Figure 3.1) and was first identified by radar data in the 1970s (Drewry, 1976). WSB stretches $\sim$ 1600 km from George V Coast towards the South Pole, while its width decreases from $\sim$ 600 km close to George V coast (Ferraccioli et al., 2009a) to < 100 km towards the South Pole (Studinger et al., 2004). The subglacial geology in WSB and TAM region is largely hidden beneath a 2-3 km thick ice sheet. Understanding the subglacial geology and crustal properties is crucial to constrain the influence of the solid Earth on the stability of the overlying ice sheet.

WSB forms one of the largest areas of bed topography below sea level in East Antarctica, reaching depths of more than 2 km below sea level in the deeply incised sub-basins (Morlighem et al., 2020) (Figure 3.1). Such sub-sea level basins pose a potentially high, but poorly understood, risk for the stability of the East Antarctic Ice Sheet (EAIS) and, therefore, for future sea level rise, as they are more vulnerable to melting by warming of the adjacent ocean. Such melting could potentially trigger mechanisms of unstable retreat (Pollard et al., 2015; Schoof, 2007). Recent studies suggest a significant long-term contribution from the WSB region to sea-level rise within the next two centuries accompanied by major retreat of the ice sheet in the WSB region by the year 2500 (DeConto and Pollard, 2016; Stokes et al., 2022).

For WSB itself, competing models for its evolution have been proposed since its discovery including a rift basin (Steed, 1983), extended terrane (Ferraccioli et al., 2001), as a basin adjacent to the remnants of a collapsed plateau (Bialas et al., 2007), or as a flexural down-warp of cratonic lithosphere as a consequence of the TAM uplift (Stern and ten Brink, 1989; Ten Brink et al., 1997). However, the modern landscape formation of WSB is generally believed to result from a combination of lithospheric flexure associated with the TAM uplift combined with glacial erosion (Ferraccioli et al., 2009a; Jordan et al., 2013; Paxman et al., 2019).

The geology of WSB remains disputed as the occurrence of direct geological samples is limited to ice free regions along the coast, or isolated nunataks, while the origin of geological material transported to the coast by glaciers is often ambiguous. Adjacent to Mertz Shear Zone (Figure 3.1), on the side of the Terre Adélie Craton, $\geq$ 2440 Ma paragneiss and granitoids are exposed, while on WSB side of the Mertz Shear Zone ca. 500 Ma granites have been mapped (Finn et al., 1999). Aeromagnetic measurements in WSB have been used to infer the presence of Beacon Supergroup sedimentary strata intruded by rocks of the Ferrar Large Igneous Province (Ferraccioli et al., 2009a). Geological interpretations of the interior

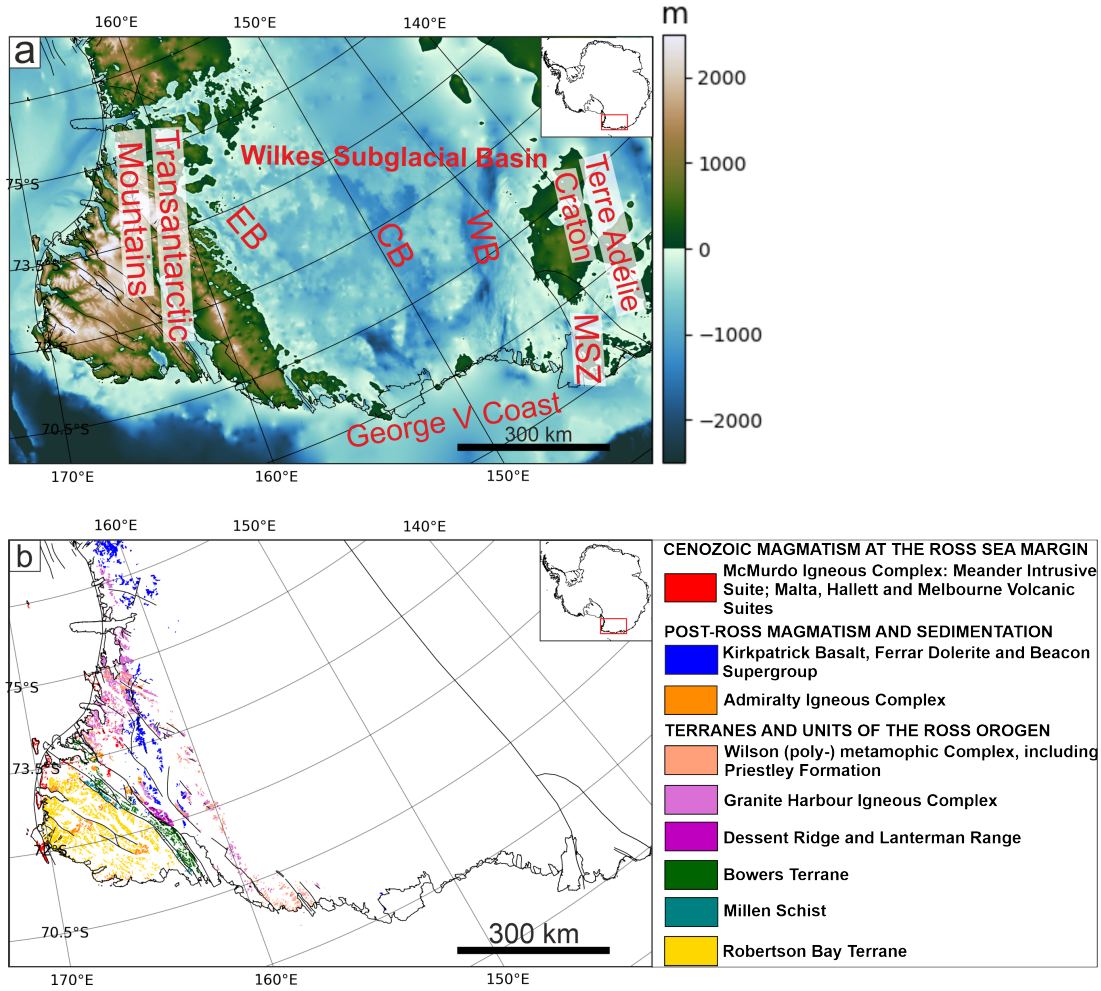

Figure 3.1: a) Bedrock topography of the Transantarctic Mountains and Wilkes Subglacial Basin (WSB) from the BedMachine Antarctica version 3 (Morlighem et al., 2020). EB: Eastern Basin; CB: Central Basin; WB: Western Basin; MSZ: Mertz Shear Zone. Black lines mark ice grounding lines and ice shelf extents from the SCAR Antarctic Digital Database. Black lines indicate faults based on Cox et al. (2023). b) Tectonic provinces. Geological information taken from Cox et al. (2023), classification adapted from Estrada et al. (2016), Läufer et al. (2011), Pertusati et al. (2016), and Roland et al. (2002).

of WSB are mainly derived from radar, gravity, and magnetic airborne measurements (e.g. Jordan et al. 2013).

A prominent positive magnetic anomaly exists in the central WSB, the origin of which is hypothesised to be either an intrusive arc associated with subduction (Ferraccioli et al., 2009a), or associated with thinned crust attributed to continental rifting (Ferraccioli et al., 2001). Another prominent feature is a positive linear gravity anomaly associated with the craton margin, which was interpreted as up-thrusted crustal material along the craton flank (Studinger et al., 2004) (Figure 3.2 a and b).

The adjacent TAM, a large non-contractional mountain range, separate the warmer litho-

sphere of the Cretaceous-Cenozoic West Antarctic Rift System and the colder and older provinces of East Antarctica (Morelli and Danesi, 2004; Robinson and Splettstoesser, 1986; Ten Brink and Stern, 1992). Direct geological information is richer in the TAM compared to WSB since more rock outcrops are present in the high mountain range.

The Neoproterozoic to early Palaeozoic Ross Orogen in Antarctica forms part of an active Gondwana-margin convergent plate boundary stretching from present-day eastern Australia to South America, but it is largely obscured by ice and younger sedimentary cover. Ross Orogeny magmatism developed over a period of ca. 100 Myr (ca. 600 - 500 Ma; (Goodge et al., 2024)), associated with multiple magmatic peaks (Paulsen et al., 2023), including the Cambro-Ordovician Granite Harbour intrusive Complex. In Northern Victoria Land, adjacent to our study area, the Ross Orogen is dominated by five geological terranes and units identified in the TAM; they are from grid-west (geographic east) (see Figure 3.1) to grid-east (geographic west) the Robertson Bay Terrane, the Millen Schist, the Bowers Terrane, the Wilson Terrane, and Granite Harbour Igneous Complex (Figure 3.1 a and b). These terranes are all intruded by doleritic sills of the Early Jurassic Ferrar large igneous province, and in places overlain by the associated Kirkpatrick basaltic lavas (Estrada et al. 2016 and references therein). Detrital zircon analysis from sedimentary rocks shows a decrease in likely depositional age from the Wilson Terrane towards grid-west to the Robertson Bay group from >550 Ma to <550 Ma (Estrada et al., 2016). The emplacement of the Granite Harbour Igneous Complex corresponds to the younger ages seen in the detrital zircon populations (Estrada et al., 2016), while the source for the older (>550 Ma) material remains speculative.

Radiogenic heat production is predicted to contribute up to 40% to the surface geothermal heat flow (Artemieva and Mooney, 2001; Haeger et al., 2022; Hasterok and Chapman, 2011). However, due to the lack of information on subglacial geology and crustal properties, incorporating accurate thermal crustal parameters, such as radiogenic heat production and thermal conductivity, is challenging. Therefore, current geophysically-derived geothermal heat flow (GHF) models commonly use global average values instead (Haeger et al., 2022; Lowe et al., 2023; Lösing and Ebbing, 2021; Martos et al., 2017; Shen et al., 2020; Stål et al., 2021). For more in depth discussion of current Antarctic geothermal heat flow models the reader is referred to Reading et al. (2022) and Burton-Johnson et al. (2020).

The objectives of this study are to identify crustal structures, crustal geological provinces, and intrusive bodies, constrain their dimensions in 3D, and to identify the Terre Adélie Craton boundary. For this purpose, we conduct a joint inversion of gravity and magnetic data to obtain petrological parameter distributions, specifically of density and susceptibility. The geophysical inversion uses the joint inversion framework JIF3D (Moorkamp et al., 2011), which implements the Variation of Information (VI) technique to introduce a coupling between the inverted density and susceptibility sources (Lösing et al., 2022; Moorkamp, 2021,2). Subsequently, the obtained density and susceptibility relationship of the inversion model is used to identify crustal rock provinces and infer potential rock types. The geophysical and petrophysical interpretation

of the inversion results is the basis for our tectonic evolution model. Although geophysical mapping can give an indication of tectonic boundaries and 2D models give some insights into the source bodies, the 3D architecture and properties of the crust are required to understand the origins and implications of this key basin more fully. We therefore turn to joint inversion of gravity and magnetic data to provide this information.

3.4 Data

This section describes the geophysical data and the boundary conditions used to obtain a joint inversion model for 3D crustal density and susceptibility distribution.

3.4.1 Gravity data

Bouguer gravity anomaly data (Figure 3.2a) are taken from AntGG (Scheinert et al., 2016). The Bouguer anomaly was calculated using a spherical prism approach with an integration radius of 300 km using standard densities of 2670 $\mathrm{kg\,m^{-3}}$ for rock, 917 $\mathrm{kg\,m^{-3}}$ for ice and 1025 $\mathrm{kg\,m^{-3}}$ for water (Scheinert et al., 2016). Where applied the Bouguer correction removes the signatures of surface and subglacial topography, as well as the gravity signature associated with the observed ice sheet and ocean basins. The AntGG gravity compilation includes airborne, terrestrial, and shipborne measurements, which are provided, after integration and correction, as a grid of points with a spacing of 10 km. Data gaps in AntGG are filled in with Bouguer gravity anomaly data from the Ganovex VII – ItaliAntartide XV survey (Reitmayr et al., 2003) and recent ground measurements conducted within the Italian National Program for Antarctic Research activities (Zanutta et al., 2018) (Figure B.1). This data compilation, including AntGG and additional ground data points, is re-gridded with a spacing of 10 km and a blanking distance of 40 km using the minimum curvature gridding function in Oasis Montaj [Seequent; Reading, England] (Smith and Wessel, 1990) to produce the Bouguer anomaly grid of WSB and TAM region. The blanking distance is the maximum distance from a valid point where values will be interpolated. Beyond this distance dummy values are returned. The Bouguer anomaly grid is subsequently upward continued to a constant observation height of 10 km above the geoid (Figure 3.2) using the Compudrape algorithm in Oasis Montaj (Cordell, 1985). This method takes data collected at various levels and generates a series of data slices using a standard fixed distance Fast Fourier Transformation continuation method (Blakely, 1996). The new field, continued to a uniform level, is interpolated from the suite of data slices. The Bouguer anomaly map shows a large negative signal in the TAM region, where a crustal root is present beneath the mountain range (Baranov et al., 2021; Block et al., 2009; Hansen et al., 2016; Pappa et al., 2019a). A prominent positive linear feature exists in the Bouguer anomaly map following the grid-east edge of WSB and might indicate the transition zone at the margin of the Terre Adélie Craton (Goodge and Finn, 2010). To

remove the gravity contribution below the Moho interface the vertical gravity response from the Antarctic continent-wide forward lithospheric model of Pappa et al. (2019b) was subtracted (Figure B.2). This model contains a homogeneous crust, where density only increases with depth due to the increasing pressure and a variable mantle. By subtracting this model, we corrected for a variable mantle and Moho depth variation and therefore the resulting residuals correspond to the crust. The lithospheric model is presented at 10 km observation height and is the reason all input data are upward continued to this constant height. In the resulting residual gravity map (Figure B.2) the large negative signal beneath the TAM is absent, while the relative positive linear crustal structure is preserved. Furthermore, the mean value (92.5 mGal) of the residual gravity field is removed to shift the residual gravity field to a mean level of 0 mGal (Figure 2b).

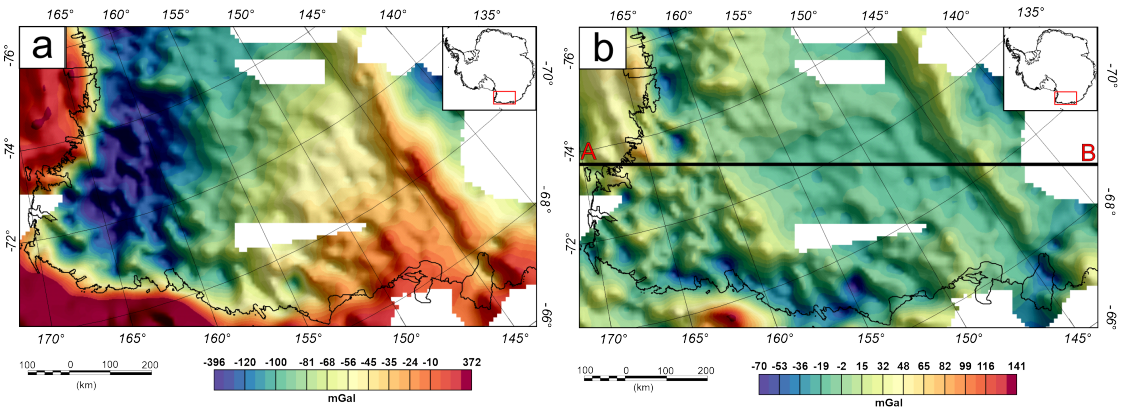

Figure 3.2: a) Bouguer Anomaly compilation including AntGG data (Scheinert et al., 2016), and regional gravity data (Reitmayr et al., 2003; Zanutta et al., 2018). b) Residual gravity map obtained by subtracting the gravity response from the lithospheric model of Pappa et al. (2019b) and then subtracting the mean value of the residual field. Both gravity grids have a grid spacing of 10 km. Black line indicates location of cross section profile in Figure 3.8.

3.4.2 Magnetic data

3.5 million line-km of aeromagnetic and marine magnetic measurements in Antarctica and the Southern Ocean are included in the ADMAP-2 magnetic data compilation (Golynsky et al., 2018). The gridded ADMAP-2 product (Figure 3a) has a grid spacing of 1.5 km. Applied data processing and corrections of the magnetic data include subtraction of the International Geomagnetic Reference Field, corrections for diurnal effects and high-frequency errors, levelling, regional gridding, and merging of regional grids into a continent-wide compilation (Golynsky et al., 2018). For the inversion, the magnetic line data from the ADMAP-2 compilation are gridded with a grid spacing of 10 km to match the grid spacing of the gravity data (section 3.4.1).

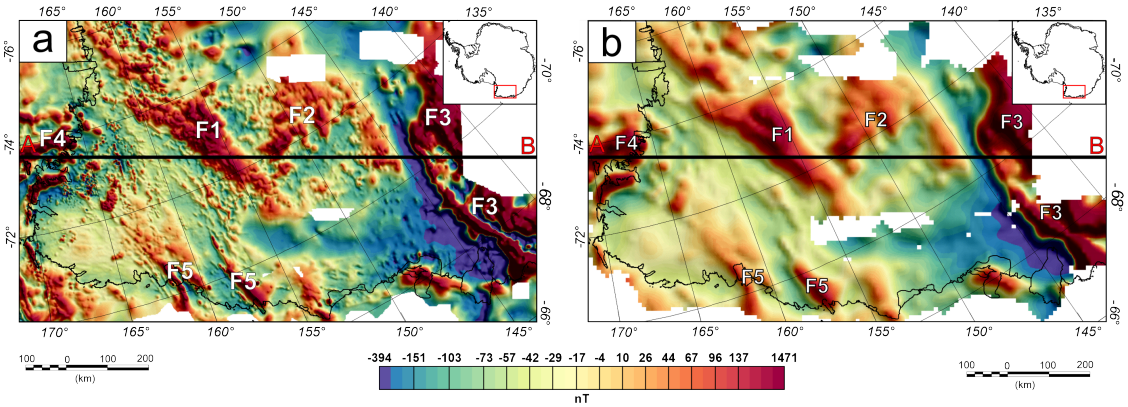

Figure 3.3: a) Magnetic anomaly grid from ADMAP-2 (Golynsky et al., 2018) with a grid spacing of 1.5 km. b) Regridded ADMAP-2 magnetic data with a grid spacing of 10 km and upward continued at a constant height of 10 km to match the resolution and upward-continued height of the gravity compilation. Black line indicates location of cross section profile in Figure 3.8. Features F1-F5 relate to magnetic anomalies discussed in the main text.

Again, the gridding was performed using the minimum curvature gridding function with a blanking distance of 10 km in Oasis Montaj. The magnetic grid is also upward continued to a height of 10 km (Figure 3.3b) to be consistent with the gravity data using again the Compudrape function within Oasis Montaj. The upward continuation of the magnetic data functions as a lowpass filter, removing high frequency content, while broad magnetic anomalies are preserved. The upward continuation of the magnetic data attenuates the short wavelengths. The minimum wavelength of the upward continued data is approximately 20 km. The magnetic anomaly grid shows a broad linear feature orientated grid-northwest – grid-southeast (Figure 3.3, F1) in the central part of WSB, the origin of which has been hypothesised to be a failed rift or an arc-related intrusive body (Ferraccioli et al., 2009b; Ferraccioli and Bozzo, 2003). Perpendicular to this feature a positive magnetic anomaly is visible (F2). A strong linear anomaly exists grid-east to WSB towards the craton margin (F3), where the magnetic anomaly rapidly increases to values of $\sim$1500 nT compared to the dominating $\pm$ 300 nT range in WSB and TAM area. Smaller magnetic anomalies are observed offshore to the grid-west (F4) and along Rennick Graben and Matusevich glacier region (F5).

3.4.3 Uncertainty of airborne data

The uncertainty of airborne gravity and magnetic measurements depends on several factors such as the sensor, the processing or turbulence during the measurement campaign. The input data are a compilation of multiple surveys with varying data uncertainty. The gravity survey WISE-ISODYN, which is the dominant survey in the data compilation, has a reported uncertainty of 2.8 mGal (Jordan et al., 2013). Error estimation of airborne magnetic data

is assessed by crossovers of flight lines. However, crossovers are used to level the survey itself, which eventually leads to a 0 nT offset at the crossovers. A conservative uncertainty estimation of airborne magnetic data is in the order of magnitude of 5 – 15 nT.

3.4.4 Moho depth and Curie depth

Moho depth estimates (Figure 3.4a) are taken from satellite gravity inversion (Pappa et al., 2019a). The Moho interface is used as the bottom boundary condition for the density inversion. Curie Point Depth (CPD) estimates (Figure 3.4.4) are taken from Chapter 2 (published as Lowe et al. 2023 and used as a bottom boundary condition for the susceptibility inversion. Below the CPD, often associated with the 580 ℃ isotherm, ferrimagnetic materials lose their ability to maintain a preferential orientation in the direction of the inducing, main field. Therefore, the joint inversion of magnetic and gravity data needs to be limited to crustal depth above the CPD. The CPD estimates from Chapter 2 have a 20 km grid spacing and are interpolated on a 7.5 km grid, matching the cell size of the inversion mesh, by applying statistical kriging using the python package PyKrig (Murphy et al., 2022), with a Gaussian variogram and a nlags (Number of averaging bins for the semivariogram) value set to 20. After interpolation, the CPD map shows some values deeper than the Moho depths from Pappa et al. (2019a) in the offshore area and along the coast. A CPD below the Moho would indicate that the upper mantle is magnetic and although this possibility has been suggested (Ferré et al., 2014), we discard CPD values below the Moho boundary and in these areas use the Moho depth as the magnetic boundary depth (Figure 3.4b).

Both CPD and Moho depth have associated uncertainties. The CPD dataset has reported

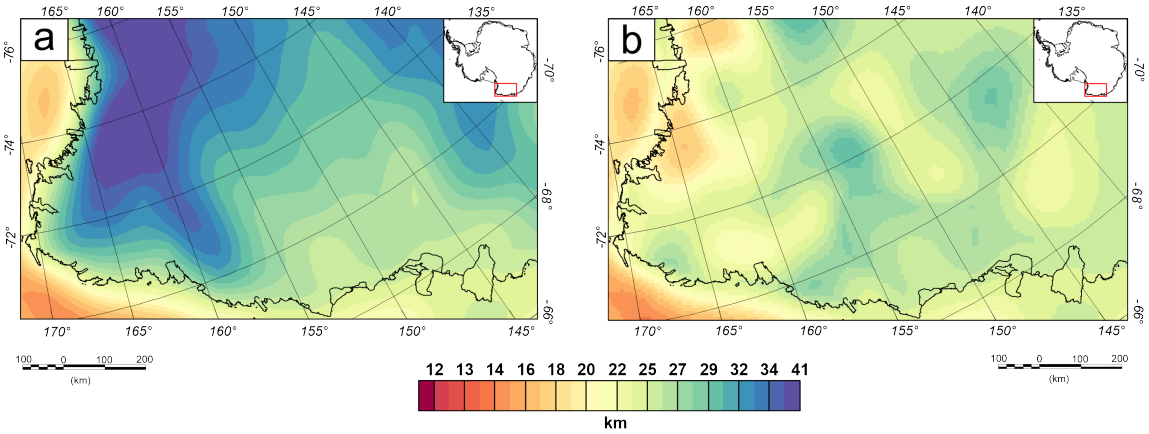

Figure 3.4: a) Moho depth map derived from satellite gravity measurements (Pappa et al., 2019a). CPD estimated from Lowe et al. (2023) based on kriging interpolation and clipped to be shallower than the Moho.

uncertainties ranging between 2-6 km (Lowe et al., 2023), while the uncertainty for the Moho depth ranges from roughly 5-8 km (Pappa et al., 2019a). Despite the uncertainty, it is beneficial to use physically derived estimates as the bottom boundary condition, rather than arbitrarily selected constant boundary depths.

3.5 Method

3.5.1 Joint inversion of gravity and magnetic data

Joint inversion of gravity and magnetic data is carried out in JIF3D (Moorkamp et al., 2011). JIF3D is a 3D joint inversion framework for geophysical data sets including magnetotelluric, seismic, magnetic data as well as scalar and tensor gravity data. JIF3D utilise a limited memory quasi-Newton approach (Avdeev and Avdeeva, 2009) for optimisation. For a complete mathematical description of the JIF3D inversion framework the reader is referred to Moorkamp (2021, 2022) and Moorkamp et al. (2011).

Inverting simultaneously for crustal density and susceptibility distribution using gravity and magnetic data in a joint inversion framework is well established (Bosch et al., 2006; Fregoso and Gallardo, 2009; Frey and Ebbing, 2020; Gallardo-Delgado et al., 2003; Guillen and Menichetti, 1984; Shamsipour et al., 2012). However, joint inversion based on VI, which allows the coupling of physical parameters, has only recently become popular in geophysical joint inversion applications (Haber and Holtzman Gazit 2013; Lösing et al. 2022; Mandolesi and Jones 2014; Moorkamp 2021, 2022) VI is related to the concept of mutual information (MI) (Moorkamp et al., 2011). VI describes the amount of shared information contained in two variables, meaning a low VI value indicates that both variables are dependent, while a high VI value indicates that information about variable 1 does not reveal meaningful information about variable 2 (Moorkamp 2021, 2022; Lösing et al. 2022; Mandolesi and Jones 2014). VI is defined as:

$$VI(x,y) = 2H(x,y) - H(x) - H(y) \tag{3.1}$$

where $H(x) = -\sum_i \rho(x_i) \log \rho(x_i)$ is the Shannon Entropy; $\rho(x_i)$ is the probability density approximated by kernel methods (Mandolesi and Jones, 2014); $H(x,y)$ is the joint entropy while $H(x)$ and $H(y)$ are the marginal entropies (Lösing et al. 2022; Moorkamp 2021, 2022). VI is incorporated into the objective function Φ_{joint} as:

$$\Phi_{joint} = \Phi_{d,grav} + \Phi_{d,mag} + \lambda_1 \Phi_{reg,\rho} + \lambda_2 \Phi_{reg,sus} + \lambda_3 \Phi_{VI} \tag{3.2}$$

where $\Phi_{d,grav}$ and $\Phi_{d,mag}$ are the root-mean-square (RMS) misfit between observed and inverted gravity and magnetic data; $\Phi_{reg,\rho}$ and $\Phi_{reg,sus}$ are regularisation terms for the density and susceptibility distribution, controlling the smoothness of the inverted model. A full description of these terms can be found in Moorkamp (2021). Φ_{VI} is a coupling term which includes VI of

recovered density and susceptibility and λ represents the weighting factors of the individual terms.

VI inversion has been successfully applied to magnetotelluric and seismic data (Mandolesi and Jones, 2014), magnetotelluric and gravity data (Moorkamp 2021, 2022), and gravity and magnetic data (Lösing et al., 2022). Lösing et al. (2022) demonstrated that VI inversion can recover density and susceptibility distributions, if it is assumed that the gravity and magnetic signals have an identical source, by performing VI inversion tests on synthetic data.

3.5.2 Inversion setup

The density and susceptibility inversion models are discretised into meshes with equal horizontal cell sizes of 7.5 km. The vertical cell size is 1 km at the surface and increases with depth by a factor 1.1 for each cell (Figure B.3). Increasing vertical cell size with depth is introduced to account for decreasing resolution with increasing distance to the source in potential field applications. A horizontal cell size of 7.5 km is chosen because the input gravity and magnetic data have a grid spacing of 10 km (see section 3.4). A cell size of 7.5 km allows the inversion to adjust on average more than one cell to fit the inversion data but is also not too small to not represent the point spacing of the input data or introduce artifacts. Additionally, a padding area of 20% around the study area is added to avoid edge effects. The resulting inversion mesh contains 244 cells in the grid-east to grid-west direction, 140 cells in the grid-north to grid-south direction and 21 cells in the z direction (above a maximum depth of 60 km below sea level). To constrain the model geometry, the bedrock topography from BedMachine Antarctica version 3 (Morlighem et al., 2020), CPD (Lowe et al., 2023), and Moho depths (Pappa et al., 2019a) are used. CPD and Moho depth estimation have their own associated uncertainties (see section 3.4.4). The vertical increase of cells in the inversion mesh is an adaptation to account for those uncertainties. For example, at depths of the CPD of 24 km the vertical cell resolution is $\sim$3.5 km and at the Moho depth of 36.5 km the vertical resolution is $\sim$4.6 km representing uncertainties within both data sets used as model boundary conditions. Furthermore, competing Moho depth models for the study area (Baranov et al., 2021; Pappa et al., 2019a) report different Moho depths but the differences are less than 8 km (Figure B.4), which is of the order of magnitude of the uncertainties and the vertical cell resolution.

The aim of the VI inversion is to invert jointly the gravity and magnetic field for the density and susceptibility of the crust. Only cells between the bedrock interface and the Moho interface are allowed any variation during the inversion. However, rocks lose their magnetic properties at the Curie temperature. Therefore, joint VI inversion for both density and susceptibility is carried out only for cells between the bedrock interface and the CPD interface. Between the CPD interface and the Moho interface density only inversion is carried out and susceptibility is held at zero.

The input gravity field for the density inversion is corrected for masses below the Moho interface by the Antarctic lithospheric model from Pappa et al. (2019b). All cells are set

Table 3.1: Inversion parameters

Coupling	25,000 run 1 and 15,000 run 2
Regularisation Density and Susceptibility	10
Error Gravity [mGal]	2
Error Magnetics [nT]	15
Min. / Max Density [$\mathrm{kg\ m^{-3}}$]	$\pm$ 250
Min. / Max Susceptibility [SI]	$\pm$ 0.1
Magnetic Field strength [nT]	64981
Inclination [°]	-84.4
Declination [°]	147.4
dens covmod (Maximum depth of density variation)	Moho depth
sus covmod (Maximum depth of susceptibility variation)	CPD depth
coupling validity (Maximum depth where coupling is assumed)	CPD depth

to a starting value of 0 $\mathrm{kg\ m^{-3}}$ for the density anomaly model and 0 SI for the magnetic susceptibility model and are iteratively updated during the VI inversion process where they fall within the geometrically defined boundaries noted above.

The first inversion run is performed with a high coupling weight in order to enforce a tight coupling between the inverted models. Subsequently, a second inversion run is carried out, which uses the resulting density and susceptibility values from the first inversion run as a starting model, but a lower coupling weight is applied. The rationale behind using two different coupling weights is that a tighter coupling in the first inversion run favours geometrical structures in both the density and susceptibility, while a second inversion run with a lower coupling provides the inversion algorithm with more freedom to fit the observed gravity and magnetic field better (Moorkamp, 2022). Coupling values were established by trial and error.

The inducing magnetic field strength (Earth's normal field) is set to 64981 nT with a constant inclination of -84.4 ° and a declination of 147.4 ° for the whole study area based on the definitive magnetic reference field (DGRF) for a longitude of 155 ° and a latitude of -73 ° for the year 2005 (the year of the aerogeophysical survey WISE-ISODYN, the main survey in the study area). Additional parameter settings of the inversion are given in table 3.1. Subsequently the relationship between the inverted relative densities and susceptibilities are used to characterise 3D crustal structures and to identify crustal units with similar relationships.

3.6 Results

The VI inversion of gravity and magnetic data for WSB and TAM region is carried out in two subsequent inversion runs with varying coupling factors of 25 000 for the first 100 iterations (inversion result shown in appendix B.3) and 15 000 for subsequent 25 iterations, while all other parameters are kept fixed as described in section (3.5.2) and table (3.1) The RMS after the combined 125 iterations is 1.5 mGal for the gravity inversion and 0.7 nT for the magnetic inversions (Figure 3.5a). VI increases sharply during the first inversion iterations, then decreases until iteration 100. After the coupling is lowered at iteration 100, VI increases instantaneously, and decreases in the subsequent iterations (Figure 3.5b). A high value of VI means that susceptibility predictions from density and vice versa are more difficult. The coupling factors are highly dataset specific. We run inversions with a range of coupling factors and choose the highest one that allows the inversion to converge to a satisfactory data fit. This produces the strongest coupled models that explain the data. As experience from other studies and this example show, it is not necessary to find an exact value, values within a factor of 2 or so produce very similar results (Franz et al., 2021; Lösing et al., 2022; Moorkamp, 2022). The RMS error decreases for the gravity and magnetic inversion sharply after the transition from a coupling of 25000 to 15000. Although the amplitude of the decrease in RMS error after lowering the coupling seems small, the long wavelength residual in the magnetic inversion model decreases significantly in the residual maps (Figure 3.6f and Figure B.6). The

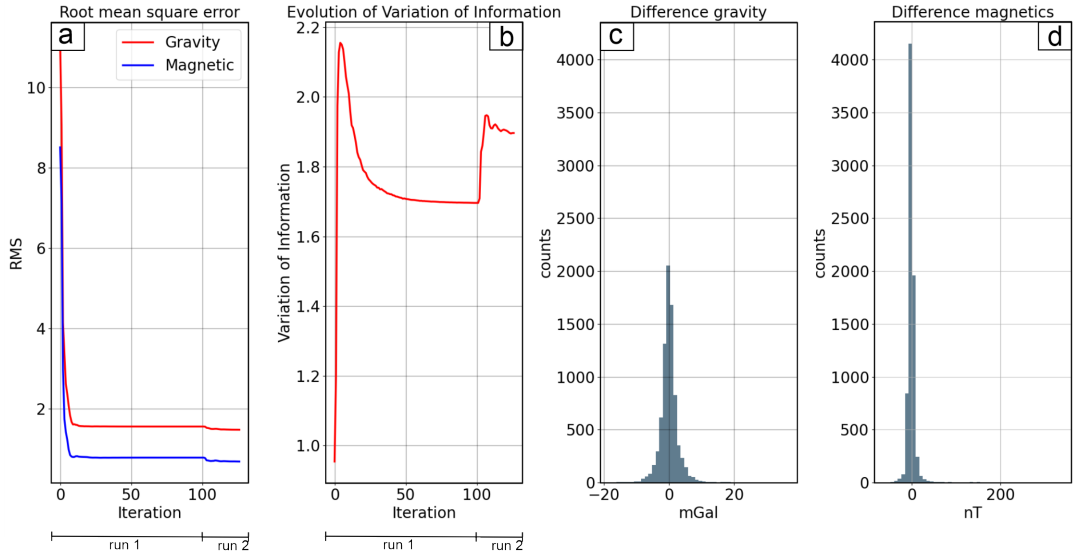

Figure 3.5: a) RMS error between observed and inverted gravity (red) and magnetic (blue) field for each inversion iteration. b) Evolution of VI. c) Gravity residual histogram between observed and inverted gravity field. d) Magnetic residual between observed and inverted magnetic field.

amplitude and distribution of anomalies within the gravity and magnetic field are reproduced well by the inversion (Figure 3.6 a, b, c and d). The end members of the residual between

observed and inverted values are +37 and -18 mGal with a standard deviation of 3 mGal for the gravity inversion and +341 and -65 nT with a standard deviation of 13 nT for the magnetic inversion (Figure 3.5 c and d). The difference maps between observed and inverted values are shown in Figure 3.6e and 3.6f. Both residual maps show a good agreement between observed and inverted gravity and magnetic field with low residuals for most of the study area. The highest misfit amplitude in the gravity field is located in the area of the TAM, in the grid-southwest part of the study area. Airborne surveys are sparse in this area resulting in significant data gaps in the AntGG (Scheinert et al., 2016) compilation. Gravity ground stations (Reitmayr et al., 2003; Zanutta et al., 2018) are used to fill the data gaps (Figure B.1 b). A possible source of the higher amplitude in the misfit cluster in the TAM region could be contributed by the low spatial coverage of the ground stations and the offset in frequency content between the airborne and ground station data and could therefore be associated with local effects.

The largest misfits between the observed and inverted magnetic data are located around prominent data gaps within WSB and the large data gap in grid-north, as well as in the gird-east of the study area, where the amplitude of the observed magnetic anomaly increases sharply from 300 nT to over 1500 nT. It is expected that the inversion algorithm struggles to reproduce a rapid variation in the magnetic field of over 1200 nT since the inversion algorithm favours smooth models. On the other hand, an error of 200 nT in a region with a field strength of over 1500 nT is less dramatic than compared to the TAM and WSB region with amplitudes of 300 nT. Additionally, a long wavelength feature exists in the magnetic residual map, which we do not further address due to the low magnitude of 5 nT.

Density and susceptibility depth slices at 5.5 km, 11.9 km and 20.5 km depths are presented in Figure 3.7. The linear grid northwest-grid southeast anomaly in the central WSB (IB1) appears to be connected at depth with the neighbouring anomaly with a grid northeast - grid southwest orientation (IB2), while both anomalies are separated at shallower depths.

The aim of the inversion is to find density and susceptibility distributions that are geometrically connected and simultaneously can explain the observed gravity and magnetic field. The underlying assumption is that a crustal rock has density and susceptibility values, which influence simultaneously the gravity and magnetic field. A cross section along profile AB (Figure 3.8 a-d) shows the similarities in the geometry of both petrophysical quantities. A large-scale negative density anomaly is located centrally in profile AB (black dotted circle in Figure 3.8b), while the susceptibility inversion model shows a high susceptibility anomaly with identical geometry. Adjacent to this anomaly is another negative density anomaly (red dotted circle in Figure 3.8b) but in this case the susceptibility values are also negative. This illustrates that a common geometry of both quantities is inverted, but the relationship between the density and susceptibility values is not linear. The cross section through the inverted density and susceptibility model indicates that the source for the linear magnetic anomaly

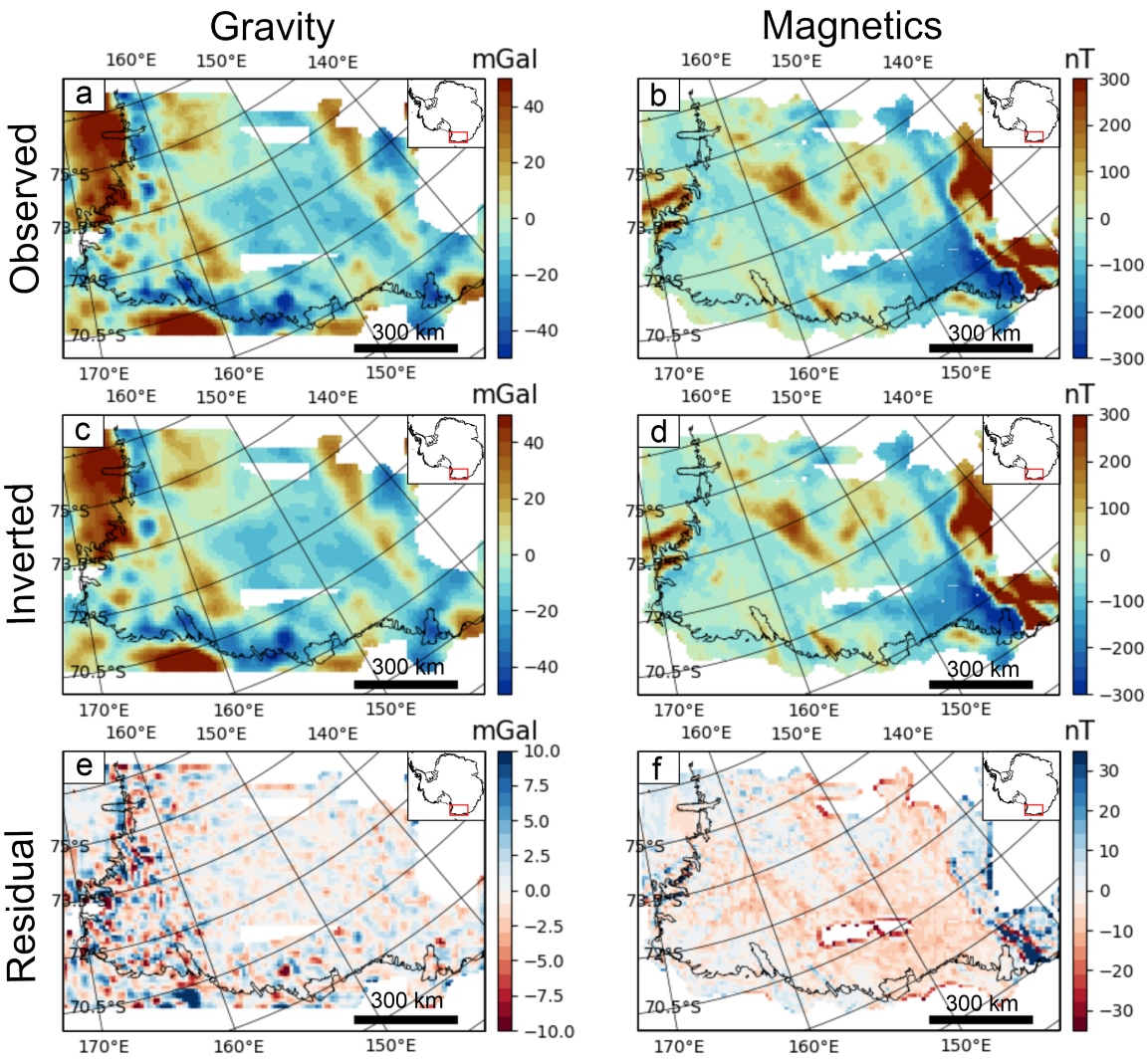

Figure 3.6: Visualisation of inversion results. a) Gravity inversion input data. b) Magnetic inversion input data. c) Final inverted gravity field. d) Final inverted magnetic field. e) Difference map between observed and inverted gravity fields (6a minus 6c). f) Difference map between observed and inverted magnetic field (6b minus 6d).

in the central WSB is connected at depth to the neighbouring positive anomaly source with a perpendicular orientation (Figure 3.8). These results illustrate the advantage of using a joint inversion approach to obtain the density and susceptibility distribution (see appendix B.4. Figure B.6 - B.9).

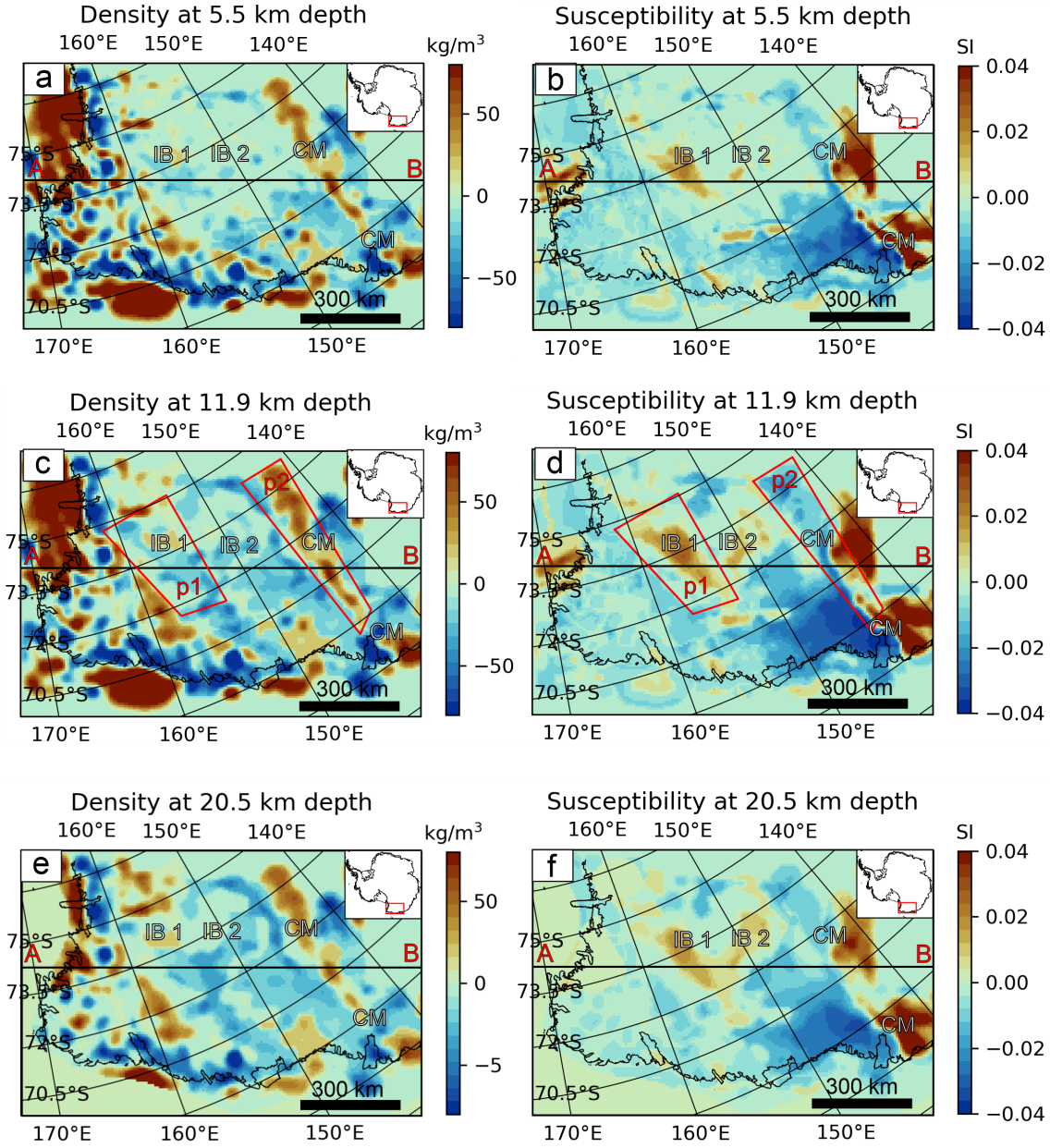

Figure 3.7: Depth slices through the inverted density and susceptibility model. a) Inverted density at 5.5km depth. b) Inverted susceptibility at 5.5 km depth. c) Inverted density at 11.9km depth. d) Inverted susceptibility at 11.9 km depth. e) Inverted density at 20.5 km depth. f) Inverted susceptibility at 20.5 km depth. Black line indicates location of cross section profile in Figure 8. P1 and P2 indicate the polygons for extracting 3D distribution of density and susceptibility bodies. IB: intrusive body; CM: craton margin.

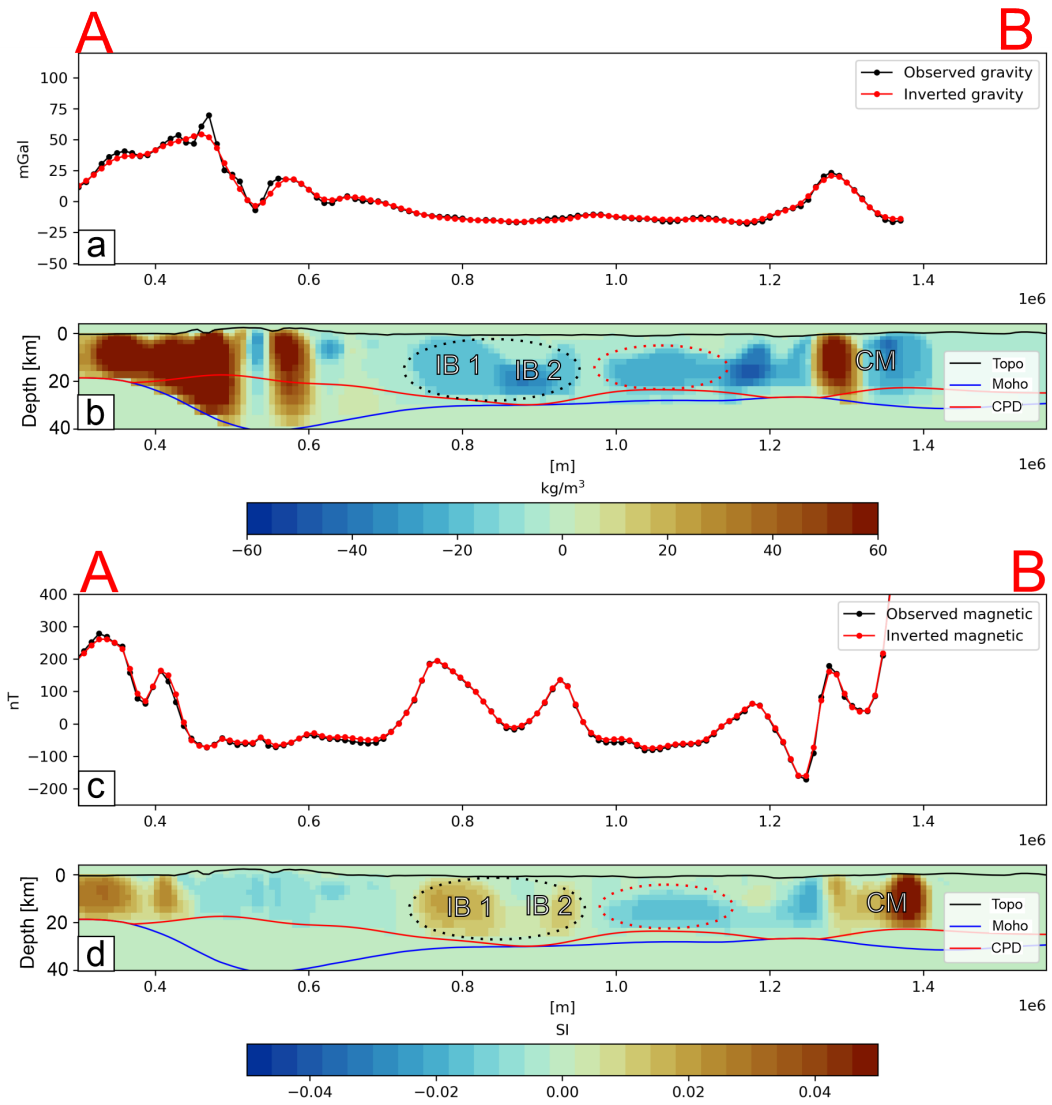

Figure 3.8: a) Observed (black line) and inverted (red line) gravity field along profile AB. Location of profile AB is given in Figure 7. b) Cross-section of the inverted density model along profile AB. c) Observed (black line) and inverted (red line) magnetic field along profile AB. d) Cross-section of the inverted susceptibility model along profile AB. IB: intrusive body; CM: craton margin.

3.6.1 Absence of sediment signature

The regional scale inversion results in WSB do not show any clear signatures of sedimentary basins, such as broad regions of shallow low density material, lacking elevated magnetic susceptibility even though previous large geophysical efforts have been undertaken to identify sedimentary basins in the broader region of Wilkes Land (Aitken et al. 2023, 2014; Frederick et al., 2016). The absence of sediment basins in the inversion result might be due to a combination of factors. 1) A sedimentary layer thicker than 1 km may be absent, as suggested by previous magnetic depth to source and 2D gravity modelling in WSB (Aitken et al., 2014;

Frederick et al., 2016). 2) Well indurated sandstones, such as the Beacon Supergroup strata, can have densities hardly distinguishable to the surrounding crustal rocks. Measured densities of Beacon strata in northern Victoria Land range from 2220 to 2610 $\mathrm{kg\,m^{-3}}$ (Barrett and Froggatt, 1978), coming close to the crustal average of 2670 $\mathrm{kg\,m^{-3}}$ assumed in the model. The close association of Beacon sandstones with intrusive Ferrar dolerites observed in outcrops (Goodge and Fanning, 2010) may further mask the presence of a sedimentary basin, as the intrusive rocks both increase the mean density and increase the apparent susceptibility of the associated crustal volume. 3) The vertical inversion mesh resolution increases with depth and at the depth of the upper crust the vertical cell size is $\sim$1200 m while the horizontal resolution is 7500 m. In order to recover a low-density sediment layer, the layer must fill the majority of an inversion cell (1200 m times 7500 m times 7500 m). Evidence of sediment layers thicker than 1200 m is currently lacking (see above).

3.6.2 Density and susceptibility relationship

A density and susceptibility cross plot illustrate the parameter relationship between both quantities (Figure 3.9). The relative inverted densities range from -160 to 250 $\mathrm{kg\,m^{-3}}$, while the inverted susceptibilities range from -0.06 to 0.9 SI. However, the density and susceptibility histograms indicate that the inverted density values are predominantly between $\pm$ 50 $\mathrm{kg\,m^{-3}}$ and inverted susceptibility values are mostly between $\pm$ 0.02 SI. High relative density values above 100 $\mathrm{kg\,m^{-3}}$ are located exclusively offshore while large negative values below -100 $\mathrm{kg\,m^{-3}}$ are located as distinct clusters in the TAM and along the coast (Figure 3.10 a-b). High relative susceptibility values above 0.025 SI are located offshore and to a much larger extent at the grid-eastern edge of WSB at the inferred craton margin (Figure 3.10 a-b). Furthermore, strong negative relative susceptibility values below -0.03 SI are limited to the craton margin (Figure 3.10 a-b). To constrain the geometry and properties of particular sub-surface source bodies we extracted the inverted density and susceptibility values within the polygons p1 and p2 (polygon location shown in Figure 3.7 c-d) and subsequently used thresholding of the susceptibility or density values to recover the approximate geometry of sources associated with specific anomalies. The source for the prominent positive magnetic anomaly in the WSB region is extracted by windowing the joint inversion output in this area for relative susceptibility values larger than 0.003 SI. The volume of the extracted body amounts to $\sim$286 000 $\mathrm{km^3}$. The source for the linear high gravity anomaly on the grid-eastern flank of WSB was extracted by windowing the joint inversion output in this area for relative density values larger than 10 $\mathrm{kg\,m^{-3}}$. The mean and standard deviation of the density and susceptibility relationship within those two extracted prominent bodies are superimposed on the density–susceptibility cross plot of the whole inversion model (Figure 3.10c). Both features cluster around distinct areas in the cross plot and are easily distinguishable (Figure 3.10c). The Central WSB source (IB1) has a mean relative density that is slightly negative (-13.1 $\mathrm{kg\,m^{-3}}$) and a mean relative susceptibility that is moderately positive (0.012 SI), while the mean relative density is positive

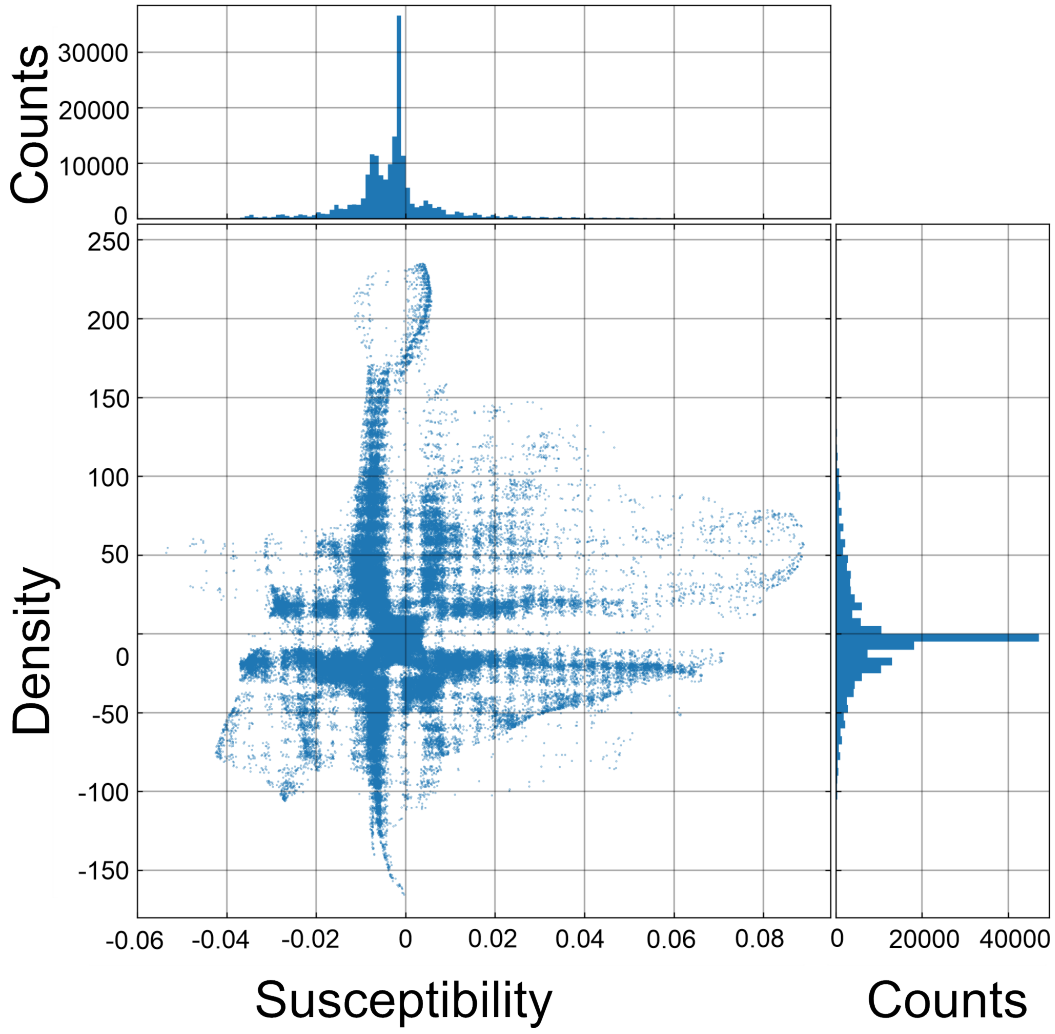

Figure 3.9: Inverted density and susceptibility cross plot and density and susceptibility histograms of the VI inversion model.

(32.1 $\mathrm{kg\,m^{-3}}$), and the mean relative susceptibility is negative (-0.003 SI) for the feature along the craton margin (CM). The standard deviation for the susceptibility of the craton margin feature is significantly larger compared to the intrusion signal (Figure 3.10c). The standard deviation range of density and susceptibility for each body is subsequently used to filter the entire inversion model to find the location of rocks with matching density and susceptibility relationships across the study area (Figure 3.10d). The location of rocks with matching susceptibility and density relationships reveals petrophysical similarities between the central WSB magnetic anomaly (F1 in Figure 3.3) and the adjacent magnetic anomaly that lies perpendicular to it (F2 in Figure 3.3), which potentially has the same origin (IB1, IB2 in Figure 3.10d). The extent and volume of those 3D structures can be extracted from the model (Figure3.11).

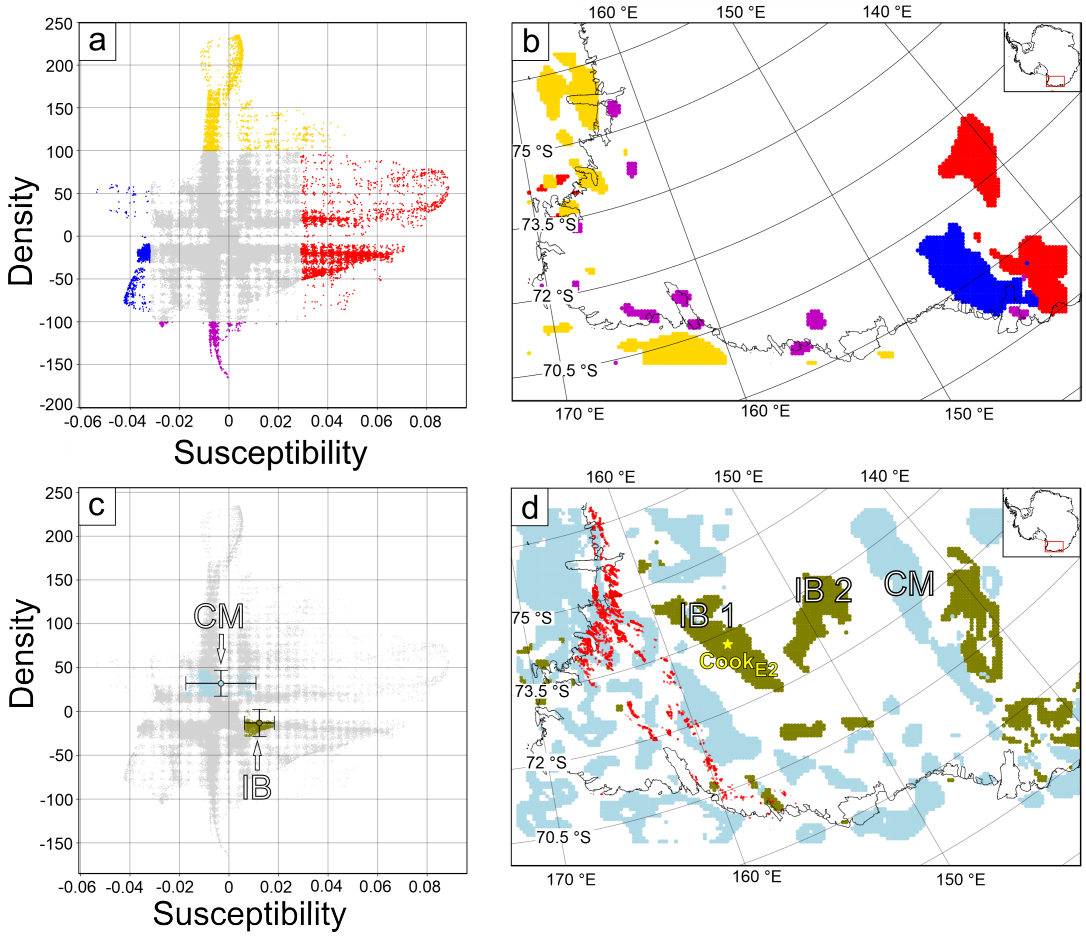

Figure 3.10: Density vs susceptibility cross-plots and province characterisation. a) Extreme susceptibility and density groupings. High inverted relative density values above 100 $\mathrm{kg\,m^{-3}}$ (yellow dots), low relative inverted density values below – 100 $\mathrm{kg\,m^{-3}}$ (purple dots), high relative inverted susceptibility values above 0.029 SI (red dots) and low relative inverted susceptibility values below -0.032 SI (blue dots) superimposed on density and susceptibility cross-plot of the entire inversion model. b) Spatial distribution of extreme density and susceptibilities highlighted in a). c) Mean and standard deviation (error bars) of interpreted intrusive body (olive green) and craton margin feature (pale blue) isolated using thresholding of standard deviation of recovered values within p1 and p2 located in Figure. 3.7. All recovered values falling within the recovered density/susceptibility ranges are colour coded accordingly and superimposed on density and susceptibility cross-plot of the entire inversion model. d) Location plot of density and susceptibility relationships within the standard deviation range of the extracted bodies in Figure 3.7. Granite Harbour Intrusive Complex (red) taken from GeoMAP (Cox et al., 2023). IB: intrusive body; CM: craton margin. Yellow star marks location of $Cook_{E2}$ subglacial lake (Li et al., 2020; McMillan et al., 2013; Smith et al., 2009).

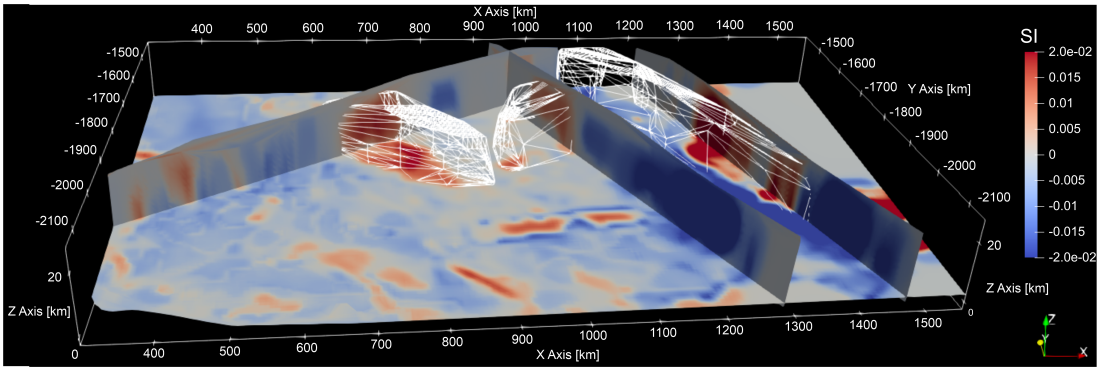

Figure 3.11: 3D intrusion and craton margin bodies (white wireframe) superimposed on slices through the 3D inverted susceptibility model. View looking grid north (approximately SSW geographically) along the axis of WSB, with two interpreted intrusive bodies in the centre and craton margin source body to the right. X, Y and Z axis in km. Z axis vertical exaggeration x5.

3.7 Interpretation and discussion

Our new inversion provides insights into the geometry and petrophysical properties of the bodies beneath WSB. As a result of an inversion of geophysical data it is, by its nature, non-unique. However, by combining magnetic and gravity data we have provided a more constrained model, consistent with both datasets, compared to previous studies, which relied on 2D models of either gravity or magnetic data in this region (Ferraccioli et al., 2009a; Jordan et al., 2013). The recovered pattern of density and susceptibility is considered robust and reveals more geologically reasonable structures compared to inverting for both quantities independently (see supporting information) and, therefore, can provide improved insights about the underlying geology. The uncertainty in boundary conditions (CPD and Moho depth) might influence the recovered density and susceptibility values in terms of amplitude, but the horizontal spatial distribution is less affected. Furthermore, the lack of external constraints such as seismic receiver function, reflection-seismic or crustal-wave velocity data precludes us from reducing the non-uniqueness of potential field data, meaning thickness remainsan estimate. It is possible that the complex superposition of bodies of varying susceptibility and density could also yield a very different structural model fitting the data equally well, but without evidence for this, we believe our inversion output to be a reasonable starting point for a discussion of the subglacial geology.

3.7.1 Batholith location, age, and potential significance

One of the most obvious features of the inversion result is the identification of a large body with elevated susceptibility and relatively low-density values (mean 13 $\mathrm{kg\ m^{-3}}$), which are confined to a narrow range of 50 $\mathrm{kg\ m^{-3}}$ in the centre of WSB. We interpret this body as a large-scale igneous batholith. Shifting the relative density values to absolute values by adding the average crustal background density of 2670 $\mathrm{kg\ m^{-3}}$ indicates that the density of the extracted body in the centre of WSB ranges from 2630 to 2680 $\mathrm{kg\ m^{-3}}$ combined with susceptibility values moderately above the general values for the region. Shifting relative susceptibility values to absolute values is more challenging compared to the density counterpart because i) no crustal susceptibility background value exists ii) the inverted susceptibility includes remanent, the impact of magnetisation which translates as relative susceptibility values which may be negative. However, the susceptibility values from our inversion show a strong peak close to zero, which we take as the crustal background, while relatively positive susceptibility values are taken as an approximation of true rock susceptibility. The density and susceptibility relationship is in accordance with the petrophysical relationship for granite rock samples from Australia (Barlow, 2004) and from the South Indian shield (Subrahmanyam et al., 1981) illustrated by Lösing et al. (2022) (see also chapter 4). However, it should be noted that susceptibility ranges for different lithologies overlap, and even within the same rock type there can be a large internal variability (Lowe et al., 2024). Granodiorite and other granitoid composition (e.g. tonalite, diorite) plutons fit comfortably within the susceptibility range as well. Susceptibility ranges from granites of the Cambro-Ordovician Granite Harbour Intrusive Complex are reported to be between 0.002 to 0.08 SI, while the majority of values are between 0.001 and 0.01 SI (Bozzo et al., 1992; Ohneiser et al., 2015). Significantly lower susceptibility values are reported for Ordovician granitoids of northern Victoria Land (0.00668 SI) (Bozzo et al., 1992; Lanza and Tonarini, 1998). The mean susceptibility recovered for the central WSB body is 0.012 SI. Although reasonable for a granite (Barlow, 2004; Maslanyj et al., 1991; Subrahmanyam et al., 1981), it is above values often quoted for the Granite Harbour Intrusive Rocks (Bozzo et al. 1995, Bozzo et al. 1992, Goodge and Finn 2010, Ohneiser et al. 2015). We therefore suggest that the central WSB body is distinct from the exposed GHI rocks.

The large-scale igneous batholith here (IB1) has an identical petrophysical signature in terms of density and susceptibility as the neighbouring body labelled IB2 in Figure 3.10d, which is associated with the magnetic anomaly labelled F2 in Figure 3.3 a and b. The density and susceptibility distribution along the profile AB (Figure 3.8 b and d) and the depth slices (Figure 3.7) indicate that these intrusive bodies (IB1 and IB2) may be connected at depth. The total combined volume of the proposed batholith IB1 and IB2 is $\sim$470 000 km^3, which constitutes a significant addition to the volume of the upper crust at the time of emplacement. However, this estimation is likely an upper bound on the volume estimation since the base of any intrusion is poorly resolved by gravity and magnetic methods, and constraints on crustal boundaries (CPD and Moho depth) are uncertain, hence thickness estimations are likely to be exaggerated.

Granites often form topographic highlands in glacial regions due to their relative resistance to erosion compared to surrounding sediments, but this is not clearly seen in WSB. IB1 is flanked by a deep trough parallel to the inferred geological contact indicating geological control of erosion on one flank, and that the intrusion may be at the ice bed interface in this area. In many other areas the topography shows no clear change at the geological boundary of IB1 or IB2, which may indicate the intrusive bodies remain at least partially buried.

The petrophysical signature of IB1 and IB2, in terms of jointly inverted density and susceptibility relationship is not present in the TAM region. This is perhaps surprising, since granites from the Granite Harbour Igneous Complex are mapped and sampled by geological surveys in this area (Cox et al., 2023). This suggests that the petrophysical signature of the proposed batholithic is fundamentally different to the lithologies of the Granite Harbour Intrusive Complex (Figure 10 d, red dots), which was emplaced during the later stages of the Ross Orogeny (Estrada et al., 2016). We cannot know the age of emplacement of the IB1 and IB2 bodies and can only speculate that they may also be associated with magmatism of the Ross Orogeny. However, their position, which is more proximal to the continental interior, suggests that they may record an episode of older arc-related magmatism relative to the Granite Harbour Igneous Complex, as arc systems often migrate outboard towards the adjacent trench through time (Gianni and Luján, 2021). We speculate that the batholith in the central WSB was emplaced during an early phase of the Ross Orogeny and maybe the source of the >550 Ma zircons in the Priestley Formation (Estrada et al., 2016) and also in WSB basement adjacent to the Mertz Shear Zone, sampled as xenoliths in later $\sim$ 500 Ma granites (Lamarque et al., 2018).

The crustal-level intrusive bodies are interpreted as a batholith, and potentially reach depths of 20-25 km, which represents the maximum extent of batholiths reported worldwide, but is also not unprecedented. As the Pacific Margin Anomaly (PMA) batholith in the central Antarctic Peninsula is predicted to reach 20 km depth (Johnson, 1999). Further, Ducea (2001) and Saleeby et al. (2003) determined the thickness of the Sierra Nevada batholith must have been $\sim$30–35 km prior to erosion. However, we acknowledge the inversion model is likely to overestimate the source thickness of this body due to a combination of factors, including loss of resolution with increasing distance between sensor and source for potential field data, uncertainty in CPD and Moho depth estimation. A lack of independent crustal parameters such as receiver functions, or active and passive seismic experiments limit the possibility to validate the geophysical inversion. Therefore, the batholith might be thinner than predicted by our regional scale joint inversion.

A batholithic intrusion, even if 5 to 10 km thinner, still represents a significant local crustal feature, which would influence the geothermal heat flow of the region if it acted to concentrate radiogenic elements. Even though the lack of direct geological samples and heat flow measurements makes it challenging to quantify the extent of this impact, many granitic batholiths are associated with elevated heat production, with global late Proterozoic granites typically

higher in heat producing elements (U, Th, K) than Phanerozoic granites (Artemieva et al., 2017). The batholith we have imaged is, therefore, likely to generate a locally elevated GHF and this impact may be quite marked for this sector of East Antarctica where heat flow values are rarely predicted to exceed $\sim 60\ \mathrm{mW\ m^{-2}}$ (An et al., 2015; Haeger et al., 2022; Lowe et al., 2023; Lösing and Ebbing, 2021; Martos et al., 2017; Purucker, 2013; Shen et al., 2020; Stål et al., 2021). The scale of the heat flow anomaly is unknown but the batholith in our model is of a similar size to the $\sim$ 200km long Cornubian batholith in SW England, where heat flow of up to 138 $\mathrm{mW\ m^{-2}}$ is reported (Beamish and Busby, 2016). This comparison illustrates the magnitude of heat flow which is potentially underestimated in geophysical geothermal heat flow models if the crustal domain is treated with global average values instead of accounting for crustal heterogeneities which can be recovered from geophysical data.

3.7.2 Continental margin

The density and susceptibility relationship for the linear structure at the craton margin is more ambiguous than for the proposed batholith structures, due to the larger standard deviation in the susceptibility values. Similar density and susceptibility relationships are present offshore, and onshore along the coast and in the TAM, but these areas may be lithologically and tectonically distinct from the craton margin structure.

There are several potential tectonic models for the high density bodies recovered along the inboard margin of WSB, which is interpreted to represent the margin of the Mawson Craton (Goodge and Finn, 2010). One hypothesis is that the positive gravity anomaly is a slice of up-thrusted crustal material loading the craton margin (Studinger et al., 2004). However, our inversion modelling does not show the strongly asymmetric pattern of densities expected for a flexural loaded margin, although we cannot rule out some degree of compressional reworking of the former rifted margin during the Ross Orogeny. An alternative model is that the observed gravity and magnetic anomalies are directly associated with processes occurring along the rifted margin. Along strike, in the Glenelg River Complex of SE Australia, it is proposed that slivers of ultramafic rocks associated with a magma-depleted hyperextended Rodinian continental margin are present, which were reworked by later compressive orogenic forces (Gibson et al., 2015). Although associated with similar margin parallel magnetic anomalies, the amplitudes of the magnetic anomalies directly associated with the Australian ultra-mafic rocks are often lower and more fragmented than observed in Antarctica. In addition, the interpreted Australian ultra-mafic rocks are not associated with a distinct positive gravity anomaly as seen in WSB. If WSB margin does reflect the relics of a magma-poor margin, we propose that it must be more intact than that in Australia to account for the very significant source bodies recovered by the inversion. As an alternative, the linear craton margin feature may be the signature of a former magmatic rifted continental margin where thick sequences of seaward-dipping basalt horizons are often combined with mafic underplating (Direen and Crawford, 2003). Both features require densities above 2700 $\mathrm{kg\ m^{-3}}$, in line with the inversion

result. Additionally, both features host the potential of significant remnant magnetisation, as suggested by the recovered negative relative susceptibility. We prefer a magmatic, rather than an amagmatic margin model, given the scale and amplitude of the observed magnetic and gravity anomalies. The presence of magmatic features associated with rifting would not be unexpected given the location on the former cratonic margin, and is not incompatible with magma-poor rifting interpreted on other parts of the margin (Gibson et al., 2015). Ultimately, a more detailed geophysical study is required to definitively reveal the nature of the margin.

3.7.3 Conceptual tectonic model

Based on our preferred interpretation of the inversion outputs and the regional geological context we propose a tentative geotectonic model for the evolution of WSB (Figure 3.12):
The first identified event is linked to continental breakup leading to the development of margin parallel gravity and magnetic anomalies, which we attribute to a magmatic rifted margin adjacent to the Mawson Craton with seaward-dipping basalt horizons and mafic underplating (Figure 3.12 a). The age of breakup is uncertain, but evidence of rifting and passive margin development along strike in the Central TAM suggests that this may have occurred around 670 Ma (Goodge, 2020; Goodge et al., 2002). Rifting would have been followed by the development of a passive margin sequence and progressive subsidence (Figure 3.12 b).
Margin inversion and development of an ocean/continent subduction system and associated continental margin arc, led to the emplacement of the large-scale batholithic intrusions, IB1 and IB2 in the central WSB area (Figure 3.12 c). Potential reworking and back thrusting of mafic components onto the craton margin may have also occurred at this time. The emplacement age of this proposed phase of arc magmatism is uncertain, but we suggest it predated the main phase of Ross Orogeny magmatism exposed as the Granite Harbour Intrusive Complex in the TAM. As such, this earlier phase of magmatism could provide a local source for >550 ma detrital zircons of otherwise unknown provenance (Estrada et al., 2016). An early Ross Orogeny phase of magmatism has also been proposed in the central TAM, with the earlier phase of magmatism generally being focused further inboard (Goodge, 2020; Goodge et al., 2024). Although slightly younger than the detrital evidence, this central TAM interpretation is consistent with our early Ross model for development of IB1 and IB2. Later Ross magmatism led to the emplacement of the Granite Harbour Intrusive Complex $\sim$500 Ma, further outboard from the craton margin, in the region of the present-day TAM (Figure 3.12 d).

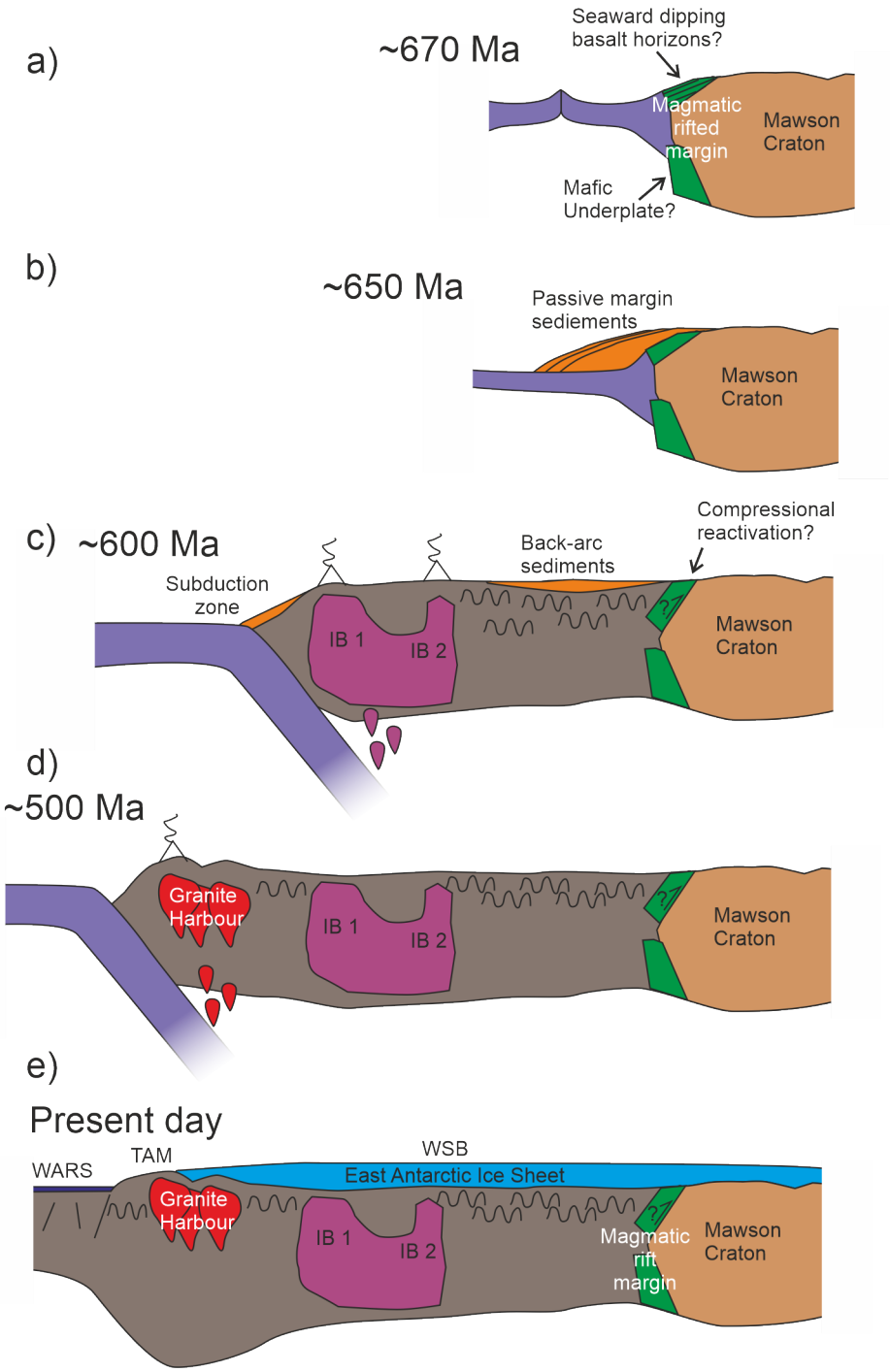

Figure 3.12: Conceptual tectonic evolution sketch: a) Rifting of Rodinia supercontinent and development of magmatic margin. b) Passive margin development and sediment deposition. c) Subduction zone development, emplacement of Central Batholith, reworking of passive margin and potentially deposition of back-arc sediments. d) Subduction zone migrates further out-board and Granite Harbour intrusive Complex is emplaced. e) Present day geological section.

3.7.4 Cryosphere implication

GHF in Antarctica is understood to be an important solid Earth contribution to the cryosphere (Livingstone et al., 2022; Reading et al., 2022; Siegert and Dowdeswell, 1996). GHF is the dominant heat source close to the ice divides (Bell, 2008; Fahnestock et al., 2001; Siegert and Dowdeswell, 1996), whilst away from the ice divides, horizontal ice deformation and basal sliding become dominant. A causal link between subglacial lakes and high GHF has previously been proposed by several authors (Fahnestock et al., 2001; Fisher et al., 2015). A prominent active subglacial lake several tens to hundred metres deep called $Cook_{E2}$ close to the ice divide (Li et al., 2020; McMillan et al., 2013; Smith et al., 2009) is located directly above the modelled batholith IB1 (Figure 3.12d). Subglacial lake $Cook_{E2}$ experienced surface subsidence of 70m between 2006 and 2008 (observed by CryoSat-2), which has been linked to a discharge event. Following the lake discharge, it has been recharging at a rate of 5.6 $\pm$ 2.8 m yr^{-1} (McMillan et al., 2013). It is notable that almost all recent GHF models (An et al., 2015; Lowe et al., 2023; Martos et al., 2017; Shen et al., 2020; Stål et al., 2021), with the exception of Lösing and Ebbing (2021) predict a local minimum GHF in the lake location above IB1 (Figure B.12). This is a consequence of all recent GHF models have in common that they are simplifying the local crust to a set of constant petrophysical values or neglect small-scale heterogeneity in the subglacial geology. It is possible, given the spatial overlap, that the $Cook_{E2}$ lake could be induced by a thermal anomaly associated with the IB1 batholith and high concentration of heat producing elements. This highlights the necessity of GHF models to incorporate subglacial and crustal heterogeneities where data is available, as also suggested in recent papers (Li and Aitken, 2024; Stål et al., 2024). It is important to note that not all subglacial lakes can be correlated to regions of high GHF. Subglacial lakes serve at best as a weak proxy for elevated heat flow since basal melt may have undergone lateral transport to the accumulation region or even refreeze during transport. However, it is notable that in the case of $Cook_{E2}$ a subglacial lake up to several hundred metres deep is located above the batholith IB1, which is likely to elevate the local heat flow. It is important to stress that the proposed batholith in this study is a geological interpretation based on airborne geophysical data and classifying this structure based on inverted petrophysical relationship as a granite-like rock type is somewhat speculative. Coupling this consideration with the poorly constrained heat flow models, the existence of the lake cannot be tied to the intrusive rock body with certainty and emphasises important questions that future studies should consider for studying solid earth and cryosphere interactions.

3.8 Conclusions and Future Work

have presented a density and susceptibility distribution model for Wilkes Subglacial Basin and the Transantarctic Mountains using joint inversion of gravity and magnetic data based on VI coupling. This model provides insight into the heterogeneity of the 3D crustal structure in WSB and TAM region and allows preliminary quantification of the volume of crustal provinces, which should be considered in future lithospheric scale thermal studies. The inversion model images a large body of slightly low density and moderately positive susceptibility values in the central WSB, which we interpret as a large-scale batholith. Based on the inverted petrophysical properties the batholith is interpreted to be granitic in composition, but it is not currently possible to further constrain the specific lithology. The density and susceptibility relationship and cross-section of the inversion model indicates that this structure is connected to the adjacent low density moderate susceptibility body, which potentially has the same origin but nearly perpendicular orientation. If so, the volume of the total granitic intrusive body increases to $\sim$470 000 km^3, which is a considerable addition to the volume of the upper crust at the time of emplacement and has the potential to have a significant impact on the local heat flow due to the likely concentration of radiogenic heat producing elements. However, the thickness of the batholith and the volume depends upon the boundary conditions, especially the CPD, with significant uncertainties and therefore the thickness and volume may represent an overestimate. Despite the absence of direct heat production and heat flow measurements, comparisons with well-studied granite intrusion provinces in the Weddell Sea (Leat et al., 2018), southern Prydz Bay (Carson et al., 2014), SW England (Beamish and Busby, 2016) and worldwide (Artemieva et al., 2017) emphasise the influence that local crustal structures such as granitic intrusive bodies can have on the local heat flow budget.

Examining the density and susceptibility relationships, we have determined that the batholith has a different petrophysical signature to the Granite Harbour Intrusive Complex of the Transantarctic Mountains. Based on our findings, the tectonic evolution of WSB may therefore include two distinct intrusion events, first emplacement of the batholith followed by the emplacement of the Granite Harbour Intrusive Complex. The batholith emplacement age is uncertain and may represent an episode of magmatism associated with the early stages of the Ross Orogeny (c. 600 Ma) or could potentially be associated with rift-margin processes in the interval, 650 – 670 Ma (Goodge et al., 2012) This could potentially provide a more proximal source for the Neoproterozoic clasts described from metaconglomerates of southern Victoria Land (Cooper et al., 2011)

The margin of the Mawson craton is identified by the inversion in the form of a positive linear gravity anomaly grid-east of WSB. We suggest these signatures reflect a passive continental margin with thick seaward-dipping basalt horizons and mafic underplating. However, alternative models of up-thrusted crustal material at the craton edge, or reworking of ultramafic material from a magma-poor rifted margin cannot be ruled out based on the geophysical inversion model. Scenarios combining some of these endmember models are also possible.

This study highlights the crustal heterogeneities on a regional scale in East Antarctica and provides evidence that by using a set of constant global average petrophysical values for the crustal domain in geophysical geothermal heat flow models is a simplification that might underestimate the contribution of geothermal heat flow beneath the ice sheets. Despite the many challenges, next generation geophysical heat flow models are required to consider crustal heterogeneities to increase the understanding of the contribution from the solid earth to the cryosphere and ultimately the stability of the ice sheet. Therefore, further geophysical, and geological research on the Antarctic subglacial geology is necessary to understand the thermal state of the most remote continent on Earth.

Chapter 4

Comparing geophysical inversion and petrophysical measurements for northern Victoria Land, Antarctica

4.1 Context

The previous chapter has illustrated the effectiveness of jointly inverting the gravity and magnetic fields to obtain a density and susceptibility distribution and its usefulness for a) revealing crustal heterogeneities and b) draw conclusions on the potential origin and geological evolution of such heterogeneity. However, little effort has been undertaken in this thesis so far to validate inverted density and susceptibility relationships with petrophysical measurements and thereby to bridge the geophysical models with geological observables. This chapter closes this gap by establishing a new petrophysical rock catalogue containing 320 density and susceptibility measurements on rock samples from the TAM region in northern Victoria Land. The new rock catalogue is used to validate the geophysical inversion model from the previous chapter. Furthermore, a local high-resolution inversion with 250 m cell size, incorporating additional high resolution aeromagnetic data, is presented and compared to the 7.5 km cell size inversion from the previous chapter. Both inversions are compared against the petrophysical measurements. The advantages of both the local and regional inversion scale are discussed as well as their sensitivities towards geological bodies.

4.2 Author contribution

The work presented in this chapter has been published as: M. Lowe, T. A. Jordan, J. Ebbing, N. Koglin, A. Ruppel, M. Moorkamp, A Läufer, C. Green, J. Liebsch, M. Ginga, R. Larter(2024) Comparing geophysical inversion and petrophysical measurements for northern Victoria Land, Antarctica *Geophysical Journal International*, ggae272.

M. Lowe (conceptualised, Data curation, Formal analysis, Investigation, Methodology, Software, Validation, visualisation, Writing –original draft, Writing –review & editing); T. A. Jordan (conceptualised, Formal analysis, Funding acquisition, Investigation, Methodology, Project administration, Supervision, Validation, visualisation, Writing –review & editing); J. Ebbing (conceptualised, Data curation, Formal analysis, Investigation, Methodology, Supervision, Validation, visualisation, Writing –review & editing); N. Koglin (Data curation, Formal analysis, Investigation, Validation, Writing –review & editing); Antonia Ruppel (Data curation, Formal analysis, Investigation, Validation, Writing –review & editing); M. Moorkamp (conceptualised, Formal analysis, Investigation, Methodology, Software, Validation, visualisation, Writing –review & editing); A. Läufer (Formal analysis, Investigation, Validation, visualisation, Writing –review & editing); C. Green (conceptualised, Formal analysis, Investigation, Methodology, Supervision, visualisation, Writing –review & editing); J. Liebsch (Data curation, Formal analysis, Writing –review & editing); M. Ginga (Data curation, Formal analysis, Writing –review & editing) and R. Larter (conceptualised, Formal analysis, Funding acquisition, Investigation, Methodology, Project administration, Supervision, Validation, visualisation, Writing –review & editing).

4.3 Introduction

One of the largest current challenges for Antarctic solid Earth research in Antarctica is reliable imaging of subglacial geology and crustal properties. The overwhelming majority of Antarctica's geology is hidden beneath thick ice sheets limiting direct geological information to ice free regions at the coast, high mountain ranges and isolated nunataks. Geological structures and sub-ice solid Earth properties are therefore inferred most commonly from geophysical approaches: i,e., airborne gravity, magnetic and radar measurements (e.g. Aitken et al. 2014; Ferraccioli et al. 2011; Gibson et al. 2015; Goodge and Finn 2010; Jordan et al. 2013, 2022, 2023; Mieth et al. 2014; Mieth and Jokat 2014; Riedel et al. 2012; Ruppel et al. 2018). A major caveat for all such aerogeophysically-derived interpretations is that the degree of complexity which can be inferred depends on the flight line spacing and altitude of the airborne surveys. High resolution surveys with tight flight line spacing ($\leq$ 500m) are rare in Antarctica and, where conducted, are usually limited to magnetic measurements over local (10s of km) surveys (e.g. Ghirotto et al. 2023; Damaske et al., 2014; Wilson et al. 2007).

Complementary to geophysical crustal forward modelling, magnetic-only and joint inversions of gravity and magnetic data have been successfully applied to different environments and scales to image crustal properties in terms of density and susceptibility distribution beneath the Antarctic Ice Sheet (e.g. Jordan et al. 2023; Lösing et al. 2022; Morales-Ocaña et al. 2023). A remaining challenge is to directly link geological information with geophysical models. Petrophysical rock properties, namely susceptibility and density, allow linking of these observations and cross-validation of hypotheses arising from geological or geophysical interpretation.

Remaining open questions are how well inverted petrophysical parameters correspond to laboratory derived petrophysical parameters measured on Antarctic rock samples, whether it is possible to separate and classify subglacial rock types based on inverted petrophysical properties, and what the possible limitations are. The lack of linkage between Antarctic geophysical models and petrological data arises from a lack of density and susceptibility measurements on the same rock samples in the literature, such that Antarctic models have conventionally been validated against catalogues of global rock properties or rock samples from Australia (e.g. Lösing et al. 2022).

To answer these questions, we present a petrophysical catalogue containing 320 measurements of susceptibility and density values. The measurements are performed on rock samples from northern Victoria Land (nVL), which are archived by the German Federal Institute for Geosciences and Natural Resources (BGR) from over 40 years of expeditions to nVL. Additionally, we present a new high resolution local susceptibility inversion of the Mesa Range area in nVL (Figure 4.1) based on a helicopter magnetic survey with a 500 m line spacing conducted by BGR in the 2009-2010 Antarctic season (Damaske et al., 2014). Gravity measurements on a comparable resolution do not exist for the local study area. Instead, we further consider the results in the context of the inverted susceptibility and crustal density distribution model introduced in Chapter 3. This model is based on a joint inversion of gravity and magnetic airborne data, which accommodates the gravity resolution and therefore adds an additional dimension that fully utilises the advantages of joint inversion of potential fields, albeit with a coarser grid resolution.

4.3.1 Regional Geology

NVL is located at the Pacific end of the Transantarctic Mountains (TAM), one of the largest non-collisional mountain chains worldwide (Figure 4.1). The basement formed by accretionary processes at the East Gondwana active continental margin during the late Ediacaran - early Palaeozoic Ross Orogeny (e.g. Goodge 2020). Geologically the TAM consist of the western and inboard polymetamorphic and magmatic Wilson Terrane, the central volcanic and clastic Bowers Terrane, and the eastern turbiditic Robertson Bay Terrane. The metamorphic basement of the Wilson Terrane comprises low- to high-grade (up to granulite-facies) metamorphic rocks, for example the Wilson metamorphic and polymetamorphic complexes, the Berg Group or the Wilson Schists, as indicated in Figure 4.1. The metamorphic country rocks are intruded by the voluminous Granite Harbour Intrusive (GHI) Complex (here also including the anatectic Oates Coast granitoids listed in Figure 4.2). The majority of the plutonic rocks consist of granitoids with subordinate intermediate to mafic varieties as well as some ultramafics. The Bowers Terrane comprises very low- to low-grade metavolcanics and associated metavolcaniclastics, which formed in an island arc or fore-/back-arc tectonic setting and grade into molasse-type clastic metasedimentary rocks (Bowers Supergroup, Figure 4.1 and 4.2). The

outboard Robertson Bay Terrane consists of mostly distal turbidites of the Robertson Bay Group deposited furthest from the continent interior (Figure 4.1 and 4.2). The Wilson-Bowers Terrane boundary is defined by the strongly deformed Lanterman-Mariner Fault Zone in the Lanterman Range and along the western margin of Mariner Glacier, whereas the Millen Schist Belt represents the boundary between the Bowers and Robertson Bay terranes. Post-Ross geology is characterised by the mid-Palaeozoic felsic Admiralty Igneous Complex comprising the Admiralty granitoids and the Gallipoli volcanics. They are unconformably overlain by late Palaeozoic to early Jurassic clastic Beacon Supergroup and sills and lavas of the Jurassic Ferrar Supergroup, i.e. Ferrar Dolerite and Kirkpatrick Basalt including the volcaniclastic Exposure Hill-type deposits (e.g. Ganovex Team and others 1987; Elliot et al. 2021).The youngest rocks in the region comprise Cenozoic alkaline to peralkaline magmatic rocks of the McMurdo Igneous Complex, related to West Antarctic rifting, and glacial sediments (Giordano et al., 2012; Kyle, 1990; Kyle and Cole, 1974; Rossetti et al., 2000).

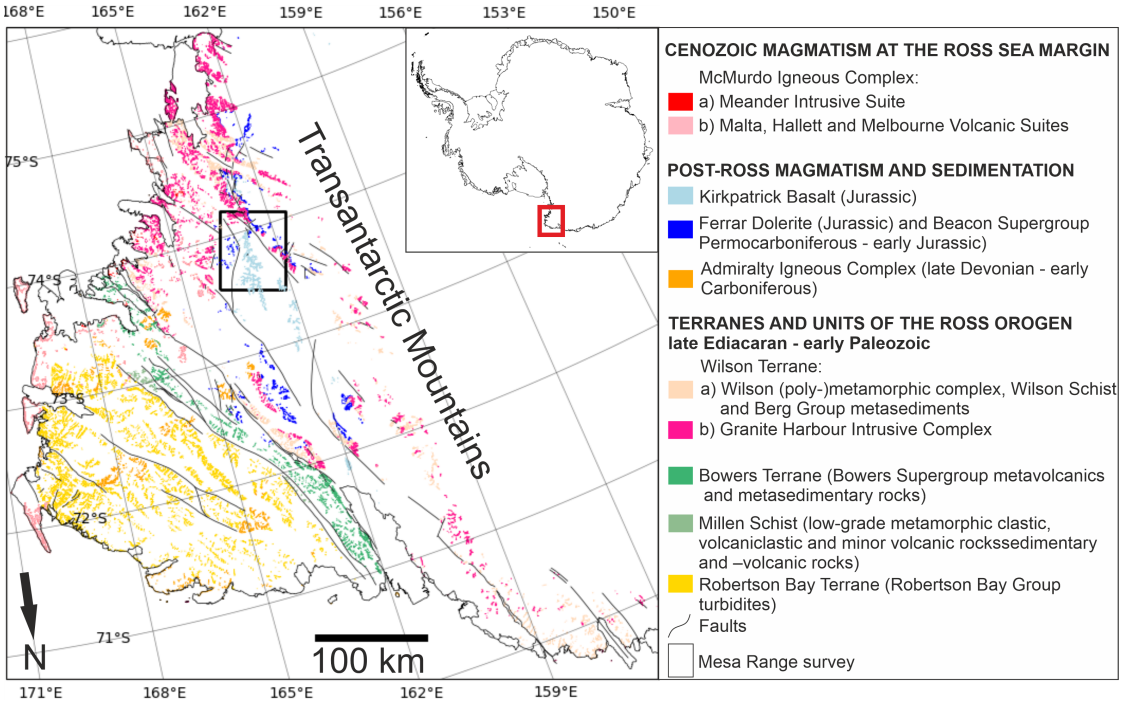

Figure 4.1: Geological map of northern Victoria Land and Oates Land. Geological data taken from Läufer et al. (2011), Pertusati et al. (2016), Roland et al. (2002). Inset shows study location (red box) in Antarctic context. Mesa Range marked as black rectangle in the main panel

4.4 Method: Petrophysical measurement and inversion

We conducted susceptibility and density measurements on 320 rock samples from nVL. 248 rock samples stored in the National Polar Sample Archive (NAPA) in Berlin-Spandau, Germany and 72 samples stored at the BGR in Hannover, Germany. The samples were pre-classified on the basis of geological formation and rock types by the sample collectors during the GANOVEX field activities.

Susceptibilities of the rock samples were measured using a handheld KAPPAMETER KM-7 (Pocket Magnetic Susceptibility Meter). For each rock sample eight repeat measurements were performed on different flat and, if possible, fresh surfaces. Density was measured by weighing the dry sample and dividing this by the volume. The volume of the sample was determined by suspending it from a string in a water container, allowing it to achieve equilibrium. The string offsets the difference of gravitational and buoyancy forces acting on the sample. Consequently, the buoyancy force acting on the sample can be quantified using a scale positioned at the base of the container. Density is then calculated using the density of water, the weight of the dry sample and the weight of displaced water (Equation 4.1).

$$Density\rho = \frac{Weight_{rock} Density_{water}}{Weight_{displacedWater}} \tag{4.1}$$

Inversion of magnetic data alone is carried out using the open-source scientific code JIF3D. The joint inversion model, based on the Variation of Information (VI) approach, also carried out in JIF3D, is discussed in depth in (Chapter 3). The theoretical background is given in detail in Moorkamp (2021, 2022) and Moorkamp et al. (2011). Therefore, we restrict the description here to the description of the objective function and its regularisation parameters. The objective function for the joint inversion Φ_{joint}, as described in Chapter 3, has five terms equation (4.2). Two misfit terms represent the difference between the gravity and magnetic field responses of the model and the observed fields. Two regularisation parameters relate to the two petrophysical quantities (density and susceptibility). JIF3D uses a finite difference approximation to the spatial gradient for regularisation, meaning differences in values between adjacent cells are penalised. Therefore, a higher regularisation value leads to a smoother model with less variation. A full description of the regularisation parameter can be found in Moorkamp (2021). The last term is the VI parameter, which enforces a coupling between both physical quantities (Lösing et al. 2022; Moorkamp 2021, 2022, Moorkamp et al. 2011).

$$\Phi_{joint} = \Phi_{d,grav} + \Phi_{d,mag} + \lambda_1 \Phi_{reg,\rho} + \lambda_2 \Phi_{reg,sus} + \lambda_3 \Phi_{VI} \tag{4.2}$$

where $\Phi_{d,grav}$ and $\Phi_{d,mag}$ are the root-mean-Square (RMS) misfit between observed and inverted gravity and magnetic data respectively, $\Phi_{reg,\rho}$ and $\Phi_{reg,sus}$ are regularisation parameters, and Φ_{VI} is the coupling term based on the VI approach (Lösing et al. 2022; Moorkamp 2021, 2022).

Table 4.1: Inversion parameters. Inclination and declination are calculated for the for the midpoint and the acquisition date of the survey using DGRF calculator implemented in Oasis Montaj (Geosoft)

Regularisation Density and Susceptibility	10
Error Magnetics [nT]	10
Min. / Max Susceptibility [SI]	$\pm$0.1
Magnetic Field strength [nT]	64411
Inclination [Rad]	-1.4566
Declination [Rad]	2.2756
Maximum depth of susceptibility variation	CPD
Observation height	Flight elevation

For the local magnetic inversion over the Mesa Range, we use the joint inversion algorithm described above but with the coupling weights and all terms associated with the gravity data set to zero. The subsurface was discretised into a mesh with a horizontal cell size of 250 m and a vertical cell size of 100 m at the surface, which increased by a constant factor of 1.1 for each layer with depth to account for decreasing resolution of potential field data with depth and to limit the computational load (Figure B.3). This results in a vertical thickness of the uppermost cell layer of 100 m, while the layer beneath has a thickness of 110 m and so on. The deepest layer of cells has a thickness of 3400 m at a model depth of 32701 m. This approach prevents the inversion from producing high frequency structures at depth, which cannot be resolved by the measured input data. For the upper boundary surface, bedrock information from BedMachine Antarctica (Morlighem et al., 2020) was used (Figure 3.1), while for the lower boundary surface, Curie Point Depth (CPD) estimates from Lowe et al. (2023) [Chapter 2 in this thesis] are used (Figure 3.4.4). The Curie Point describes the Curie temperature of around 580℃, the temperature at which minerals that dominate the magnetic characteristics of crustal rocks lose their magnetic properties (Blakely, 1996; Haggerty, 1978; Núñez Demarco et al., 2020; Telford et al., 1990). Moreover, the inversion meshes are extended laterally with a 20% buffer around the target area to reduce edge effects. The regularisation for the susceptibility is set to a value of 10. The appendix provides alternative runs with varying regularisation values Figure C.2 and C.3. Further parameters for the local inversion are given in Table 4.1. The regional joint inversion model (Chapter 3) is based on airborne gravity and magnetic data (Golynsky et al., 2018; Reitmayr et al., 2003; Scheinert et al., 2016; Zanutta et al., 2018) (Figure 3.3 and 3.2). The joint inversion model is also confined to the upper boundary condition defined by bedrock topography data from BedMachine Antarctica (Morlighem et al., 2020), while the boundary condition for the base of the model differs. For the susceptibility model the CPD (Figure 3.4 b) (Lowe et al., 2023) (Chapter 2) are used again as boundary condition while Moho depths (Figure 3.4 a) (Pappa et al., 2019a) are used for the density model.

4.5 Results

4.5.1 Laboratory-measured susceptibility and density values

In general, metamorphic and sedimentary rocks exhibit low susceptibility, while higher susceptibilities were measured for plutonic and volcanic rocks (Figure 4.2c, 4.2e, 4.3a and 4.3c). Susceptibility measurements of granitoids from the GHI Complex (Figure 4.3a) show a low mean and median value but include some outliers with high susceptibility values. Outliers are defined as >1.5 times the interquartile ranges. It is worthwhile to point out that the location of the rock samples shows a bias towards the GANOVEX focus (Figure 4.2a and 4.2b). This bias occurs because only rock samples from the GANOVEX field surveys are stored in those two rock archives. Regardless, geological formations from across the whole of nVL are represented.

Gabbro from the Oates Coast Granites and GHI Complex followed by Kirkpatrick Basalt (KPB) and Ferrar Dolerites (FD) show the largest measured susceptibility ranges (ignoring outliers) (Figure 4.3a and 4.3 c). Density measurements show larger variation across the formations (Figure 4.3b). Distinct clusters of density values are evident for the FD, KPB, and GHI Complex, which are the dominant geological formations in the Mesa Range area (Figure 4.3b). This difference is even stronger when considering the dominant rock types for each formation: dolerites for the FD (mean 2.88 $\mathrm{g\,cm^{-3}}$, basalt for the KPB (mean 2.75 $\mathrm{g\,cm^{-3}}$ (excluding the lighter tuff samples) and granites for GHI Complex (mean 2.6 $\mathrm{g\,cm^{-3}}$). The differences in susceptibility are more nuanced between KPB and FD with a mean value of 0.006 SI for FD and 0.0069 SI for KPB, while the median shows a larger difference with values of 0.003 SI for FD and 0.005 SI for KPB (Figure 4.3a and 4.3c). Granites exhibit significantly lower mean and median susceptibility values (mean: 0.002 SI median: 8.12e-05 SI) compared to basalts and dolerites (Figure 3c).

The FD, KPB, and GHI Complex show significant outliers in both susceptibility and density. These large ranges of overlapping density and susceptibility values including outliers highlights a need for caution when attributing characteristic density and susceptibility values to specific rock types (Figure 4.3). Nevertheless, the combination of susceptibility and density measurements on the same rock samples decreases the uncertainty in clustering rocks based on those petrophysical properties. Our new density measurements are broadly in line with previous density measurements on rock samples from nVL (e.g. Barrett and Froggatt 1978), while the susceptibility measurements for the GHI Complex are broadly in line with previously reported susceptibility values (Bozzo et al. 1992, 1995)

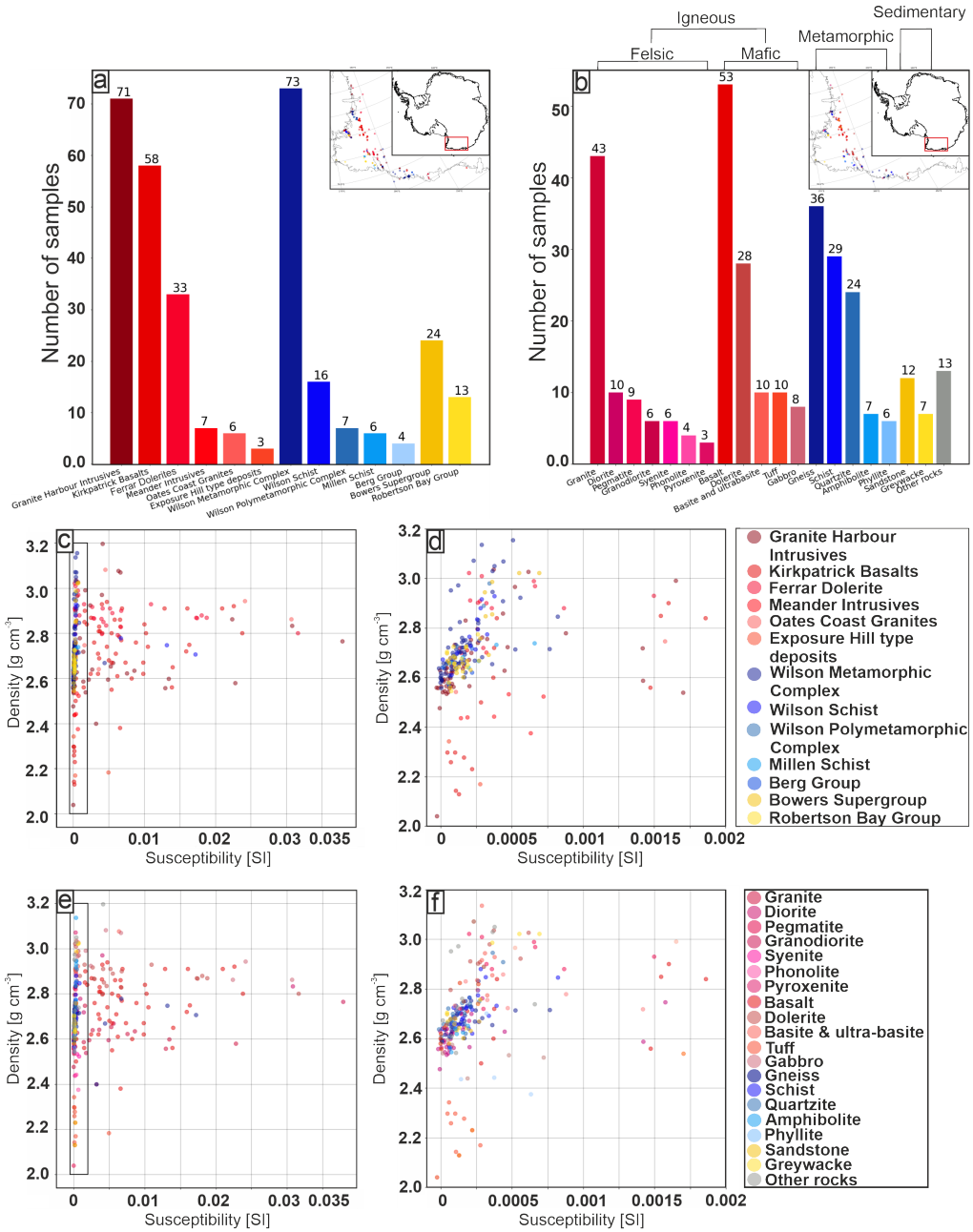

Figure 4.2: Petrophysical measurement on Antarctic rock samples. a) Histogram of measured rock samples and location plot classified by geological formation. b) Histogram of measured rock samples and location plot classified by rock type. c) Susceptibility and density cross plot of measured rock samples classified by geological formation. d) Zoomed in cross plot to low susceptibility range indicated in c. e) Susceptibility and density cross plot of measured rock samples classified by rock type. f) Zoomed in cross plot to low susceptibility range indicated in e.

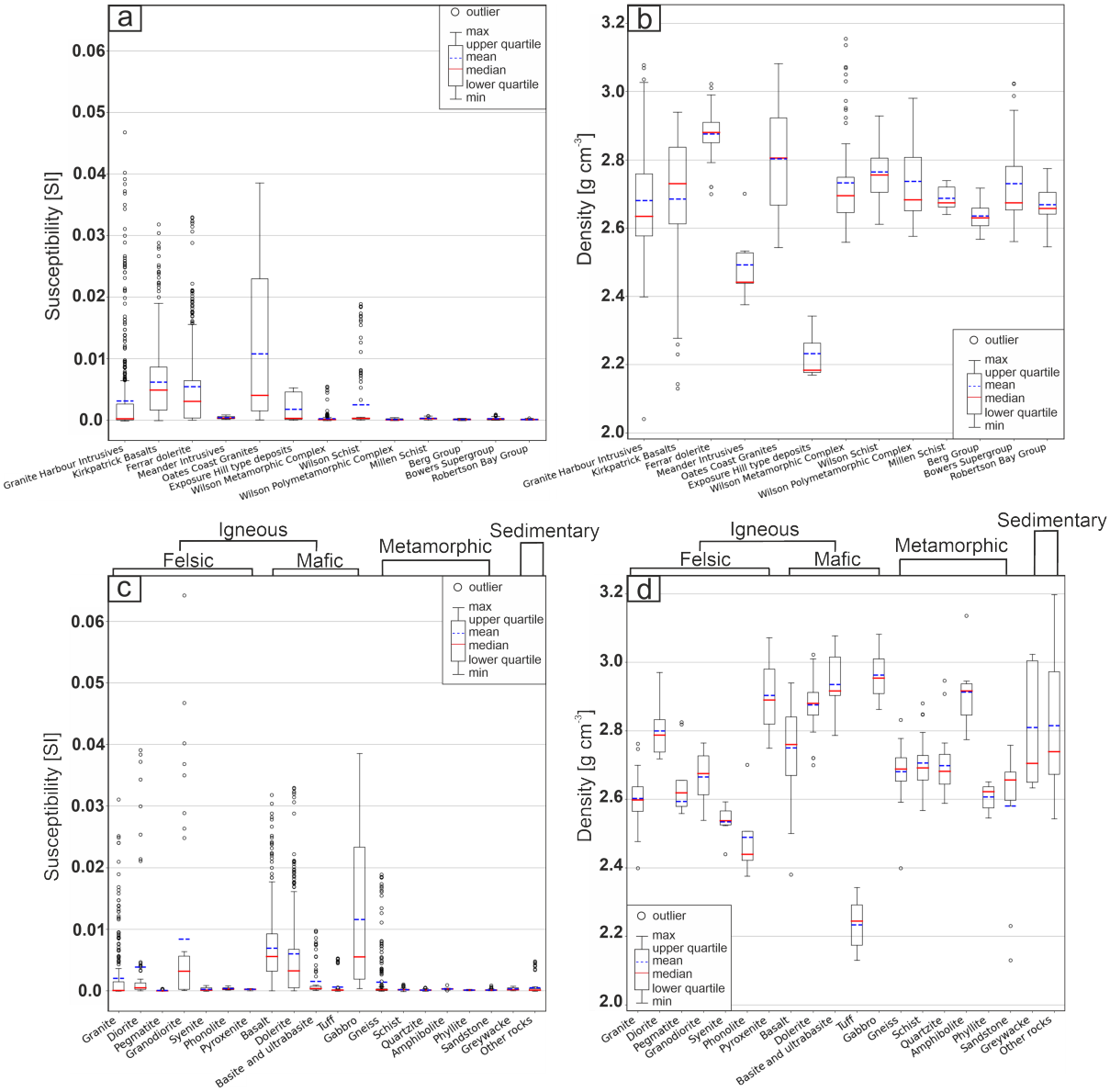

Figure 4.3: Statistics of measured rock samples. a) Boxplot of susceptibility measurements sorted by geological formation. b) Boxplot of density measurements sorted by geological formation. c) Boxplot of susceptibility measurements sorted by rock type. d) Boxplot of density meassurments sorted by rock type. Outliers defined as >1.5 times the inner quartile ranges.

4.5.2 Comparison of the petrophysical measurements to literature values

Density and susceptibility measurements are important for validating geophysical models. Both petrophysical quantities are reported in the literature for Antarctic rock samples, but are typically reported separately (e.g. Bozzo et al. 1992, 1995; Maslanyj et al. 1991; Sanchez et al. 2021). Due to the lack of Antarctic rock outcrops petrophysical measurements on rock samples from Australia (Barlow, 2004) and the Indian shield (Subrahmanyam et al., 1981) have previously been used to validate geophysical models (e.g. Lösing et al. 2022). Selected

rock types of the petrophysical catalogue from this study are therefore compared to existing literature values to test the validity of this assumption. An obstacle confounding the comparison of our measurements to previously reported values from the literature is that often the petrophysical measurements have only been reported as a mean value, and only sometimes with a standard deviation, for the dataset. Therefore, we plot the reported mean values and, where possible, the standard deviation on top of the boxplots of our petrophysical catalogue (Figure 4.4 and 4.5). An exception is the Antarctic-wide PetroChron dataset (Sanchez et al., 2021), which is a full dataset. Therefore, it is possible to plot boxplots for the PetroChron dataset as well, which allows the best possible comparison between both datasets (Figure 4.5).

Susceptibility values measured in this study and literature values are overall in good agree-

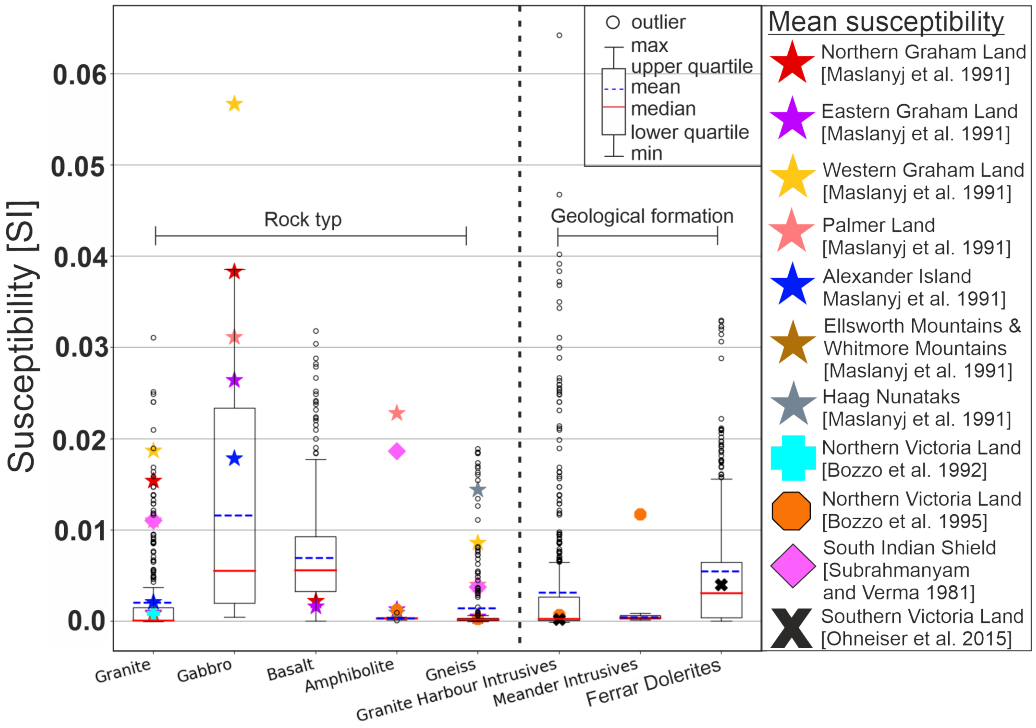

Figure 4.4: Susceptibility measurements compared to literature values. Susceptibility measurements from this study presented as boxplots. Mean susceptibility mean measurements on Antarctic rocks displayed as stars (Maslanyj et al., 1991), cross (Bozzo et al., 1992), hexagon (Bozzo et al., 1995), and x (Ohneiser et al., 2015). Mean susceptibility measurements on rocks from the Indian shield as Rhombus (Subrahmanyam et al., 1981).

ment. Some reported mean values for granites, GHI, amphibolite and FD from the literature fit the mean values of this study. However, there are exceptions to this observation. Most prominent, perhaps, are the mean susceptibilities reported for gabbro from the Antarctic Peninsula. The mean values are significantly higher and even outside the maximum of the box plot for the nVL rock samples from this study. Some of the mean susceptibilities reported for granite rock samples from the Antarctic Peninsula and the Indian Shield also show significant high

susceptibilities outside the boxplot for nVL and are only matched by outliers from nVL. Similar behaviour is observed for amphibolite and gneiss. Overall, susceptibility measurements on rock samples from nVL (Bozzo et al., 1995,9; Ohneiser et al., 2015) seem to agree best with our measurements conducted on rock samples from nVL (Figure 4.4). This shows that there is a geographical variation that subsequently illustrates the need for caution if rock catalogues including rock samples from geographically distant locations even from other continents, are used for validation.

Mean densities from this study are in strong agreement with density estimations on Antarctic

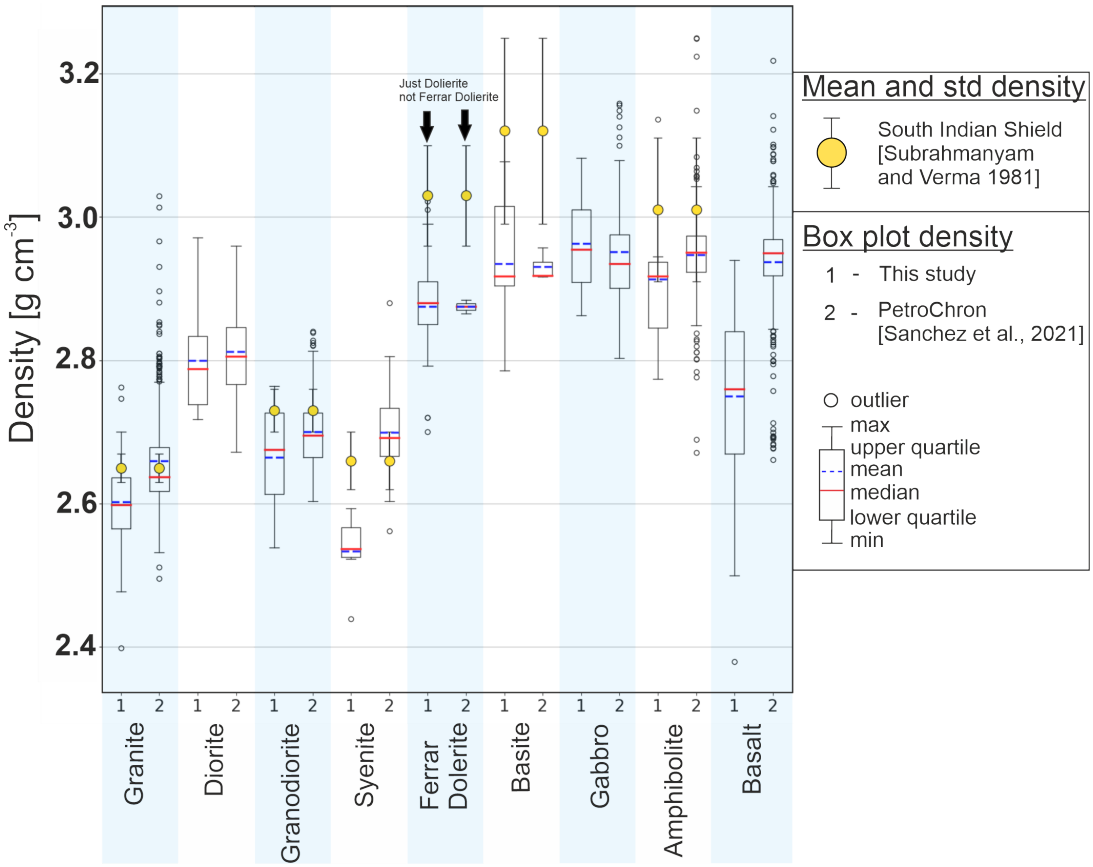

Figure 4.5: Density measurements from this study compared to literature values. Density estimation from this study and PetroChron (Sanchez et al., 2021) displayed as box plots. Mean density estimation on rock samples from Indian Shield (Subrahmanyam et al., 1981) are displayed as yellow dots. The displayed errors bars illustrate the reported standard deviation.

rock samples from the PetroChron dataset (Sanchez et al., 2021) (Figure 4.5). A discrepancy between the two datasets is evident for basaltic rocks. Overall, the density range for basalt from PetroChron is tighter. However, the minima and maxima for both datasets defined by their boxplots overlap, especially when considering the outliers for the PetroChron dataset. The outliers might indicate geographically clustered samples, which seems to align with the measurements from nVL rock samples from this study. A second mismatch between the two

datasets is observed for syenite rocks. Here PetroChron seems to be in an agreement with measurements on rock samples from the Indian Shield, while measurements from this study report lower densities. It is worthwhile to point out that in this study only 6 measurements have been conducted on syenite (Figure 4.2b), which might not be statistically significant. Furthermore, density measurements on rock samples from the Indian Shield show overall a good agreement with measurements from this study and from PetroChron. Nevertheless, the densities of rocks from the Indian Shield are systematically higher compared to the Antarctic rock samples. This systematic shift might be related to geographical circumstances.

Comparisons between density and susceptibility measurements on rock samples from nVL to rock samples from both the Antarctic Peninsula and Indian Shield indicate that geographical variability can be important (Figure 4.4 and 4.5). This highlights the need for caution if such measurements are used to validate geophysical models. Geophysical joint inversion models report density and susceptibility relationships as cross plots (Chapter 3 and Lösing et al. 2022). However, if the density and susceptibility measurements have not been conducted on the same rock sample, then cross plots of density and susceptibility measurements might be inadequate to validate geophysical inversion models. Mean and standard deviations of density and susceptibility measurements on Australian rocks are simultaneously reported by Barlow (2004). This dataset allows a cross plot comparison between measurements on nVL rock samples, from this study and Australian rock samples. All rock types show a systematic shift to higher mean susceptibility values for Australian rocks (Figure 4.6).Similarly, the mean density values are systematically higher for Australian rocks. This shift reinforces the idea of significant geographical variability in petrophysical characteristics in such datasets, especially, when considering the good agreement between density estimation for Antarctic rocks from the PetroChron (Sanchez et al., 2021) dataset and this study.

Therefore, rock samples geographically closely located should always be given preference before employing global rock catalogues or rock samples from neighbouring continents to validate geophysical inversion models. Moreover, this section illustrates that for meaningful comparison it is crucial to have access to the full petrophysical dataset (Figure 4.5) instead of relying on reported mean values and standard deviations. The internal variability of measurements for a certain rock type is not captured by mean values, while the boxplot comparison (Figure 4.5) between density estimation from this study and PetroChron (Sanchez et al., 2021) provide a higher confidence in the comparison and illustrate the internal variability for a given rock type.

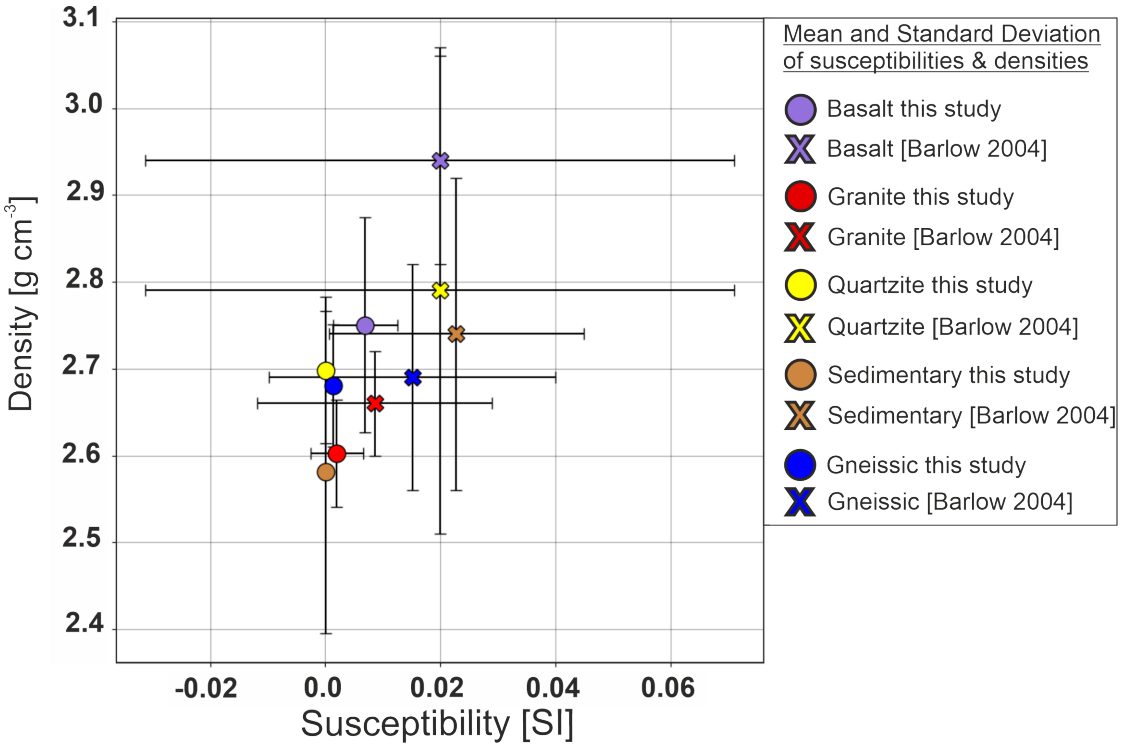

Figure 4.6: Density and susceptibility cross plot compared to published values from Australia (Barlow, 2004). Measurements from this study are plotted as circles, measurements from Barlow (2004) as crosses. Standard deviation for both datasets is displayed as error bars.

4.6 Regional joint inversion of magnetic and gravity data

Regional scale VI inversion of magnetic and residual gravity airborne data (Figure 3.2 and 3.3),which was corrected for gravity contribution from the mantle and below using the (Pappa et al., 2019b) model with a cell size of 7.5 km in nVL and WSB was carried out and previously described in (Chapter 3). We used geological classification polygons provided by GeoMap (Cox et al., 2023) to sample the susceptibility and density values at a depth slice of 2 km below sea level (Figure 4.7a and b) from the inversion model at the locations of specific outcropping rock types. The depth of 2 km was chosen, so that the density and susceptibility values sampled lie within the crust rather than in the domain of the ice sheet, where the inversion cells were set to 0 $\mathrm{kg\ m^{-3}}$ and 0 SI and excluded from the inversion, but also shallow enough that those cells likely correspond to geological classification from GeoMap (Cox et al., 2023) at the surface.

Here we sample the GHI Complex (Figure 4.8a) at a depth slice of 2 km below sea level and plot the petrological relationship between susceptibility and density as red dots (Figure 4.8b) together with laboratory susceptibility (mean susceptibility of eight repeat measurements) and density measurements on GHI Complex rock samples conducted at NAPA and BGR as blue dots (Figure 4.8b).The inverted susceptibilities are relative values. Therefore, we have

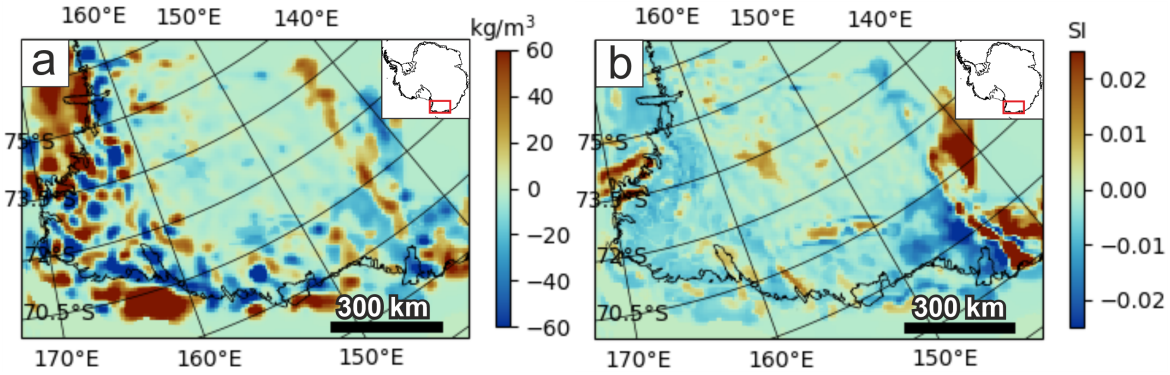

Figure 4.7: Inverted density and susceptiblity distribution of regional scale joint inversion model (Chapter 3). a) Inverted relative density at 2 km depth. b) Inverted relative susceptibility at 2 km depth. Inverted crustal density and susceptibility distribution from regional scale VI inversion with a horizontal cell resolution of 7.5 km (Chapter 3).

shifted the inverted values by 0.008 SI. The value, by which the inverted susceptibilities were shifted was chosen so that the inverted low susceptibility cluster plots around the 0 value and therefore resembles the range of measured susceptibilities more closely. Most of the measured and inverted susceptibilities are low values with occasional outliers. The amplitude ranges of outliers from the measured and inverted values approximately match one another. The points with error bars marked in Figure 4.8b represent the means of measured and inverted values, while the error bars represent the standard deviations of the respective datasets. The inverted relative density values were shifted to absolute values by adding the background density value of 2670 $\mathrm{kg\,m^{-3}}$. Measured densities of the GHI Complex samples show a larger range than recovered by the VI inversion, but the measured and inverted mean values are located close to one other. However, the density range of the inversion is much narrower compared to the measured density range and does not reproduce the measured high densities above 2900 $\mathrm{kg\,m^{-3}}$ (Figure 4.8b).

Subdividing the rock samples from the GHI Complex into rock types reveals some lithologies which are poorly fitted and some that are better fitted by the inversion (Figure 4.8d). Measured rock types that fall in the inversion density range are granites, granodiorites, gneiss, and diorites, while denser rock types that are not well represented by the inversion include hornblendite, ultrabasites and gabbro. The poor representation of the denser rock types by the inversion can be explained by considering the 7.5 km cell size used in this regional inversion. A cell in the inversion mesh represents an average density and susceptibility value of all rock types present in the volume of the cell. In order to reproduce a cell with a density of 3200 $\mathrm{kg\,m^{-3}}$ representing densities of hornblendite, the hornblendite needs to fill the full volume of a 7.5 by 7.5 km lateral cell. However, high density lithologies are not dominant in the continental crust. Furthermore, hornblendite rocks have densities that are typically associated with density values commonly found in the mantle. The lesson here is that cells of the size

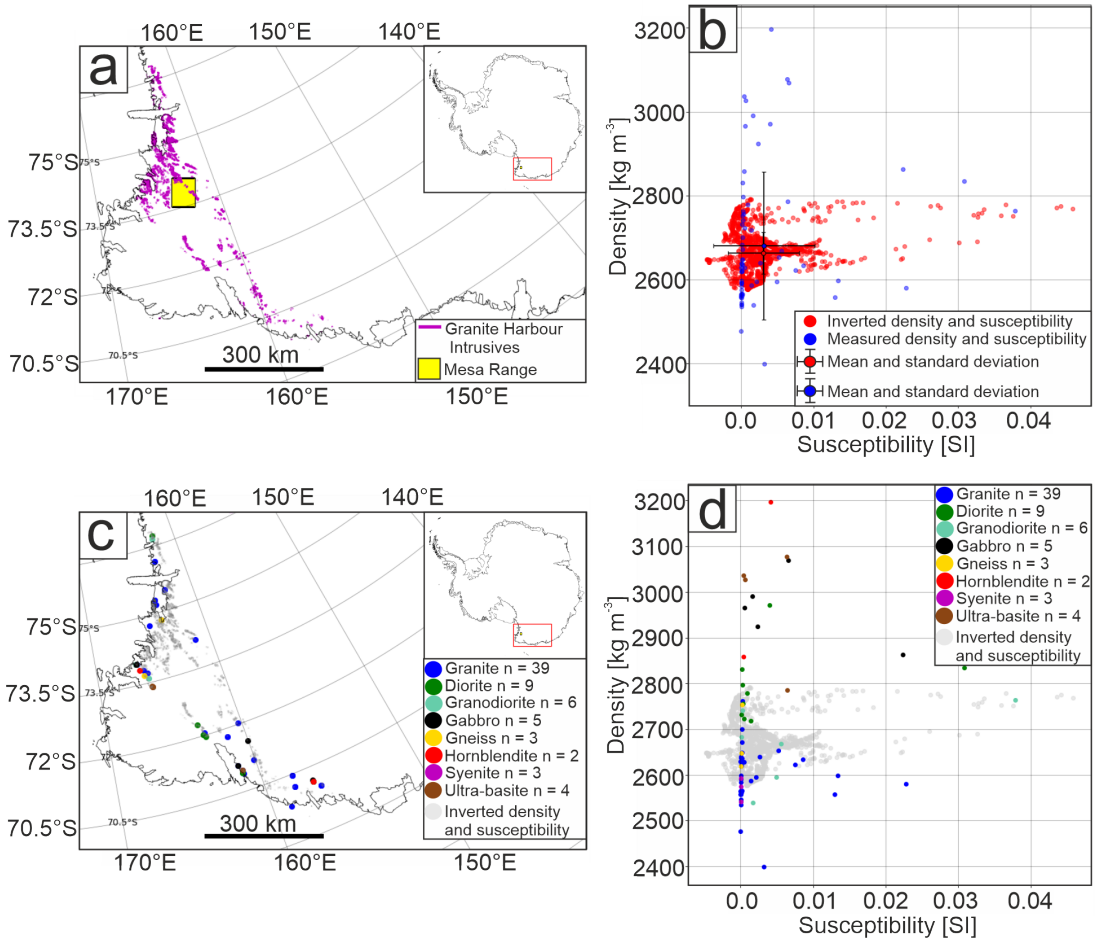

Figure 4.8: Validating regional scale joint inversion model. a) GHI Complex polygons from GeoMap (Cox et al., 2023). b) Inverted (red) and measured (blue) susceptibility and density crossplot for GHI Complex (here the susceptibility values describe the mean value of eight repeat measurements). Datapoints with error bars represent the mean datapoints of inverted and measured datasets, while the error bars represent the standard deviation of each dataset. c) Locations of rock samples within the GHI Complex coloured by rock type superimposed on GHI Complex polygon from GeoMap (Cox et al., 2023). d) Measured susceptibility and density crossplot for the GHI Complex, coloured by rock type and superimposed on GHI Complex inverted susceptibility and density crossplot (grey).

used in a regional scale inversion cannot reproduce local small scale geological variation. A regional inversion represents rather large-scale crustal variations and can only reproduce the density/susceptibility of the dominant crustal rocks (average value of all rocks within a given cell). Furthermore, fine scale geological features are often limited to finite depth intervals. For example, individual outcropping Sills usually do not exceed thicknesses of ∼200 m and 900 m for the Ferrar and the KPB, respectively (Elliot and Fleming 2018, 2008). A regional inversion

with vertical cell size of 1 km (reasonable representation of airborne data with 10 km flight line spacing) is unable to resolve the vertical dimensions of such features and will overestimate the thickness. To resolve features like the FD with a 200 m vertical extent, higher resolution airborne data is required.

4.7 High resolution local single magnetic inversion

Magnetic-only inversion is applied to a local helicopter high-resolution magnetic survey of the Mesa Range in nVL, East Antarctica (Figure 4.9a). The survey was conducted by the BGR in January 2010 (Damaske et al., 2014) with a flight line spacing of 500 m and was flown in draped mode with a ground clearance of about 500 m. The aim of the survey was to determine if prominent circular magnetic anomalies visible in earlier magnetic surveys with wider line spacing are the signals of a feeder dyke complex. Joint inversion is not carried out because only long wavelength airborne gravity data exists in the target area based on three flight lines (Jordan et al., 2013), which does not contain comparable short wavelength content to the magnetic dataset. Jointly inverting potential field data with a strong discrepancy in wavelength content does not produce meaningful results.

The topography of the target area includes flat-topped mesas as well as deep valleys covered by the overriding Rennick and Aeronaut glaciers (Damaske et al., 2014). GeoMap (Cox et al., 2023) shows three dominant geological formations present in the target area, which are KPB, confined to the Mesa topography, FD and the GHI Complex (Figure 4.9b, c). The magnetic forward calculated response (Figure 4.9b) of the 3D inverted susceptibility model and the observed magnetic field (Figure 4.9a) match closely (Figure 4.9c). The mean misfit between the observed and inverted magnetic field is 0.9 nT with a standard deviation of 12 nT. The maximum misfit is 551 nT and the minimum misfit is -130 nT. Areas of significant misfits are limited to a region where the magnetic field rapidly increases locally from $\pm$ 200 nT to over 1000 nT, in the area of the Mesa Range topography. The misfit arises from a combination of inversion resolution (250 m cell size) and because the inversion favours smooth models compared to steep gradients in the observed magnetic field. The 3D inversion shows that the dominant magnetic bodies are limited to the volcanic topographic features consisting of KPB. Our inversion indicates these basalts are restricted to high topography and are unlikely to reach depths below sea level, giving a maximum thickness of 2 km, but probably less (Figure 4.9d and 4.9e). The strong susceptibility signals caused by KPB overlying the Beacon sediments and crustal basement appear to spread into the underlying crustal basement and the Beacon sediment deposits (Figure 4.9d and 4.9e). Inverting jointly with gravity data of matching resolution could help to focus the source bodies and reduce the vertical smearing of the anomalies. This spreading effect lets the susceptibility source bodies appear to reach thicknesses of 2 km while the source body with the highest susceptibilities is limited to thicknesses of less than 1 km. Geological evidence exists that the thickness of KPB is limited to a

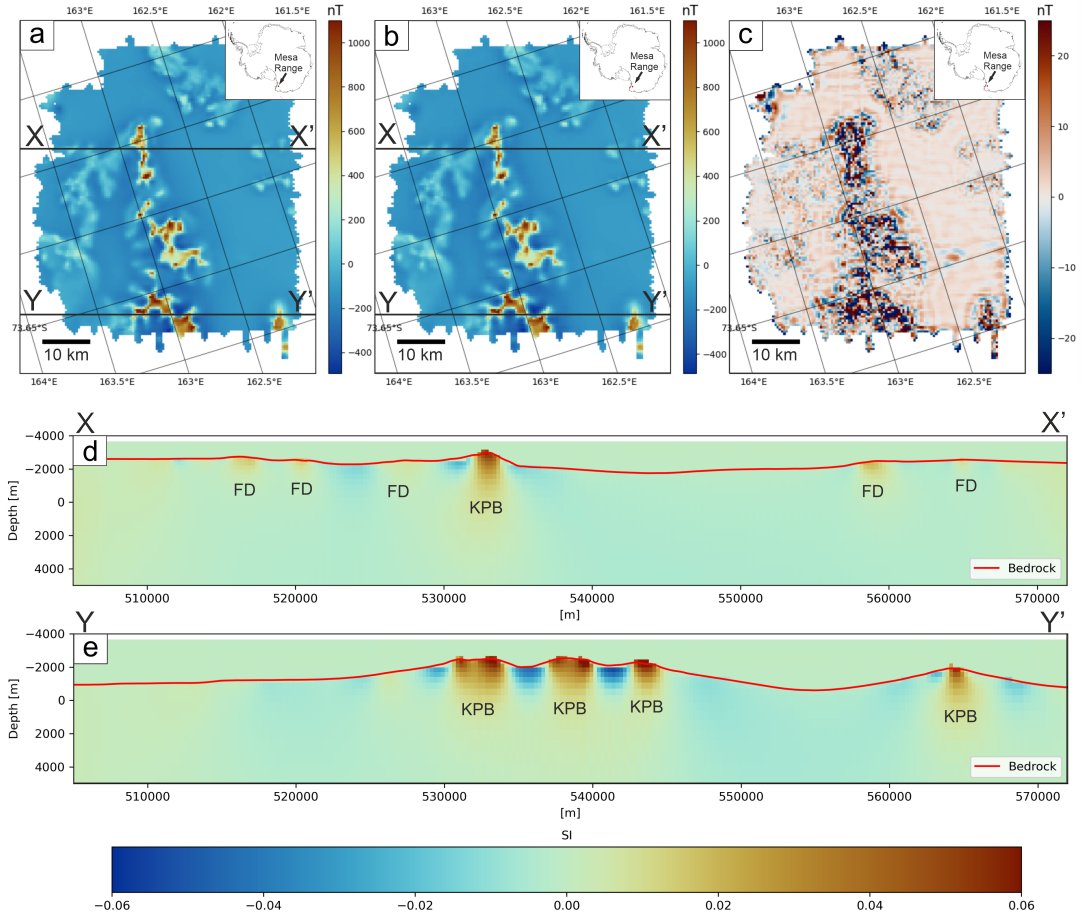

Figure 4.9: Magnetic data and inversion results over the Mesa Range. a) Observed magnetic field. b) Inverted magnetic field. c) Misfit between a and b. d and e) Cross-Section through inverted susceptibility distribution along profile lines indicated in a and b.

maximum of 900 m in nVL (Elliot and Fleming 2018, 2008).

We do not see evidence for a feeder dyke complex in our high-resolution 3D susceptibility inversion, due to the absence of deeper magnetic bodies in the Mesa Range area. This result is in line with previous 2D modelling from Damaske et al. (2014) who did not find feeder dykes for the basalt sheets either but identified circular-shaped anomalies visible in an earlier aerogeophysical survey as artefacts due to wider line spacings. Furthermore, both results are in line with the absence of geological evidence for feeder dykes, dyke swarms, or vents in nVL. The pathways of magma emplacement are currently unknown (e.g. Elliot et al. 2021, Elliot and Fleming 2018).

A secondary prominent magnetic signature in the area is visible with a lower magnitude (Figure 4.9d). This signature also correlates closely with the topography but does not coincide with the highest topographic peaks. Those magnetic bodies match with the areas in which there are outcrops classified as FD (Figure 4.10b and c) based on GeoMap (Cox et al., 2023).

These dolerite sills intruded into the surrounding sedimentary Beacon Supergroup (Ferraccioli et al., 2009a). FD and KPB can be separated based on the inverted susceptibility intensity and based on the correlation with topographic highs displayed in cross section view (Figure 4.9d). We can also use the inverted susceptibility distribution to separate the three dominant geological units namely KPB, FD and GHI Complex. Figure 4.10a shows the inverted susceptibility distribution sampled for each geological unit in the Mesa Range at a depth of 1.8 km above sea level using the GeoMap (Cox et al., 2023). In addition to the histogram of the inverted susceptibility for each rock type, kernel density estimates (KDE) are plotted to illustrate the bulk susceptibility distribution for each rock type. The area beneath each KDE curve is 1 and therefore illustrates that KBP has a larger distribution compared to FD and GHI which are confined to finite ranges (Figure 4.10 a). The rock classification polygons are shown in Figure 4.10b. The 1.8 km depth slice was chosen so that near surface susceptibility values are extracted, which relate to surface geological classifications based on GeoMap (Cox et al., 2023) and the main units are well represented in the model (within the crustal domain). The large range of inverted KPB susceptibilities partly overlaps with the inverted susceptibility range of the FD (Figure 4.10a). However, the inverted susceptibilities from the KPB unit extend to higher values (0.019 – 0.08 SI), while the inverted susceptibilities of the FD are concentrated at medium values. The medium susceptibility range is populated by all three geological units, while the low susceptibility range is dominated by FD and GHI Complex. The inverted susceptibilities are in line with laboratory measurements on rock samples from nVL (Figure 4.2 and 4.3).

Based on the susceptibility distribution we filter the inversion model for two susceptibility ranges which we attribute to KPB and FD (Figure 4.10 a). Susceptibility values above 0.019 SI match very well with the KPB locations from GeoMap (Cox et al., 2023) (Figure 4.10 c) and the laboratory measured susceptibility (Figure 4.10 d). The intermediate ranges correspond to the dominant FD susceptibility distribution from 0.0047 to 0.018 and match well with the locations of FD from GeoMap (Cox et al., 2023) (Figure 4.10c). Even though the FD and GHI Complex overlap strongly in the low susceptibility range, the chosen susceptibility range for FD shows a good fit with classified rock outcrops from GeoMap (Cox et al., 2023) and a sharp boundary between FD and GHI Complex is observed in the inversion results (dotted yellow lines in Figure 4.10 c). From the geophysical inversion model, based on the FD susceptibility range, we can identify locations with high likelihood of FD occurrence where geological mapping is missing, marked as “F” in Figure 4.10b and 4.10c. Figure 4.10d shows density and susceptibility measurements on rock the three main rock units from Mesa Range. The cross plot of the measured values indicates that those rock types can be better differentiated using both density and susceptibility instead of only the susceptibility. Therefore, highlighting that geophysical studies, which aim to reveal subglacial geology, will benefit from high resolution airborne gravity surveys. Linking susceptibility values from Antarctic rock samples with forward or inverse models is rare in the literature, due to the limited number of measurements on

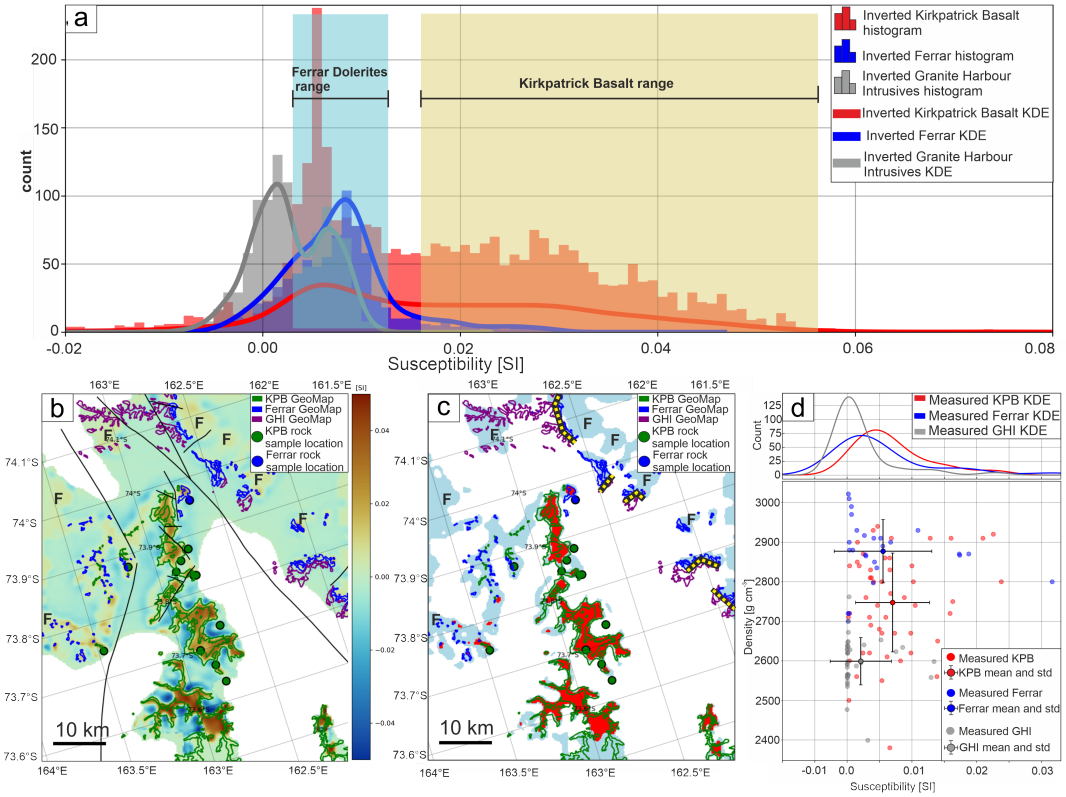

Figure 4.10: Validating local magnetic inversion in the Mesa Range. a) Inverted susceptibility distribution of geological units sampled against GeoMap (Cox et al., 2023) polygons at a depth of 1.8 km above the sea level. Area beneath each kernel density estimation (KDE) curve adds up to 1. b) GeoMap (Cox et al., 2023) classification superimposed on susceptibility depth slice from high-resolution magnetic data inversion at 1.8 km above sea level. Additionally, locations of rock samples are marked. Areas where the depth slice is above the bedrock appear white. Black lines indicate faults after (Cox et al., 2023) c) Location plot of susceptibility values wihin predefined susceptibility ranges for each lithology shown in a. Yellow dotted lines are interpreted lithological boundaries between Ferrar and GHI Complex. “F” indicates region of high probability of FD rocks buried beneath the ice. d) Density susceptibility crossplot of measured rock types present in the Mesa Range. .

Antarctic rock samples, but such efforts have been made before (e.g. Maslanyj et al. 1991, Bozzo et al. 1992, 1995). Histogram distributions of measured and inverted susceptibilities for the Mesa Range highlight that the susceptibility ranges are well represented (Figure 4.11). However, although end-member values are similar, the peak accumulations of measured and inverted susceptibilities for FD are offset (Figure 4.11). The broad range of susceptibilities for the KPB is also recovered by measurements, but it is apparent that higher susceptibilities are required by the inversion model for the KPD to fit the observed magnetic field than were recovered from the rock sample measurements (Figure 4.11). In both cases, it is worth remembering that the sample size from the inversion is significantly larger than the rock sample size presented in this study.

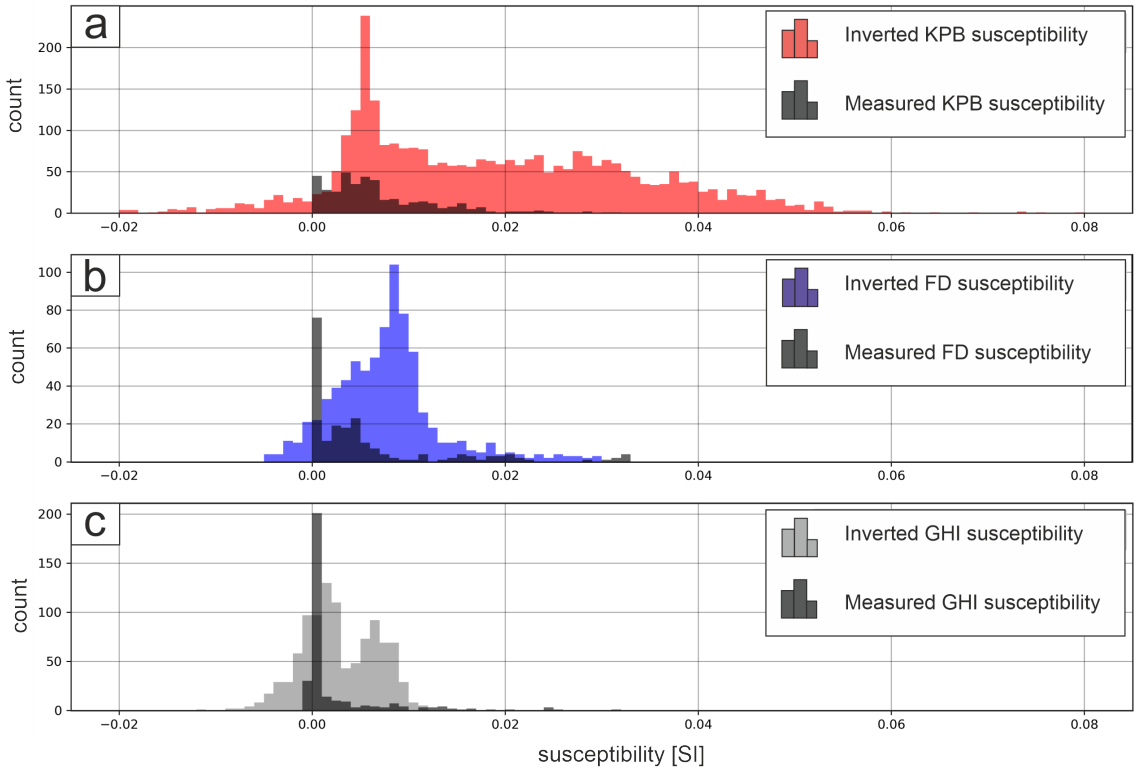

Figure 4.11: Comparison of measured and inverted susceptibility for a) KPB b) FD and c) GHI Complex.

Density measurements on the same rock samples as the susceptibility measurements indicated that FD (average 2877 $\mathrm{kg\ m^{-3}}$), KPB (average 2747 $\mathrm{kg\ m^{-3}}$) and GHI Complex (average 2603 $\mathrm{kg\ m^{-3}}$) can be distinguished by density. Discrimination of rock units like KPB, FD and GHI Complex could be significantly improved by using density inversions and measurements (Figure 4.10 d). However, as discussed before, gravity measurements with similar resolution to that of the Mesa Range magnetic survey are currently missing in Antarctica. Regardless, the laboratory density measurements indicate the high potential of using joint density and susceptibility inversion of ultra-high-resolution gravity and magnetic data to reveal subglacial geology in the future.

It is apparent from the laboratory petrological measurements and the inversion models that the geological units have high internal variability. Therefore, there is a strong incentive for crustal Antarctic models to use the sparse existing rock samples / rock outcrop data to validate geophysical models with local geological information rather than relying on rock property catalogues consisting of global or Australian rock samples (Section 4.5.2), and to solve or incorporate the internal variability into geophysical crustal models.

4.8 Conclusion and future work

We have demonstrated that our new petrological measurements on 320 rock samples can help to interpret geophysical models on both regional and local scales in nVL. VI inversion can reproduce the susceptibility distribution on a regional scale, but the inverted density distribution has the caveat that only the average density value is reproduced for each cell, meaning that only the dominant lithology (average physical properties) can be recovered. Additionally, comparison between this petrophysical rock catalogue and literature values shows that significant geographical variability can be observed. This finding highlights that rock samples geographically close to the study area should always be prioritised before using petrophysical catalogues including global rock samples. If more general petrophysical catalogues are used to validate geophysical models, caution is required to not overinterpret results since local variability might not be reflected.

Additionally, we demonstrate that high resolution 3D susceptibility inversion on a local scale with a mesh cell size of 250 m is capable of identifying KPB and constraining the depth extent of those magnetic bodies to a thickness of less than 2 km. KPB and FD can be reliably discriminated by the susceptibility inversion. The predicted location based on susceptibility ranges matches well with geological classification from GeoMap (Cox et al., 2023) and allows us to predict locations with a high probability of FD in ice-covered areas and where geological mapping is missing.

Furthermore, no evidence is visible in the high resolution 3D magnetic inversion for the presence of feeder dykes in the Mesa Range in nVL, due to the absence of deeper magnetic bodies as previously concluded by magnetic anomaly map interpretation combined with 2D profile modelling by (Damaske et al., 2014).

Separating the FD and the GHI Complex using inverted susceptibility is more challenging due to their overlapping susceptibility range in the low value domain. Density measurements show that all three dominating geological units present in the Mesa Range (KPB, FD and GHI Complex) show distinct density clusters. FD and GHI Complex could be separated by inverted densities and the uncertainty of the discrimination between KPB, and FD would be further reduced by utilising inverted densities. However, this would require high resolution gravity surveys (with less than 1 km flight line spacing and high-resolution along line) that can resolve suitable short wavelength anomalies. Such surveys are currently missing in Antarctica. This study highlights the high potential of joint inversion of high-resolution gravity and magnetic data in combination with local petrological catalogues to reveal fine scale subglacial geological structures. It also shows the potential of this approach to relate geological and geophysical models on a local scale in regions where a high density or susceptibility contrast is expected to occur due to strong lithological changes. Furthermore, this study illustrates how high-resolution airborne gravity surveys would enable more reliable discrimination of different rock types and provides motivation to consider ways to incorporate internal variability of density and susceptibility of geological units in geophysical crustal forward or inverse models.

Chapter 5

Synthesis, conclusions, and directions for future work

Solid Earth properties are crucial for understanding the evolution of Antarctica on geological time scales. The solid Earth interacts with the overlying ice sheets. Making Solid Earth important for understanding of cryospheric processes too. However, the solid Earth in Antarctica is poorly constrained in regions where ice sheets are present. Especially, the heterogeneity of the crust and lithosphere with depth remains unresolved. The overarching aim of this thesis, which links together all three research chapters, was to image the solid Earth beneath the thick ice sheet and capture the variability of crustal properties using geophysical applications and datasets with a strong focus on airborne gravity and magnetic data. Further unifying objectives across the three research chapters were data coverage, dealing with data gaps, choosing appropriate model resolution for the wavelength content of airborne data and flight line spacing, and quantifying uncertainties and limitations of the geophysical forward and inverse modelling approaches.

More precise research questions addressed in chapter 2 are estimating variability of CPD in nVL and WSB, investigating the robustness of the estimated CPD and quantifying their uncertainties. Further aims were to examine the appropriate magnetic wavelengths for this approach, and most importantly, perhaps, to predict the GHF based on CPD and consider its implications for the thermal regime and isostatic equilibrium beneath the TAM.

Chapter 3 aims to resolve the question of crustal heterogeneities in nVL and WSB by applying joint inversion of airborne gravity and magnetic data. In doing so it also demonstrates the advantage of using joint inversion compared to separate single inversion of gravity and magnetic data. Moreover, the study demonstrates how inverted density and susceptibility distribution can help characterise, for example, intrusive bodies by examining the relationship between both inverted quantities, and how geophysical inverse modelling can guide geological and tectonic evolution models. Lastly, the study illustrates the influence crustal heterogeneities might have on the cryosphere by comparing intrusion location with the location of subglacial lakes.

Chapter 4 addresses perhaps one of the most important questions in geophysical and solid Earth research, which is validating geophysical models on different scales by linking them to

geological observables using petrophysical measurements.
The thesis structure is governed by addressing the research questions above. It is crucial to establish at the beginning the CPD in chapter 2 based on only magnetic airborne measurements. This chapter also assesses the uncertainty of the CPD estimation and the implication of CPD for GHF, assuming a simplified homogeneous crust. Chapter 3 builds upon the previous chapter by using the established CPD as a boundary condition for the inverse modelling of the crustal heterogeneities, and also by utilizing gravity airborne data in addition to the airborne magnetic data. The increased sophistication of the modelling approach should increase confidence in the result by not relying on a single geophysical observable. Chapter 4 completes the research chapters by validating the joint inversion model from the previous chapter. This is achieved by providing new petrophysical measurements on Antarctic rock samples and linking them to geophysical inverse models on different scales. Therefore, each chapter builds on the previous ones to form a coherent thesis.

5.1 Advances made in this thesis

The most important advancement, perhaps, in chapter 2 is to demonstrate that the TAM are thermally supported, instead of being in isostatic equilibrium, using an independent geophysical method to the previous methods proposing this hypothesis (e.g. Hansen et al. 2016). Further important findings in this chapter are assessing additional sources of uncertainties beside the commonly used slope misfit between the linear regression of the straight segments of the magnetic spectra, such as window sizes, variation of wavelength range of the magnetic spectra, and the impossible to quantify source of uncertainty due to variations in geochemical composition. All those additional sources lead to larger uncertainty than usually reported (e.g. Dziadek et al. 2021, Martos et al. 2017. The generally larger uncertainty casts doubt on how robust forward calculated GHF based on CPD really is, especially because any crustal variability is also neglected. Regardless, CPD remains a suitable data product for identifying regions of elevated or decreased thermal structure, can supplement multi geophysical data assessment and is a suitable boundary condition for susceptibility modelling. However, exact heat flow predictions purely based on CPD should be used with extreme caution. CPD should rather be treated as a proxy for heat flow which can provide a broad regional overview of the thermal structure.
Moreover, chapter 2 demonstrates the importance of choosing adequate wavelengths for the chosen window size. The chosen window functions as a high pass filter meaning that no wavelengths longer than the given window size can be present in the magnetic spectra. This limits the usage of satellite measurements and is a potential source of misuse of the method. For example using a window size of 200km and merging satellite data for areas were airborne data is missing with the MF7 magnetic satellite model, which contains wavelengths above

300km, results in a physically meaningless data compilation since no wavelengths larger than 200km can be present as done by authors on a West Antarctic study (Dziadek et al., 2021). With advancements of the SWARM satellite mission operated by the European Space Agency the newest magnetic satellite model LCS-1 contains wavelengths of 200km and longer (Olsen et al., 2017). Therefore, satellite data are not by default unusable, but caution is required when relying on satellite and the chosen window size needs to be large enough to recover reasonable results. Where possible airborne data should be given preference. The way CPD results are often reported in Antarctic studies is also flawed, since the locations of the windows, the magnetic spectra, and the linear regression parameter, which are required to reproduce the study, are not reported, as pointed out by Núñez Demarco et al. (2020). This chapter provided for the first time in Antarctic research all window locations, magnetic spectra, the slope and intercept point which allows the linear regression on the associated magnetic spectra to be plotted, as well as the complete python code, making it the first CPD publication which is fully reproducible and transparent. This hopefully serves as blueprint to the Antarctic community on how to report CPD studies in the future.

Advances presented in chapter 3 towards the inverse modelling approach are the introduction of boundary conditions to build a model with realistic and physically meaningful boundaries. The presented inversion approach builds upon previous work from Lösing et al. (2022), which provided a proof of concept of Variation of Information joint inversion of gravity and magnetic data in East Antarctica. However, the previous study used a constant model box, which in theory allows density and susceptibility values to be placed in the air, ice domain or in the case of susceptibilities in the lower crust, below the CPD, where rocks can be expected to have lost their magnetic properties due to exceeding the 580°C Curie Temperature. Therefore, chapter 3 advances the ideas developed by Lösing et al. (2022) and refines the model setup by introducing the bedrock topography as a top boundary and introducing two separate bottom boundaries, the CPD and Moho depth for the susceptibility and density inversion respectively. Joint inversion of gravity and magnetic data itself is not well established in the Antarctic literature even though some publications exist (e.g. Lösing et al. 2022, Morales-Ocaña et al. 2022). Hopefully, advances in the model setup presented in this chapter and the corresponding publication will enhance the confidence of the community in the methodology and facilitate future usage of joint inversion applications in Antarctica where adequate data coverage exists. Scientific advances include the identification of an intrusive structure in the interior of WSB, based on the inverted density and susceptibility relationship. This structure is interpreted as a granite-like batholith, which might have been emplaced before the Ross Orogeny. This is consistent with a geological hypothesis articulated independently by Goodge (2020) and Goodge et al. (2024). The chapter also suggested that the cryosphere, in particular the location of subglacial lakes might be taken into consideration for validating the location of granite-like intrusions, which commonly have a high concentration of heat producing elements, leading to locally elevated heat flow. However, this particular link between subglacial lakes and

a geophysically inferred intrusion is rather weak due to all the associated uncertainties and underlying assumptions. More work is needed to establish subglacial lakes as a proxy for the underlying subglacial geology.

Chapter 4 has advanced the validation of geophysical models using petrophysical measurements. Linking geology and geophysics on different scales through petrophysical characteristics. To do so 320 new, paired density and susceptibility measurements on rock samples from Antarctica were made. This constitutes a significant advances for validating geophysical models. Previously there was a prominent gap in the Antarctic literature regarding density and susceptibly values measured on the same rock samples. Susceptibility and density catalogues exist for Antarctic rock samples e.g., for susceptibility (Bozzo et al., 1992; Lanza and Tonarini, 1998; Ohneiser et al., 2015), and for density (Sanchez et al., 2021). However, paired measurements have not been performed on the same rock samples.

Therefore, robust density-susceptibility cross plots could not be generated until now. Although there may be lots of density and susceptibility measurements, unless they are conducted on the same rock sample it is not really viable to make a cross plot, or to do any statistics on it with confidance, or to assess if there are patterns within a rock type. Previously, authors (e.g. Lösing et al. 2022) have used petrophysical catalogues containing rocks from Australia (Barlow, 2004) and the Indian Shield (Subrahmanyam et al., 1981). I recoomend that the new rock catalogue will be picked up by the community and used to validate future geophysical models. It would also form a good basis for future work where paired density and susceptibility measurements are taken to improve the ability to constrain future geophysical models Furthermore, advantages and disadvantages of modelling crustal properties on different scales are highlighted. Geophysical modelling based on high resolution magnetic surveys with flight line spacing of 500 m or below can facilitate constraining subglacial geology on a scale which is compatible with geological surveying, while regional scale modelling based on airborne measurements in the order of 10 km flight line spacing will facilitate covering spatially large areas, which robustly images large crustal structure while fine, geological survey scale features are impossible to detect due to the lack of short wavelength content and model resolution. The petrophysical data provide a strong motivation to fly high resolution gravity surveys with a comparable flight line spacing to high resolution magnetic surveys, which would help to resolve the source bodies in inversion applications and would allow rock types hidden beneath the ice to be discriminated with a higher confidence. Such high-resolution gravity surveys have not been possible hitherto but with recent advances in downsizing gravity sensor and UAV technology high resolution gravity surveys should become a reality in the near future (Jordan and Robinson, 2024).

5.2 Directions for future work

Future work directions, which are easily achievable based on the presented thesis, include applying CPD estimation based purely on airborne data to areas in Antarctica with sufficient airborne magnetic coverage. They also include applying joint inversion of gravity and magnetic data to various other regions in Antarctica on different scales suitable for different questions regarding the crustal architecture in Antarctica. For example in West Antarctica including Thwaites Glacier and Pine Island Glacier or in East Antarctica including Dronning Maud Land, South Pole region, Recovery region and Gamburtsev Subglacial Mountains. Furthermore, the petrophysical measurement of Antarctic rocks could be carried out more systematically, including rocks outside the TAM, to provide more petrophysical data from a variety of rock types and thus a more statistically relevant picture of internal variability of different rock types. Broader directions of future research include the advancement of the inversion algorithms. One possibility is that during the joint inversion of gravity and magnetic data the inversion is only allowed to draw from predefined density and susceptibility relationship ranges of rock types that are suspected to be present. Therefore, solving simultaneously for rock province as well as explaining the obsevered potential fields iteratively during the joint inversion. Additionally, the internal variability of geological units could be incorporated into the inversion application. An obvious future step is to incorporate crustal heterogeneities obtained through a joint inversion into lithospheric scale models. Lithospheric scale models utilise mainly long wavelength gravity data measurements from gravity satellite missions in order to be sensitive to deeper lithospheric or even sub lithospheric structures used to solve for density and temperature distribution (Haeger et al. 2019, Pappa et al. 2019b). The model by Pappa et al. (2019b) treats the crustal domain with a constant set of parameters in terms of densities, thermal conductivity and heat production. A straightforward advancement would be to incorporate a heterogenous density distribution in the crust resulting from a crustal joint inversion. However, this might be only an incremental advance, since the thermal conductivity and heat production values would still have to be based on global average values. Measuring thermal conductivity and radiogenic heat production in addition to the susceptibility and density measurements could close the current gap in available petrophysical information and improve the next generation of lithospheric scale models. Regardless of the lack of petrophysical measurements, a combined crustal and lithospheric (sub crustal) model could still be useful to estimate the influence of a large-scale batholith intrusion by applying typical thermal conductivity and heat production values found in intrusive rocks, thereby providing an end member estimate to the contribution to the cryosphere. Merging crustal and mantle scale models based on both satellite and airborne potential field measurements and petrophysical information, additionally incorporating seismological information, for example seismic travel times from tomography models, could provide a cross disciplinary approach to solve for the thermal state of the lithosphere and provide robust GHF estimation in Antarctica. Moreover, studies utilizing synthetic GHF variation already illustrate the necessity of robust GHF estimates (McCormack et al.,

2022). Therefore, future projects that aim to resolve GHF in Antarctica should undertake the effort of incorporating GHF estimation into ice sheet models to prove the importance of correct GHF estimation and to illustrate the influence the solid Earth potentially has on the cryosphere. I want to end this thesis by a generalised statement that the solid Earth in Antarctica is far from being well resolved and that there is enough work for generations of geophysicists and geologists to come. Even though more airborne data are always desirable, which could close the remaining data gaps in Antarctica or provide high resolution through tighter flight line spacing, the amount of existing airborne data compiled in data compilations such as AntGG (Scheinert et al., 2016) and ADMAP-2 (Golynsky et al., 2018) is already breathtaking. Application of advancements in modelling approaches utilizing these legacy data has the potential to illuminate solid Earth structures and therefore deepen our understanding of the Antarctic geology and its evolution. This thesis is a testimony to this statement since the thesis is entirely built upon legacy data which was mostly collected before I had even entered a university.

Appendix A

Supplementary information for Chapter 2

This appendix chapter provides information on the upward continuation of the magnetic data in section (A.1), the effect of step sizes between the windows (Section (A.2), a sensitivity test of a dry ice sheet base scenario and ice-free scenario (Section (A.3), and an illustration of the effect of varying wavenumber range on the CDP estimation (Section (A.4).

A.1 Upward continuation

The selected magnetic data from ADMAP-2 (Golynsky et al., 2018) (Figure A.1) was upward continued using the Compudrape extension of Geosoft. In order to perform the upward continuation of the magnetic data an elevation grid is required containing the flight height of the magnetic measurements (Figure A.1b). This elevation grid was produced by gridding the flight heights reported in the ADMAP-2 database. The magnetic data was then upward continued to a constant elevation of 4000 m, which corresponds to the highest flight altitude of the magnetic surveys.

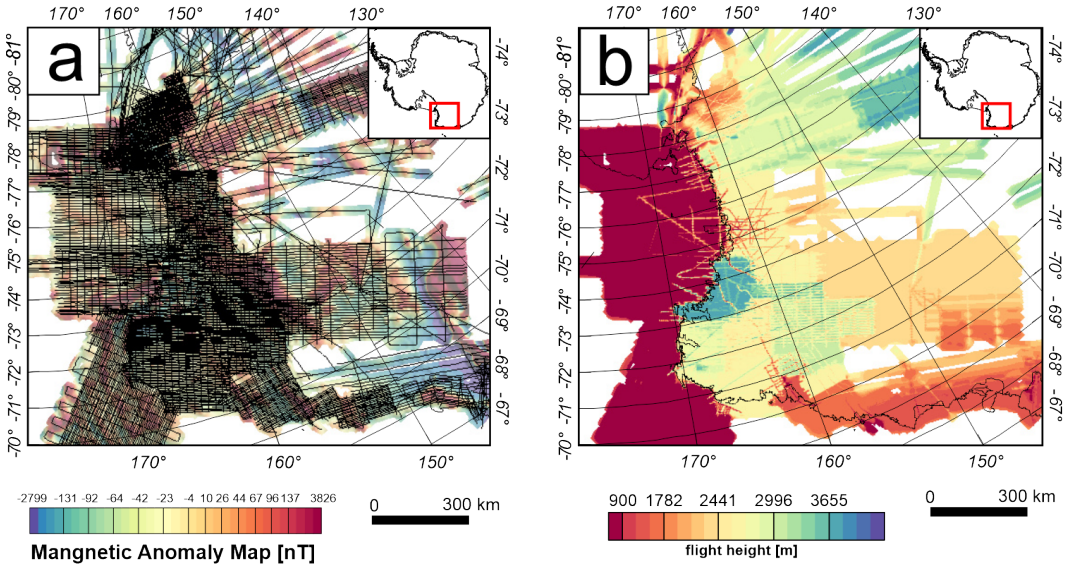

Figure A.1: a) flight lines of selected ADMAP-2 data superimposed on ADMAP-2 magnetic data. b) flight height grid for upward continuation.

A.2 Shifting windows

The spacing between the windows in which the radially averaged power spectrum is calculated has a considerable influence on the high frequency variation within the CPD map and consequently the GHF map. A larger window spacing will result in a smoother map of CDP and GHF estimates. This effect is illustrated in Figure A.2. Here, window spacing of 50 km (Figure A.2a) is compared to a window spacing of 20 km (Figure A.2b). Both estimates are based on a window size of 300 km. The GHF map inferred from a 50 km window spacing is considerably smoother. Nevertheless, the main GHF features are present in both maps

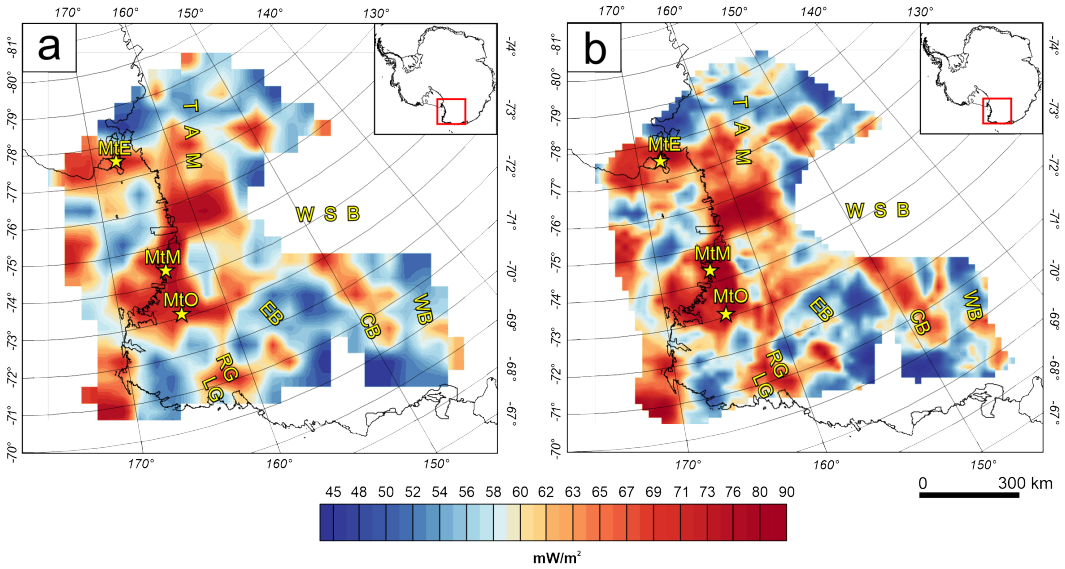

Figure A.2: a) GHF estimates based on a window spacing of 50 km b) GHF estimates based on a window spacing of 20 km. LG, Lillie Graben; RG, Rennick Graben; EB, Eastern Basin, CB, Central Basin; WB, Western Basin; WBS, Wilkes Subglacial Basin; TAM, Transantarctic Mountains; MtE: Mount Erebus; MtM: Mount Melbourne; MtO: Mount Overlord

A.3 Dry base ice sheet and ice-free scenario

Surface temperatures are assumed to be 0℃ in equation 2.8. This assumption assumes a wet base of the ice sheet close to the pressure melting point of -2℃ $\pm$ a few degrees. However, temperatures are significantly lower if the base of the ice sheet is dry, or no ice cover is present. In such scenarios the ice surface temperature is closer to the annual mean temperature. We performed a sensitivity test for a dry base scenario assuming a surface temperature of -30 degrees. The difference between a wet and dry base scenario is between 3 and 6 $\frac{mW}{m^2}$, which is below the uncertainty of GHF inferred from Curie depth points (CPD) (Figure A.3).

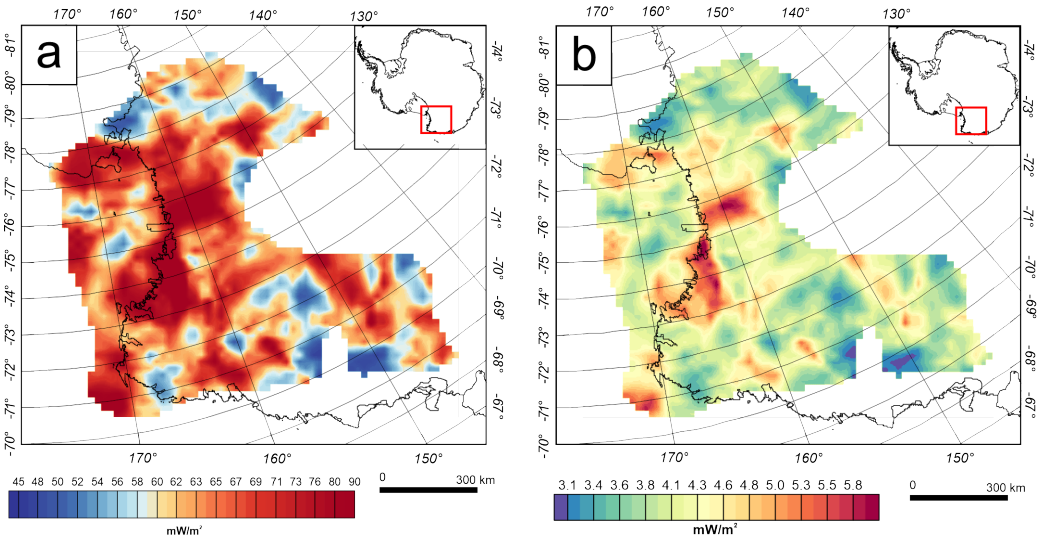

Figure A.3: a) GHF estimates with a surface temperature of -30 °C for an ice sheet with a dry base or ice-free scenario. b) Difference between GHF estimates using ice surface temperature of -30 °C representing dry base of the ice sheet and ice-free scenario and bedrock surface temperature of 0 °C representing an ice sheet with a wet base.

A.4 Wavenumber variation

Selecting the correct wavenumber range to estimate Z_0 and Z_t is crucial for the estimation of the bottom of magnetic source which is interpreted as the CPD. Varying the low wavenumber range (long wavelength content) can change the result for Z_0 by several km (Figures A.4 – A.13). Including or excluding one data point in the low wavenumber part of the power spectrum results in a variation of Z_0 estimation of a few km (Figure A.4 b-d, A.6b-d, A.8 b-d, A.10 b-d, A.12 b-d). Equation 2.6 (main manuscript) states that Z_0 is multiplied by two. Therefore, the uncertainty which originates from a poorly selected wavenumber range for Z_0 is magnified. The low wavenumber content between the different windows does not vary significantly in our study and hence a suitable wavenumber range for Z_0 can be identified and selected by inspecting power spectra from different windows (Figures A.4, A.6, A.8, A.10, A.12). The high wavenumber content differs strongly for different windows in our study (Figures A.5, A.7, A.9, A.11, A.13). However, the influence of different wavenumber ranges has only a little effect on the Z_t estimation (Figures A.5 b-d, A.7 b-d, A.9 b-d, A.11 b-d, A.13 b-d). Including or excluding a large portion of data points to estimate Z_t results only in a variation of roughly 300 meters (Figure A.12 b-d). In contrast to Z_0 the Z_t value is not multiplied in equation 2.6 and is therefore overall, less dominant than the Z_0 value to estimate the CDP. Using a constant wavenumber range for all windows in an automated process is robust because i) the low wavenumber range to estimate Z_0 is very stable, and a suitable wavenumber range can be selected and

ii) the strong variation in the high wavenumber range is negligible since choosing a wrong wavenumber range (Figures A.5, A.7, A.9, A.11, A.13) results in a variation of the CPD below the formal uncertainty. In other words, the method is not sensitive to variation in a sub km scale.

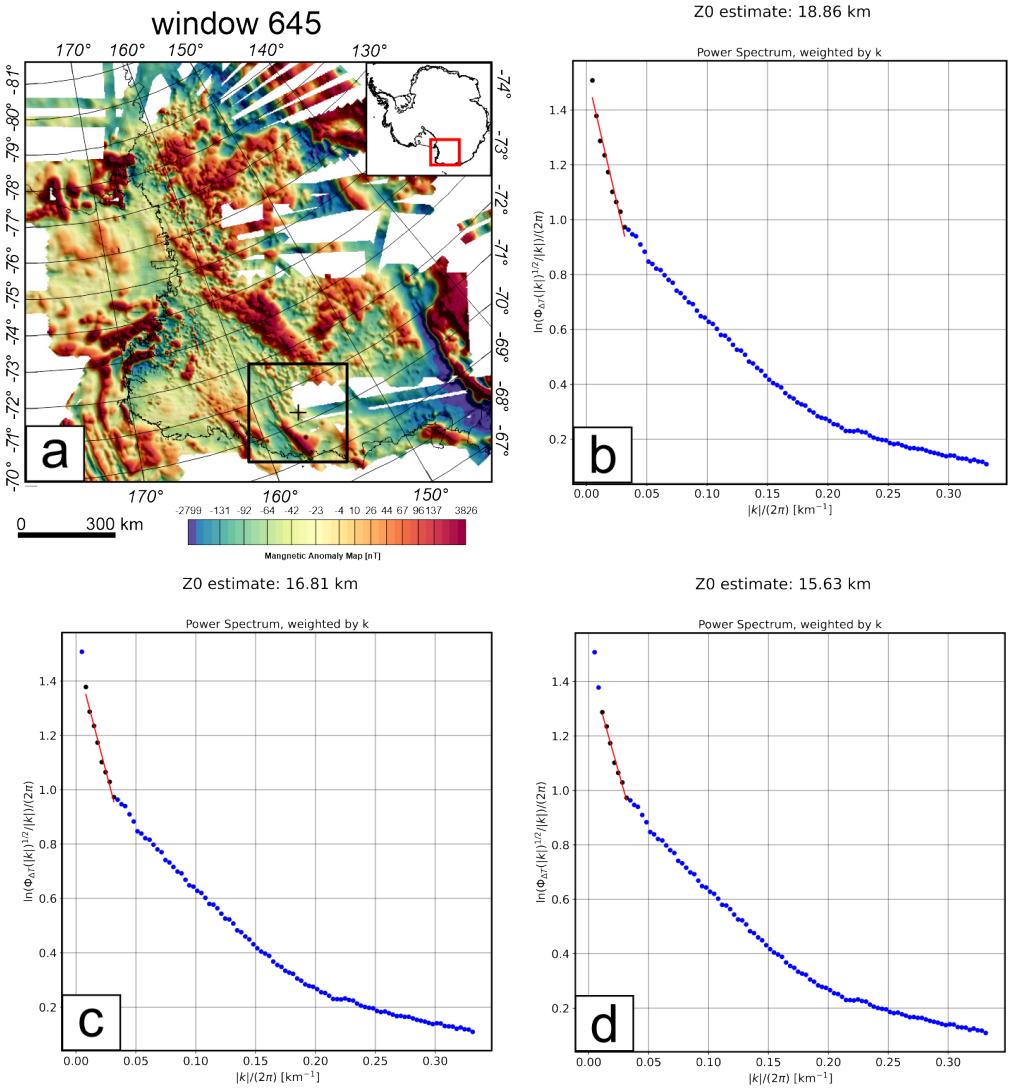

Figure A.4: Power spectrum from window 645 with a window size of 300 km. Blue dots power spectrum data points. Black dots indicate data points used for the linear regression. Red line linear fit to estimate Z_0 a) Window location and extent superimposed on magnetic data. b) wavenumber range 0 – 0.033 $\frac{|k|}{2\pi}$, Z_0 estimate: 18.86 km. c) wavenumber range wavenumber range 0.006 – 0.033 $\frac{|k|}{2\pi}$, Z_0 estimate: 16.91 km. d) wavenumber range 0.01 – 0.033 $\frac{|k|}{2\pi}$, Z_0 estimate: 15.63 km.

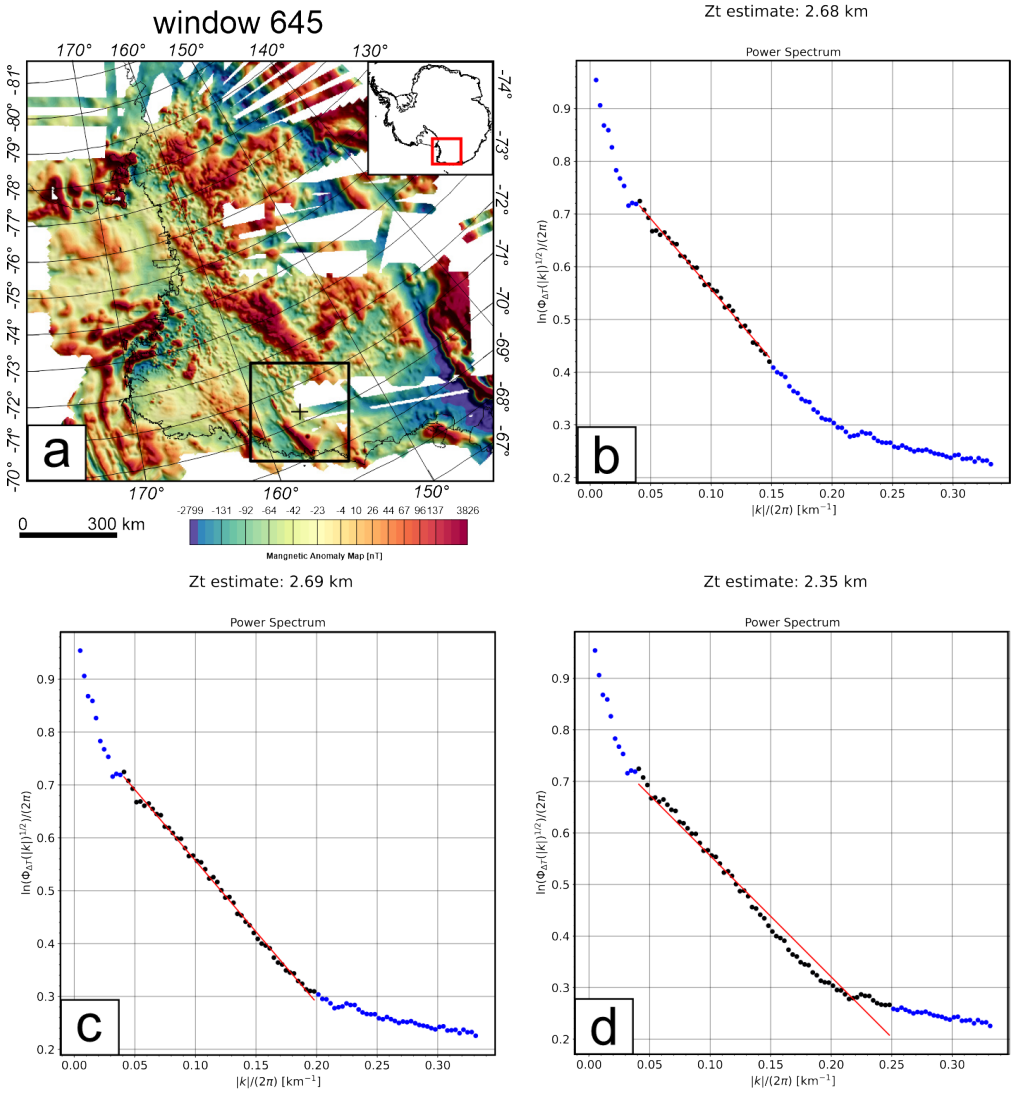

Figure A.5: Power spectrum from window 645 with a window size of 300 km. Blue dots power spectrum data points. Black dots indicate data points used for the linear regression. Red line linear fit to estimate Z_t. a) Window location and extent superimposed on magnetic data. b) wavenumber range 0.04 – 0.25 $\frac{|k|}{2\pi}$, Z_t estimate: 2.68 km. c) wavenumber range 0.04 – 0.2 $\frac{|k|}{2\pi}$, Z_t estimate: 2.69 km d) wavenumber range 0.04 – 0.15 $\frac{|k|}{2\pi}$, Z_t estimate: 2.35 km.

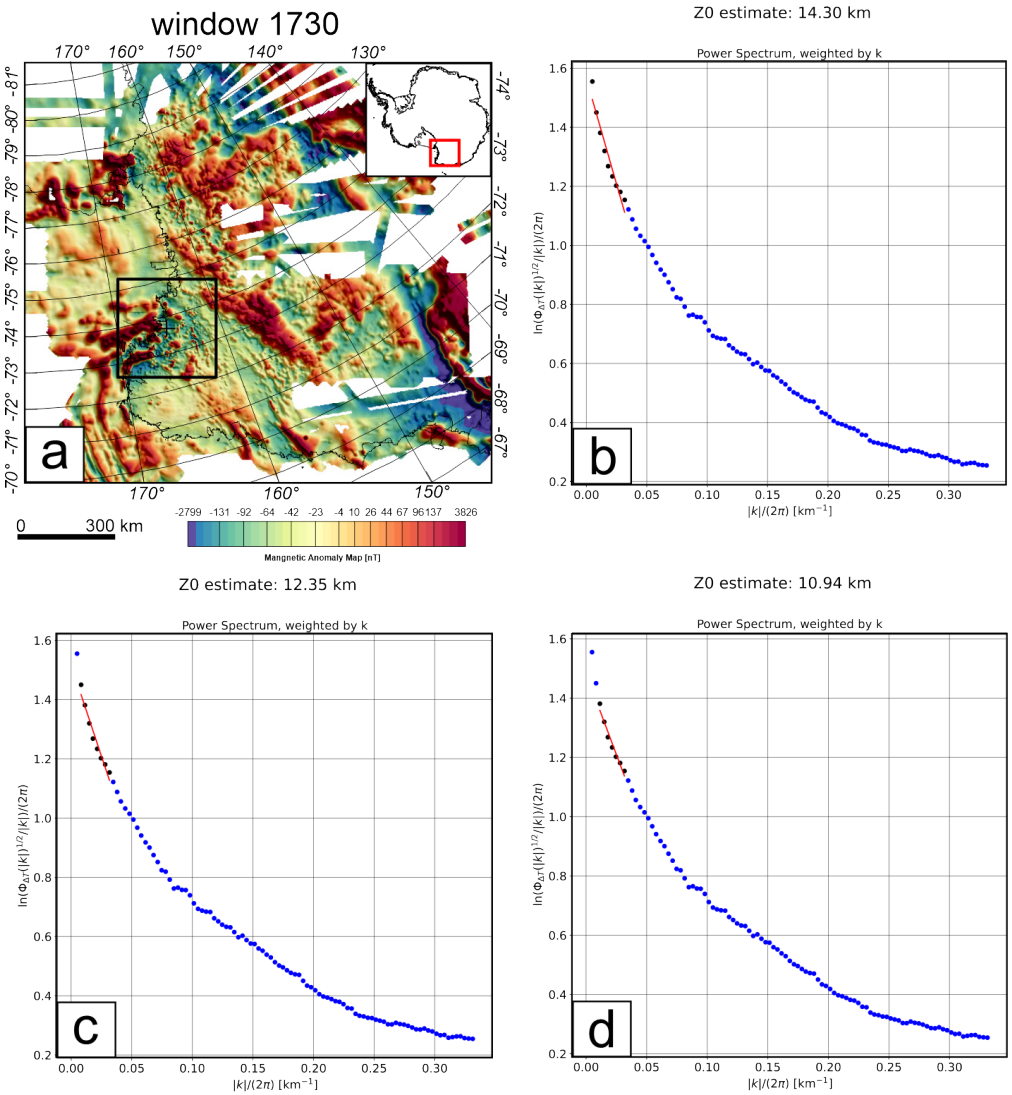

Figure A.6: Power spectrum from window 1730 with a window size of 300 km. Blue dots power spectrum data points. Black dots indicate data points used for the linear regression. Red line linear fit to estimate Z_0 a) Window location and extent superimposed on magnetic data. b) wavenumber range 0 – 0.033 $\frac{|k|}{2\pi}$, Z_0 estimate: 14.3 km. c) wavenumber range wavenumber range 0.006 – 0.033 $\frac{|k|}{2\pi}$, Z_0 estimate: 12.35 km. d) wavenumber range 0.01 – 0.033 $\frac{|k|}{2\pi}$, Z_0 estimate: 10.94 km.

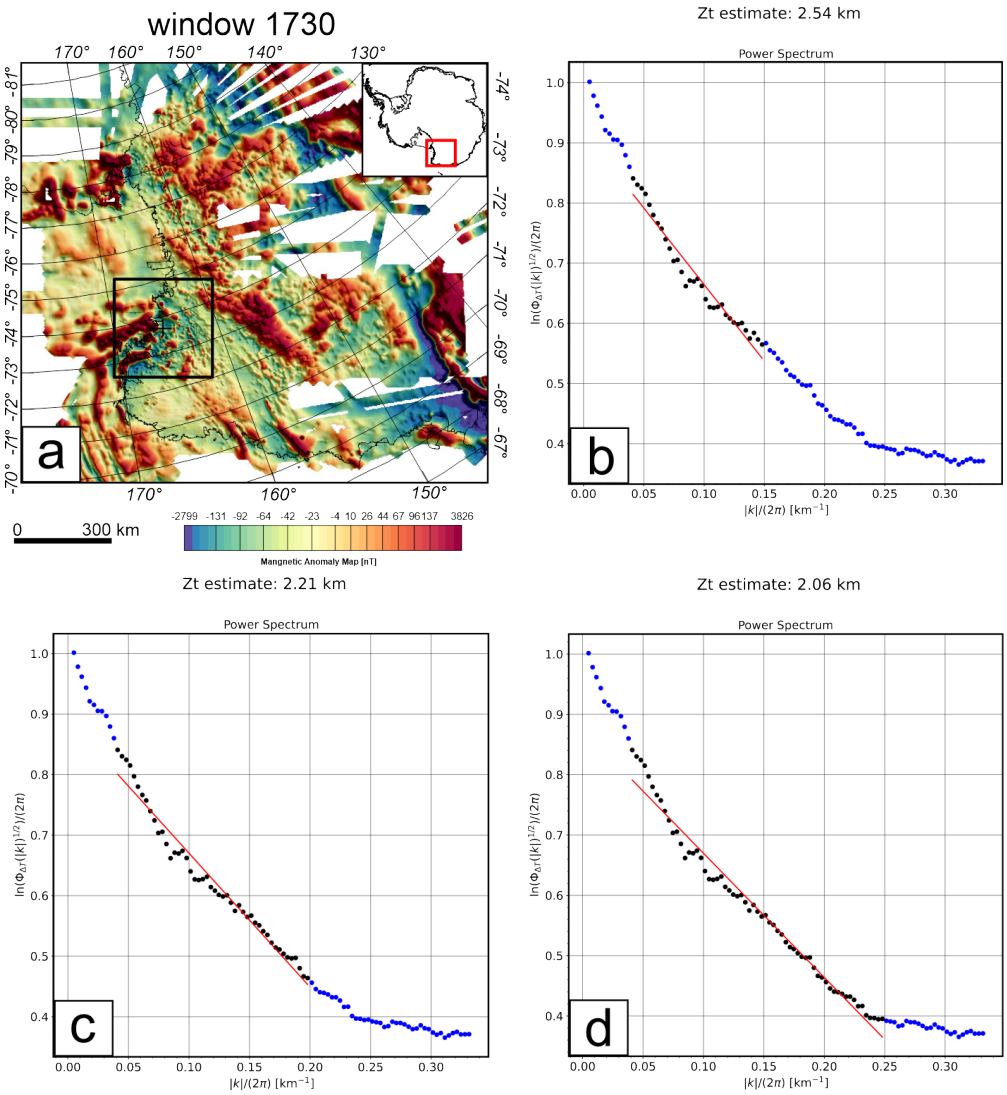

Figure A.7: Power spectrum from window 1730 with a window size of 300 km. Blue dots power spectrum data points. Black dots indicate data points used for the linear regression. Red line linear fit to estimate Z_t. a) Window location and extent superimposed on magnetic data. b) wavenumber range 0.04 – 0.25 $\frac{|k|}{2\pi}$, Z_t estimate: 2.54 km. c) wavenumber range 0.04 – 0.2 $\frac{|k|}{2\pi}$, Z_t estimate: 2.21 d) wavenumber range 0.04 – 0.15 $\frac{|k|}{2\pi}$, Z_t estimate: 2.06 km.

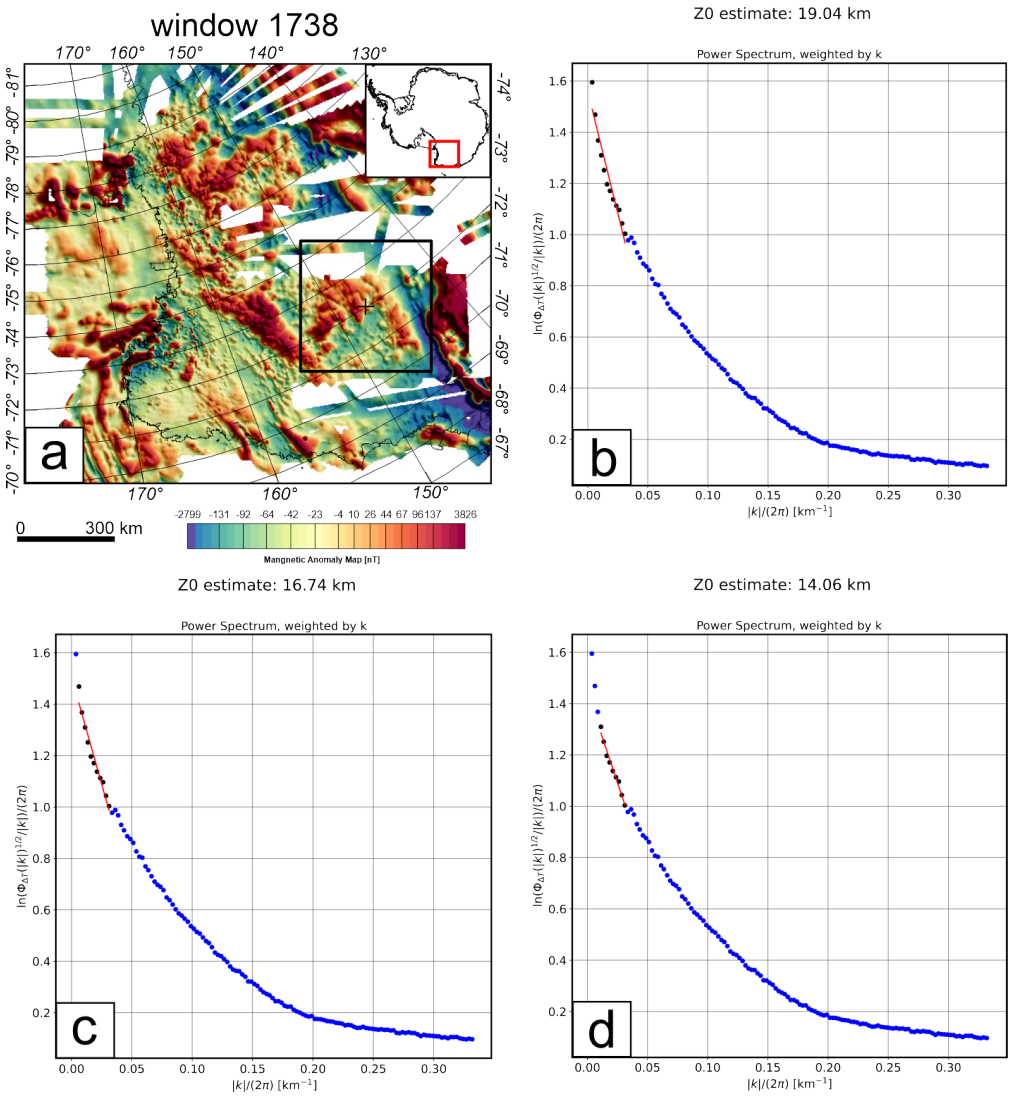

Figure A.8: Power spectrum from window 1738 with a window size of 400 km. Blue dots power spectrum data points. Black dots indicate data points used for the linear regression. Red line linear fit to estimate Z_0 a) Window location and extent superimposed on magnetic data. b) wavenumber range 0 – 0.033 $\frac{|k|}{2\pi}$, Z_0 estimate: 19.04 km. c) wavenumber range wavenumber range 0.006 – 0.033 $\frac{|k|}{2\pi}$, Z_0 estimate: 16.74 km. d) wavenumber range 0.01 – 0.033 $\frac{|k|}{2\pi}$, Z_0 estimate: 14.06 km.

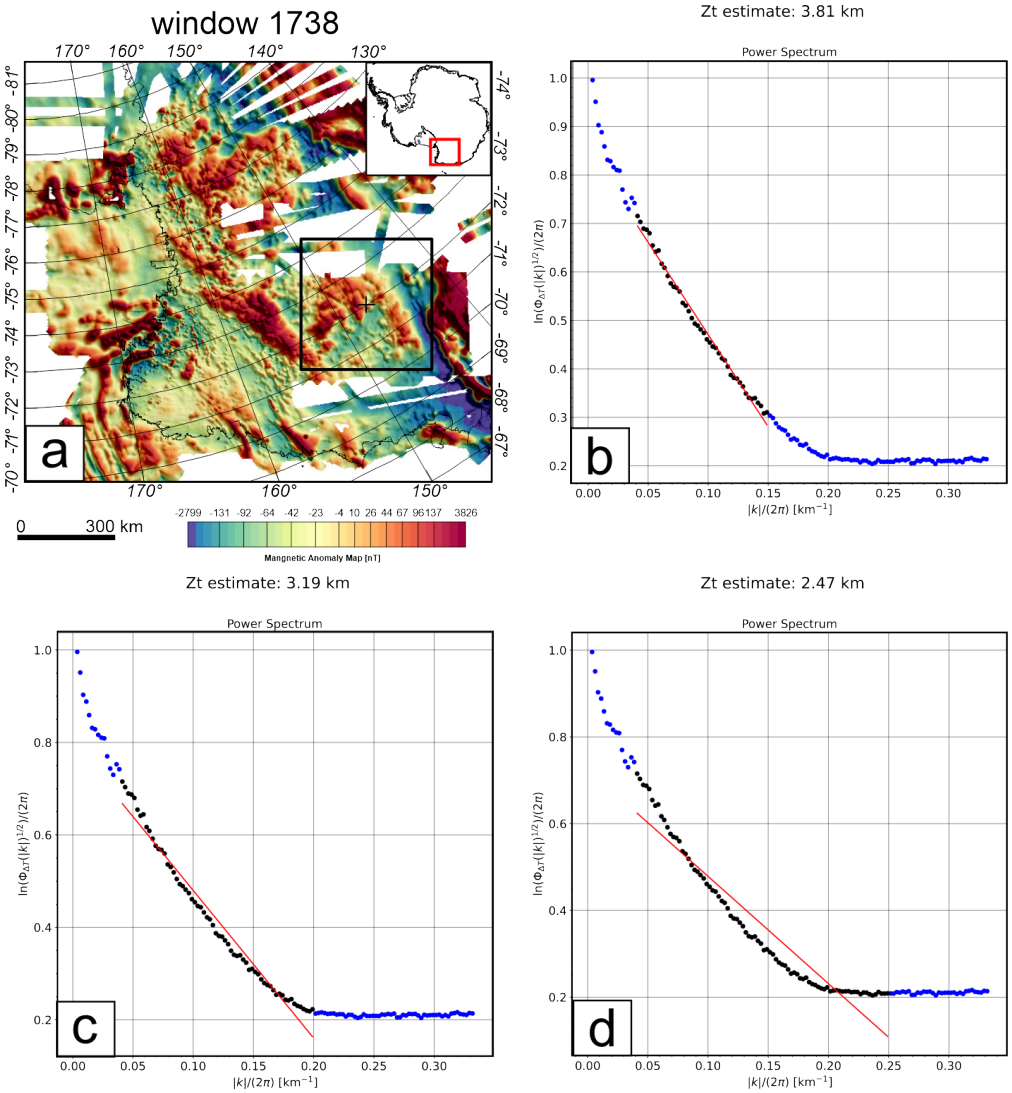

Figure A.9: Power spectrum from window 1738 with a window size of 400 km. Blue dots power spectrum data points. Black dots indicate data points used for the linear regression. Red line linear fit to estimate Z_t. a) Window location and extent superimposed on magnetic data. b) wavenumber range 0.04 – 0.25 $\frac{|k|}{2\pi}$, Z_t estimate: 3.81 km. c) wavenumber range 0.04 – 0.2 $\frac{|k|}{2\pi}$, Z_t estimate: 3.19 km d) wavenumber range 0.04 – 0.15 $\frac{|k|}{2\pi}$, Z_t estimate: 2.47 km.

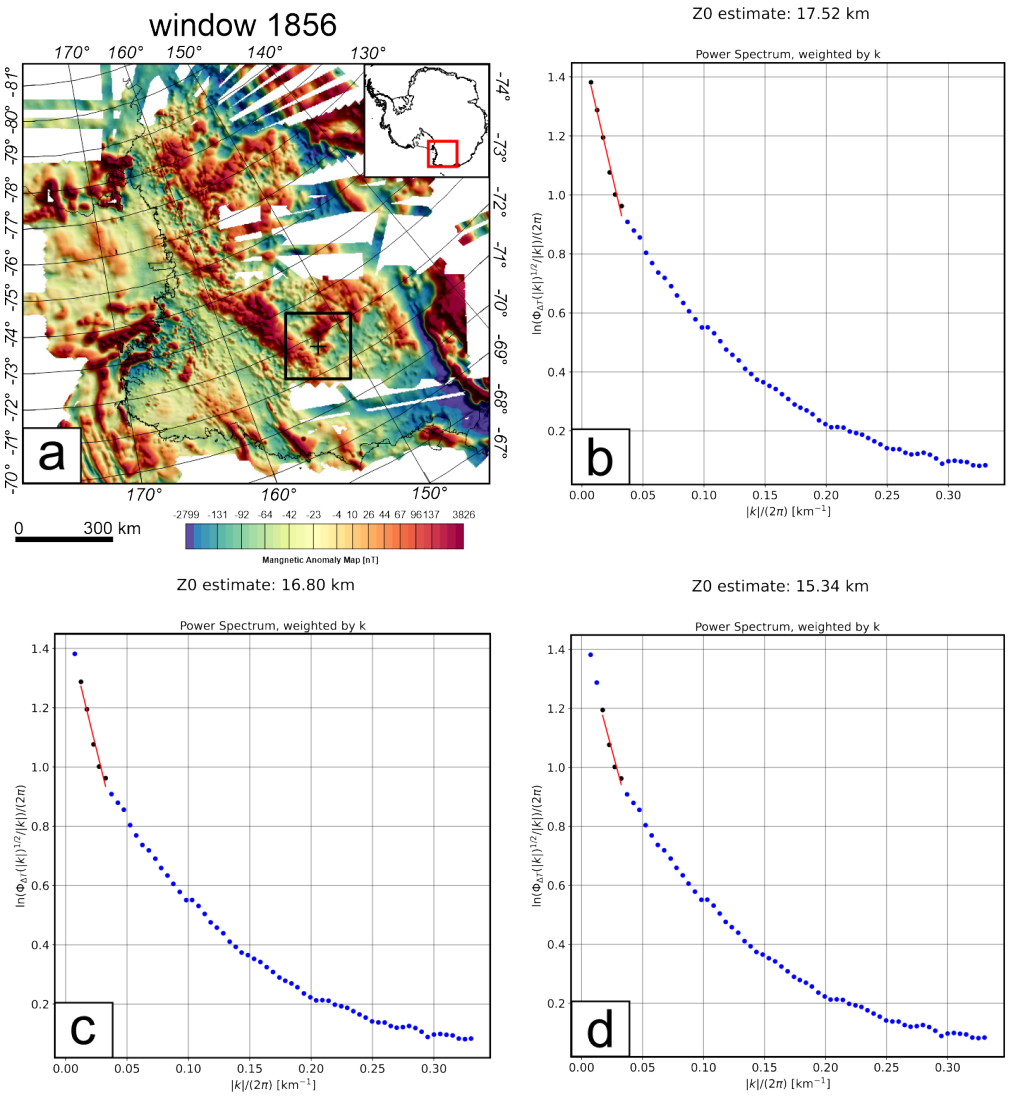

Figure A.10: Power spectrum from window 1856 with a window size of 200 km. Blue dots power spectrum data points. Black dots indicate data points used for the linear regression. Red line linear fit to estimate Z_0 a) Window location and extent superimposed on magnetic data. b) wavenumber range 0 – 0.033 $\frac{|k|}{2\pi}$, Z_0 estimate: 17.52 km. c) wavenumber range wavenumber range 0.01 – 0.033 $\frac{|k|}{2\pi}$, Z_0 estimate: 16.8 km. d) wavenumber range 0.015 – 0.033 $\frac{|k|}{2\pi}$, Z_0 estimate: 15.34 km.

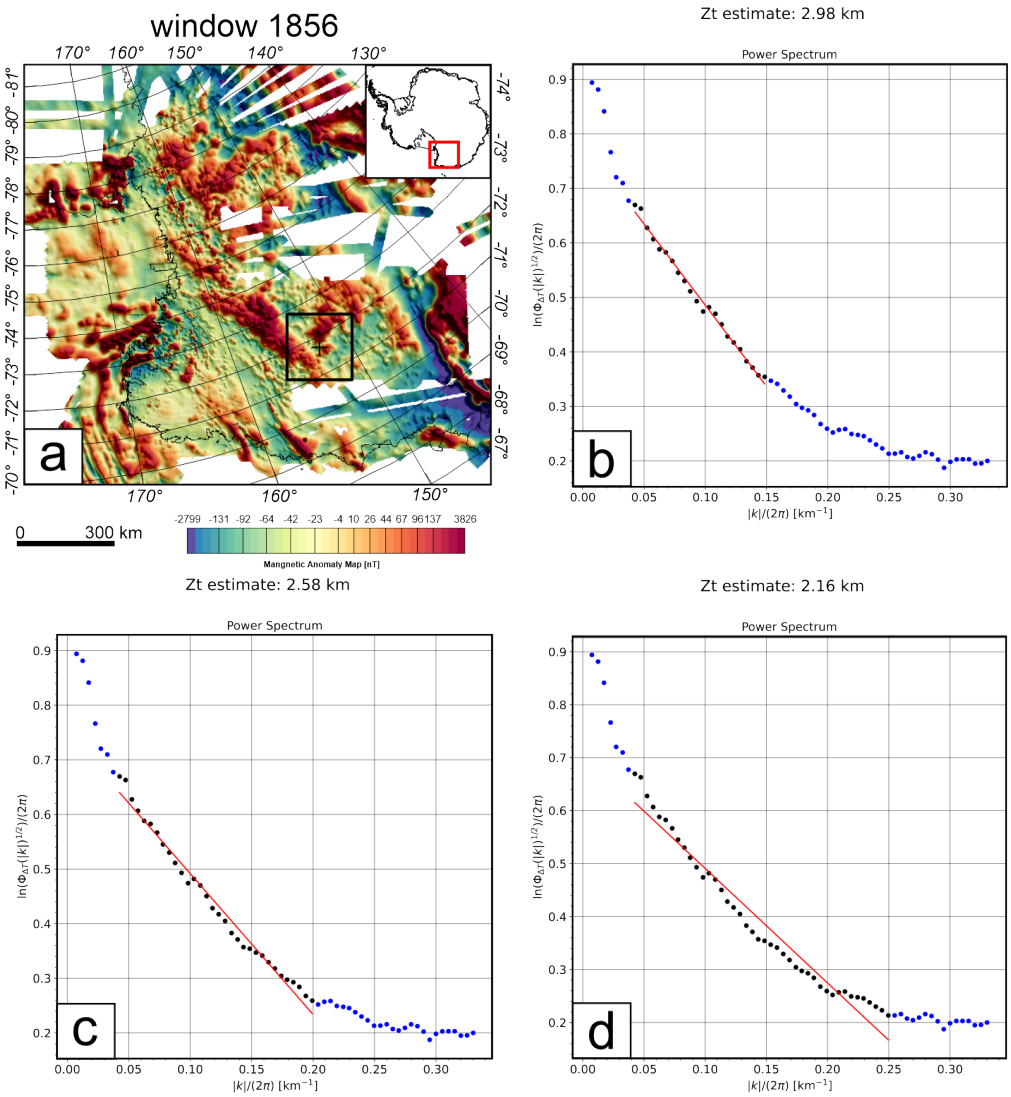

Figure A.11: Power spectrum from window 1856 with a window size of 200 km. Blue dots power spectrum data points. Black dots indicate data points used for the linear regression. Red line linear fit to estimate Z_t. a) Window location and extent superimposed on magnetic data. b) wavenumber range 0.04 – 0.25 $\frac{|k|}{2\pi}$, Z_t estimate: 2.98 km. c) wavenumber range 0.04 – 0.2 $\frac{|k|}{2\pi}$, Z_t estimate: 2.58km d) wavenumber range 0.04 – 0.15 $\frac{|k|}{2\pi}$, Z_t estimate: 2.16 km.

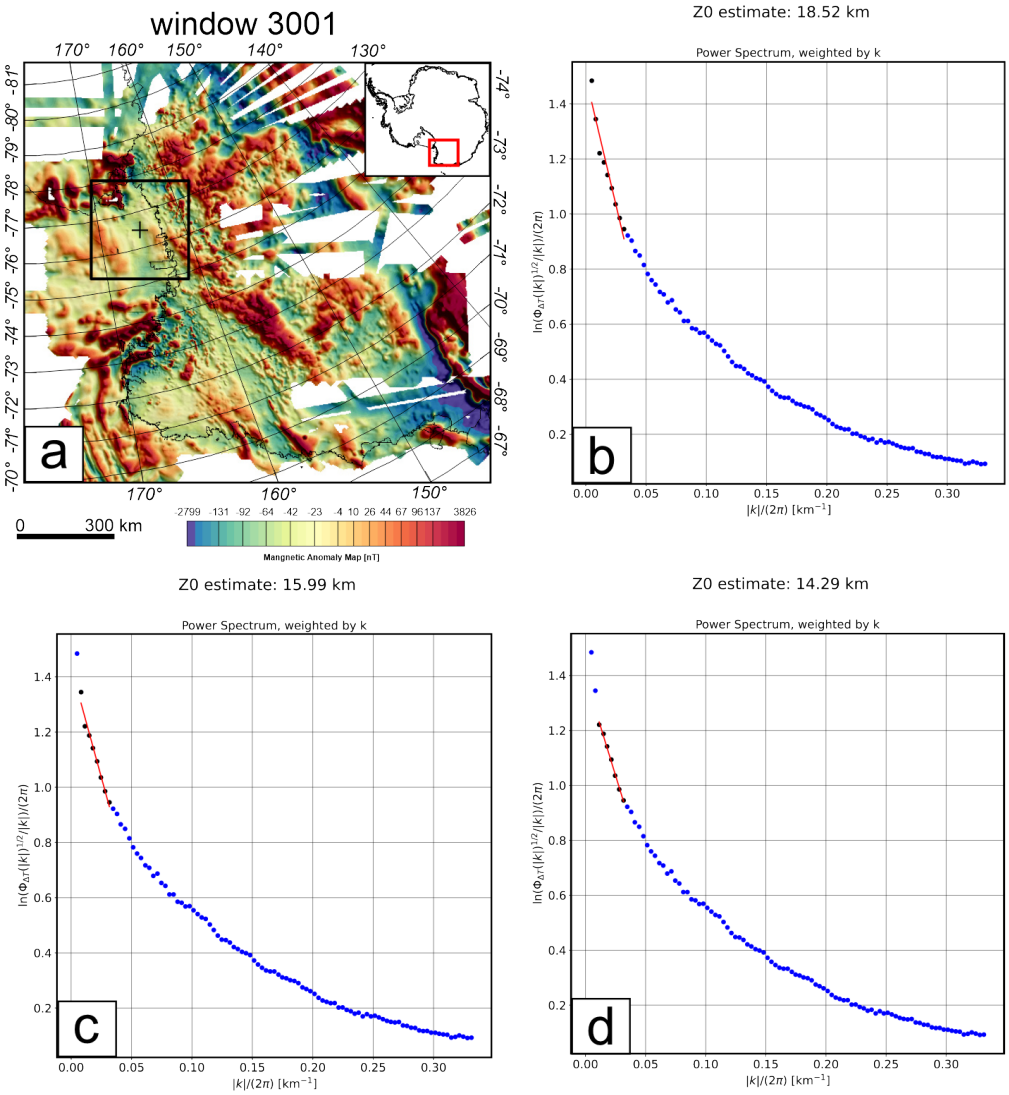

Figure A.12: Power spectrum from window 3001 with a window size of 300 km. Blue dots power spectrum data points. Black dots indicate data points used for the linear regression. Red line linear fit to estimate Z_0 a) Window location and extent superimposed on magnetic data. b) wavenumber range 0 – 0.033 $\frac{|k|}{2\pi}$, Z_0 estimate: 18.52 km. c) wavenumber range wavenumber range 0.006 – 0.033 $\frac{|k|}{2\pi}$, Z_0 estimate: 15.99 km. d) wavenumber range 0.01 – 0.033 $\frac{|k|}{2\pi}$, Z_0 estimate: 14.29 km.

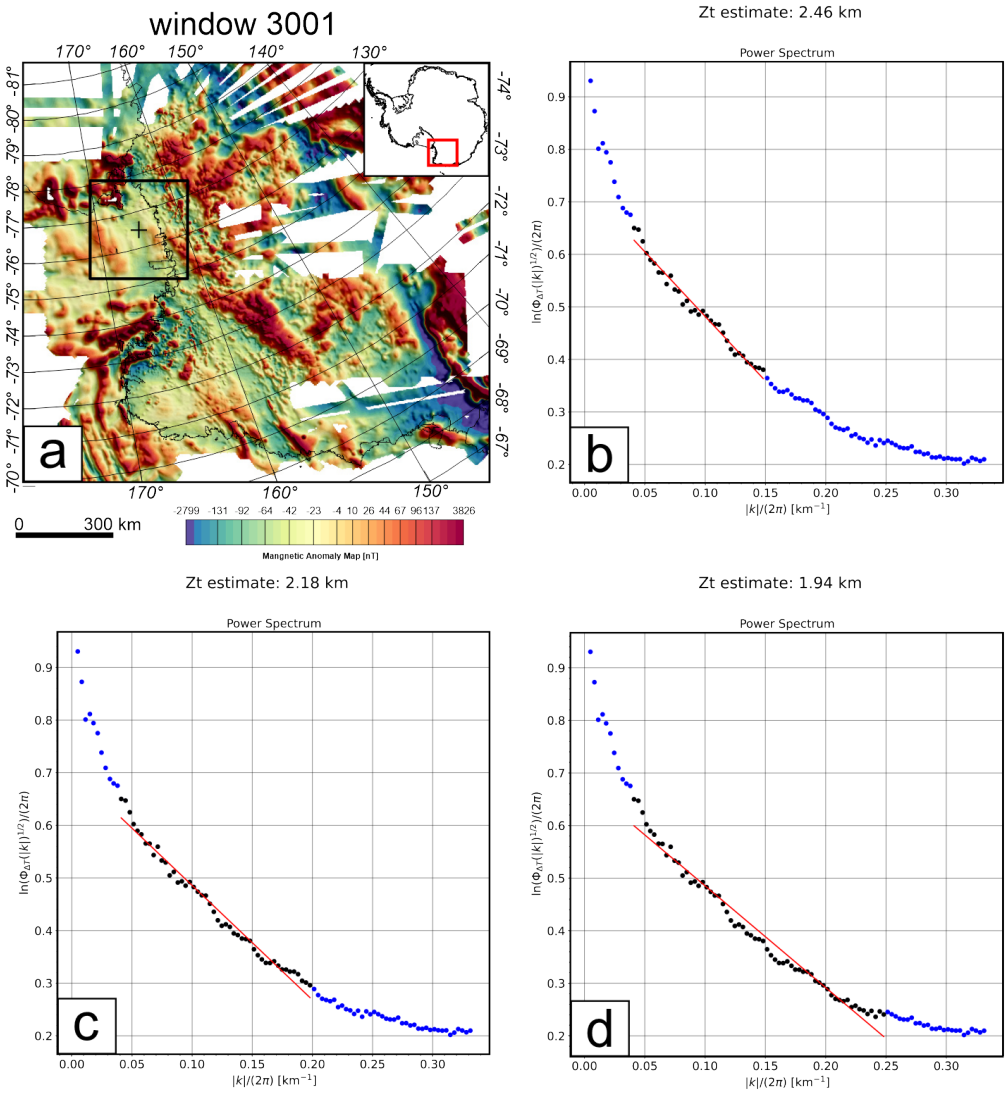

Figure A.13: Power spectrum from window 3001 with a window size of 300 km. Blue dots power spectrum data points. Black dots indicate data points used for the linear regression. Red line linear fit to estimate Z_t. a) Window location and extent superimposed on magnetic data. b) wavenumber range 0.04 – 0.25 $\frac{|k|}{2\pi}$, Z_t estimate: 2.46 km. c) wavenumber range 0.04 – 0.2 $\frac{|k|}{2\pi}$, Z_t estimate: 2.18 km d) wavenumber range 0.04 – 0.15 $\frac{|k|}{2\pi}$, Z_t estimate: 1.94 km.

Appendix B

Supplementary information for Chapter 3

This appendix chapter provides information on the compilation of the gravity data, upward continuation of the gravity data and the correction to the gravity data to obtain a residual gravity field associated with crustal masses (Section B.1 including Figure B.1 – B.2). Illustration of the inversion setup including boundary conditions (Section B.2 including Figure B.3 - B.4). Furthermore, results of VI inversion run1 with a coupling factor of 25000 are presented (Section B.3 including Figure B.6 - B.9) as well as gravity only and magnetic only inversion in contrast to the joint inversion of gravity and magnetic data using a Variation of Information algorithm (Section B.4 including Figure B.10 - B.12). Additionally, subglacial lakes superimposed on recent geothermal heat flow models (GHF) are presented (Section B.5 including Figure B.12)

B.1 Gravity compilation

The main gravity dataset used in this study (chapter 3), is the Bouguer anomaly grid (Figure B.1 a) with a grid spacing of 10 km taken from AntGG (Scheinert et al., 2016). Additional Bouguer anomaly data (Figure B.1) are taken from Ganovex VII – ItaliAntartide XV survey (Reitmayr et al., 2003) and recent ground station measurements conducted within the Italian National Program for Antarctic Research activities (Zanutta et al., 2018). To fill the AntGG data gaps in the Transantarctic Mountains we masked the additional data from (Reitmayr et al., 2003; Zanutta et al., 2018) to regions where no data is available from AntGG (Figure B.1c). Subsequently both datasets were gridded together using the minimum curvature gridding function implemented in Oasis Montaj with a grid spacing of 10 km and a blanking distance of 40 km. The resulting gravity compilation grid was then upward continued to a constant station height of 10 km using the Compudrape function in Oasis Montaj.

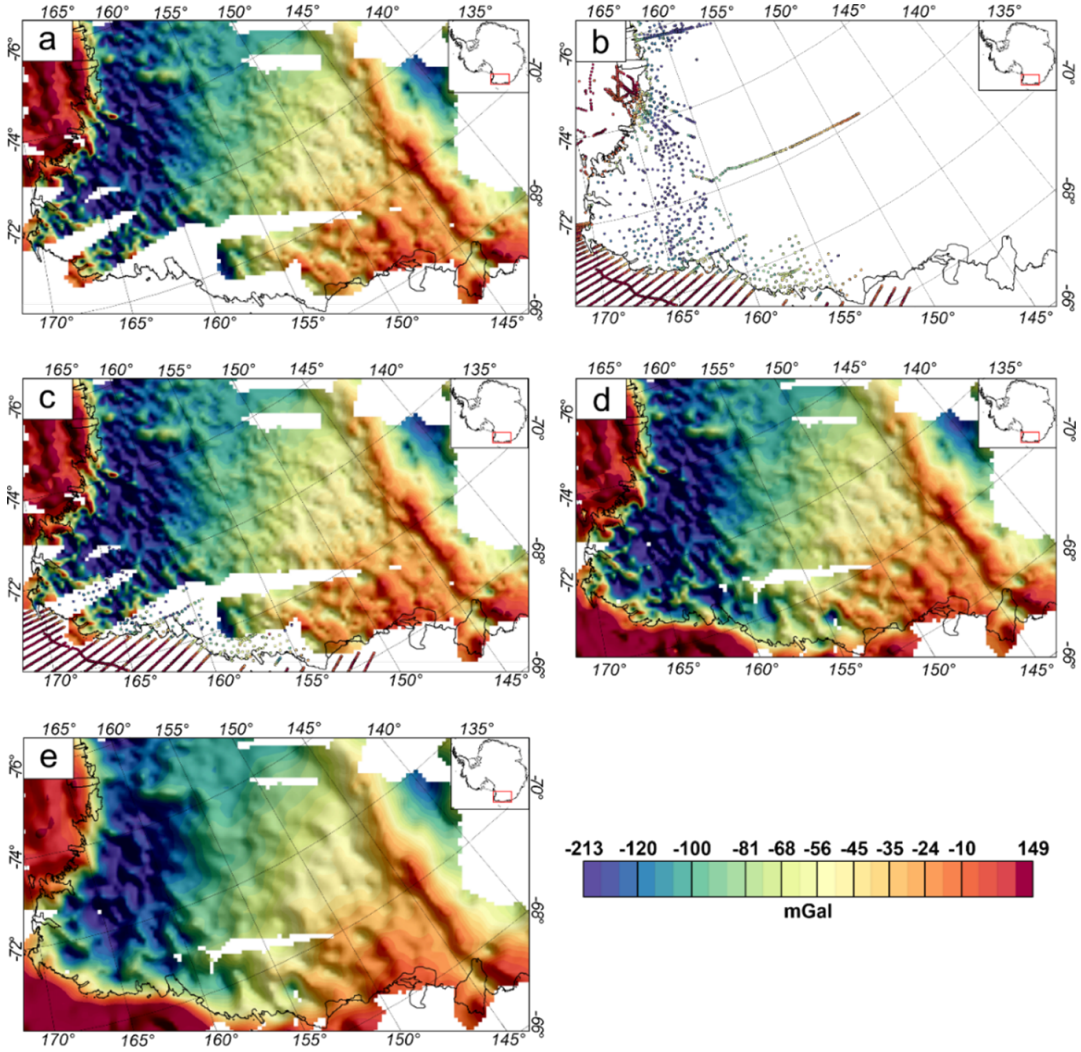

Figure B.1: a) Bouguer anomaly map taken from AntGG (Scheinert et al., 2016). B) Bouguer anomaly measurements from (Reitmayr et al., 2003; Zanutta et al., 2018). c) Masked Bouguer anomaly data to fill data gaps in AntGG. d) combined Bouguer anomaly compilation grid of both databases. e) Upward continued Bouguer anomaly compilation to a constant height of 10 km. Colourmap identical for all subfigures.

The upward continued gravity compilation (Figure B.2 a) was corrected for variable mantle densities by subtracting lithospheric scale model by (Pappa et al., 2019b) (Figure B.2 b). The resulting residual gravity grid (Figure B.2 c) was additionally corrected by subtracting the mean value of the residual gravity field (92.5mGal) to shift the mean residual gravity field to 0 mGal level (Figure B.2 d).

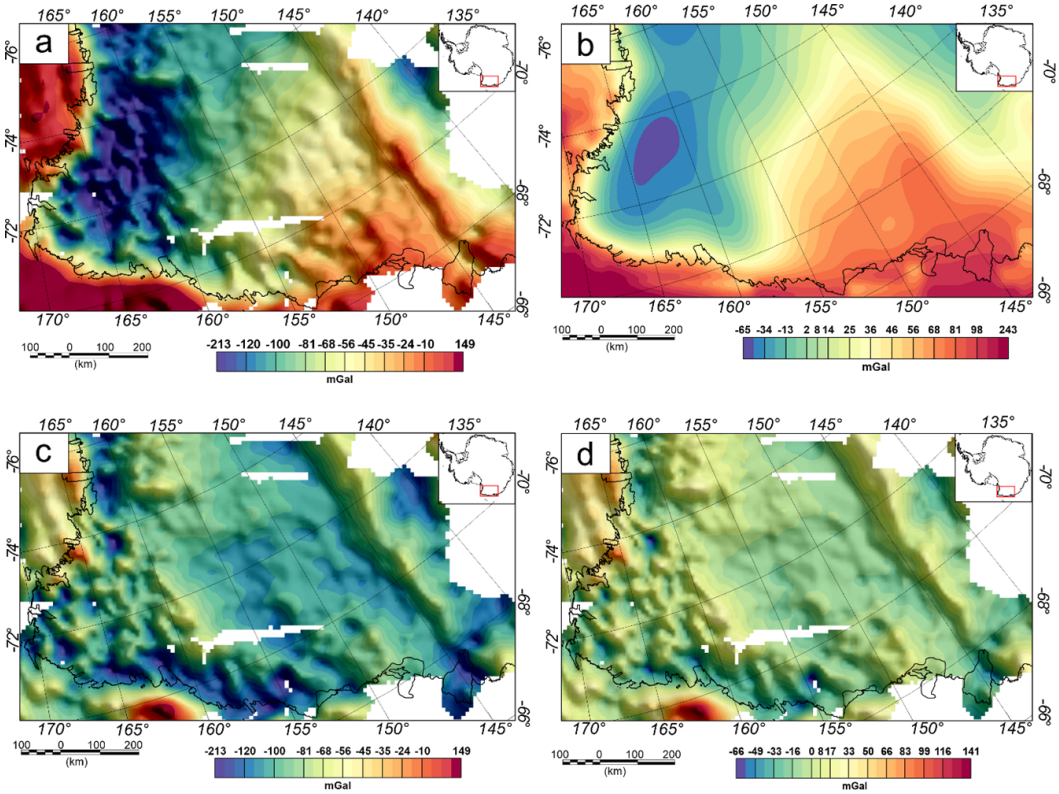

Figure B.2: a) Bouguer anomaly compilation containing data from Reitmayr et al. (2003), Scheinert et al. (2016), Zanutta et al. (2018). b) gz component from lithospheric scale model by (Pappa et al., 2019b). c) Residual map obtained by subtracting the grid shown in Figure B.2b from the one shown in Figure B.2a. d) Residual map obtained by subtracting the mean value of Figure B.2c.

B.2 Inversion set up

Vertical cell size of the inversion mesh increases by a factor of 1.1 for each cell row starting from 1 km vertical cell extent. Cell resolution is illustrated in Figure B.3b and B.3 c. Joint inversion is carried out from topography down to the Curie Point Depth and gravity inversion is carried out down to the Moho depth (Figure B.3 b-c). Yellow cells are illustrated as active cells while purple cells are not allowed to vary during the inversion. Vertical cell increase is incorporated to recognise uncertainties of CPD and Moho depth estimation. At the depth of the crustal mantle interface the vertical cell size is around 5km. The error of Moho depth estimation is in the same order of magnitude. The Moho depth is taken from Pappa et al. (2019a). Additional crustal disagreement between Moho models (Baranov et al., 2021; Pappa et al., 2019a) usually do not exceed $\sim$8 km (Figure B.4 c). The crustal thickness would also only influence long wavelength features.

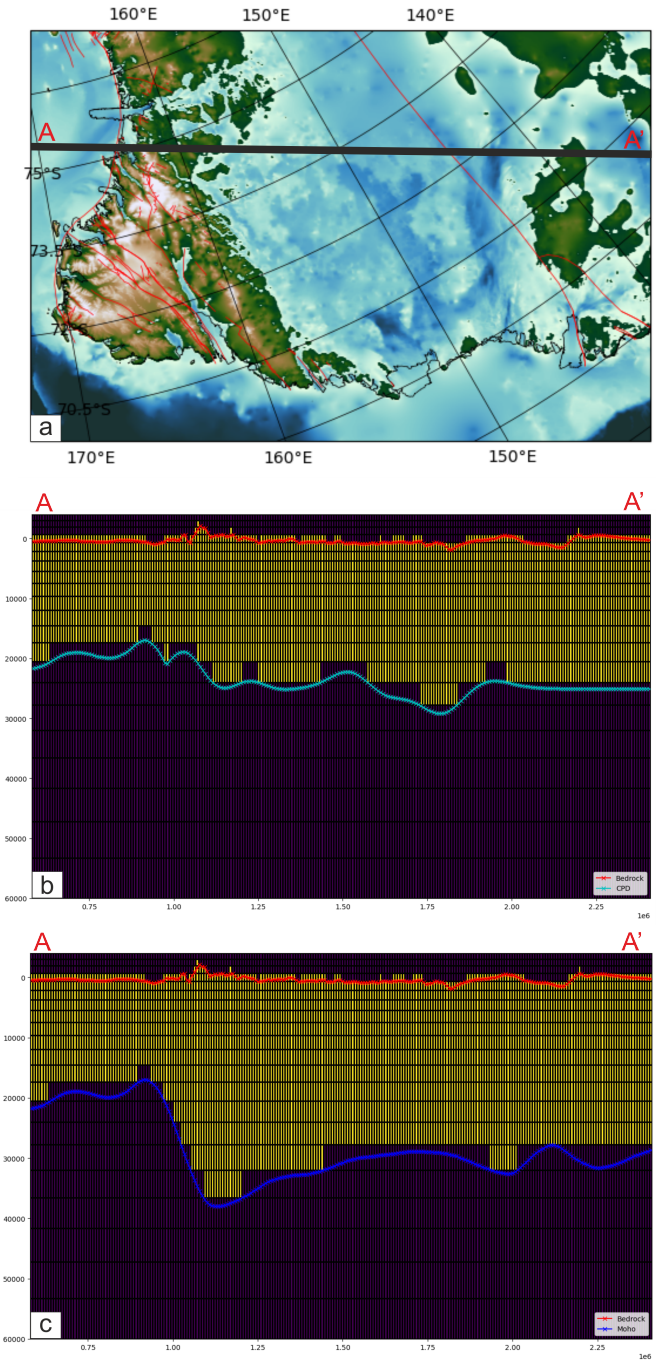

Figure B.3: Inversion mesh a) profile location superimposed on bedrock topography from BedMachine (Morlighem et al., 2020). Red line indicates faults after GeoMap (Cox et al., 2023). b) active cell (yellow) and inactive cell (purple) during magnetic inversion. Red line indicates the bedrock topography (Morlighem et al., 2020). Teal line indicates the CPD (Lowe et al., 2023). c) active cell (yellow) and inactive cell (purple) during gravity inversion. Red line indicates the bedrock topography (Morlighem et al., 2020). Blue line indicates the Moho depth (Pappa et al., 2019a).

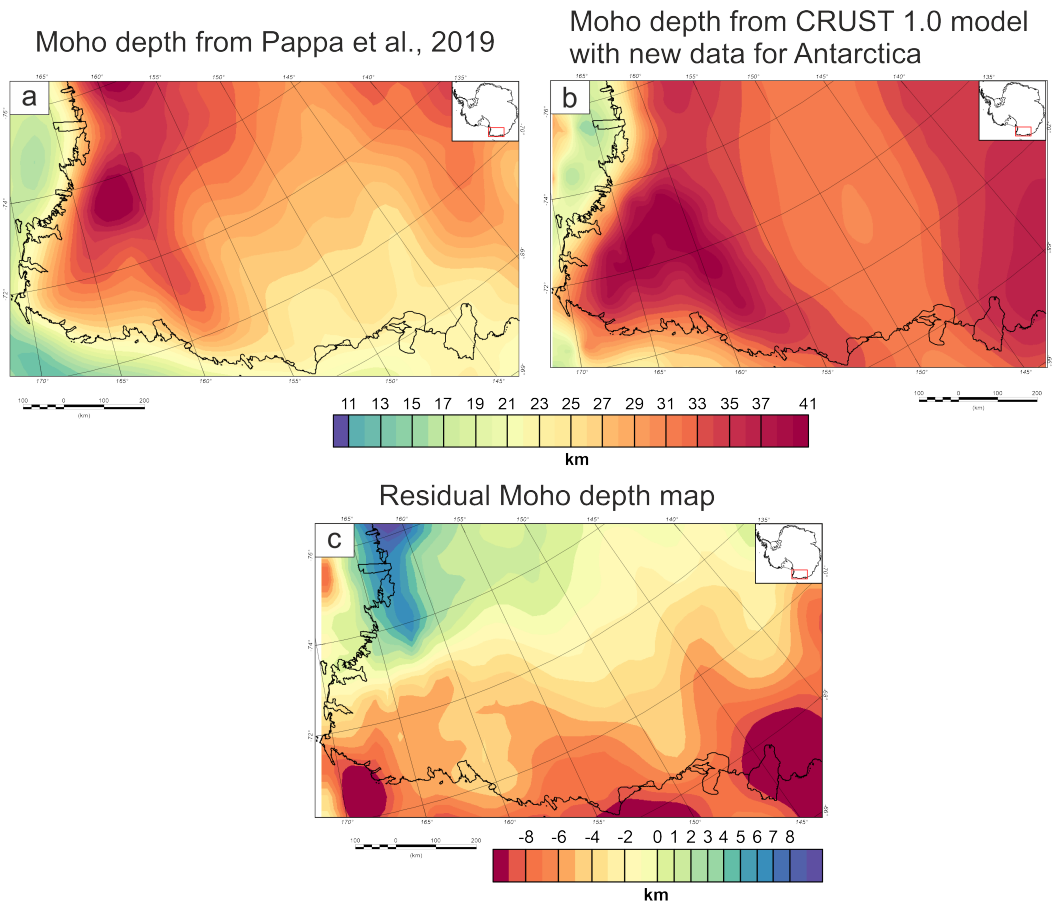

Figure B.4: a) Moho depth from (Pappa et al., 2019a) b) Moho depth from (Baranov et al., 2021) c) Difference in results between Figure B.4 a and B.4 b.

B.3 VI inversion result after inversion set up with 25000 coupling factors

Inversion results including inversion statistics (Figure B.5), resulting inversion maps (Figure B.6), residual maps (Figure B.6 e, f), and density and susceptibility relationship cross plot (Figure B.7) are presented for a first inversion run (run 1). Run 1 obtains a satisfactory RMS error between the observed and inverted potential fields of 1.6 mGal and 0.8 nT (Figure B.5). The end members of the residual between observed and inverted values are + 36.7 and -18.7 mGal with a standard deviation of 3.1 mGal for the gravity inversion and for the magnetic inversion +343.9 and -64.1 nT with a standard deviation of 14.2 nT. The residual map between the observed and inverted magnetic field (Figure B.6f) shows a long wavelength trend which is reduced by a subsequent second inversion run with a looser coupling factor of 15000.

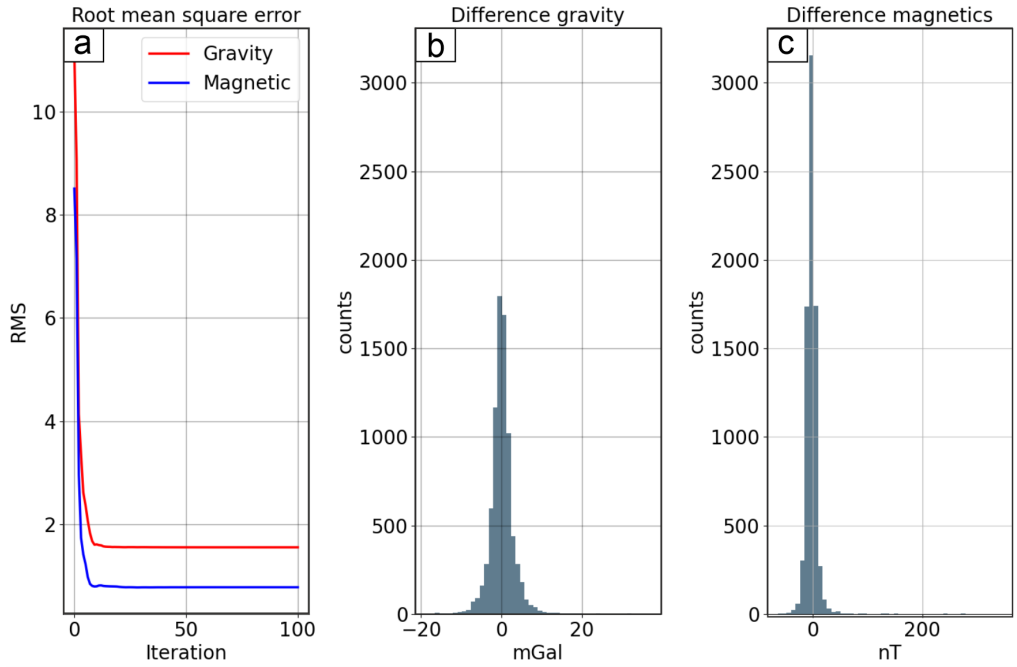

Figure B.5: a) Root mean square (RMS) error between observed and inverted gravity (red) and magnetic (blue) field for each gravity and magnetic only inversion iteration for single inversion run (run1) with a coupling factor of 25000. b) Gravity residual histogram between observed and inverted gravity field based on single inversion run (run1) with a coupling factor of 25000. c) Magnetic residual between observed and inverted magnetic field for single inversion run (run1) with a coupling factor of 25000.

Additionally, the density and susceptibility relationship cross plot for inversion run1 is strongly scattered (Figure B.7). A subsequent inversion run with a looser coupling factor of 15000 results in a more continuous density-susceptibility distribution in the model.

B.4 Density and Susceptibility only inversion vs VI inversion

Gravity only and magnetics only inversion has been performed with the identical inversion set up as the joint inversion to illustrate the improvement that coupling of density and susceptibility through incorporating Variation of Information (VI) in the objective function provides. Statistics of gravity or magnetic data only inversion show that both inversions converge faster compared to the VI inversion with simlar residual histograms between observed and inverted fields (Figure B.8).

Gravity and magnetic only inversions reproduce the observed gravity and magnetic field to a satisfactory degree (Figure B.9). Surprisingly, the long wavelength trend in the residual magnetic inversion is more prominent than for the VI inversion.

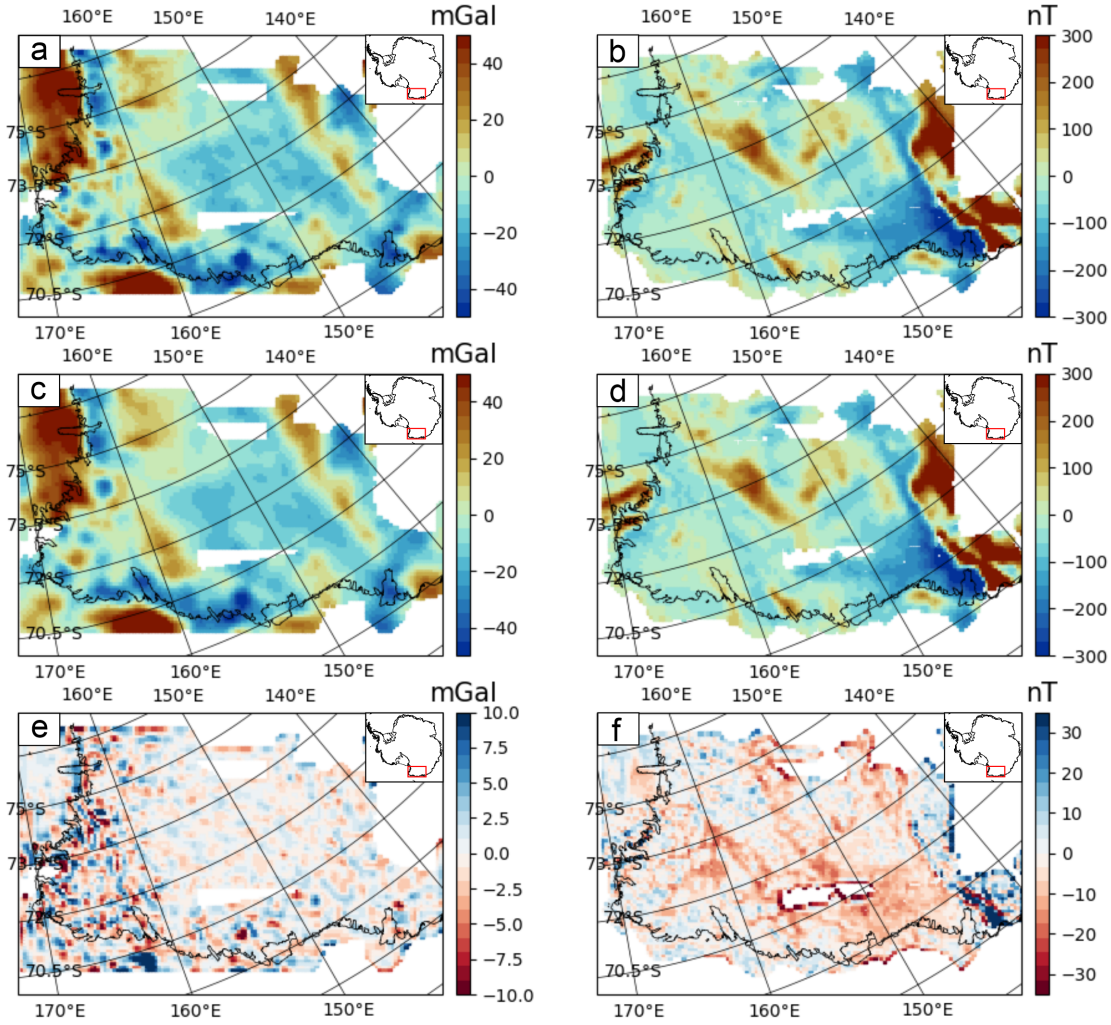

Figure B.6: Inversion result maps for a single inversion run (run1) with a set coupling factor of 25000. a) Gravity input data. b) Magnetic input data. c) Inverted gravity field. d) Inverted magnetic field. e) Difference map between observed and inverted gravity fields (Figure B.6a minus Figure B.6c). Difference map between observed and inverted magnetic field (Figure B.6b minus Figure B.6d).

A cross-section through the individually inverted density and susceptibility distribution (Figure B.10) at the identical position as the cross-section (Figure 3.8) in the chapter (3) shows that the gravity and magnetic only inversions reproduce anomalies in the same location. However, those anomalies are much more spheroidal diffuse anomalies, while the anomalies produced by the VI inversion (Figure 3.8 b, d) are more focused and appear to resolve more geologically realistic shapes. The large scale anomaly with negative density and postive susceptibilty values in the profile centre (black dotted oval) is pushed to deeper depths in the VI inversion model (Figure 8 b, d) compared to the gravity and magnetic only inversion (Figure B.10).

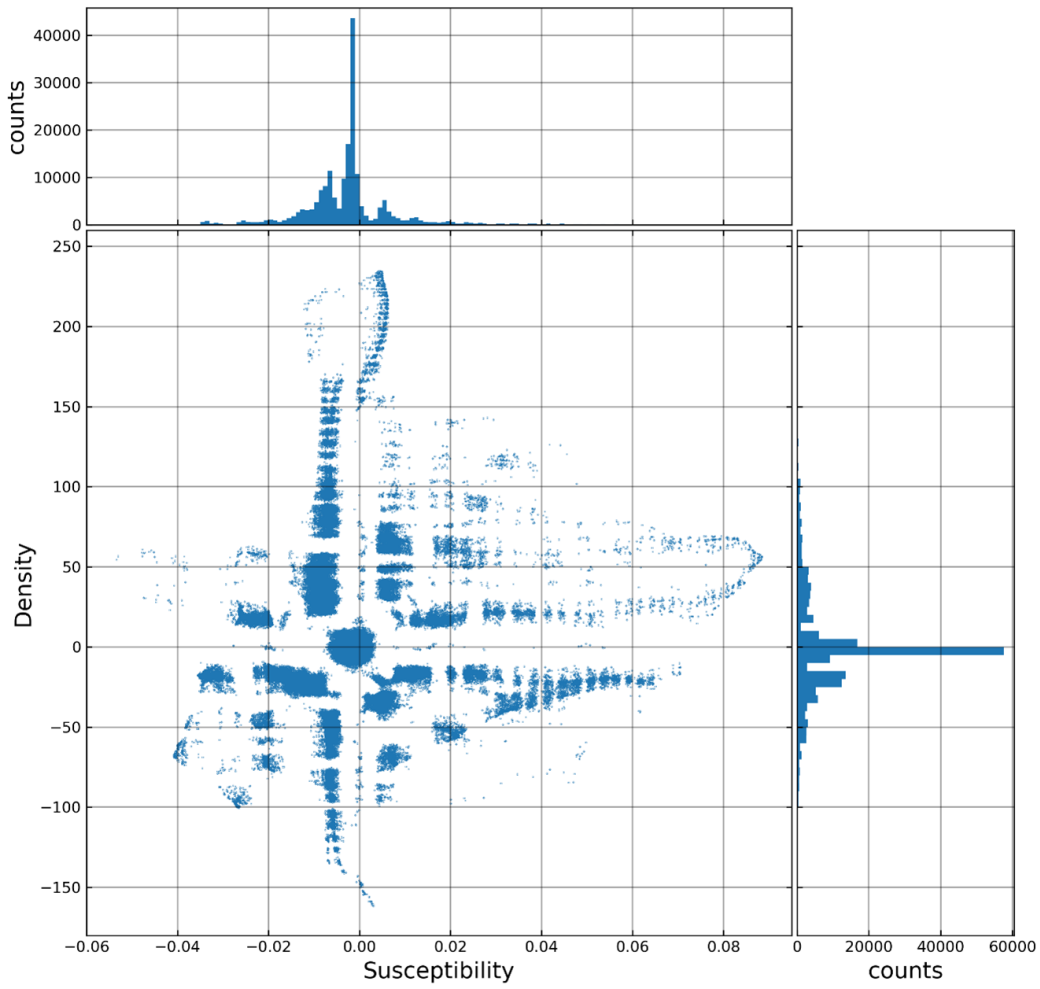

Figure B.7: Inverted density and susceptibilty cross plot and density and susceptibility histogram of the first VI inversion run (run1) with a coupling factor of 25000.

Additionally, the inverted density and susceptibility relationship is much more diffuse (Figure B.11) compared to the VI inversion, almost certainly due to the spheroidal diffuse anomalies in the subsurface, which are inferred by the gravity and magnetic only inversions.

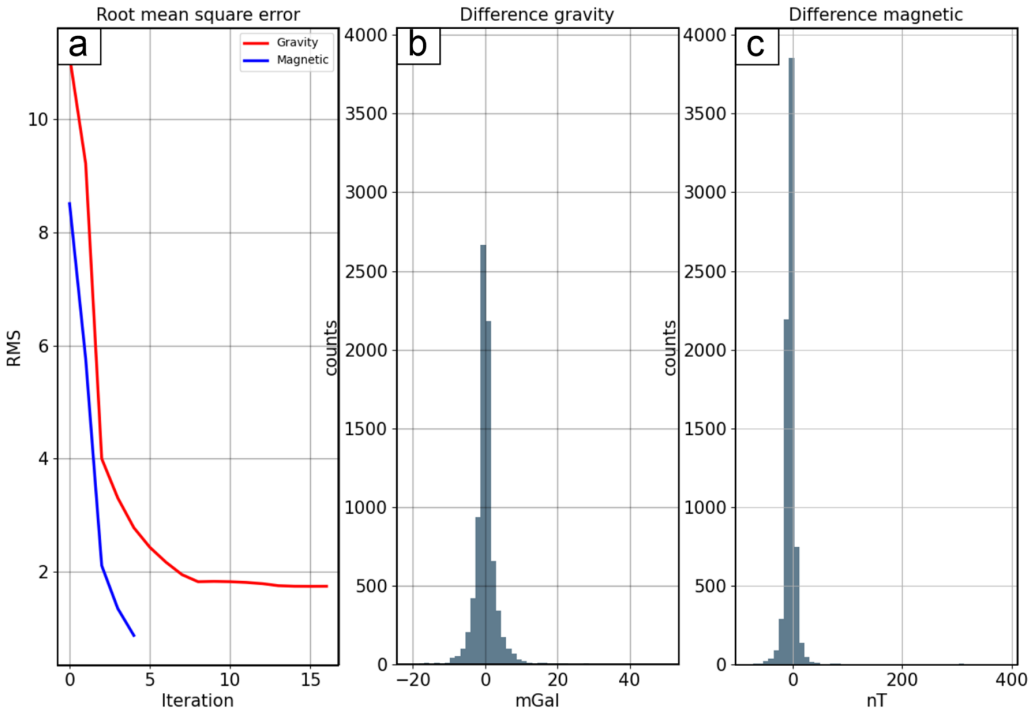

Figure B.8: a) Root mean square (RMS) error between observed and inverted gravity (red) and magnetic (blue) field for each gravity and magnetic only inversion iteration. b) Gravity residual histogram between observed and gravity inverted gravity field based on gravity only inversion. c) Magnetic residual between observed and inverted magnetic field based on magnetic only inversion.

B.5 Subglacial lake

Subglacial lakes from the inventory by Livingstone et al. (2022) in WSB region superimposed on current GHF (Figure B.12) shows no clear correlation between heat flow models and the location of subglacial lakes. Location of $Cook_{E2}$ subglacial lake is highlighted as yellow star.

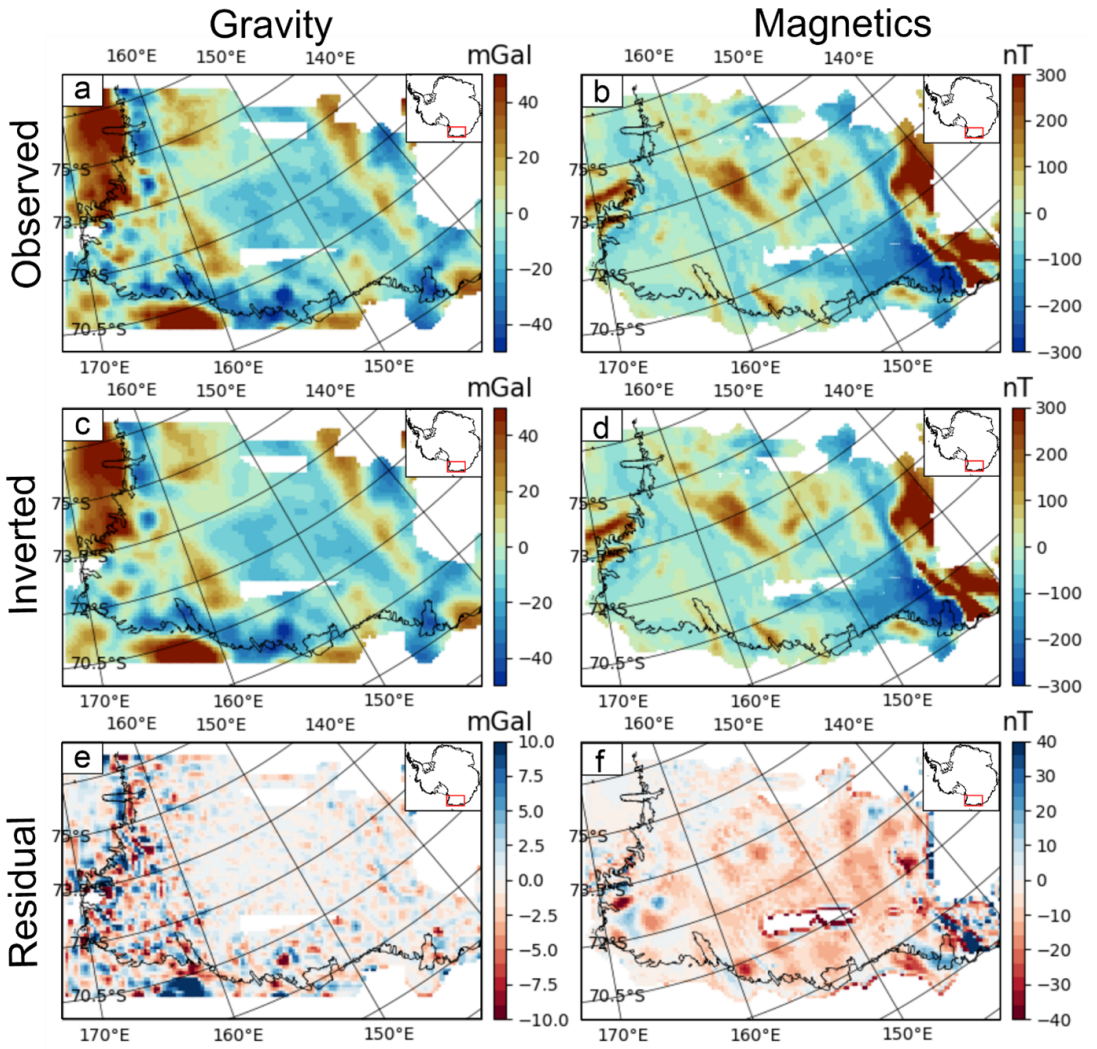

Figure B.9: Gravity input data for gravity only inversion. b) Magnetic input data for magnetic only inversion. c) Final inverted gravity field. d) Final inverted magnetic field. e) Difference map between observed and inverted gravity fields based on gravity only inversion (Figure B.9 a minus Figure B.9 c). Difference map between observed and inverted magnetic field based on magnetic only inversion (Figure B.9 b minus Figure B.9 d).

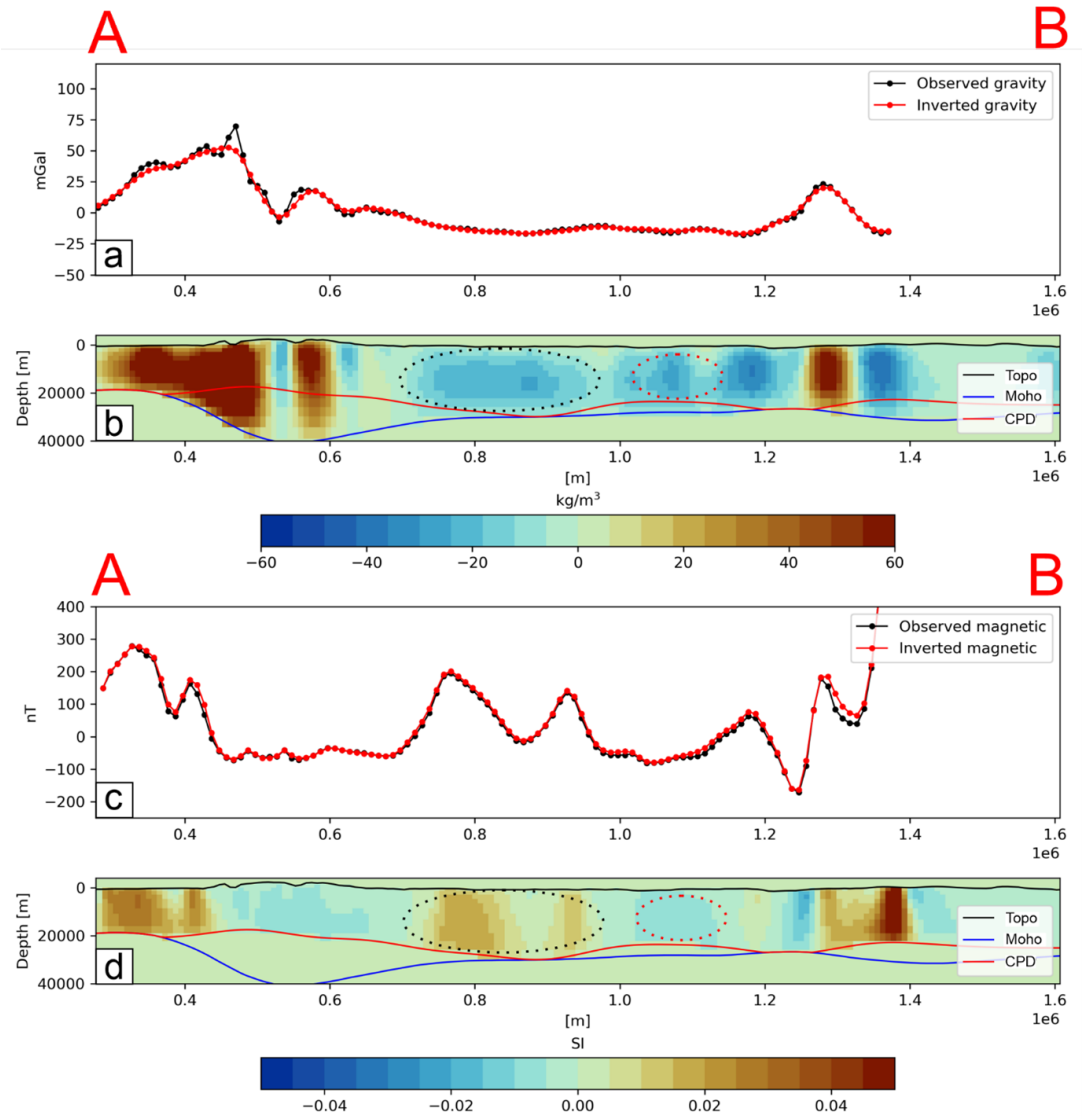

Figure B.10: Observed (black line) and inverted (red line) gravity field along profle AB from the gravity-only inversion. Location of profile AB is given in (Figure 3.7 of chapter 3). Cross section of the inverted density model along profile AB. c) observed (black line) and inverted (red line) magnetic field along profle AB from the magnetics-only inversion. Cross section of the inverted susceptibility model along profile AB.

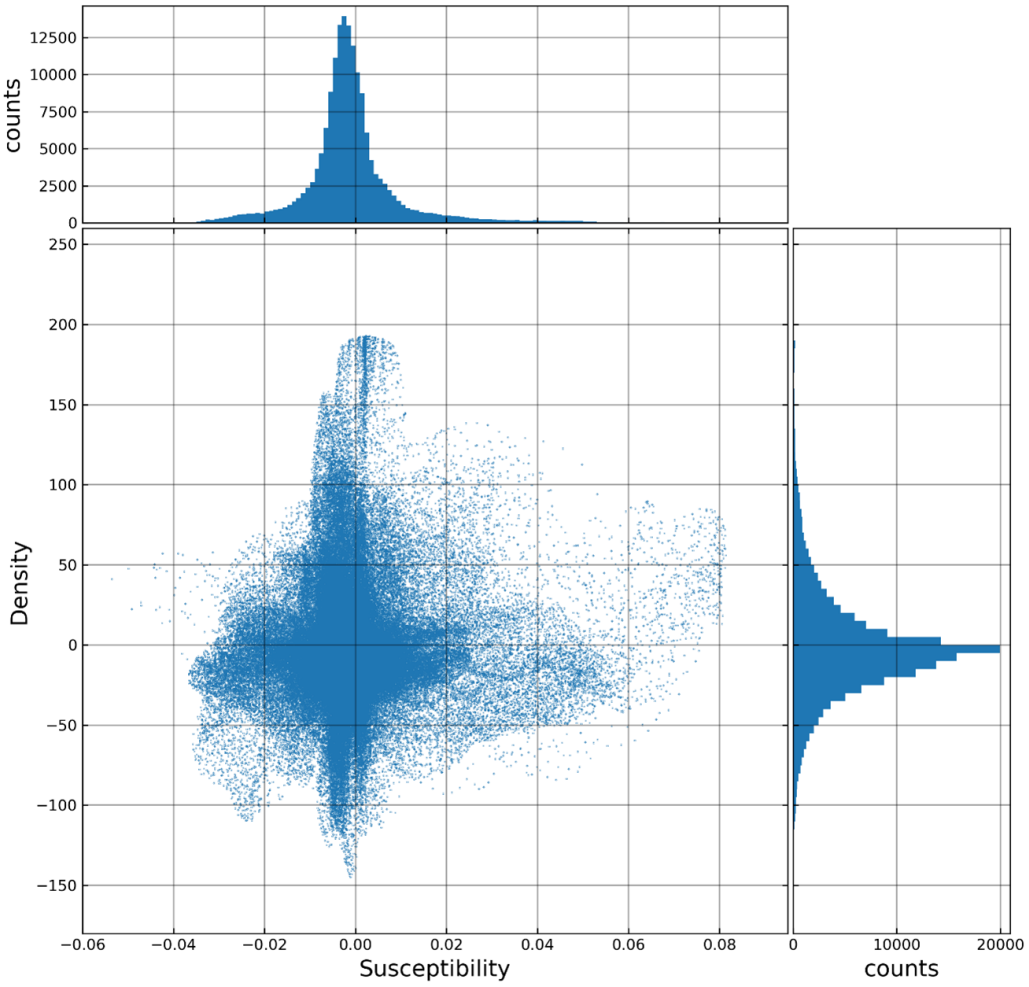

Figure B.11: Inverted density and susceptibilty cross plot and density and susceptibility histogram of the gravity and magnetic individual inversion models.

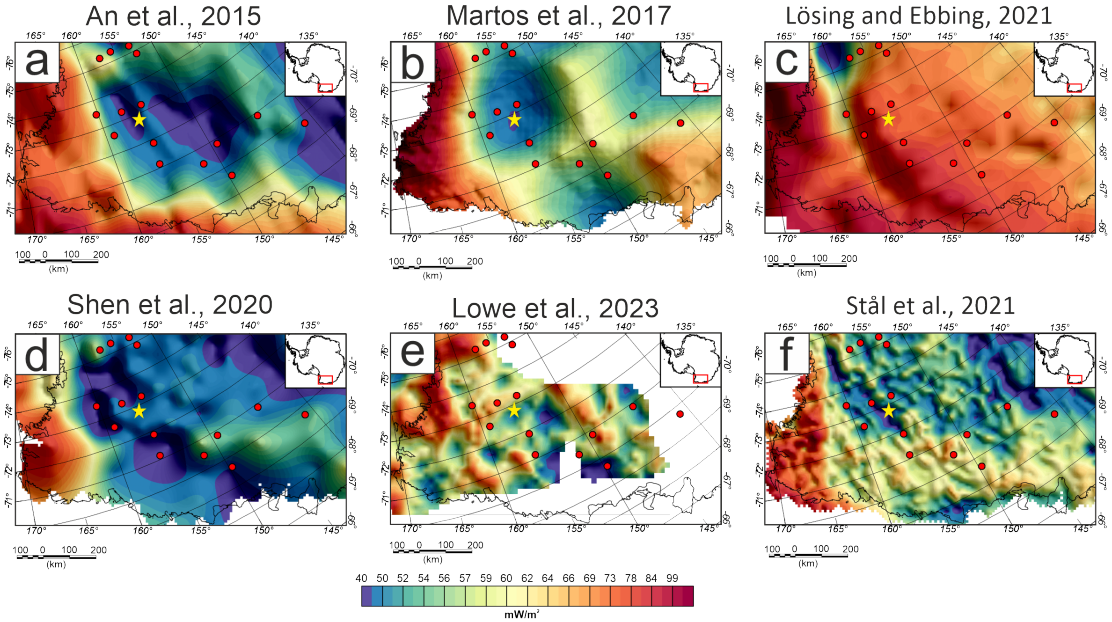

Figure B.12: Location of $Cook_{PE2}$ subglacial lake given as yellow star. Location of all other subglacial lakes from Livingstone et al. (2022) are given as red dots. All lakes are superimposed on recent GHF models. a) (An et al., 2015). b) (Martos et al., 2017). c) (Lösing and Ebbing, 2021). d) (Shen et al., 2020). e) (Lowe et al., 2023). f) (Stål et al., 2021).

Appendix C

Supplementary information for Chapter 4

This appendix chapter provides information of the inversion mesh setup. It also provides information on the boundary condition data used for the local inversion in the Mesa Range as well as alternative inversion runs with varing regularisation values

C.1 Inversion mesh set up

The local inversion mesh set up increases vertically with increasing depth by a constant factor of 1.1 for each layer of cells. Furthermore, the horizontal cell size is incrementally increased outside the study area. The upper model boundary is constraint by the bedrock topography from Morlighem et al. (2020). The bottom of the model is constraint by CPD from Lowe et al. (2023).

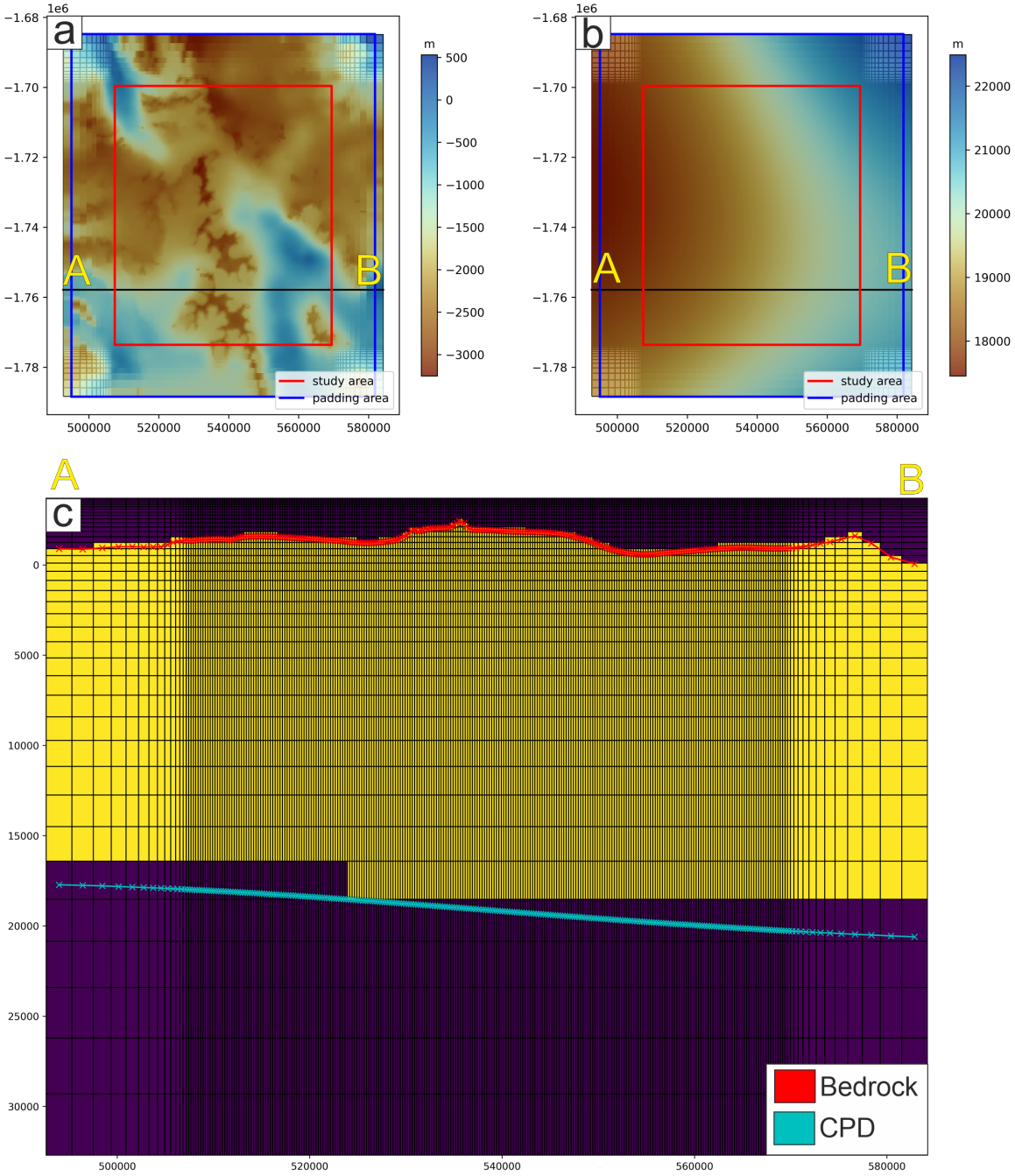

Figure C.1: Local inversion model setup in the Mesa Range region. a) Bedrock topography from BedMachine (Morlighem et al., 2020). b) Curie Point Depths (CPD) from (Lowe et al., 2023). c) cross plot through inversion model set up. Cells between bedrock and CPD are allowed to vary during the inversion, marked as yellow cells. Purple coloured cells represent air and cells below the CPD, which are not allowed to vary during the inversion. Cells increase vertically with depth and horizontal within the padding area.

C.2 Inversion runs with varing regularisation values

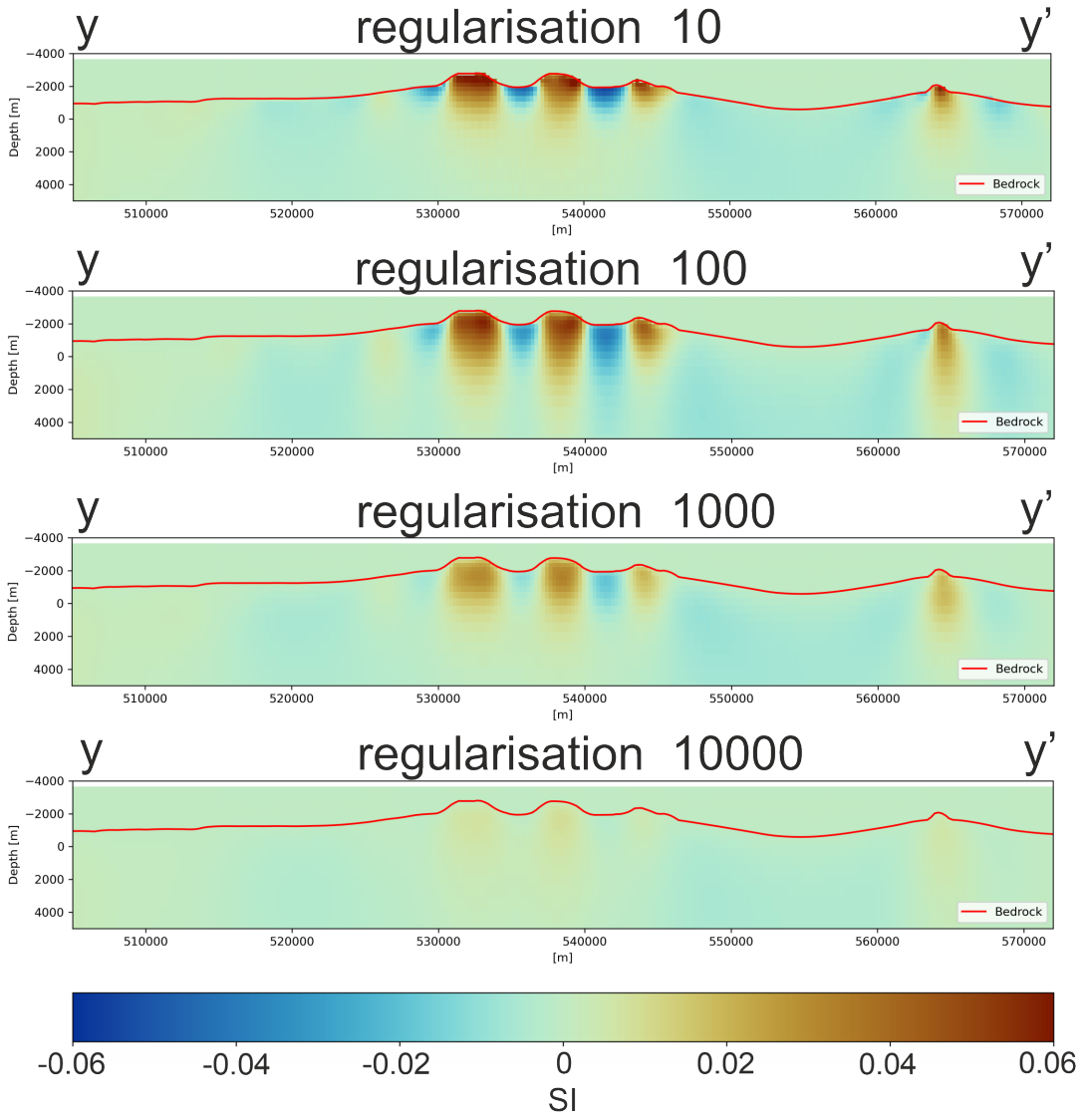

Figure C.2: Inverted susceptibility distribution based on different inversion runs with varying regularisation parameters. Profile location given in Figure C.4. Regularisation values influences any inversion. In this study (chapter 4) we have chosen a very low regularisation value of 10. With increasing regularisation parameter, the misfit between observed and inverted field increases. The inversion, with a regularisation value of 100 produces a susceptibility distribution, which is in the same susceptibility range as the inversion with a regularisation of 10. However, this inversion recovers deeper structures, which are inconsistent with geological information and the standard deviation is slightly larger. Regularisation parameter values above 1000 do not reproduce the amplitude of the observed magnetic field anymore.

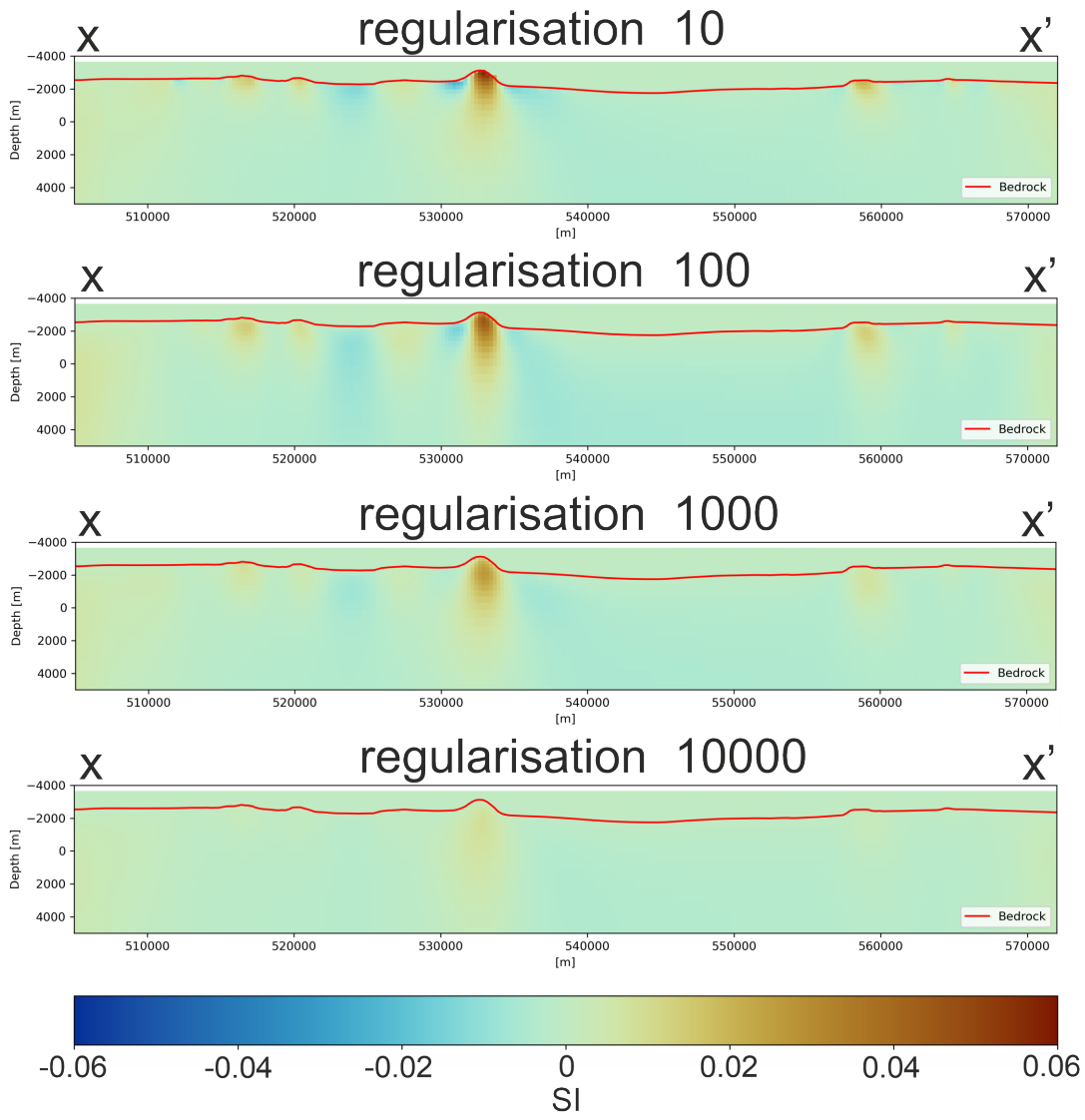

Figure C.3: Inverted susceptibility distribution based on different inversion runs with varying regularisation parameters. Profile location given in Figure C.4. Regularisation values influences any inversion. In this study (chapter 4) we have chosen a very low regularisation value of 10. With increasing regularisation parameter, the misfit between observed and inverted field increases. The inversion, with a regularisation value of 100 produces a susceptibility distribution, which is in the same susceptibility range as the inversion with a regularisation of 10. However, this inversion recovers deeper structures, which are inconsistent with geological information and the standard deviation is slightly larger. Regularisation parameter values above 1000 do not reproduce the amplitude of the observed magnetic field anymore.

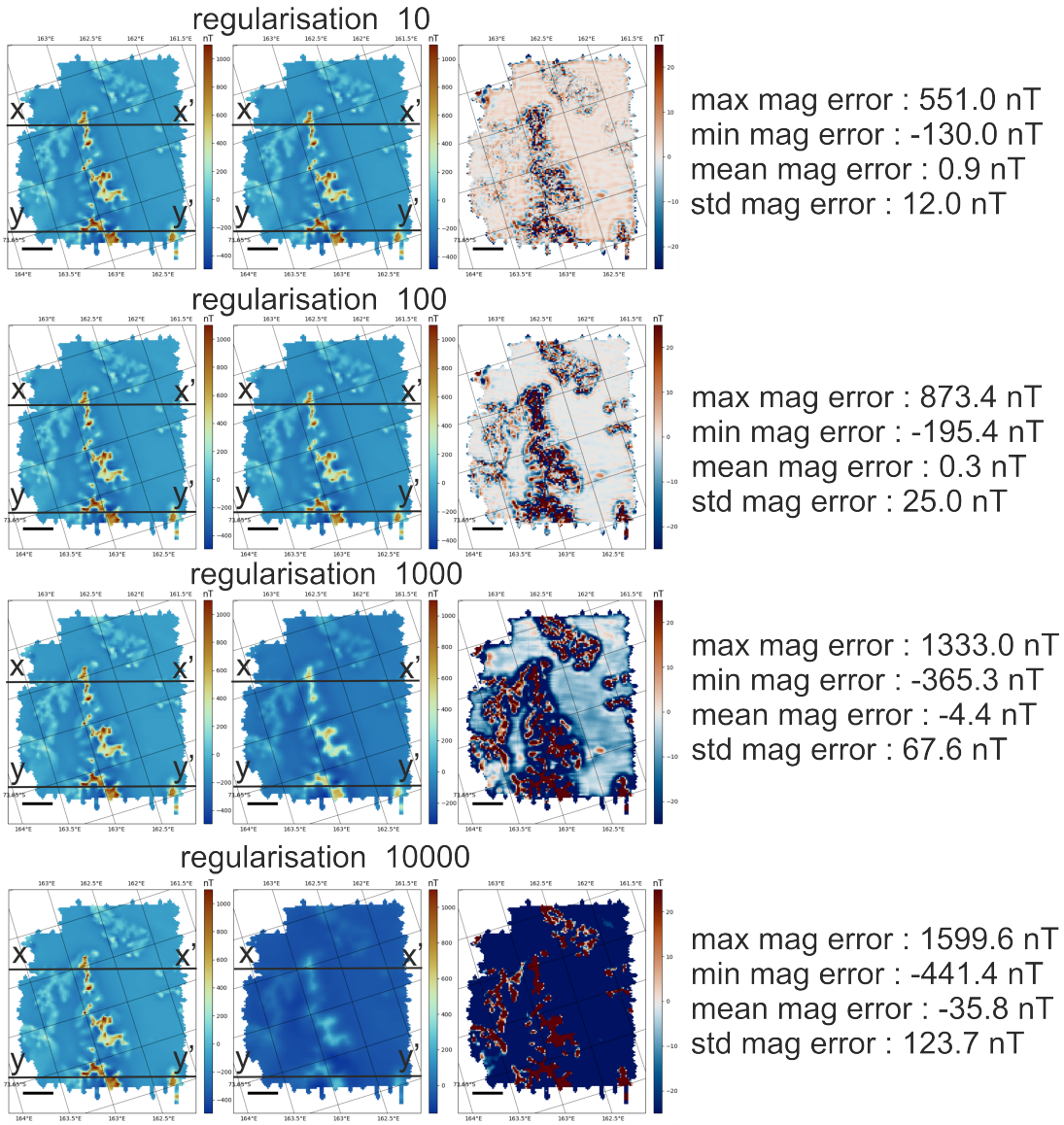

Figure C.4: Comparison of observed magnetic data (left panel) to the inverted magnetic field (middle panel). Difference between both fields is given on the right panel. Left and middle panel provide location of the profiles shown in Figure C.2 and C.3

Bibliography

Agostinetti, N. P., Amato, A., Cattaneo, M., and Di Bona, M. (2004). Crustal structure of Northern Victoria Land from receiver function analysis. *Terra Antarctica*, 11(1):5–14.

Aitken, A. R. A., Li, L., Kulessa, B., Schroeder, D., Jordan, T. A., Whittaker, J. M., Anandakrishnan, S., Dawson, E. J., Wiens, D. A., Eisen, O., and Siegert, M. J. (2023). Antarctic sedimentary basins and their influence on ice-sheet dynamics. *Reviews of Geophysics*, 61(3):e2021RG000767.

Aitken, A. R. A., Young, D. A., Ferraccioli, F., Betts, P. G., Greenbaum, J. S., Richter, T. G., Roberts, J. L., Blankenship, D. D., and Siegert, M. J. (2014). The subglacial geology of Wilkes Land, East Antarctica. *Geophysical Research Letters*, 41(7):2390–2400.

An, M., Wiens, D. A., Zhao, Y., Feng, M., Nyblade, A., Kanao, M., Li, Y., Maggi, A., and Lévêque, J.-J. (2015). Temperature, lithosphere-asthenosphere boundary, and heat flux beneath the Antarctic Plate inferred from seismic velocities. *Journal of Geophysical Research: Solid Earth*, 120(12):8720–8742.

Artemieva, I. M. and Mooney, W. D. (2001). Thermal thickness and evolution of Precambrian lithosphere: A global study. *Journal of Geophysical Research: Solid Earth*, 106(B8):16387–16414.

Artemieva, I. M., Thybo, H., Jakobsen, K., Sørensen, N. K., and Nielsen, L. S. (2017). Heat production in granitic rocks: Global analysis based on a new data compilation granite2017. *Earth-Science Reviews*, 172:1–26.

Audet, P. and Gosselin, J. M. (2019). Curie depth estimation from magnetic anomaly data: a re-assessment using multitaper spectral analysis and Bayesian inference. *Geophysical Journal International*, 218(1):494–507.

Avdeev, D. and Avdeeva, A. (2009). 3D magnetotelluric inversion using a limited-memory quasi-Newton optimization. *Geophysics*, 74(3):F45–F57.

Bansal, A. and Dimri, V. (2005). Depth determination from a non-stationary magnetic profile for scaling geology. *Geophysical Prospecting*, 53(3):399–410.

Bansal, A. R., Gabriel, G., Dimri, V. P., and Krawczyk, C. M. (2011). Estimation of depth to the bottom of magnetic sources by a modified centroid method for fractal distribution of sources: An application to aeromagnetic data in Germany. *Geophysics*, 76(3):L11–L22.

Baranov, A., Tenzer, R., and Morelli, A. (2021). Updated Antarctic crustal model. *Gondwana Research*, 89:1–18.

Barlow, M. (2004). Density and Susceptibility Characterization of Major Rock Units and Rock Types of Mount Isa Inlier i1 i2 projects pmdCRC Internal Report. eCatId: 67942. Commonwealth of Australia (Geoscience Australia).

Barrett, P. J. and Froggatt, P. C. (1978). Densities, porosities, and seismic velocities of some rocks from Victoria Land, Antarctica. *New Zealand Journal of Geology and Geophysics*, 21(2):175–187.

Beamish, D. and Busby, J. (2016). The Cornubian geothermal province: heat production and flow in SW England: estimates from boreholes and airborne gamma-ray measurements. *Geothermal Energy*, 4:1–25.

Beardsmore, G. R. and Cull, J. P. (2001). *Crustal heat flow: a guide to measurement and modelling*. Cambridge university press.

Bell, R. E. (2008). The role of subglacial water in ice-sheet mass balance. *Nature Geoscience*, 1(5):297–304.

Bhattacharyya, B. K. and Leu, L. (1975a). Spectral analysis of gravity and magnetic anomalies due to two-dimensional structures. *Geophysics*, 40(6):993–1013.

Bhattacharyya, B. K. and Leu, L.-K. (1975b). Analysis of magnetic anomalies over Yellowstone National Park: Mapping of Curie point isothermal surface for geothermal reconnaissance. *Journal of Geophysical Research (1896-1977)*, 80(32):4461–4465.

Bialas, R. W., Buck, W. R., Studinger, M., and Fitzgerald, P. G. (2007). Plateau collapse model for the Transantarctic Mountains–West Antarctic Rift System: Insights from numerical experiments. *Geology*, 35(8):687–690.

Bingham, R. G., Ferraccioli, F., King, E. C., Larter, R. D., Pritchard, H. D., Smith, A. M., and Vaughan, D. G. (2012). Inland thinning of West Antarctic Ice Sheet steered along subglacial rifts. *Nature*, 487(7408):468–471.

Blakely, R. J. (1988). Curie temperature isotherm analysis and tectonic implications of aeromagnetic data from Nevada. *Journal of Geophysical Research: Solid Earth*, 93(B10):11817–11832.

Blakely, R. J. (1996). *Potential theory in gravity and magnetic applications*. Cambridge university press.

Block, A. E., Bell, R. E., and Studinger, M. (2009). Antarctic crustal thickness from satellite gravity: Implications for the Transantarctic and Gamburtsev Subglacial Mountains. *Earth and Planetary Science Letters*, 288(1):194–203.

Bosch, M., Meza, R., Jiménez, R., and Hönig, A. (2006). Joint gravity and magnetic inversion in 3D using Monte Carlo methods. *Geophysics*, 71(4):G153–G156.

Bouligand, C., Glen, J. M. G., and Blakely, R. J. (2009). Mapping curie temperature depth in the western united states with a fractal model for crustal magnetization. *Journal of Geophysical Research: Solid Earth*, 114(B11):e2009JB006494.

Bouman, J., Ebbing, J., Fuchs, M., Sebera, J., Lieb, V., Szwillus, W., Haagmans, R., and Novak, P. (2016). Satellite gravity gradient grids for geophysics. *Scientific reports*, 6(1):21050.

Bozzo, E., Caneva, G., Capponi, G., and Colla, A. (1995). Magnetic investigations of the junction between Wilson and Bowers terranes (northern Victoria Land, Antarctica). *Antarctic Science*, 7(2):149–157.

Bozzo, E., Colla, A., and Meloni, A. (1992). Ground magnetics in North Victoria Land (East Antarctica). *Recent Progress in Antarctic Earth Sciences, TERRAPUB, Tokyo*, pages 563–569.

Brenn, G. R., Hansen, S. E., and Park, Y. (2017). Variable thermal loading and flexural uplift along the Transantarctic Mountains, Antarctica. *Geology*, 45(5):463–466.

Burton-Johnson, A., Dziadek, R., and Martin, C. (2020). Review article: Geothermal heat flow in Antarctica: current and future directions. *The Cryosphere*, 14(11):3843–3873.

Carson, C. J., McLaren, S., Roberts, J. L., Boger, S. D., and Blankenship, D. D. (2014). Hot rocks in a cold place: high sub-glacial heat flow in East Antarctica. *Journal of the Geological Society*, 171(1):9–12.

Chaput, J., Aster, R. C., Huerta, A., Sun, X., Lloyd, A., Wiens, D., Nyblade, A., Anandakrishnan, S., Winberry, J. P., and Wilson, T. (2014). The crustal thickness of West Antarctica. *Journal of Geophysical Research: Solid Earth*, 119(1):378–395.

Clauser, C. and Huenges, E. (1995). *Thermal Conductivity of Rocks and Minerals*, pages 105–126. American Geophysical Union (AGU).

Connard, G., Couch, R., and Gemperle, M. (1983). Analysis of aeromagnetic measurements from the Cascade Range in central Oregon. *Geophysics*, 48(3):376–390.

Cook, C. P., Hemming, S. R., van de Flierdt, T., Pierce Davis, E. L., Williams, T., Galindo, A. L., Jiménez-Espejo, F. J., and Escutia, C. (2017). Glacial erosion of East Antarctica in the Pliocene: A comparative study of multiple marine sediment provenance tracers. *Chemical Geology*, 466:199–218.

Cooper, A. F., Maas, R., Scott, J. M., and Barber, A. J. (2011). Dating of volcanism and sedimentation in the Skelton Group, Transantarctic Mountains: Implications for the Rodinia-Gondwana transition in southern Victoria Land, Antarctica. *GSA Bulletin*, 123(3-4):681–702.

Cordell, L. (1985). Techniques, applications, and problems of analytical continuation of New Mexico aeromagnetic data between arbitrary surfaces of very high relief. *Institute de Geophysique Université de Lausanne Bulletin*, 7:96–101.

Cox, S. C., Smith Lyttle, B., Elkind, S., Smith Siddoway, C., Morin, P., Capponi, G., Abu-Alam, T., Ballinger, M., Bamber, L., Kitchener, B., et al. (2023). A continent-wide detailed geological map dataset of Antarctica. *Scientific Data*, 10(1):250.

Damaske, D., Schreckenberger, B., and Goldmann, F. (2014). A high resolution aeromagnetic survey over the Mesa Range, northern Victoria Land, Antarctica. *Polarforschung*, 84(1):1–13.

Davies, J. H. (2013). Global map of solid Earth surface heat flow. *Geochemistry, Geophysics, Geosystems*, 14(10):4608–4622.

DeConto, R. M. and Pollard, D. (2016). Contribution of Antarctica to past and future sea-level rise. *Nature*, 531(7596):591–597.

Direen, N. G. and Crawford, A. J. (2003). Fossil seaward-dipping reflector sequences preserved in southeastern Australia: a 600 Ma volcanic passive margin in eastern Gondwanaland. *Journal of the Geological Society*, 160(6):985–990.

Drewry, D. J. (1976). Sedimentary basins of the East Antarctic craton from geophysical evidence. *Tectonophysics*, 36(1):301–314. Sedimentary basins of continental margins and cratons.

Ducea, M. (2001). The California arc: Thick granitic batholiths, eclogitic residues, lithospheric-scale thrusting, and magmatic flare-ups. *GSA today*, 11(11):4.

Dziadek, R., Ferraccioli, F., and Gohl, K. (2021). High geothermal heat flow beneath Thwaites Glacier in West Antarctica inferred from aeromagnetic data. *Communications Earth & Environment*, 2(1):162.

Ebbing, J., Dilixiati, Y., Haas, P., Ferraccioli, F., and Scheiber-Enslin, S. (2021). East Antarctica magnetically linked to its ancient neighbours in Gondwana. *Scientific reports*, 11(1):5513.

Ebbing, J., Gernigon, L., Pascal, C., Olesen, O., and Osmundsen, P. T. (2009). A discussion of structural and thermal control of magnetic anomalies on the mid-Norwegian margin. *Geophysical Prospecting*, 57(4):665–681.

Eisen, O., Hofstede, C., Diez, A., Kristoffersen, Y., Lambrecht, A., Mayer, C., Blenkner, R., and Hilmarsson, S. (2015). On-ice vibroseis and snowstreamer systems for geoscientific research. *Polar Science*, 9(1):51–65. Recent Advance in Polar Seismology: Global Impact of the International Polar Year.

Elliot, D. and Fleming, T. (2008). Physical volcanology and geological relationships of the Jurassic Ferrar Large Igneous Province, Antarctica. *Journal of Volcanology and Geothermal Research*, 172(1):20–37. Physical Volcanology of Large Igneous Provinces.

Elliot, D. H. and Fleming, T. H. (2018). The Ferrar Large Igneous Province: field and geochemical constraints on supra-crustal (high-level) emplacement of the magmatic system. In *Large Igneous Provinces from Gondwana and Adjacent Regions*. Geological Society of London.

Elliot, D. H., White, J. D. L., and Fleming, T. H. (2021). Chapter 2.1a Ferrar Large Igneous Province: volcanology. *Geological Society, London, Memoirs*, 55(1):75–91.

Estrada, S., Läufer, A., Eckelmann, K., Hofmann, M., Gärtner, A., and Linnemann, U. (2016). Continuous Neoproterozoic to Ordovician sedimentation at the East Gondwana margin — Implications from detrital zircons of the Ross Orogen in northern Victoria Land, Antarctica. *Gondwana Research*, 37:426–448.

Fahnestock, M., Abdalati, W., Joughin, I., Brozena, J., and Gogineni, P. (2001). High Geothermal Heat Flow, Basal Melt, and the Origin of Rapid Ice Flow in Central Greenland. *Science*, 294(5550):2338–2342.

Ferraccioli, F., Armadillo, E., Jordan, T., Bozzo, E., and Corr, H. (2009a). Aeromagnetic exploration over the East Antarctic Ice Sheet: A new view of the Wilkes Subglacial Basin. *Tectonophysics*, 478(1):62–77. Magnetic Anomalies.

Ferraccioli, F., Armadillo, E., Zunino, A., Bozzo, E., Rocchi, S., and Armienti, P. (2009b). Magmatic and tectonic patterns over the Northern Victoria Land sector of the Transantarctic Mountains from new aeromagnetic imaging. *Tectonophysics*, 478(1):43–61. Magnetic Anomalies.

Ferraccioli, F. and Bozzo, E. (2003). Cenozoic strike-slip faulting from the eastern margin of the Wilkes Subglacial Basin to the western margin of the Ross Sea Rift: an aeromagnetic connection. *Geological Society, London, Special Publications*, 210(1):109–133.

Ferraccioli, F., Coren, F., Bozzo, E., Zanolla, C., Gandolfi, S., Tabacco, I., and Frezzotti, M. (2001). Rifted(?) crust at the East Antarctic Craton margin: gravity and magnetic interpretation along a traverse across the Wilkes Subglacial Basin region. *Earth and Planetary Science Letters*, 192(3):407–421.

Ferraccioli, F., Finn, C. A., Jordan, T. A., Bell, R. E., Anderson, L. M., and Damaske, D. (2011). East Antarctic rifting triggers uplift of the Gamburtsev Mountains. *Nature*, 479(7373):388–392.

Ferré, E. C., Friedman, S. A., Martín-Hernández, F., Feinberg, J. M., Till, J. L., Ionov, D. A., and Conder, J. A. (2014). Eight good reasons why the uppermost mantle could be magnetic. *Tectonophysics*, 624-625:3–14. Crustal and mantle sources of magnetic anomalies.

Finn, C., Moore, D., Damaske, D., and Mackey, T. (1999). Aeromagnetic legacy of early Paleozoic subduction along the Pacific margin of Gondwana. *Geology*, 27(12):1087–1090.

Finn, C. A., Goodge, J. W., Damaske, D., and Fanning, C. M. (2006). *Scouting Craton's Edge in Paleo-Pacific Gondwana*, pages 165–173. Springer Berlin Heidelberg, Berlin, Heidelberg.

Finotello, M., Nyblade, A., Julia, J., Wiens, D., and Anandakrishnan, S. (2011). Crustal Vp-Vs ratios and thickness for Ross Island and the Transantarctic Mountain front, Antarctica. *Geophysical Journal International*, 185(1):85–92.

Fisher, A. T., Mankoff, K. D., Tulaczyk, S. M., Tyler, S. W., Foley, N., , and the WISSARD Science Team (2015). High geothermal heat flux measured below the West Antarctic Ice Sheet. *Science Advances*, 1(6):e1500093.

Fleming, T. H., Elliot, D. H., Foland, K. A., Jones, L. M., and Bowman, J. R. (1993). Disturbance of Rb-Sr and K-Ar isotopic systems in the Kirkpatrick Basalt, north Victoria Land, Antarctica: implications for middle Cretaceous tectonism. *Gondwana Eight: assembly, evolution and dispersal. Balkema, Hobart*, pages 411–424.

Fox Maule, C., Purucker, M. E., Olsen, N., and Mosegaard, K. (2005). Heat Flux Anomalies in Antarctica Revealed by Satellite Magnetic Data. *Science*, 309(5733):464–467.

Franz, G., Moorkamp, M., Jegen, M., Berndt, C., and Rabbel, W. (2021). Comparison of Different Coupling Methods for Joint Inversion of Geophysical Data: A Case Study for the Namibian Continental Margin. *Journal of Geophysical Research: Solid Earth*, 126(12):e2021JB022092. e2021JB022092 2021JB022092.

Frederick, B. C., Young, D. A., Blankenship, D. D., Richter, T. G., Kempf, S. D., Ferraccioli, F., and Siegert, M. J. (2016). Distribution of subglacial sediments across the Wilkes Subglacial Basin, East Antarctica. *Journal of Geophysical Research: Earth Surface*, 121(4):790–813.

Fregoso, E. and Gallardo, L. A. (2009). Cross-gradients joint 3D inversion with applications to gravity and magnetic data. *GEOPHYSICS*, 74(4):L31–L42.

Fretwell, P., Pritchard, H. D., Vaughan, D. G., Bamber, J. L., Barrand, N. E., Bell, R., Bianchi, C., Bingham, R. G., Blankenship, D. D., Casassa, G., Catania, G., Callens, D., Conway, H., Cook, A. J., Corr, H. F. J., Damaske, D., Damm, V., Ferraccioli, F., Forsberg, R., Fujita, S., Gim, Y., Gogineni, P., Griggs, J. A., Hindmarsh, R. C. A., Holmlund, P., Holt, J. W., Jacobel, R. W., Jenkins, A., Jokat, W., Jordan, T., King, E. C., Kohler, J., Krabill, W., Riger-Kusk, M., Langley, K. A., Leitchenkov, G., Leuschen, C., Luyendyk, B. P., Matsuoka, K., Mouginot, J., Nitsche, F. O., Nogi, Y., Nost, O. A., Popov, S. V., Rignot, E., Rippin, D. M., Rivera, A., Roberts, J., Ross, N., Siegert, M. J., Smith, A. M., Steinhage, D., Studinger, M., Sun, B., Tinto, B. K., Welch, B. C., Wilson, D., Young, D. A., Xiangbin, C., and Zirizzotti, A. (2013). Bedmap2: improved ice bed, surface and thickness datasets for Antarctica. *The Cryosphere*, 7(1):375–393.

Frey, M. and Ebbing, J. (2020). The deep geothermal potential of the radiogenic Løvstakken Granite in western Norway. *Norwegian Journal of Geology*, 100(1).

Gallardo-Delgado, L. A., Pérez-Flores, M. A., and Gómez-Treviño, E. (2003). A versatile algorithm for joint 3D inversion of gravity and magnetic data. *Geophysics*, 68(3):949–959.

Gambino, S., Armienti, P., Cannata, A., Carlo, P. D., Giudice, G., Giuffrida, G., Liuzzo, M., and Pompilio, M. (2021). Chapter 7.3 Mount Melbourne and Mount Rittmann. *Geological Society, London, Memoirs*, 55(1):741–758.

Ganovex Team and others (1987). Geological map of North Victoria land, Antarctica, 1: 500,000—explanatory notes. *Geologisches Jahrbuch B*, 66:7–79.

Ghirotto, A., Armadillo, E., Crispini, L., Zunino, A., Tontini, F. C., and Ferraccioli, F. (2023). The Sub-Ice Structure of Mt. Melbourne Volcanic Field (Northern Victoria Land, Antarctica) Uncovered by High-Resolution Aeromagnetic Data. *Journal of Geophysical Research: Solid Earth*, 128(7):e2022JB025687.

Gianni, G. M. and Luján, S. P. (2021). Geodynamic controls on magmatic arc migration and quiescence. *Earth-Science Reviews*, 218:103676.

Gibson, G. M., Champion, D. C., and Ireland, T. R. (2015). Preservation of a fragmented late Neoproterozoic–earliest Cambrian hyper-extended continental-margin sequence in the Australian Delamerian Orogen. *Geological Society, London, Special Publications*, 413(1):269–299.

Giordano, G., Lucci, F., Phillips, D., Cozzupoli, D., and Runci, V. (2012). Stratigraphy, geochronology and evolution of the Mt. Melbourne volcanic field (North Victoria Land, Antarctica). *Bulletin of Volcanology*, 74:1985–2005.

Goes, S., Hasterok, D., Schutt, D. L., and Klöcking, M. (2020). Continental lithospheric temperatures: A review. *Physics of the Earth and Planetary Interiors*, 306:106509.

Golynsky, A. V., Ferraccioli, F., Hong, J. K., Golynsky, D. A., von Frese, R. R. B., Young, D. A., Blankenship, D. D., Holt, J. W., Ivanov, S. V., Kiselev, A. V., Masolov, V. N., Eagles, G., Gohl, K., Jokat, W., Damaske, D., Finn, C., Aitken, A., Bell, R. E., Armadillo, E., Jordan, T. A., Greenbaum, J. S., Bozzo, E., Caneva, G., Forsberg, R., Ghidella, M., Galindo-Zaldivar, J., Bohoyo, F., Martos, Y. M., Nogi, Y., Quartini, E., Kim, H. R., and Roberts, J. L. (2018). New Magnetic Anomaly Map of the Antarctic. *Geophysical Research Letters*, 45(13):6437–6449.

Goodge, J. W. (2020). Geological and tectonic evolution of the Transantarctic Mountains, from ancient craton to recent enigma. *Gondwana Research*, 80:50–122.

Goodge, J. W. and Fanning, C. M. (2010). Composition and age of the East Antarctic Shield in eastern Wilkes Land determined by proxy from Oligocene-Pleistocene glaciomarine sediment and Beacon Supergroup sandstones, Antarctica. *GSA Bulletin*, 122(7-8):1135–1159.

Goodge, J. W., Fanning, C. M., Fisher, C. M., and Vervoort, J. D. (2024). Crustal Architecture of the Paleo-Pacific Rift Margin of East Antarctica: Evidence From U-Pb Ages and O-Hf Isotope Compositions of Ross Orogen Granitoids. *Geochemistry, Geophysics, Geosystems*, 25(4):e2024GC011435. e2024GC011435 2024GC011435.

Goodge, J. W., Fanning, C. M., Norman, M. D., and Bennett, V. C. (2012). Temporal, Isotopic and Spatial Relations of Early Paleozoic Gondwana-Margin Arc Magmatism, Central Transantarctic Mountains, Antarctica. *Journal of Petrology*, 53(10):2027–2065.

Goodge, J. W. and Finn, C. A. (2010). Glimpses of East Antarctica: Aeromagnetic and satellite magnetic view from the central Transantarctic Mountains of East Antarctica. *Journal of Geophysical Research: Solid Earth*, 115(B9).

Goodge, J. W., Myrow, P., Williams, I. S., and Bowring, S. A. (2002). Age and Provenance of the Beardmore Group, Antarctica: Constraints on Rodinia Supercontinent Breakup. *The Journal of Geology*, 110(4):393–406.

Graw, J. H., Adams, A. N., Hansen, S. E., Wiens, D. A., Hackworth, L., and Park, Y. (2016). Upper mantle shear wave velocity structure beneath northern Victoria Land, Antarctica: Volcanism and uplift in the northern Transantarctic Mountains. *Earth and Planetary Science Letters*, 449:48–60.

Guillen, A. and Menichetti, V. (1984). Gravity and magnetic inversion with minimization of a specific functional. *Geophysics*, 49(8):1354–1360.

Haber, E. and Holtzman Gazit, M. (2013). Model fusion and joint inversion. *Surveys in Geophysics*, 34:675–695.

Haeger, C., Kaban, M. K., Tesauro, M., Petrunin, A. G., and Mooney, W. D. (2019). 3-D Density, Thermal, and Compositional Model of the Antarctic Lithosphere and Implications for Its Evolution. *Geochemistry, Geophysics, Geosystems*, 20(2):688–707.

Haeger, C., Petrunin, A. G., and Kaban, M. K. (2022). Geothermal Heat Flow and Thermal Structure of the Antarctic Lithosphere. *Geochemistry, Geophysics, Geosystems*, 23(10):e2022GC010501.

Haggerty, S. E. (1978). Mineralogical contraints on Curie isotherms in deep crustal magnetic anomalies. *Geophysical Research Letters*, 5(2):105–108.

Hansen, S. E., Julià, J., Nyblade, A. A., Pyle, M. L., Wiens, D. A., and Anandakrishnan, S. (2009). Using S wave receiver functions to estimate crustal structure beneath ice sheets: An application to the Transantarctic Mountains and East Antarctic craton. *Geochemistry, Geophysics, Geosystems*, 10(8).

Hansen, S. E., Kenyon, L. M., Graw, J. H., Park, Y., and Nyblade, A. A. (2016). Crustal structure beneath the Northern Transantarctic Mountains and Wilkes Subglacial Basin: Implications for tectonic origins. *Journal of Geophysical Research: Solid Earth*, 121(2):812–825.

Hasterok, D. and Chapman, D. (2011). Heat production and geotherms for the continental lithosphere. *Earth and Planetary Science Letters*, 307(1):59–70.

Hasterok, D., Gard, M., and Webb, J. (2018). On the radiogenic heat production of metamorphic, igneous, and sedimentary rocks. *Geoscience Frontiers*, 9(6):1777–1794. Reliability Analysis of Geotechnical Infrastructures.

Huerta, A. D. (2007). Lithospheric structure across the Transantarctic Mountains constrained by an analysis of gravity and thermal structure. *Antarctica: A Keystone in a Changing World–Online Proceedings of the 10th ISAES*, 1047.

Hussein, M., Mickus, K., and Serpa, L. F. (2013). Curie point depth estimates from aeromagnetic data from Death Valley and surrounding regions, California. *Pure and Applied Geophysics*, 170:617–632.

Idárraga-García, J. and Vargas, C. A. (2018). Depth to the bottom of magnetic layer in South America and its relationship to Curie isotherm, Moho depth and seismicity behavior. *Geodesy and Geodynamics*, 9(1):93–107. Seismological advances in Latin America.

Jennings, S., Hasterok, D., and Payne, J. (2019). A new compositionally based thermal conductivity model for plutonic rocks. *Geophysical Journal International*, 219(2):1377–1394.

Johnson, A. C. (1999). Interpretation of new aeromagnetic anomaly data from the central Antarctic Peninsula. *Journal of Geophysical Research: Solid Earth*, 104(B3):5031–5046.

Jordan, T., Ferraccioli, F., Armadillo, E., and Bozzo, E. (2013). Crustal architecture of the Wilkes Subglacial Basin in East Antarctica, as revealed from airborne gravity data. *Tectonophysics*, 585:196–206. Recent advances in Antarctic geomagnetism and lithosphere studies.

Jordan, T., Ferraccioli, F., and Forsberg, R. (2022). An embayment in the East Antarctic basement constrains the shape of the Rodinian continental margin. *Communications Earth & Environment*, 3(1):52.

Jordan, T., Martin, C., Ferraccioli, F., Matsuoka, K., Corr, H., Forsberg, R., Olesen, A., and Siegert, M. (2018). Anomalously high geothermal flux near the South Pole. *Scientific reports*, 8(1):16785.

Jordan, T. and Robinson, C. (2024). Demonstrating a large UAV for Antarctic environmental science. Technical report, Copernicus Meetings.

Jordan, T. A., Thompson, S., Kulessa, B., and Ferraccioli, F. (2023). Geological sketch map and implications for ice flow of Thwaites Glacier, West Antarctica, from integrated aerogeophysical observations. *Science Advances*, 9(22):eadf2639.

Kumar, R., Bansal, A. R., Betts, P. G., and Ravat, D. (2021). Re-assessment of the depth to the base of magnetic sources (DBMS) in Australia from aeromagnetic data using the defractal method. *Geophysical Journal International*, 225(1):530–547.

Kyle, P. (1990). *A. McMurdo Volcanic Group Western Ross Embayment*, pages 18–145. American Geophysical Union (AGU).

Kyle, P. and Cole, J. (1974). Structural control of volcanism in the McMurdo Volcanic Group, Antarctica. *Bulletin volcanologique*, 38:16–25.

Lamarque, G., Bascou, J., Ménot, R.-P., Paquette, J.-L., Couzinié, S., Rolland, Y., and Cottin, J.-Y. (2018). Ediacaran to lower Cambrian basement in eastern George V Land (Antarctica): Evidence from UPb dating of gneiss xenoliths and implications for the South Australia- East Antarctica connection. *Lithos*, 318-319:219–229.

Langel, R. A. and Hinze, W. J. (1998). *The magnetic field of the Earth's lithosphere: The satellite perspective*. Cambridge University Press.

Lanza, R. and Tonarini, S. (1998). Palaeomagnetic and geochronological results from the Cambro-Ordovician Granite Harbour Intrusives inland of Terra Nova Bay (Victoria Land, Antarctica). *Geophysical Journal International*, 135(3):1019–1027.

Larour, E., Morlighem, M., Seroussi, H., Schiermeier, J., and Rignot, E. (2012). Ice flow sensitivity to geothermal heat flux of Pine Island Glacier, Antarctica. *Journal of Geophysical Research: Earth Surface*, 117(F4).

Läufer, A. L., Lisker, F., and Phillips, G. (2011). Late Ross-orogenic deformation of basement rocks in the northern Deep Freeze Range, Victoria Land, Antarctica: the Lichen Hills shear zone. *Polarforschung*, 80(2):60–70.

Lawrence, J. F., Wiens, D. A., Nyblade, A. A., Anandakrishnan, S., Shore, P. J., and Voigt, D. (2006). Crust and upper mantle structure of the Transantarctic Mountains and surrounding regions from receiver functions, surface waves, and gravity: Implications for uplift models. *Geochemistry, Geophysics, Geosystems*, 7(10).

Leat, P. T., Jordan, T. A., Flowerdew, M. J., Riley, T. R., Ferraccioli, F., and Whitehouse, M. J. (2018). Jurassic high heat production granites associated with the Weddell Sea rift system, Antarctica. *Tectonophysics*, 722:249–264.

Leseane, K., Atekwana, E. A., Mickus, K. L., Abdelsalam, M. G., Shemang, E. M., and Atekwana, E. A. (2015). Thermal perturbations beneath the incipient Okavango Rift Zone, northwest Botswana. *Journal of Geophysical Research: Solid Earth*, 120(2):1210–1228.

Li, C.-F., Lu, Y., and Wang, J. (2017). A global reference model of Curie-point depths based on EMAG2. *Scientific reports*, 7(1):45129.

Li, C.-F., Zhou, D., and Wang, J. (2019). On application of fractal magnetization in Curie depth estimation from magnetic anomalies. *Acta Geophysica*, 67:1319–1327.

Li, L. and Aitken, A. R. A. (2024). Crustal Heterogeneity of Antarctica Signals Spatially Variable Radiogenic Heat Production. *Geophysical Research Letters*, 51(2):e2023GL106201.

Li, Y., Lu, Y., and Siegert, M. J. (2020). Radar Sounding Confirms a Hydrologically Active Deep-Water Subglacial Lake in East Antarctica. *Frontiers in Earth Science*, 8.

Livingstone, S. J., Li, Y., Rutishauser, A., Sanderson, R. J., Winter, K., Mikucki, J. A., Björnsson, H., Bowling, J. S., Chu, W., Dow, C. F., et al. (2022). Subglacial lakes and their changing role in a warming climate. *Nature Reviews Earth & Environment*, 3(2):106–124.

Lloyd, A. J., Wiens, D. A., Zhu, H., Tromp, J., Nyblade, A. A., Aster, R. C., Hansen, S. E., Dalziel, I. W. D., Wilson, T., Ivins, E. R., and O'Donnell, J. P. (2020). Seismic Structure of the Antarctic Upper Mantle Imaged with Adjoint Tomography. *Journal of Geophysical Research: Solid Earth*, 125(3).

Llubes, M., Lanseau, C., and Rémy, F. (2006). Relations between basal condition, subglacial hydrological networks and geothermal flux in Antarctica. *Earth and Planetary Science Letters*, 241(3):655–662.

Lowe, M., Jordan, T., Ebbing, J., Koglin, N., Ruppel, A., Moorkamp, M., Läufer, A., Green, C., Liebsch, J., Ginga, M., and Larter, R. (2024). Comparing geophysical inversion and petrophysical measurements for northern Victoria Land, Antarctica. *Geophysical Journal International*, 239(1):276–291.

Lowe, M., Mather, B., Green, C., Jordan, T. A., Ebbing, J., and Larter, R. (2023). Anomalously High Heat Flow Regions Beneath the Transantarctic Mountains and Wilkes Subglacial Basin in East Antarctica Inferred From Curie Depth. *Journal of Geophysical Research: Solid Earth*, 128(1):e2022JB025423.

Lowrie, W. (2007). *Fundamentals of Geophysics*. Cambridge University Press, 2 edition.

Lucazeau, F. (2019). Analysis and Mapping of an Updated Terrestrial Heat Flow Data Set. *Geochemistry, Geophysics, Geosystems*, 20(8):4001–4024.

Lösing, M. and Ebbing, J. (2021). Predicting Geothermal Heat Flow in Antarctica With a Machine Learning Approach. *Journal of Geophysical Research: Solid Earth*, 126(6):e2020JB021499.

Lösing, M., Ebbing, J., and Szwillus, W. (2020). Geothermal Heat Flux in Antarctica: Assessing Models and Observations by Bayesian Inversion. *Frontiers in Earth Science*, 8.

Lösing, M., Moorkamp, M., and Ebbing, J. (2022). Joint inversion based on variation of information—a crustal model of Wilkes Land, East Antarctica. *Geophysical Journal International*, 232(1):162–175.

Mandolesi, E. and Jones, A. G. (2014). Magnetotelluric inversion based on mutual information. *Geophysical Journal International*, 199(1):242–252.

Martos, Y. M., Catalán, M., Jordan, T. A., Golynsky, A., Golynsky, D., Eagles, G., and Vaughan, D. G. (2017). Heat Flux Distribution of Antarctica Unveiled. *Geophysical Research Letters*, 44(22):11,417–11,426.

Martos, Y. M., Jordan, T. A., Catalán, M., Jordan, T. M., Bamber, J. L., and Vaughan, D. G. (2018). Geothermal Heat Flux Reveals the Iceland Hotspot Track Underneath Greenland. *Geophysical Research Letters*, 45(16):8214–8222.

Maslanyj, M. P., Garrett, S. W., Johnson, A., Renner, R., and Smith, A. (1991). Aeromagnetic anomaly map of West Antarctica (Weddell Sea sector).

Mather, B. and Delhaye, R. (2019). PyCurious: A Python module for computing the Curie depth from the magnetic anomaly. *Journal of Open Source Software*, 4(39):1544.

Mather, B. and Fullea, J. (2019). Constraining the geotherm beneath the British Isles from Bayesian inversion of Curie depth: integrated modelling of magnetic, geothermal, and seismic data. *Solid Earth*, 10(3):839–850.

Matsuoka, K., MacGregor, J. A., and Pattyn, F. (2012). Predicting radar attenuation within the Antarctic ice sheet. *Earth and Planetary Science Letters*, 359-360:173–183.

Maus, S. and Dimri, V. (1995). Potential field power spectrum inversion for scaling geology. *Journal of Geophysical Research: Solid Earth*, 100(B7):12605–12616.

Maus, S., Gordon, D., and Fairhead, D. (1997). Curie-temperature depth estimation using a self-similar magnetization model. *Geophysical Journal International*, 129(1):163–168.

Maus, S., Lühr, H., Rother, M., Hemant, K., Balasis, G., Ritter, P., and Stolle, C. (2007). Fifth-generation lithospheric magnetic field model from CHAMP satellite measurements. *Geochemistry, Geophysics, Geosystems*, 8(5).

McCormack, F. S., Roberts, J. L., Dow, C. F., Stål, T., Halpin, J. A., Reading, A. M., and Siegert, M. J. (2022). Fine-Scale Geothermal Heat Flow in Antarctica Can Increase Simulated Subglacial Melt Estimates. *Geophysical Research Letters*, 49(15):e2022GL098539.

McDonough, W. and s. Sun, S. (1995). The composition of the Earth. *Chemical Geology*, 120(3):223–253. Chemical Evolution of the Mantle.

McMillan, M., Corr, H., Shepherd, A., Ridout, A., Laxon, S., and Cullen, R. (2013). Three-dimensional mapping by CryoSat-2 of subglacial lake volume changes. *Geophysical Research Letters*, 40(16):4321–4327.

Mercer, J. H. (1978). West Antarctic ice sheet and CO2 greenhouse effect: a threat of disaster. *Nature*, 271(5643):321–325.

Mieth, M., Jacobs, J., Ruppel, A., Damaske, D., Läufer, A., and Jokat, W. (2014). New detailed aeromagnetic and geological data of eastern Dronning Maud Land: Implications for refining the tectonic and structural framework of Sør Rondane, East Antarctica. *Precambrian Research*, 245:174–185.

Mieth, M. and Jokat, W. (2014). New aeromagnetic view of the geological fabric of southern Dronning Maud Land and Coats Land, East Antarctica. *Gondwana Research*, 25(1):358–367.

Moorkamp, M. (2021). *Joint inversion of gravity and magnetotelluric data from the Ernest-Henry IOCG deposit with a variation of information constraint*, pages 1711–1715.

Moorkamp, M. (2022). Deciphering the State of the Lower Crust and Upper Mantle With Multi-Physics Inversion. *Geophysical Research Letters*, 49(9):e2021GL096336.

Moorkamp, M., Heincke, B., Jegen, M., Roberts, A. W., and Hobbs, R. W. (2011). A framework for 3-D joint inversion of MT, gravity and seismic refraction data. *Geophysical Journal International*, 184(1):477–493.

Morales-Ocaña, C., Bohoyo, F., Escutia, C., Marín-Lechado, C., Rey-Moral, C., Druet, M., Galindo-Zaldívar, J., and Maestro, A. (2023). 3D Geophysical and Geological Modeling of the South Orkney Microcontinent (Antarctica): Tectonic Implications for the Scotia Arc Development. *Tectonics*, 42(4):e2022TC007602.

Morelli, A. and Danesi, S. (2004). Seismological imaging of the Antarctic continental lithosphere: a review. *Global and Planetary Change*, 42(1):155–165. Ice sheets and neotectonics.

Morlighem, M., Rignot, E., Binder, T., Blankenship, D., Drews, R., Eagles, G., Eisen, O., Ferraccioli, F., Forsberg, R., Fretwell, P., et al. (2020). Deep glacial troughs and stabilizing ridges unveiled beneath the margins of the Antarctic ice sheet. *Nature geoscience*, 13(2):132–137.

Murphy, B., Yurchak, R., and Müller, S. (2022). GeoStat-Framework/PyKrige: v1.7.0.

Núñez Demarco, P., Prezzi, C., and Sánchez Bettucci, L. (2020). Review of Curie point depth determination through different spectral methods applied to magnetic data. *Geophysical Journal International*, 224(1):17–39.

Ohneiser, C., Wilson, G., and Cox, S. (2015). Characterisation of magnetic minerals from southern Victoria Land, Antarctica. *New Zealand Journal of Geology and Geophysics*, 58(1):52–65.

Okubo, Y., Graf, R. J., Hansen, R. O., Ogawa, K., and Tsu, H. (1985). Curie point depths of the Island of Kyushu and surrounding areas, Japan. *Geophysics*, 50(3):481–494.

Olsen, N., Ravat, D., Finlay, C. C., and Kother, L. K. (2017). LCS-1: a high-resolution global model of the lithospheric magnetic field derived from CHAMP and Swarm satellite observations. *Geophysical Journal International*, 211(3):1461–1477.

Pappa, F. and Ebbing, J. (2023). Gravity, magnetics and geothermal heat flow of the Antarctic lithospheric crust and mantle. In *The Geochemistry and Geophysics of the Antarctic Mantle*. Geological Society of London.

Pappa, F., Ebbing, J., and Ferraccioli, F. (2019a). Moho Depths of Antarctica: Comparison of Seismic, Gravity, and Isostatic Results. *Geochemistry, Geophysics, Geosystems*, 20(3):1629–1645.

Pappa, F., Ebbing, J., Ferraccioli, F., and van der Wal, W. (2019b). Modeling Satellite Gravity Gradient Data to Derive Density, Temperature, and Viscosity Structure of the Antarctic Lithosphere. *Journal of Geophysical Research: Solid Earth*, 124(11):12053–12076.

Pattyn, F. (2010). Antarctic subglacial conditions inferred from a hybrid ice sheet/ice stream model. *Earth and Planetary Science Letters*, 295(3):451–461.

Pattyn, F., Carter, S. P., and Thoma, M. (2016). Advances in modelling subglacial lakes and their interaction with the Antarctic ice sheet. *Philosophical Transactions of the Royal Society A: Mathematical, Physical and Engineering Sciences*, 374(2059):20140296.

Paulsen, T., Encarnación, J., Grunow, A., Benowitz, J., Layer, P., Deering, C., and Sliwinski, J. (2023). Outboard Onset of Ross Orogen Magmatism and Subsequent Igneous and Metamorphic Cooling Linked to Slab Rollback during Late-Stage Gondwana Assembly. *Geosciences*, 13(4):126.

Paxman, G. J. G., Jamieson, S. S. R., Ferraccioli, F., Bentley, M. J., Ross, N., Armadillo, E., Gasson, E. G. W., Leitchenkov, G., and DeConto, R. M. (2018). Bedrock Erosion Surfaces Record Former East Antarctic Ice Sheet Extent. *Geophysical Research Letters*, 45(9):4114–4123.

Paxman, G. J. G., Jamieson, S. S. R., Ferraccioli, F., Bentley, M. J., Ross, N., Watts, A. B., Leitchenkov, G., Armadillo, E., and Young, D. A. (2019). The Role of Lithospheric Flexure in the Landscape Evolution of the Wilkes Subglacial Basin and Transantarctic Mountains, East Antarctica. *Journal of Geophysical Research: Earth Surface*, 124(3):812–829.

Perinelli, C., Gaeta, M., and Armienti, P. (2017). Cumulate xenoliths from Mt. Overlord, northern Victoria Land, Antarctica: A window into high pressure storage and differentiation of mantle-derived basalts. *Lithos*, 268-271:225–239.

Pertusati, P. C., Ricci, C. A., and Tessensohn, F. (2016). *German-Italian Geological Antarctic Map Programme: The Italian Contribution: a Map Case for 30 Years of the Italian Research Programme in Antarctica (1985-2015).* Terra Antarctica Publication.

Pittard, M. L., Galton-Fenzi, B. K., Roberts, J. L., and Watson, C. S. (2016). Organization of ice flow by localized regions of elevated geothermal heat flux. *Geophysical Research Letters*, 43(7):3342–3350.

Pollack, H. N., Hurter, S. J., and Johnson, J. R. (1993). Heat flow from the Earth's interior: Analysis of the global data set. *Reviews of Geophysics*, 31(3):267–280.

Pollard, D., DeConto, R. M., and Alley, R. B. (2015). Potential Antarctic Ice Sheet retreat driven by hydrofracturing and ice cliff failure. *Earth and Planetary Science Letters*, 412:112–121.

Purucker, M. (2013). Geothermal heat flux data set based on low resolution observations collected by the CHAMP satellite between 2000 and 2010, and produced from the MF-6 model following the technique described in Fox Maule et al.(2005).

Ravat, D., Pignatelli, A., Nicolosi, I., and Chiappini, M. (2007). A study of spectral methods of estimating the depth to the bottom of magnetic sources from near-surface magnetic anomaly data. *Geophysical Journal International*, 169(2):421–434.

Reading, A. M., Stål, T., Halpin, J. A., Lösing, M., Ebbing, J., Shen, W., McCormack, F. S., Siddoway, C. S., and Hasterok, D. (2022). Antarctic geothermal heat flow and its implications for tectonics and ice sheets. *Nature Reviews Earth & Environment*, 3(12):814–831.

Reitmayr, G., Korth, W., Caneva, G., and Ferraccioli, F. (2003). Gravity Survey at the Oates Coast Area, East Antarctica, during the Joint German-Italian Expedition 1999/2000. *TERRA ANTARTICA*, 10:97–104.

Riedel, S., Jokat, W., and Steinhage, D. (2012). Mapping tectonic provinces with airborne gravity and radar data in Dronning Maud Land, East Antarctica. *Geophysical Journal International*, 189(1):414–427.

Robinson, E. S. and Splettstoesser, J. F. (1986). Structure of the Transantarctic Mountains determined from geophysical surveys. *Geology of the central transantarctic mountains*, 36:119–162.

Roland, N. W., Henjes-Kunst, F., Kleinschmidt, G., Olesch, M., Pertusati, P. C., Schüssler, U., and Skinner, D. N. B. (2002). Geologic Map of the Matusevich Glacier Quadrangle, Victoria Land, Antarctica, 1:250000. *Budesanstalt für Geowissenschaften und Rohstoffe (BGR)*.

Rossetti, F., Lisker, F., Storti, F., and Läufer, A. L. (2003). Tectonic and denudational history of the Rennick Graben (North Victoria Land): Implications for the evolution of rifting between East and West Antarctica. *Tectonics*, 22(2).

Rossetti, F., Storti, F., and Salvini, F. (2000). Cenozoic noncoaxial transtension along the western shoulder of the Ross Sea, Antarctica, and the emplacement of McMurdo dyke arrays. *Terra Nova*, 12(2):60–66.

Ruppel, A., Jacobs, J., Eagles, G., Läufer, A., and Jokat, W. (2018). New geophysical data from a key region in East Antarctica: Estimates for the spatial extent of the Tonian Oceanic Arc Super Terrane (TOAST). *Gondwana Research*, 59:97–107.

Saleeby, J., Ducea, M., and Clemens-Knott, D. (2003). Production and loss of high-density batholithic root, southern Sierra Nevada, California. *Tectonics*, 22(6).

Salem, A., Green, C., Ravat, D., Singh, K. H., East, P., Fairhead, J. D., Mogren, S., and Biegert, E. (2014). Depth to Curie temperature across the central Red Sea from magnetic data using the de-fractal method. *Tectonophysics*, 624-625:75–86. Crustal and mantle sources of magnetic anomalies.

Sanchez, G., Halpin, J. A., Gard, M., Hasterok, D., Stål, T., Raimondo, T., Peters, S., and Burton-Johnson, A. (2021). PetroChron Antarctica: A Geological Database for Interdisciplinary Use. *Geochemistry, Geophysics, Geosystems*, 22(12):e2021GC010154.

Scheinert, M., Ferraccioli, F., Schwabe, J., Bell, R., Studinger, M., Damaske, D., Jokat, W., Aleshkova, N., Jordan, T., Leitchenkov, G., Blankenship, D. D., Damiani, T. M., Young, D., Cochran, J. R., and Richter, T. D. (2016). New Antarctic gravity anomaly grid for enhanced geodetic and geophysical studies in Antarctica. *Geophysical Research Letters*, 43(2):600–610.

Schoof, C. (2007). Ice sheet grounding line dynamics: Steady states, stability, and hysteresis. *Journal of Geophysical Research: Earth Surface*, 112(F3).

Shamsipour, P., Marcotte, D., and Chouteau, M. (2012). 3D stochastic joint inversion of gravity and magnetic data. *Journal of Applied Geophysics*, 79:27–37.

Shen, W., Wiens, D. A., Anandakrishnan, S., Aster, R. C., Gerstoft, P., Bromirski, P. D., Hansen, S. E., Dalziel, I. W. D., Heeszel, D. S., Huerta, A. D., Nyblade, A. A., Stephen, R., Wilson, T. J., and Winberry, J. P. (2018). The Crust and Upper Mantle Structure of Central and West Antarctica From Bayesian Inversion of Rayleigh Wave and Receiver Functions. *Journal of Geophysical Research: Solid Earth*, 123(9):7824–7849.

Shen, W., Wiens, D. A., Lloyd, A. J., and Nyblade, A. A. (2020). A geothermal heat flux map of antarctica empirically constrained by seismic structure. *Geophysical Research Letters*, 47(14):e2020GL086955.

Siegert, M. J. and Dowdeswell, J. A. (1996). Spatial variations in heat at the base of the Antarctic ice sheet from analysis of the thermal regime above subglacial lakes. *Journal of Glaciology*, 42(142):501–509.

Sims, K. W. W., Aster, R. C., Gaetani, G., Blichert-Toft, J., Phillips, E. H., Wallace, P. J., Mattioli, G. S., Rasmussen, D., and Boyd, E. S. (2021). Chapter 7.2 Mount Erebus. In *Volcanism in Antarctica: 200 Million Years of Subduction, Rifting and Continental Break-up*. Geological Society of London.

Smith, A. and Drewry, D. (1984). Delayed phase change due to hot asthenosphere causes Transantarctic uplift? *Nature*, 309(5968):536–538.

Smith, B. E., Fricker, H. A., Joughin, I. R., and Tulaczyk, S. (2009). An inventory of active subglacial lakes in Antarctica detected by ICESat (2003–2008). *Journal of Glaciology*, 55(192):573–595.

Smith, W. H. F. and Wessel, P. (1990). Gridding with continuous curvature splines in tension. *GEOPHYSICS*, 55(3):293–305.

Sobh, M., Gerhards, C., Fadel, I., and Götze, H.-J. (2021). Mapping the Thermal Structure of Southern Africa From Curie Depth Estimates Based on Wavelet Analysis of Magnetic Data With Uncertainties. *Geochemistry, Geophysics, Geosystems*, 22(11):e2021GC010041.

Spector, A. and Grant, F. S. (1970). Statistical models for interpreting aeromagnetic data. *Geophysics*, 35(2):293–302.

Steed, R. N. (1983). Structural interpretations of Wilkes Land, Antarctica. In *Antarctic earth science. International symposium. 4*, pages 567–572.

Stern, T. A. and ten Brink, U. S. (1989). Flexural uplift of the Transantarctic Mountains. *Journal of Geophysical Research: Solid Earth*, 94(B8):10315–10330.

Stokes, C. R., Abram, N. J., Bentley, M. J., Edwards, T. L., England, M. H., Foppert, A., Jamieson, S. S., Jones, R. S., King, M. A., Lenaerts, J. T., et al. (2022). Response of the East Antarctic Ice Sheet to past and future climate change. *Nature*, 608(7922):275–286.

Studinger, M., Bell, R. E., Buck, W., Karner, G. D., and Blankenship, D. D. (2004). Sub-ice geology inland of the Transantarctic Mountains in light of new aerogeophysical data. *Earth and Planetary Science Letters*, 220(3):391–408.

Stål, T., Halpin, J. A., Goodge, J. W., and Reading, A. M. (2024). Geology Matters for Antarctic Geothermal Heat. *Geophysical Research Letters*, 51(13):e2024GL110098.

Stål, T., Reading, A. M., Halpin, J. A., and Whittaker, J. M. (2021). Antarctic Geothermal Heat Flow Model: Aq1. *Geochemistry, Geophysics, Geosystems*, 22(2):e2020GC009428.

Subrahmanyam, C., Verma, R., et al. (1981). Densities and magnetic susceptibilities of Precambrian rocks of different metamorphic grade (southern Indian shield). *Journal of Geophysics*, 49(1):101–107.

Szwillus, W., Baykiev, E., Dilixiati, Y., and Ebbing, J. (2022). Linearized Bayesian estimation of magnetization and depth to magnetic bottom from satellite data. *Geophysical Journal International*, 230(3):1508–1533.

Tanaka, A., Okubo, Y., and Matsubayashi, O. (1999). Curie point depth based on spectrum analysis of the magnetic anomaly data in East and Southeast Asia. *Tectonophysics*, 306(3):461–470.

Telford, W. M., Geldart, L. P., and Sheriff, R. E. (1990). *Applied geophysics*. Cambridge university press.

Ten Brink, U. and Stern, T. (1992). Rift flank uplifts and Hinterland Basins: Comparison of the Transantarctic Mountains with the Great Escarpment of southern Africa. *Journal of Geophysical Research: Solid Earth*, 97(B1):569–585.

Ten Brink, U. S., Hackney, R. I., Bannister, S., Stern, T. A., and Makovsky, Y. (1997). Uplift of the Transantarctic Mountains and the bedrock beneath the East Antarctic ice sheet. *Journal of Geophysical Research: Solid Earth*, 102(B12):27603–27621.

Thomson, J. W. and Cooper, A. P. R. (1993). The SCAR Antarctic digital topographic database. *Antarctic Science*, 5(3):239–244.

Todoeschuck, J. P., Pilkington, M., and Gregotski, M. E. (1992). If geology is fractal, what do we do next? *The Leading Edge*, 11(10):29–35.

Treitel, S., Clement, W. G., and Kaul, R. K. (1971). The Spectral Determination of Depths to Buried Magnetic Basement Rocks. *Geophysical Journal International*, 24(4):415–428.

Turcotte, D. and Schubert, G. (2014). *Geodynamics*. Cambridge University Press, 3 edition.

Van Liefferinge, B., Pattyn, F., Cavitte, M. G. P., Karlsson, N. B., Young, D. A., Sutter, J., and Eisen, O. (2018). Promising Oldest Ice sites in East Antarctica based on thermodynamical modelling. *The Cryosphere*, 12(8):2773–2787.

Virtanen, P., Gommers, R., Oliphant, T. E., Haberland, M., Reddy, T., Cournapeau, D., Burovski, E., Peterson, P., Weckesser, W., Bright, J., et al. (2020). Scipy 1.0: fundamental algorithms for scientific computing in python. *Nature methods*, 17(3):261–272.

Wang, Y. and Hou, S. (2009). A new interpolation method for Antarctic surface temperature. *Progress in Natural Science*, 19(12):1843–1849.

Wannamaker, P., Hill, G., Stodt, J., Maris, V., Ogawa, Y., Selway, K., Boren, G., Bertrand, E., Uhlmann, D., Ayling, B., et al. (2017). Uplift of the central Transantarctic Mountains. *Nature Communications*, 8(1):1588.

Wasilewski, P. J., Thomas, H. H., and Mayhew, M. A. (1979). The Moho as a magnetic boundary. *Geophysical Research Letters*, 6(7):541–544.

Whitehouse, P. L., Gomez, N., King, M. A., and Wiens, D. A. (2019). Solid Earth change and the evolution of the Antarctic Ice Sheet. *Nature communications*, 10(1):503.

Wiens, D. A., Shen, W., and Lloyd, A. J. (2023). The seismic structure of the Antarctic upper mantle. In *The Geochemistry and Geophysics of the Antarctic Mantle*. Geological Society of London.

Wilson, G., Damaske, D., Möller, H.-D., Tinto, K., and Jordan, T. (2007). The geological evolution of southern McMurdo Sound - new evidence from a high-resolution aeromagnetic survey. *Geophysical Journal International*, 170(1):93–100.

Winkelmann, R., Martin, M. A., Haseloff, M., Albrecht, T., Bueler, E., Khroulev, C., and Levermann, A. (2011). The Potsdam Parallel Ice Sheet Model (PISM-PIK) – Part 1: Model description. *The Cryosphere*, 5(3):715–726.

Winsborrow, M. C., Clark, C. D., and Stokes, C. R. (2010). What controls the location of ice streams? *Earth-Science Reviews*, 103(1):45–59.

Yamasaki, T., Miura, H., and Nogi, Y. (2008). Numerical modelling study on the flexural uplift of the Transantarctic Mountains. *Geophysical Journal International*, 174(1):377–390.

Zanutta, A., Negusini, M., Vittuari, L., Martelli, L., Cianfarra, P., Salvini, F., Mancini, F., Sterzai, P., Dubbini, M., and Capra, A. (2018). New Geodetic and Gravimetric Maps to Infer Geodynamics of Antarctica with Insights on Victoria Land. *Remote Sensing*, 10(10).